SONICALLY INDUCED NARROWING OF THE NMR SPECTRA OF SOLIDS AND OTHER NOVEL NMR TECHNIQUES.

STUART ALEXANDER PALFREYMAN

Doctor of Philosophy

THE UNIVERSITY OF ASTON IN BIRMINGHAM

September 1996

The University of Aston in Birmingham

SONICALLY INDUCED NARROWING OF THE NMR SPECTRA OF SOLIDS AND OTHER NOVEL NMR TECHNIQUES.

STUART ALEXANDER PALFREYMAN

Doctor of Philosophy

1996

A typical liquid state NMR spectrum is composed of a number of discrete absorptions which can be readily interpreted to yield detailed information about the chemical environment of the nuclei found within the sample. The same cannot be said about the spectra of solid samples. For these the absorptions are typically broad, featureless and yield little information directly. This situation may be further exacerbated by the characteristically long T_1 values of nuclei bound within a solid lattice which, consequently, require long inter-sequence delays that necessitate lengthy experiments. This work attempts to address both of these inherent problems.

Classically, the resolution of the broad-line spectra of solids into discrete resonances has been achieved by imparting to the sample coherent rotation about specific axes in relation to the polarising magnetic field, as implemented in the magic-angle spinning (MAS) [1], dynamic angle spinning (DAS) [2] and double rotation (DOR) [3] NMR experiments. Recently, an alternative method, sonically induced narrowing of the NMR spectra of solids (SINNMR) [4], has been reported which yields the same well resolved solid-state spectra as the classic solid-state NMR experiments, but which achieves the resolution of the broad-line spectra through the promotion of incoherent motion in a suspension of solid particles. The first part of this work examines SINNMR and, in particularly, concentrates on ultrasonically induced cavitation, a phenomena which is thought to be essential to the incoherent averaging mechanism.

The second part of this work extends the principle of incoherent motion, implicit in SINNMR, to a new genre of particulate systems, air fluidized beds, and examines the feasibility of such systems to provide well resolved solid state NMR spectra. Samples of trisodium phosphate dodecahydrate and of aluminium granules are examined using the new method with partially resolved spectra being reported in the case of the latter.

Finally, the problem of long relaxation times is addressed. A new pulse sequence is developed, initially for liquids but for adaptation to solid state work, which makes the most efficient use of the available magnetization in many spin systems found in NMR spectroscopy. Using such a sequence time savings of 30% are reported over those sequences usually employed in routine NMR investigations.

Key Words: SINNMR, ESR, Cavitation, Fluidized Beds, SNARE.

This thesis is dedicated to my grandmother, the late Clare Palfreyman, whose positive influence on my life has helped me through this and many other 'impossible' tasks.

Chop off your legs and you will
never go astray.

ACKNOWLEDGEMENTS

I would like to express my sincere gratitude to both my supervisor, Dr. John Homer, for his continued advice and assistance over the last four years, and to the EPSRC for the provision of a research grant.

I would also like to express my thanks to Dr. Mike Perry for running many of the experiments on which this work is based, Professor Jacques Reisse (Universite Libre de Brusselles) for providing the Chemsonics apparatus and Dr. Jeremy Lee (while at Brüker Spectrospin, Coventry) for providing a Brüker EMS 104 EPR Analyzer.

I am also grateful for the support from a number of other academic staff; Professor W.R. McWhinnie, Dr Martin Beevers, Dr. Jack McCoubrey and Dr. Tony Kakhu from within the department of Chemical Engineering and Applied Chemistry; Mr. George Pearce, from the department of Electrical Engineering; Dr. Christian Jaeger of the University of Jena and Professor Martyn Symons (FRS) previously of Leicester University.

My thanks are also due to my colleagues, past and present, who have worked alongside me in the NMR spectroscopy research group; Dr. Mark Howard, Mr. Gavin Tilstone, Mr. Steven Reynolds, Miss Anna Weekes, Mr. Spencer Davies and Dr. John Robson.

This section would not be complete without me offering thanks to my family. I would, therefore, like to offer my most profound gratitude to my parents, Alan and Margaret, whose never-ending emotional and financial support made all of this possible; to my brother, James, for keeping me in touch with the real world; and to my grandparents, Norman and Winifred Wells, for their continued interest and encouragement.

Finally, I would like to thank the many people who have kept me sane, provided me with emotional sandbags and with whom I have had coffee breaks during my time in Birmingham. On this front I would particularly like to acknowledge the efforts of Nickie Coleman who, in addition to the above, also provided me with Guiness, Murphy's, hangovers, tea by the gallon, munchies, eggy bread, games of pool . . . . .

Stuart Palfreyman, 1996.

Table of Contents.

Part 4 : The Use of Fluidized Beds in NMR Spectroscopy.

List of Figures.

Part 2 : Introduction to Nuclear Magnetic Resonance Spectroscopy.

Part 4 : The Use of Fluidized Beds in NMR Spectroscopy.

Appendices.

List of Tables.

Part 2 : Introduction to Nuclear Magnetic Resonance Spectroscopy.

Part 3 : The Use of Ultrasound in Magnetic Resonance Spectroscopy.

Part 4 : The Use of Fluidized Beds in NMR Spectroscopy.

Part 5 : New Pulse Sequences for NMR Spectroscopy.

Appendices.

List of Schemes.

Part 2 : Introduction to Nuclear Magnetic Resonance Spectroscopy.

Part 5 : New Pulse Sequences for NMR Spectroscopy.

Part 1

Overview

1 Introduction

In the 50 year life of NMR spectroscopy, following the first NMR spectroscopic observations made independently by Purcell *et al.*[5] and Bloch *et al.*[6] the analytical power of the technique has increased phenomenally. The steady march of innovation in NMR during this period has been down two distinct paths *viz.* on the one hand hardware advances, which include the development of stable magnetic fields, micro-computer controlled consoles and highly specialised NMR probes and on the other hand conceptual advances, which include the development of new theories and their implementation to produce new NMR experiments. Both these paths are not, however, independent of each other, advances in one area commonly driving advances in the other. The work presented here attempts to continue these advances both in the invention and development of new NMR techniques and in the further investigation and development of established techniques.

The main thrust of this thesis is concerned with furthering the applicability of the 'sonically induced narrowing of the NMR spectra of solids' - SINNMR [4] (part 3) and the adaptation of incoherent averaging techniques to generate new solid state NMR experiments (part 4). Initially, it was hoped that SINNMR might be able to resolve J-coupling in solids. As, according to Dr C. Jaeger (University of Jena), it is now possible to adapt any experiment that relies on J-coupling to yield comparable experiments that rely on dipolar coupling [7], investigations into new pulse sequences for NMR were also undertaken with a view to their implementation in the NMR study of solids (part 5).

Part 2 provides an introduction to the theory and practice of NMR spectroscopy which is the basis of the work presented in the other parts: corresponding introductions to ultrasound and fluidized beds are given in parts 3 and 4 for a similar reason. Further reading on aspects of NMR, ultrasound or fluidized beds can be gained from the texts listed in the relevant bibliographies.

Part 2

Introduction to Nuclear Magnetic Resonance Spectroscopy.

Chapter 1

Nuclear Magnetic Resonance.

1.1 Introduction.

It is not possible to perform nuclear magnetic resonance (NMR) spectroscopy on all nuclei, for although all nuclei possess the properties of mass and charge, not all possess nuclear spin angular momentum[8] that is characterized by the spin quantum number, I. Only when this nuclear spin operates on the nuclear charge is a nuclear magnetic moment formed, the manipulation of which forms the basis of nuclear magnetic resonance spectroscopy. Given the atomic number and atomic mass of a nucleus it is possible to predict, to a certain extent, the nuclear spin quantum number. (table 2.1)

Table 2.1 : A relationship between atomic mass, atomic number and nuclear spin (I).

Atomic mass (A)	Atomic number (Z)	Nuclear spin quantum number(I)
Even	Even	Zero
Odd	Any value	A half-integral value.
Odd	Odd	A non-zero integral value.

Those nuclei which are detectable by NMR fall into one of two classifications. These are dipolar nuclei which have a spin quantum number equal to ½ and the quadrupolar nuclei which have a spin quantum number greater than ½. It is interesting to point out that ^{12}C, the 99% abundant isotope of carbon, has I=0 (A=12, Z=6), and as such is invisible to NMR. Fortunately, for synthetic organic chemists, the 1% naturally abundant ^{13}C isotope of carbon is a dipolar nucleus which is readily observable using todays modern spectrometers.

The quantum mechanical relationship [9-13] between the spin quantum number, I, and the nuclear angular momentum, **P**, is derived in appendix 1. This relationship shows that **P** has a magnitude, P, defined by;

$$P = \frac{h}{2\pi}\sqrt{I(I+1)} \quad = \quad \hbar\sqrt{I(I+1)} \tag{2.1}$$

where h is Planck's constant and $\hbar$ is the reduced Planck's constant ($\hbar = h/2\pi$). The derivation shows that simultaneously to the magnitude of **P**, one of the cartesian components of **P** may also be known. If this component is chosen to be the z component of **P**, P_z, then it is also shown that **P** is quantized in P_z in terms of a quantum number 'm_z' such that;

$$P_z = \hbar m_z \qquad m_z = -I, -I+1, -I+2, \ldots, I-2, I-1, I \tag{2.2}$$

where m ranges from -I to I in integral steps as indicated.

Incorporating these quantum mechanical descriptions of angular momentum into a classical vector description necessitates that **P** be inclined at an angle to the z-axis, but that its orientation in the x-y plane be unspecified, figure 2.1.

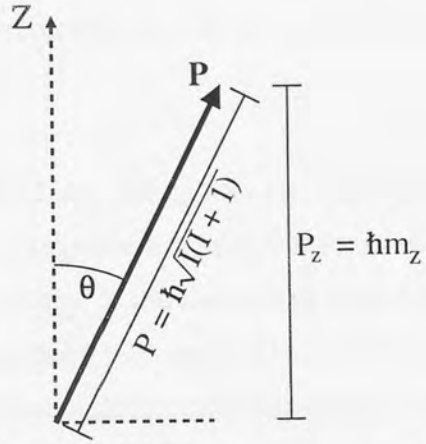

Figure 2.1 : Orientation of **P** as required by the quantum mechanical restrictions imposed on P and P_z.

Thus, the angle, θ, that **P** makes to the z-axis is defined by;

$$\cos\theta = \frac{m_z}{\sqrt{I(I+1)}} \tag{2.3}$$

Figure 2.2 shows the possible orientations of the angular momentum for a nucleus with a spin quantum number of 3/2, allowing 'm_z' to have values -3/2, -1/2, 1/2 and 3/2.

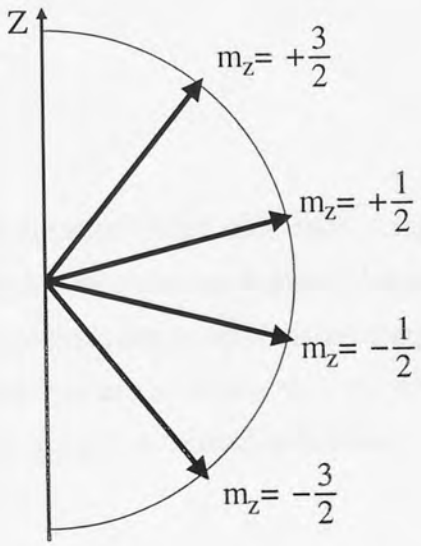

Figure 2.2 : Possible orientations of **P** for a I =3/2 nucleus.

1.2 The Isolated Nucleus in a Magnetic Field.

The terms 'spin quantum number' and 'angular momentum' both imply that the nucleus is spinning about an axis. If this is considered to be the case then the motion of nuclear charge about this axis must induce a magnetic moment, $\boldsymbol{\mu}$, the size and direction of which is directly proportional to the angular momentum. The magnetogyric ratio, γ, is used to relate these two parameters and adopts a characteristic value for each nucleus;

$$\boldsymbol{\mu} = \gamma \mathbf{P} \tag{2.4}$$

When the nucleus is placed into a magnetic field, $\mathbf{B}$ (the direction of which defines the z-axis of the system), the magnetic moment and magnetic field will interact with each other causing the total energy of the nucleus to be dependent on their relative orientations. However, as has been previously discussed, the spatial orientation of the angular momentum is quantized, necessitating the spatial quantization of the magnetic moment. Consequently, only distinct orientations of the magnetic moment are available to interact with the external magnetic field, resulting in the formation of distinct energy levels. The energy, U, of the interaction between a magnetic moment and a magnetic field is given by the dot product of $\mathbf{B}$ and $\boldsymbol{\mu}$, this essentially being the product of the z component of the magnetic moment, μ_z, and the z component of magnetic field, B;

$$U = -\boldsymbol{\mu} \cdot \mathbf{B} = -\mu_z B \tag{2.5}$$

which in terms of the angular momentum quantum number, m_z, becomes;

$$\begin{aligned} U &= -\boldsymbol{\mu} \cdot \mathbf{B} \\ &= -\gamma \mathbf{P} \cdot \mathbf{B} \\ &= -\gamma \hbar \mathbf{m} \cdot \mathbf{B} \\ &= -\gamma \hbar m_z B \end{aligned} \tag{2.6}$$

Thus, 2I+1 energy levels are established with each being separated from adjacent energy levels by $\gamma\hbar B$. Given this information it should be possible to cause transitions between these energy levels by applying an appropriate frequency of radiation. As the selection rules for NMR transitions are such that m_z can only change by ± 1, an absorption of energy corresponding to a transition between quantum states should, therefore, occur at;

$$\begin{aligned} h\nu &= |\gamma \hbar B| \\ \nu &= \left| \frac{\gamma B}{2\pi} \right| \end{aligned} \tag{2.7}$$

where ν is the required frequency of the incident radiation. Figure 2.3 exemplifies how, for an I=3/2 nucleus, the separation of the energy levels and corresponding frequency of incident radiation is dependent on magnetic field strength.

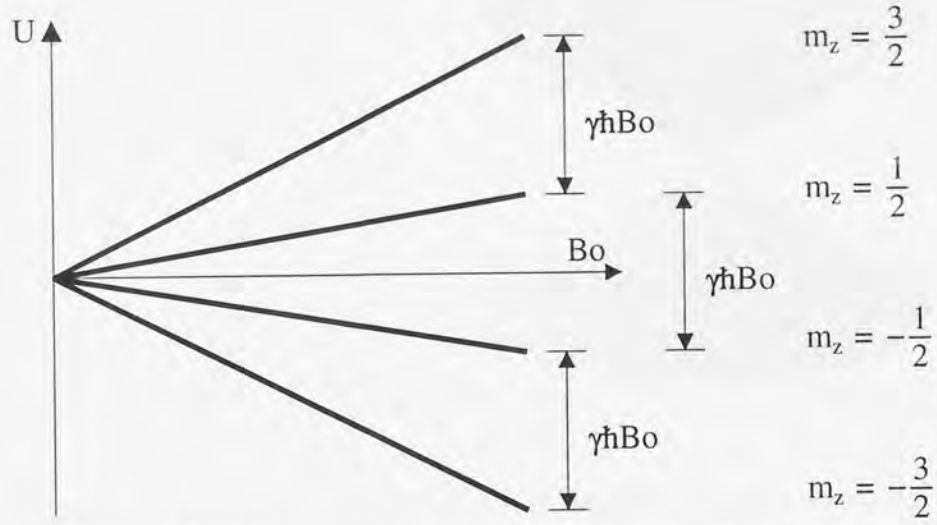

Figure 2.3 : Change in energy levels with magnetic field , $\mathbf{B_0}$.

1.3 Classical Motion of the Magnetic Moment - Larmor Precession

Considering the classical interaction between a magnetic field, $\mathbf{B_0}$, and a magnetic moment, $\boldsymbol{\mu}$, a torque acts which attempts to align the magnetic moment with the magnetic field. However, if the nucleus is energetically isolated from its environment, it must be under conditions of constant energy and, as such, the z component of $\boldsymbol{\mu}$ must remain unaltered. This limitation forces the torque to act perpendicularly to the magnetic field, causing the magnetic moment to precess around $\mathbf{B_0}$. The name given to this precession is Larmor precession which occurs at an angular velocity ω such that;

$$\omega = -\gamma \mathbf{B_o} \tag{2.8}$$

Due to the quantization of angular momentum, as show in equation(2.2), only discrete orientations of the angular momentum relative to the magnetic field are possible. As the angular momentum is co-linear with the magnetic moment the half angle, θ, of the Larmor precessional cone must similarly be restricted. Figure 2.4.a shows the precession of a magnetic moment about $\mathbf{B_0}$ and figure 2.4.b shows the precessional cones for a I=½ nucleus, one cone at 54.73° to the z axis the other at 125.26°.

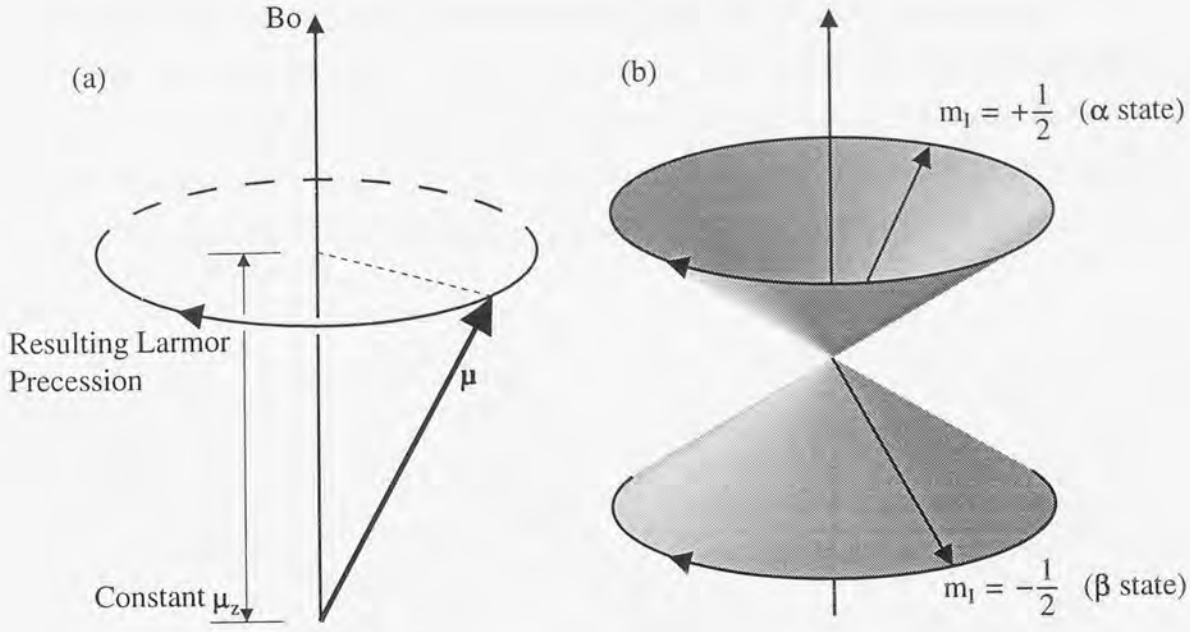

Figure 2.4 (a) : Larmor precession of a magnetic moment about $\mathbf{B_0}$.
(b) : Precessional cones for a I=½ nucleus.

1.4 Effect of a Second, Small Magnetic Field.

If a second, small static magnetic field, $\mathbf{B_1}$, is applied to the nucleus the magnetic moment will precess about the resultant magnetic vector and appears to wobble about $\mathbf{B_0}$. If, however, $\mathbf{B_1}$ is perpendicular to $\mathbf{B_0}$ and is allowed to rotate with the same angular velocity as the magnetic moment, the magnetic moment will always be under the influence of a torque forcing it away from the z axis, nutating it initially down into the xy plane. As a consequence of this nutation the z component of the magnetic moment is altered and the energy of the spin system changed. As this only occurs when ω is equal to the Larmor precessional frequency of the nucleus the energy transfer is said to occur via a resonance mechanism. The angular velocity (and hence the frequency ν) of $\mathbf{B_1}$, required to meet this resonant condition is;

$$\begin{aligned} \omega_I &= -\gamma \mathbf{B_o} \\ 2\pi\nu_I &= -\gamma \mathbf{B_o} \\ \nu_I &= \left|\frac{\gamma}{2\pi}\right| \mathbf{B_o} \end{aligned} \qquad (2.9)$$

Initially it would appear that to cause resonant absorption it is necessary to provide a circularly polarised source of B_1 radiation. This is not the case and B_1 is usually provided by irradiating the sample with a sinusoidally oscillating electromagnetic wave: Such an electromagnetic wave of frequency ν and amplitude $2B_1$ may be considered as being composed of two contra-rotating, circularly polarized, electromagnetic waves; one component propagating with the phase twist of the magnetic vector occurring at a

frequency of $+\nu$ relative to the constant phase of the sinusoidal wave, the other component propagating with a phase twist frequency of $-\nu$, both having an amplitude B_1 (Figure 2.5). The component with a phase twist frequency of $-\nu$ is incapable of perturbing the nuclear system, but that component with a phase twist frequency of $+\nu$ satisfies the requirement of equation(2.9) and the resonant absorption of energy occurs.

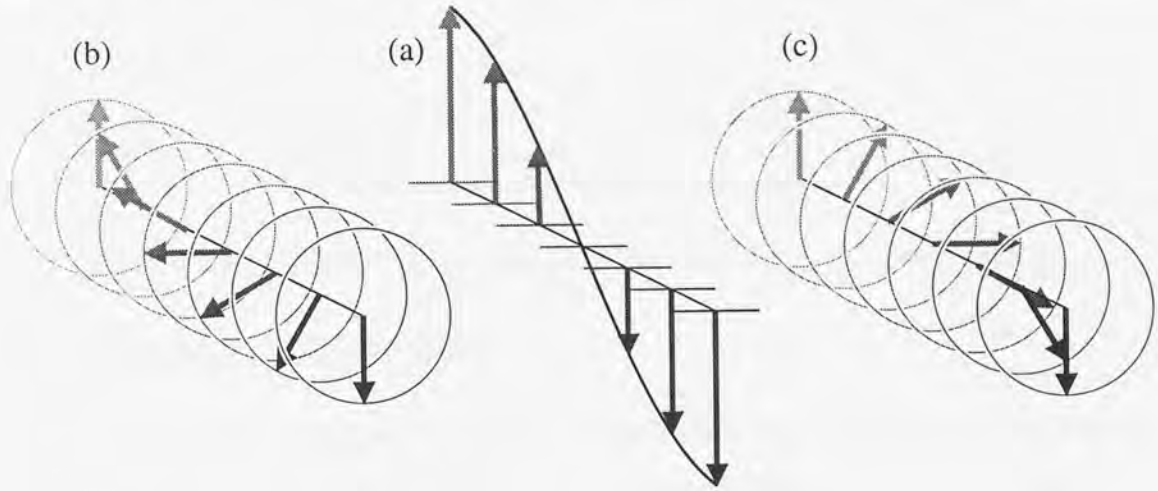

Figure 2.5 : (**a**) A sinusoidal wave of frequency ν and amplitude $2B_1$ with its circularly polarised components of amplitude B_1 and frequency (**b**)-ν and (**c**)+ν.

1.5 The Rotating Frame.

When discussing the action of a $\mathbf{B_1}$ field on a magnetic moment it is useful to shift our frame of reference from one based on the static laboratory frame with axes x,y and z, to one that rotates about $\mathbf{B_0}$ with an angular velocity ω_r (with axes x',y' and z). When a magnetic moment of angular velocity ω is viewed from such a frame of reference it appears to be rotating with an angular velocity of $(\omega-\omega_r)$ about an apparent magnetic field, $\mathbf{B_{app}}$, of magnitude $(\omega-\omega_r)/\gamma$ which is co-linear with $\mathbf{B_0}$. Thus, when ω_r is identical to the Larmor precessional rate of the nuclear spin, $\boldsymbol{\mu}$ appears stationary in the rotating frame.

When a $\mathbf{B_1}$ magnetic field is introduced to the nuclear system it is useful to choose a frame of reference that rotates with the same angular velocity as $\mathbf{B_1}$ so that, when viewed using this reference, $\mathbf{B_1}$ remains stationary. In the laboratory frame, while $\mathbf{B_1}$ is active, $\boldsymbol{\mu}$ precesses about the total magnetic field vector, $\mathbf{B_{tot}}$, which is the resultant of $\mathbf{B_1}$ and $\mathbf{B_0}$. In the rotating frame $\boldsymbol{\mu}$ precesses about an effective magnetic field $\mathbf{B_{eff}}$ which is the resultant of $\mathbf{B_1}$ and $\mathbf{B_{app}}$. Thus, when the frequency of $\mathbf{B_1}$ is identical to the Larmor precessional rate of the magnetic moment, $\mathbf{B_{app}}$ is the null vector and $\boldsymbol{\mu}$ appears, in the rotating frame, to precesses about $\mathbf{B_1}$ alone.

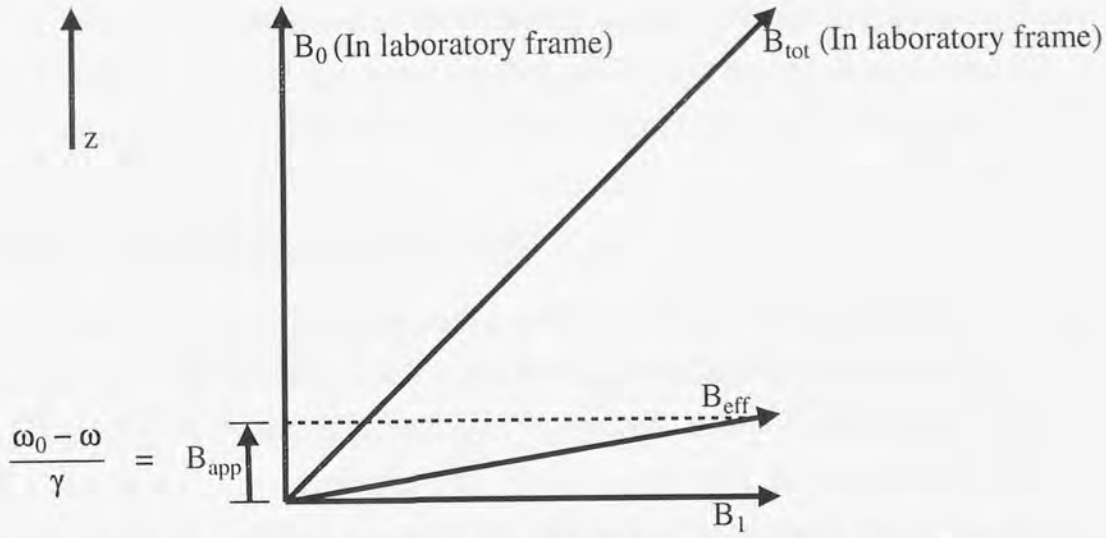

Figure 2.6 : Magnetic fields present in the laboratory and rotating frame.

1.6 An Ensemble of Dipolar Nuclei.

So far the discussion has been concerned with individual nuclei which, for dipolar nuclei, have either been aligned parallel with or anti-parallel to the applied magnetic field, in states referred to as α and β respectively. If an ensemble of such spins is now consider it will show a Boltzmann distribution across the occupancy of the spin states. Given that the spin populations of the α and β spin states are N_α and N_β respectively ($N_\alpha + N_\beta = N_{tot}$), the relative occupancy of the two energy states can be deduced from the Boltzmann equation to be;

$$\frac{N_\beta}{N_\alpha} = e^{\left(-\frac{\Delta E}{kT}\right)} = e^{\left(-\frac{\gamma\hbar B}{kT}\right)} \qquad (2.10)$$

where the absolute temperature is T and the energy difference, ΔE, between the energy levels is $\gamma\hbar B$. Equation(2.10) can be approximated to;

$$\frac{N_\beta}{N_\alpha} = 1 - \frac{\gamma\hbar B}{kT} \qquad (2.11)$$

For a sensitive nucleus such as the proton, placed in a 5.8 Tesla magnetic field (causing the protons to resonate at approximately 250MHz), the energy difference between the two levels is very small ($\Delta E = 1.636\times10^{-25}$J). Consequently there is only a small population difference, Δn_0, (0.002% of the sample at 298K) between the α and β states, equation(2.12).

$$\Delta n_o = \frac{N_{tot}\gamma\hbar B_o}{2kT} \qquad (2.12)$$

As nuclear magnetic resonance spectroscopy works by manipulating the excess of spins populating one of the spin states, and that this excess makes up only a small fraction of the sample, nuclear magnetic resonance spectroscopy is a relatively insensitive technique.

1.7 Bulk Magnetization of a NMR Sample.

Due to the excess of nuclei populating the lower energy state, the sample develops a bulk magnetization, **M**, ($\mathbf{M_0}$, if this at the Boltzmann equilibrium) caused by the cumulative effect of the individual magnetic moments. As all of the excess magnetic moments are in the same energy state they must each have a component of their individual moments which acts in the same direction as the magnetic field. However, as the magnetic moments are spread out randomly about their precessional cones, a similar coherence does not naturally occur in the x-y plane. Consequently, a bulk magnetization ($\mathbf{M_0}$) is generated co-linearly to $\mathbf{B_0}$, the magnitude being related to the excess spin population in the system;

$$M_0 = N_\alpha \mu_{z\alpha} + N_\beta \mu_{z\beta}$$

$$= \Delta n_o \mu_{z\alpha}$$

$$= \frac{\gamma\hbar\Delta n_o}{2}$$

$$M_0 = \frac{N_{tot}(\gamma\hbar)^2 B_o}{4kT} \qquad (2.13)$$

Figure 2.7.a shows the generation of the bulk magnetization vector from the excess α spin states.

The action of the $\mathbf{B_1}$ magnetic field causes each of the individual magnetic moments to nutate about it. As all of the magnetic moments making up the precessional cone are rotated to the same degree, their resultant magnetic moment, $\mathbf{M_o}$, is also rotated by the same amount. Figure 2.7.b

It is, therefore, possible to consider the bulk magnetization vector as representative of the whole sample and, when considering simple NMR experiments, it is only necessary to consider the action of the $\mathbf{B_1}$ magnetic field on the bulk magnetization vector alone.

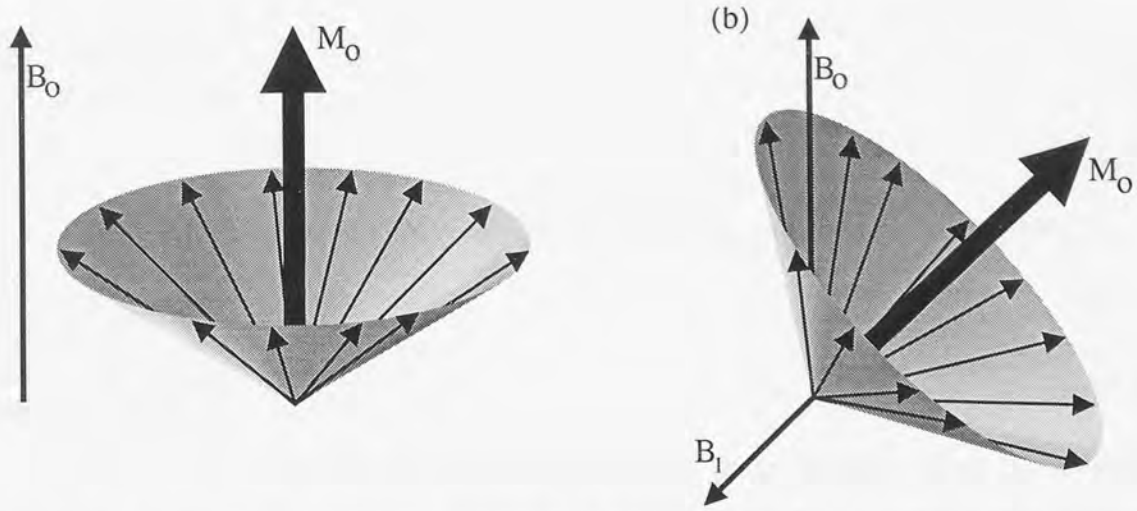

Figure 2.7 : Bulk magnetization vector **(a)** at equilibrium and **(b)** while being nutated about $\mathbf{B_1}$.

1.8 The Bloch Equations

Given that the classical vector model of NMR predicted that a sample would have a bulk magnetization vector, Bloch [14] attempted to devise a number of equations the solution to which [15] could describe the magnetic resonance phenomenon and NMR experiments.

Initially it was assumed that the bulk magnetization vector, **M**, could be resolved into three components, M_x, M_y and M_z in the laboratory frame (Figure 2.8)

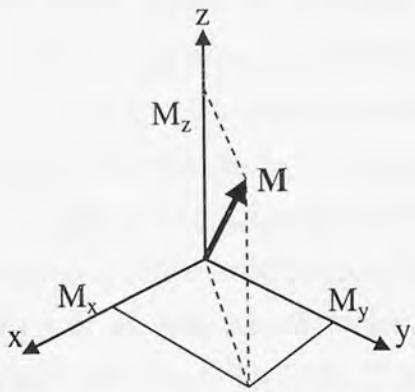

Figure 2.8 : Components of the Bulk Magnetization Vector.

If the sample is energetically isolated then M_z remains unchanged, while the x and y components vary due to the Larmor precession of the bulk magnetization vector. As the angular velocity of the bulk magnetization vector is the same as the individual magnetic moments the rate of change for each component can be defined as;

$$\frac{dM_x}{dt} = \gamma B_o M_y \qquad (2.14)$$

$$\frac{dM_y}{dt} = -\gamma B_o M_x \tag{2.15}$$

$$\frac{dM_z}{dt} = 0 \tag{2.16}$$

The perturbing $\mathbf{B_1}$ field may also be split into two orthogonal components;

$$B_{1x} = B_1\cos(\omega t) \tag{2.17}$$

$$B_{1y} = -B_1\sin(\omega t) \tag{2.18}$$

If the $\mathbf{B_1}$ field is now allowed to perturb the bulk magnetization vector the x and y components of $\mathbf{B_1}$ act on the respective components of the bulk magnetization vectors resulting in the x-axis containing a component of M_y rotating about $\mathbf{B_0}$ as well as a component of M_z rotating about $\mathbf{B_1}$. The rate equation in equations(2.14),(2.15) and (2.16) can, therefore, be adjusted to;

$$\frac{dM_x}{dt} = \gamma(B_o M_y - B_{1y} M_z) \tag{2.19}$$

$$\frac{dM_y}{dt} = -\gamma(B_o M_x + B_{1x} M_z) \tag{2.20}$$

$$\frac{dM_z}{dt} = -\gamma(B_{1y} M_x - B_{1x} M_y) \tag{2.21}$$

Bloch also assumed that the NMR system had mechanisms present whereby the components of the perturbed system could relax, exponentially, back to their Boltzmann equilibrium conditions (Section 1.9). It was further assumed that the relaxation mechanisms of those components perpendicular to the magnetic field would be different from those which were parallel to it. Consequently the x and y components of bulk magnetization vector are given a different relaxational rate, characterized by T_2, to the relaxational rate of the z component, which is characterized by T_1. When these relaxational effects are introduced into equations(2.19), (2.20) and (2.21) the Bloch equations for the laboratory frame are obtained.

$$\frac{dM_x}{dt} = \gamma\left[B_o M_y - M_z B_1\sin(\omega t)\right] - \frac{M_x}{T_2} \tag{2.22}$$

$$\frac{dM_y}{dt} = -\gamma\left[B_o M_x + M_z B_1\cos(\omega t)\right] - \frac{M_y}{T_2} \tag{2.23}$$

$$\frac{dM_z}{dt} = -\gamma\left[-M_x B_1\sin(\omega t) - M_z B_1\cos(\omega t)\right] - \frac{M_z - M_o}{T_1} \tag{2.24}$$

Once again it is simpler to consider the action of the bulk magnetization vector in the rotating frame rather than in the laboratory frame. If this is the case and the $\mathbf{B_1}$ field defines the x'-axis then for a Larmor frequency of ω_0 and a rotating frame frequency of ω, equations (2.22), (2.23) and (2.24) become;

$$\frac{dM_{x'}}{dt} = (\omega_0 - \omega)M_{y'} - \frac{M_{x'}}{T_2} \tag{2.25}$$

$$\frac{dM_{y'}}{dt} = -(\omega_0 - \omega)M_{x'} - \frac{M_{y'}}{T_2} + \gamma B_1 M_{z'} \tag{2.26}$$

$$\frac{dM_{z'}}{dt} = -\gamma B_1 M_{y'} - \frac{M_z - M_0}{T_1} \tag{2.27}$$

Under steady state conditions, where the power of the radio frequency stimulation is low ($\gamma \mathbf{B_1^2} T_1 T_2 \ll 1$), the x, y and z components of **M** are;

$$M_{x'} = M_0 \frac{\gamma B_1 T_2^2 (\omega_0 - \omega)}{1 + 4\pi T_2^2 (\omega_0 - \omega)^2} \tag{2.28}$$

$$M_{y'} = M_0 \frac{\gamma B_1 T_2}{1 + 4\pi T_2^2 (\omega_0 - \omega)^2} \tag{2.29}$$

$$M_z = M_0 \frac{1 + 4\pi T_2^2 (\omega_0 - \omega)^2}{1 + 4\pi T_2^2 (\omega_0 - \omega)} \tag{2.30}$$

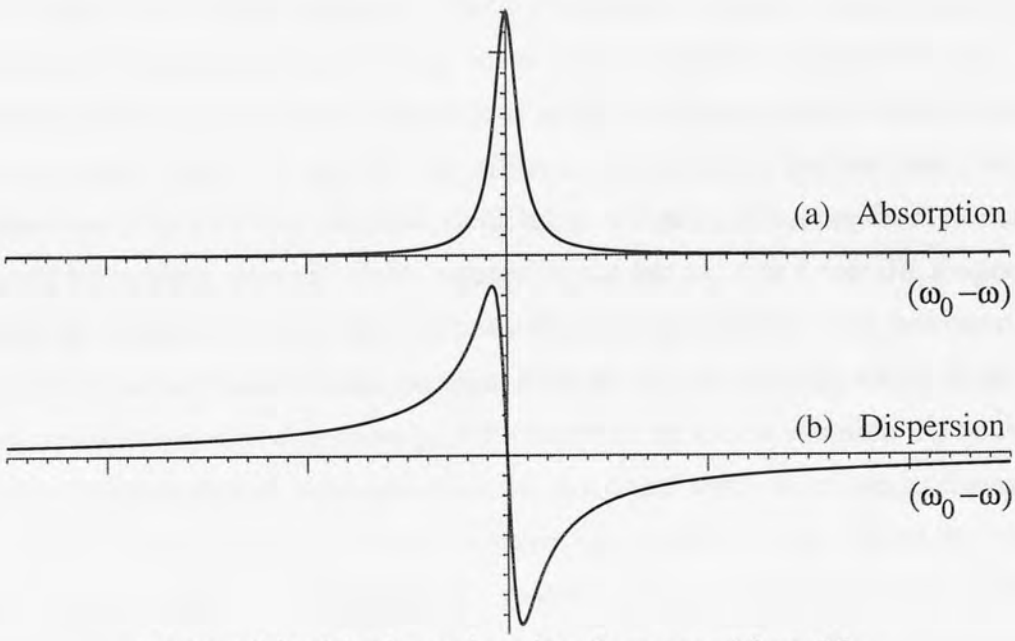

Figure 2.9 : (a) Absorption signal generated from $M_{y'}$.
(b) Dispersion signal generated from $M_{x'}$.

Thus, the Bloch equations predict that, under conditions where a weak $\mathbf{B_1}$ field is used to continuously stimulate the sample, two detectable components of the bulk magnetization vector are generated in the x'-y' plane. The signal from the $M_{x'}$ component gives a dispersion signal while the signal from the $M_{y'}$ component gives an absorption signal. Indeed the detection of these signals was the basis of the first NMR spectrometers, which employed a weak $\mathbf{B_1}$ field to scan the resonant frequencies and a phase sensitive detector to measure the $M_{y'}$ component of **M**. Figure 2.9 shows the absorption and dispersion signals as the frequency of the rotating frame is scanned from below ω_0 to above ω_0 .

1.9 Relaxation in Nuclear Magnetic Resonance Spectroscopy.

The derivation of the Bloch equations in the previous section assumed mechanisms whereby the perturbed NMR system can relax back toward its Boltzmann equilibrium state and that the relaxational rate depends on whether the relaxation occurred parallel with or perpendicular to the applied magnetic field. This is indeed the case with spin-lattice relaxation governing the relaxation of M_z towards $\mathbf{M_0}$ along the z-axis and spin-spin relaxation governing the relaxation both M_x and M_y to $M_x=M_y=0$. Both spin-lattice and spin-spin relaxation occur a different rates and these are characterised by the times T_1 and T_2 respectively.

1.9.1 Spin-Lattice Relaxation.

All spins in the NMR system are linked to each other by their weak magnetic interactions. This conglomeration of spins, collectively known as the lattice, is constantly producing fluctuating interactions as the constituent nuclei undergo random thermal motion. If we now consider the effect at one nucleus it can seen that, besides the influence of the external magnetic field, there will be an influence from a small, randomly fluctuating magnetic field, induced by the lattice. For a specific magnetic moment the x-y component of the randomly fluctuating magnetic field generated by the lattice will, at some instantaneous moment, have an angular velocity which is the same as the Larmor precessional frequency of the nucleus. In such a situation the nucleus and the lattice couple and, if the nucleus is in an excited state, this enables the excess energy to be transferred away from the nucleus, allowing it to relax. Equation(2.31) relates the spin-lattice relaxation time, T_1, to the spectral density, $J(\omega)$, of the random magnetic field and the root mean square amplitude of the random field along the x axis $|B^0_{1x}|$.

$$\frac{1}{T_1} = \gamma^2 |B_{1x}^0|^2 J(\omega) \tag{2.31}$$

In certain situations it is possible to manipulate the bulk magnetization vector so that it lies along either the x' or y' axis. Applying a $\mathbf{B_1}$ field along the appropriate axis now has the effect of locking the bulk magnetization vector along the respective axis, a process called spin locking. In such a situation the $\mathbf{B_0}$ field is replaced by the $\mathbf{B_1}$ field and relaxation in the $\mathbf{B_1}$ direction occurs that is analogous to spin-lattice relaxation. This process has a characteristic value of $T_{1\rho}$, and is usually referred to as T_1 in the rotating frame. Equation(2.32) relates $T_{1\rho}$ to the spectral density in a manner that is analogous to equation(2.31).

$$\frac{1}{T_{1\rho}} = \frac{1}{6}\gamma^2\left(|B_{x1}^0|^2 + |B_{y1}^0|^2 + |B_{z1}^0|^2\right)\left(J(\Omega) + J(\omega_0)\right) \tag{2.32}$$

where $J(\Omega)$ is the spectral density function when applied to the rotating frame, $\Omega=\gamma\mathbf{B_1}$.

As, in the absence of the B_1 field, the relaxation in the x'-y' plane occurs via spin-spin relaxation (section 1.9.2), $T_{1\rho}$ relaxation is also related to T_2 relaxation, indeed in most liquids $T_{1\rho}=T_2$.

1.9.2 Spin-Spin Relaxation

Whereas spin-lattice relaxation results in the net transfer of energy away from the spin system, spin-spin relaxation results in the energy interchange of two spins, with no net effect on the total energy of the spin system.

A coherence in the x-y plane occurs only after the bulk magnetization vector has been nutated away from its equilibrium value by the application of a $\mathbf{B_1}$ field. As the sample undergoes thermal motion, two nuclei with identical Larmor precessional frequencies but in different spin states may come into intimate contact with each other. During this contact period the magnetic moment of each nucleus will induce an oscillating magnetic field at the position of the other. As both nuclei have the same Larmor precessional frequency the induced magnetic fields will be of the correct frequency to cause an NMR transition in the other, causing both spins to simultaneously flip their spin states. As the relative population of the α and β spin states have not been altered (the α spin is now a β spin, while the β spin is now an α spin) there is no change in the total energy of the system. However, as the relative phase of the two magnetic moments is random, any x-y coherence that the original α spin had with the ensemble of spins is lost. As with spin-lattice relaxation the rate of spin-spin relaxation can be

related to the spectral density of 'magnetic noise';

$$\frac{1}{T_2} = \frac{1}{2T_1} + \frac{\gamma^2 |B^0_{z1}|^2 J(0)}{2} \qquad (2.33)$$

The action of the spin-flipping involved in spin-spin relaxation reduces the time each spin spends in each of its energy states. Due to the Heisenburg uncertainty principle [16,17] the reduction in the occupancy time of the spin states causes a decrease in the certainty of the energy separation between the levels. As a result of this uncertainty the NMR absorption from a particular nuclear system occurs over a range of frequencies, giving the NMR absorption width as well as intensity (as seen previously in figure 2.9.a), the frequency width of the absorption measured at half the maximum height $\Delta\nu_{1/2}$ being given by equation(2.34). It must also be noted that any inhomogeneity in the external magnetic field will cause identical nuclei in different parts of the NMR sample to precess at different rates, resulting in additional broadening of the NMR signal. Therefore, the frequency width measured from the NMR spectrum incorporates the actual spin-spin relaxational mechanism (T_2) and that induced by inhomogeneities in the magnetic field (T_2^{Inhomo}), equation(2.35).

$$\Delta\nu_{\frac{1}{2}} = \frac{1}{\pi T_2} \qquad (2.34)$$

$$\Delta\nu_{\frac{1}{2}} = \frac{1}{\pi T_2^*} \qquad \text{where } \frac{1}{T_2^*} = \frac{1}{T_2} + \frac{1}{T_2^{Inhomo}} \qquad (2.35)$$

1.9.3 The Effect of Molecular Motion on Relaxation.

Both T_1 and T_2 relaxational mechanisms are dependent on the random motion of the constituent nuclei in the NMR sample and if this random motion is altered then so too is the efficiency of the relaxational pathways. Therefore, when describing the relaxational processes in NMR it is also necessary to characterize the random motions within the sample. To this end a NMR system has associated with it a molecular correlation time, τ_c. The exact definition of τ_c is dependent on the type of motion under consideration: in translational motion it is the average time that the constituent molecules take to move over a distance comparable to their own dimensions, whereas in rotational motion it relates to the time that a molecule takes to rotate by one radian. Clearly the molecular correlation time depends on many factors, the most obvious being molecular size, larger molecules having longer correlation times. Table 2.2 gives some typical correlation times for some aqueous molecular systems.

Table 2.2 : Typical correlation times of molecules.

Type of Molecule	Correlation Time τ_c/s
Small molecules with molecular weights <100	10^{-12}-10^{-13}
Larger molecules with molecular weights >500	10^{-10}
Macromolecules (such as globular protein)	10^{-8}

Bloembergen, Purcell and Pound [18] extended Debye's theory of dielectric dispersion of polar liquids so that it could be used to determine the molecular correlation time. The theory predicting the correlation time assumes that the molecules in the sample are spherical, of radius r and that they move through a liquid of viscosity η. Under such conditions τ_c is given as;

$$\tau_c = \frac{4\pi r^3 \eta}{3kT} \tag{2.36}$$

The molecular correlation time directly accounts for the random motion of the magnetic moments which are ultimately responsible for the relaxation of the NMR system. The spectral density function, $J(\omega)$, defines the intensity of the individual frequency components of the fluctuating magnetic field generated by the lattice which, as this is generated by the random motion of the constituent nuclei, can be related to the molecular correlation time, equation (2.37).

$$J(\omega) = \frac{2\tau_c}{1 + \omega^2\tau_c^2} \tag{2.37}$$

A plot of the spectral density for a range of correlation times is shown in figure 2.10. In each case there is a plateau, where the spectral density of the magnetic noise remains constant. This occurs where $\omega\tau_c \ll 1$ and is called the region of extreme narrowing.

Equation(2.37) can now be substituted into equation(2.31) to obtain the spin-lattice relaxation time for a particular Larmor precessional frequency, ω_0, in terms of the molecular correlation time through equation(2.38). This, under the conditions of extreme narrowing, becomes equation(2.39).

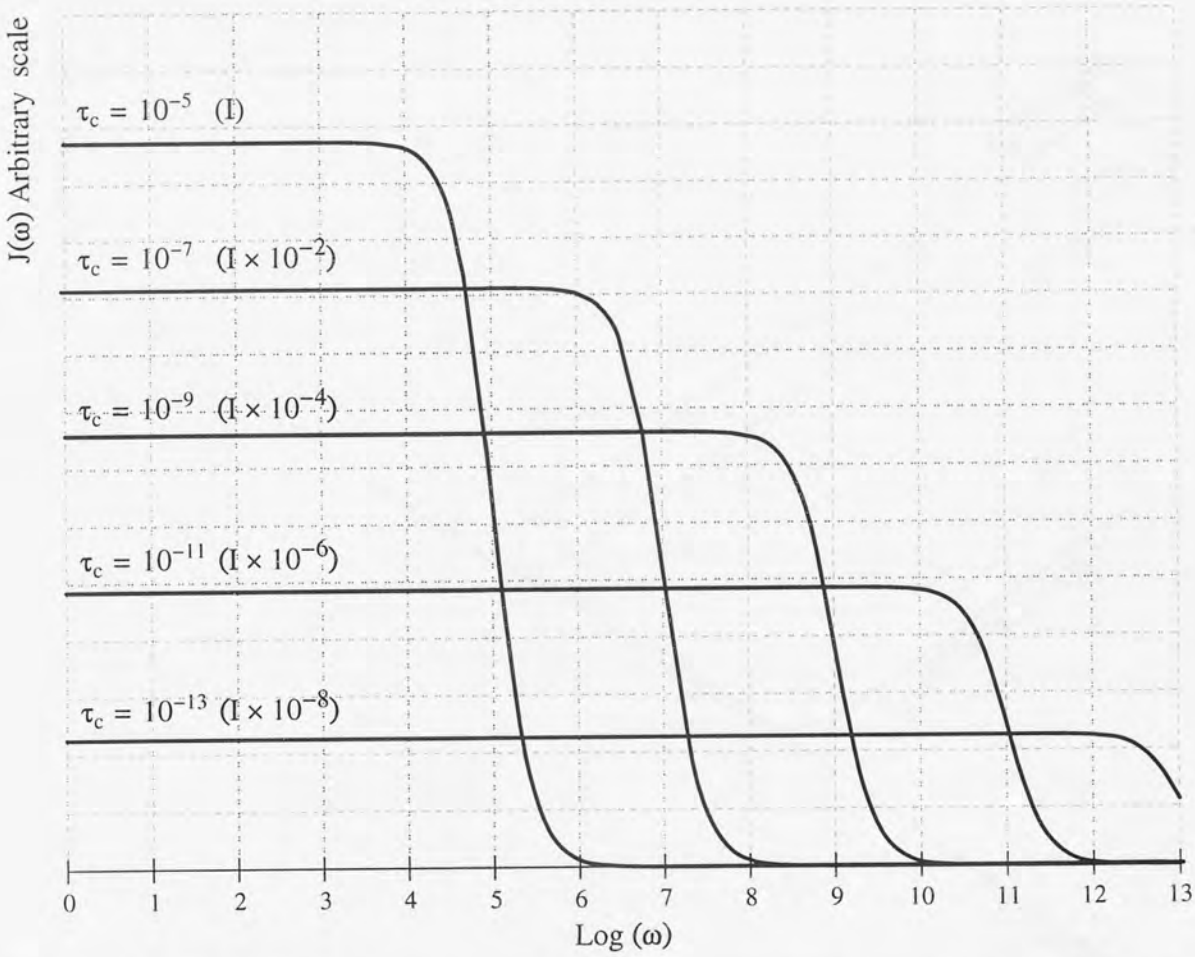

Figure 2.10 : Spectral density function for various correlation times. (Note : The exact intensity relationship between the plateaus for the different correlation times is annotated, in terms of I, adjacent to the value of τ_c)

$$\frac{1}{T_1} = \gamma^2 |B_{1x}^0|^2 \frac{2\tau_c}{1+\omega_0^2\tau_c^2} \tag{2.38}$$

$$\frac{1}{T_1} = 2\gamma^2 |B_{1x}^0|^2 \tau_c \tag{2.39}$$

The appropriate equation for spin-lattice relaxation in the rotating frame becomes;

$$\frac{1}{T_{1\rho}} = \frac{1}{6}\gamma^2\left(|B_{x1}^0|^2 + |B_{y1}^0|^2 + |B_{z1}^0|^2\right)\left(\frac{2\tau_c}{1+\Omega^2\tau_c^2} + \frac{2\tau_c}{1+\omega_0^2\tau_c^2}\right) \tag{2.40}$$

Spin-spin relaxation is also induced by the random magnetic field characterized by $J(\omega)$. Using a value $\omega=0$ in the spectral density equation gives a value of $J(0)$ to be $2\tau_c$, which when substituted into equation(2.33) gives equation(2.41).

$$\frac{1}{T_2} = \frac{1}{2T_1} + \gamma^2 |B_{z1}^0|^2 \tau_c \tag{2.41}$$

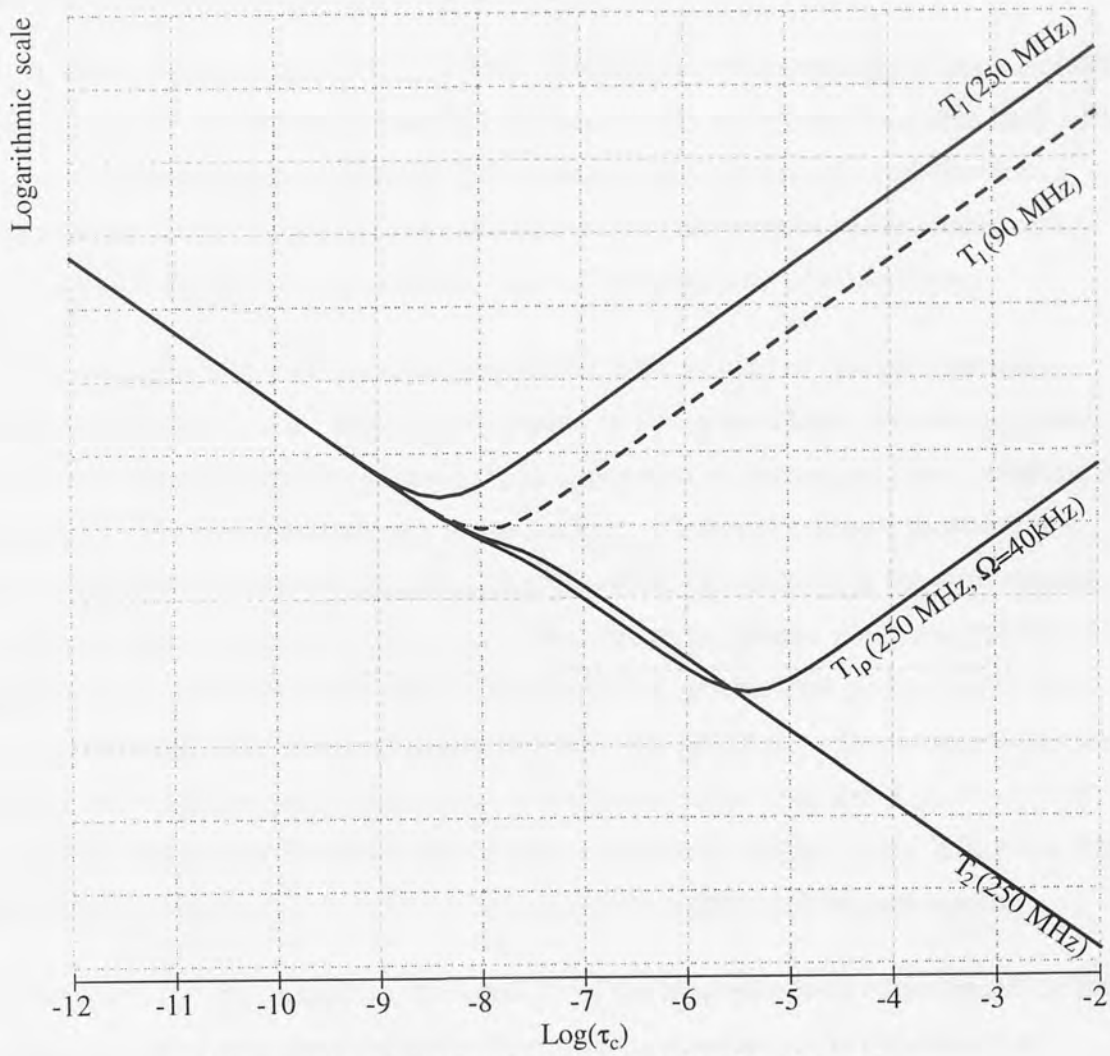

Figure 2.11 : Relationship between T_1, $T_{1\rho}$, T_2 and τ_c.

Figure 2.11 shows the relationship between T_1, T_2 and $T_{1\rho}$ for a Larmor precessional frequency of 250MHz, and T_1 for a Larmor precessional frequency of 90MHz, each over a range of correlation times.

1.10 Appearance of a NMR Spectrum.

If nuclear magnetic resonance spectroscopy were to produce just one absorption for each nuclide present in a sample its use would be severely limited. Fortunately the energy levels in the nucleus are sensitive to the chemical and magnetic environment that are imposed on the nucleus by its position within a molecule. This results in NMR spectra showing a number of absorption for each nuclear isotope, the position and intensity of which are directly related to the molecular structure of the sample.

1.10.1 Nuclear Screening and Chemical Shift.

In earlier sections the nuclei in NMR samples have been considered to be isolated from each other and the effect that the electronic shells around each nucleus have on the magnetic moment has been ignored. Once these nuclei are brought together into a molecule the effect of the electronic shells, bonding, differences in electronegativity and the establishment of ring currents, must all be taken into consideration.

As the electronic shells may be considered to be a cloud of charged particles orbiting the nucleus their motion, when placed in a magnetic field, will become such that they generate a small magnetic field in opposition to the applied field, resulting in a magnetic field of reduced intensity at the nucleus. Clearly the degree to which this nuclear screening occurs is dependent on the number of electrons in the surrounding electronic shells. If this population is reduced due to the greater electronegativity of an adjacent atom in the molecule, the nucleus becomes 'de-shielded' and experiences a greater magnetic field. As a consequence of this the spin energy level separations are slightly enhanced and resonance occurs at a slightly higher frequency. Consequently the signal undergoes a 'chemical shift' [19-21] and moves further to the left of the NMR spectrum (conventionally frequency increases from right to left in such spectra).

To allow for the changes in the intensity of the magnetic field experienced by the nucleus, manifest as a chemical shift, the screening constant, σ, is introduced to equation(2.9) giving;

$$\nu = \frac{\gamma B_0(1-\sigma)}{2\pi} \tag{2.42}$$

The chemically shifted frequency is clearly dependent on the polarizing field strength of the spectrometer and to quote the chemical shift in terms of frequency is meaningless unless $\mathbf{B_0}$ is also known. It is, therefore, usual to quote the chemical shift as a δ value which is the ratio of the frequency shift ($\nu - \nu_r$) to the frequency of a reference signal (ν_r), as in equation(2.43). This is directly related to the difference in the screening constant of the two nuclei by equation(2.44).

$$\delta = \frac{\nu_a - \nu_r}{\nu_r} \times 10^6 \tag{2.43}$$

$$\delta = (\sigma_r - \sigma_a) \times 10^6 \tag{2.44}$$

The chemical shift as defined in equation(2.43) is in accordance with the IUPAC convention [22,23] which state;

i. $\delta > 0$ for any resonance detected which has a frequency greater than that of the chosen reference (de-shielded or downfield).

ii. $\delta < 0$ for any resonance detected which has a frequency less than that of the chosen reference (shielded or upfield).

A number of factors contribute to the chemical shift of a nuclear species which, although difficult to accurately characterize individually, may be discussed empirically;

1.10.1.1 Paramagnetic Contribution.

The contribution of the paramagnetic term to σ cannot readily be described classically. It may be envisaged as the generation of an electronic asymmetry by the electric fields of nearby nuclei and results in the mixing of 'excited' electronic states into the ground state wavefunction. The principal extra energy term in this mixed state appears as a result of the Zeeman energy interacting with the electron orbital angular momentum. In the case of protons we are only concerned with s-electrons which, having no angular momentum, make no paramagnetic contribution to σ. For other nuclei this is the dominant effect and usually greatly out weighs any diamagnetic effects (section1.10.1.2). For this reason the range of chemical shifts for the proton are small in comparison with other nuclei.

1.10.1.2 Diamagnetic Contribution.

The initial description of a difference in electronegativity causing a change in the population of the electron cloud surrounding a nucleus is an example of a diamagnetic contribution to σ. Due to the lack of a paramagnetic contribution, the diamagnetic contributions dominate the spectra of protons.

1.10.1.3 Magnetic Anisotropy

The action of certain groups in a molecule may actually enhance the $\mathbf{B_0}$ field experienced by other groups. Of particular importance is the reaction of delocalized electrons in aromatic moieties to an external magnetic field. As with the electron cloud surrounding a nucleus, the applied magnetic field causes the electrons in the delocalized bonds to migrate about the ring system, causing ring currents that induce a field which opposes the external magnetic field at the centre of the aromatic ring. Because the induced field is of a toroidal nature, any nuclei on the periphery of the ring experience a magnetic field that, due to the constructive addition of the applied field

and the induced field, is stronger than usual. As the degree of shielding about the nucleus has not been altered the field it experiences increases and a deshielded chemical shift observed. Figure 2.12 shows a proton on the periphery of a benzene ring, experiencing the magnetic field induced by the delocalized electrons.

Similar shielding effects can be generated by anisotropic chemical bonds.

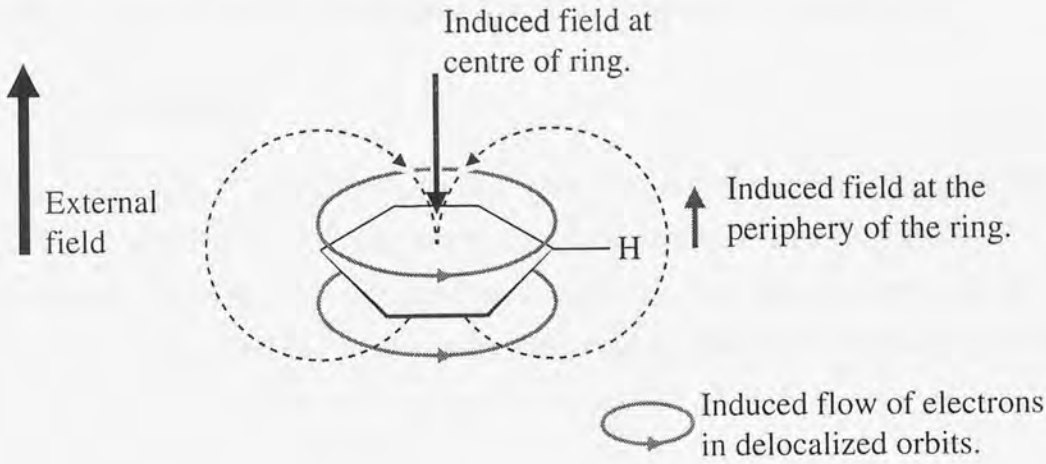

Figure 2.12 : Magnetic field induced by delocalized electrons.

1.10.1.4 Electric Fields

If a strongly polar group is present in a molecule the molecular electron distribution will be influenced. This has two affects on σ; the first is caused by any shielding/de-shielding this redistribution of the electrons may have, the second is as a result of the asymmetry this action induces in the bonds and the enhancement of the paramagnetic contribution to which this leads.

1.10.1.5 Unpaired Electron Shifts

The very large magnetic moment of an unpaired electron can have a dramatic effect on a NMR spectrum:

As well as the observation of the hyperfine coupling usually found in ESR spectra, dipolar coupling between the electron and the nucleus may significantly broaden the NMR resonance.

Alternatively, if the magnitude of the hyperfine coupling is very much less than the electron relaxation rate, then sharp lines are observed in the NMR spectrum which show large chemical shifts. This is known as a Knight shift [24,25], a characteristic of the NMR spectra of metals, and results from the interaction of the nucleus with the

delocalized conductance electrons through the hyperfine coupling. As a given nucleus is coupled to many electrons this coupling is averaged out over the electron spin orientations of many electrons. However, the electron spins are polarized in the $\mathbf{B_0}$ field, and thus there is a residual coupling, not averaged out by the motion of the electrons. Since the interaction corresponds to the nucleus experiencing a magnetic field parallel to the electron magnetic moment, and since the electron moment is preferentially parallel to $\mathbf{B_0}$, the effective field at the nucleus is increased.

1.10.1.6 Solvent Effects.

The total effect of the solvent on the chemical shift of the solute, $\sigma_{solvent}$, can be expressed as the sum of five contributory terms; σ_b, from the bulk magnetic susceptibility; σ_w, from weak van der Waals forces; σ_a, from any magnetic anisotropy in the solvent molecules; σ_E, from electric field effects; and σ_h, from specific solute-solvent interactions.

$$\sigma_{solvent} = \sigma_b + \sigma_w + \sigma_a + \sigma_E + \sigma_h \qquad (2.45)$$

1.10.1.6.1 Bulk Magnetic Susceptibility, σ_b.

The solvent in an NMR sample reacts to an external magnetic field in a similar way to the orbiting electrons about a nucleus, a diamagnetic solvent inducing a magnetic field which opposes the external field, reducing the magnetic field experienced by the solute. Conversely, a paramagnetic solvent will increase the magnetic field experienced by the solute. The reaction of the solvent in this manor is accounted for by the bulk magnetic susceptibility term, σ_b.

Where a sample is internally referenced the effect of σ_b is removed from the measured chemical shift as, in general, σ_b contributes equally to the screening constants of the dissolved sample and the reference.

1.10.1.6.2 Van Der Waals Forces, σ_w.

There may be a 'van der Waals' interaction between the solvent and solute molecules which results in the distortion of the electronic environment about a given nucleus. The effect of this interaction on the screening constant of the nucleus is accounted for by the term σ_w.

1.10.1.6.3 Magnetic Anisotropy, σ_a.

It is possible for the ring currents discussed in section 1.10.1.3 to be formed in the solvent used (e.g. benzene) in the preparation of the NMR sample. The effects of the magnetic field induced by these ring current may be passed onto the solute molecule, resulting in the solvent contributing to the chemical shift of the solute.

1.10.1.6.4 Electric Field Effects, σ_E.

When a polar molecule or a molecule containing polar groups is dissolved in a dielectric medium, it induces a "reaction field", the effect of which is usually to reduce the shielding around nuclei in the solute, accounted for by the term σ_E.

1.10.1.6.5 Solvent-Solute Interactions, σ_h.

The solvent and solute molecules may not be entirely independent of each other, forming semi-permanent bonds (such as hydrogen bonding). Such bonds may alter the screening constants associated with the solute molecule, these changes accounted for by σ_h.

1.10.2 Internuclear Spin-Spin Coupling.

Close scrutiny of a NMR spectrum will reveal that many of the NMR absorption are composed of a number resonances and that the frequency spacing of these resonances is independent of the magnetic field strength used by the spectrometer.

Consider a situation where two I=½ nuclei, of different chemical shifts, are bonded to each other within a molecular structure; e.g. an AX spin system. The influence of the magnetic moment of the 'A' spin is not confined to its locality, but is weakly transmitted by its bonding electrons to its nearest neighbours. As the populations of α and β states are almost identical there is a 50% chance that we will find the 'X' spin next to an 'A' spin in its α state and a 50% chance that it will be in its β state. When this probability is applied to the whole ensemble of molecules making up the NMR sample, half of the AX systems will be $A_\alpha X$ and the other half will be $A_\beta X$. The magnitude of the magnetic field generated at X by A in the two AX systems will identical. However, the orientation of the field in each system will be opposed to each other and so perturb the spin energy levels in each of the possible systems by equal, but opposite amounts. The resulting NMR spectrum, therefore, shows two signals of equal intensity shifted to the same extent on either side of the chemical shift position of X. This phenomenon is

called scalar, spin-spin or J-coupling [26, 27]; The frequency separation of the peaks being quoted in Hertz as J-coupling is independent of the magnetic field employed. Figure 2.13 shows the effect of J-coupling to the X nucleus in the AX system.

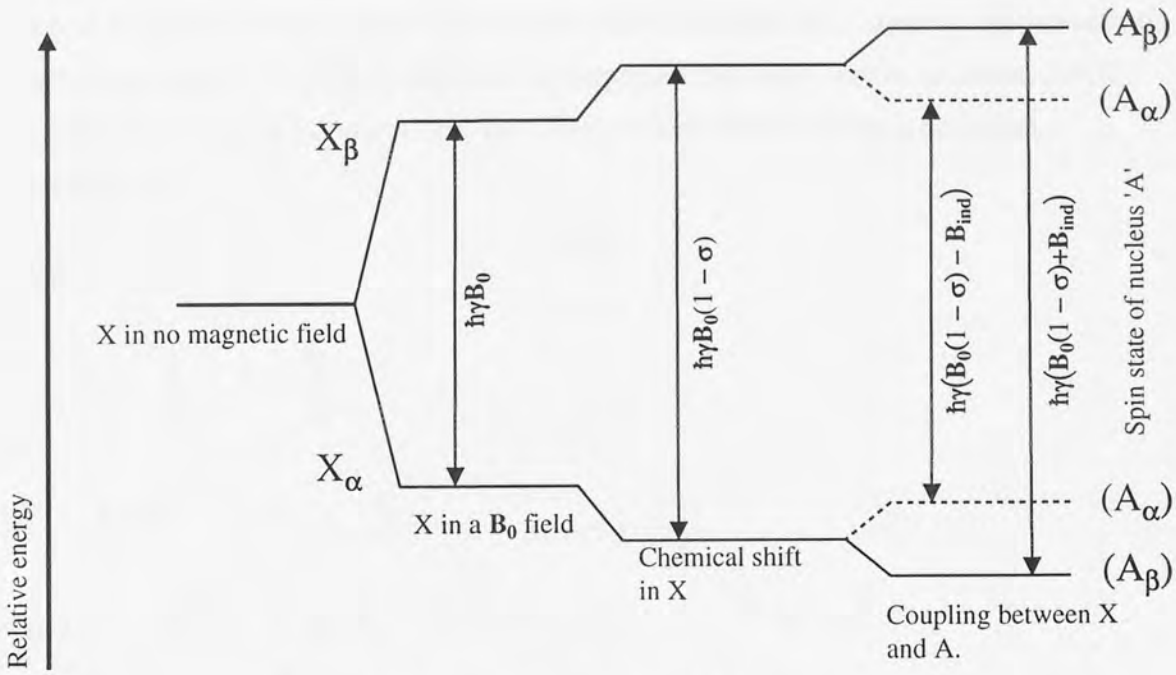

Figure 2.13 : J-coupling in the AX spin system.

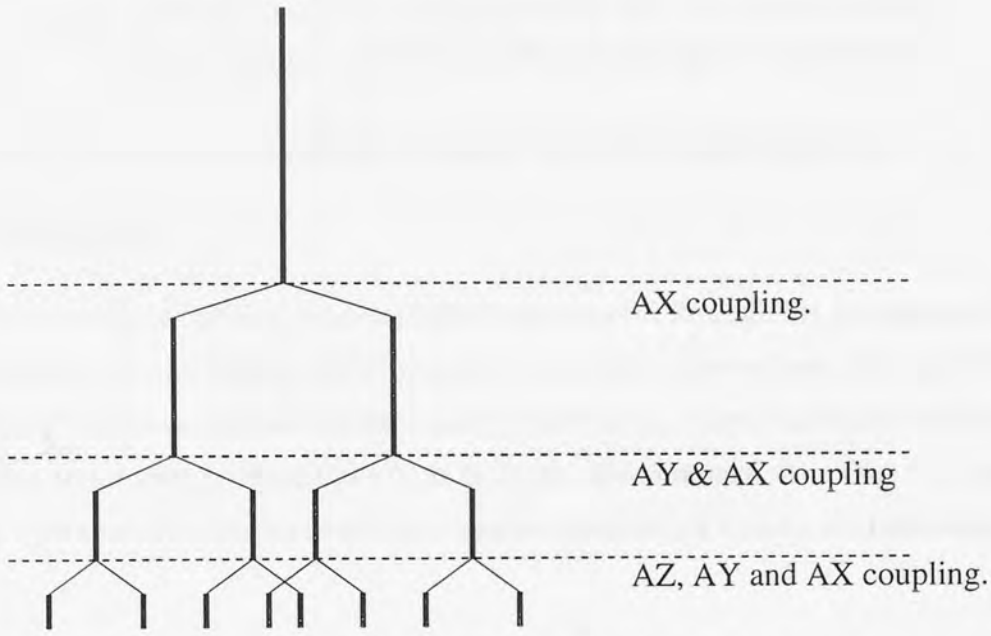

Figure 2.14 : Coupling between A and three other nuclei.

If we were to observe the NMR spectrum of A it too would be split into a doublet, with the same J-coupling constant as found in X. 'A' may of course be coupled to any number of other nuclei and, assuming there are 'n' non-equivalent nuclei all of spin I=½, the NMR signal from 'A' will be split into 2^n signals, each coupling halving the

intensity of the resultant signals. Figure 2.14 shows the splitting generated by an A-XYZ system, where A is coupled to three other, different nuclei.

Often the 'X' nuclei to which 'A' is coupled to have the same coupling constants for each of the interactions as each 'X' is in the same chemical and magnetic environments (an AX_n system). The superposition of absorptions that now occurs splits the NMR signal from A into n+1 absorptions, the intensities of which follow a binomial distribution;

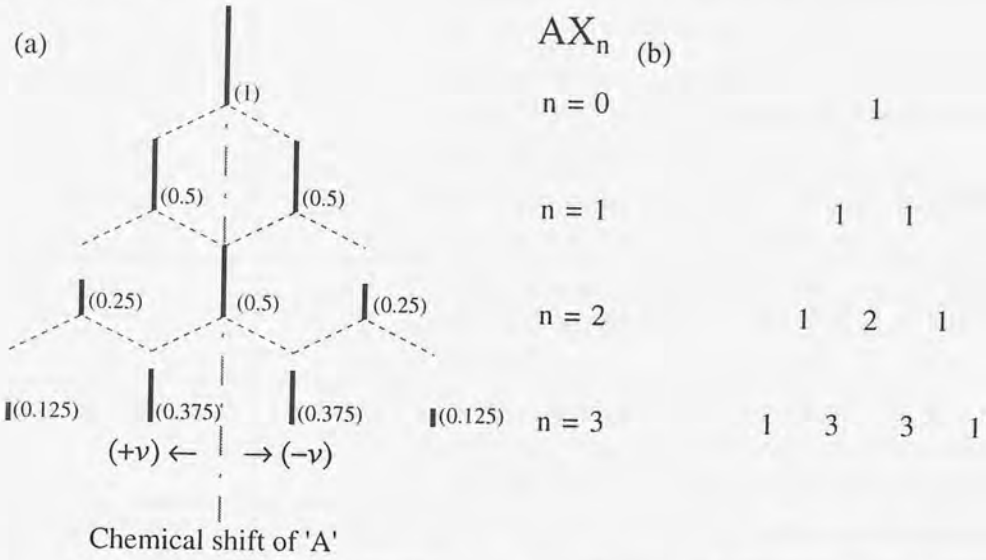

Figure 2.15 : (a) Multiplets generated by an AX_n system. **(b)** Binomial distribution giving relative intensities of multiplet components.

1.11 The Quantum Mechanical Description of NMR : Hamiltonians.

1.11.1 Introduction

The features of NMR spectra described above occur through the perturbation of nuclear energy levels through intra- and inter- molecular interactions. To more fully understand these interactions it is necessary to turn to quantum mechanics and, in particular, to the energy functions which describe these interactions. These functions or 'energy operator' are referred to as Hamiltonian operators or simply as Hamiltonians ($\mathcal{H}$).

The total energy Hamiltonian of a spin system is made up from the linear combination of a number of Hamiltonians, equation(2.46), each of which describes a particular mechanism whereby the nuclear spins interact with their environment.

$$\mathcal{H}_{tot} = \sum_{\lambda}^{\text{inter-actions}} \mathcal{H}_{\lambda} \qquad \text{where each different type of interaction is denoted by } \lambda. \qquad (2.46)$$

Table 2.3 lists the components of the total energy Hamiltonian giving a brief description of nature of the interactions they describe.

Table 2.3 : Component Hamiltonians of the Total Energy Hamiltonian.

Interaction Type	Symbol	Description
Zeeman	$\mathcal{H}_Z$	The is interaction between the nuclear spins and the external magnetic field of the spectrometer.
Scalar Coupling	$\mathcal{H}_J$	This is the interaction between pairs of nuclear spins transmitted through the bonding electrons (J - coupling or Spin-spin coupling)
Chemical Shift	$\mathcal{H}_{CS}$	This interactions accounts for the modifications in the density of the surrounding electron cloud and to the static magnetic field.
Dipole-Dipole	$\mathcal{H}_{DIP}$	This accounts for the direct, through space interactions that a pair of nuclear spins may have.
Quadrupolar	$\mathcal{H}_Q$	The quadrupolar interaction accounts for the interaction that nuclear spins with $I>\frac{1}{2}$ have with an electric field gradient.
Spin-Rotation	$\mathcal{H}_{SR}$	Certain molecules can spin coherently, generating a magnetic field. The spin-rotation interaction allows for the coupling of this field and the nuclear spins.
Random Field	$\mathcal{H}_{RDM}$	This interaction is between the nuclear spins and the random magnetic field generated throughout the NMR sample.
r.f Field	$\mathcal{H}_1$	This is the interaction between the nuclear spins and the externally applied r.f. field.
Relaxation	$\mathcal{H}_2$	This is an all embracing term that covers any time-dependent, random interactions that lead to relaxation

Most of these interactions may be considered to be made up from a time independent and a time dependent expression, respectively referred to as the Hamiltonians isotropic and anisotropic components. Table 2.4.

It is, therefore, possible to quote the total energy Hamiltonian of a sample, when measured in the laboratory frame, as being composed of time-independent components, $\mathcal{H}_0$ (commonly know as the static, high resolution NMR Hamiltonian), external time-dependent components $\mathcal{H}_1$, and internal time-dependent components $\mathcal{H}_2$;

$$\mathcal{H}_{tot}(t_{Lab}) = \mathcal{H}_{0\,Lab} + \mathcal{H}_1(t_{Lab}) + \mathcal{H}_2(t_{Lab}) \qquad \begin{aligned} \mathcal{H}_0 &= \mathcal{H}_Z + \mathcal{H}_{JI} + \mathcal{H}_{CSI} \\ \mathcal{H}_1 &= \text{Applied r.f. field} \\ \mathcal{H}_2 &= \mathcal{H}_{DIP}(t) + \mathcal{H}_{CSA}(t) \\ &\quad + \mathcal{H}_{RDM}(t) + \mathcal{H}_{JA}(t) \end{aligned} \tag{2.47}$$

Table 2.4 : Isotropic and Anisotropic Hamiltonian components.

Interaction	Isotropic Term	Anisotropic Term
$\mathcal{H}_Z$	$\mathcal{H}_Z$	None
$\mathcal{H}_J$	$\mathcal{H}_{JI}$	$\mathcal{H}_{JA}$
$\mathcal{H}_{CS}$	$\mathcal{H}_{CSI}$	$\mathcal{H}_{CSA}$
$\mathcal{H}_{DIP}$	None	$\mathcal{H}_{DIP}$
$\mathcal{H}_Q$	None	$\mathcal{H}_Q$
$\mathcal{H}_{SR}$	None	$\mathcal{H}_{SR}$
$\mathcal{H}_{RDM}$	None	$\mathcal{H}_{RDM}$
$\mathcal{H}_1$	None	$\mathcal{H}_1$
$\mathcal{H}_2$	None	$\mathcal{H}_2$

Each of the interaction Hamiltonians can themselves be broken into the contribution from individual nuclear spins, equation(2.48), or individual spin pairs equation(2.49).

$$\mathcal{H}_\lambda = \sum_{i}^{\text{All Spins}} \mathcal{H}_\lambda(i) \tag{2.48}$$

$$\mathcal{H}_\lambda = \sum_{i}^{\text{All Spins}} \sum_{j>i}^{\text{All Spins}} \mathcal{H}_\lambda(i,j) \tag{2.49}$$

The actual form of the Hamiltonian equations depends on the interaction and on its relative motion within the NMR sample. The effect of this motion on the Hamiltonians is discussed in the next section.

1.11.2 Implications of Molecular Motion in the NMR Sample.

Considering a sample of N atoms, there are 3N degrees of freedom, each atom having translational, rotational and vibrational components. The form of a Hamiltonian describing an interaction will be strongly dependent on how relevant each of these motions are to the NMR experiment.

1.11.2.1 Translational Motion

As a spin moves through space it will encounter a time dependent magnetic field. Essentially, this constitutes a modulation and contributions to this are made from interactions with passing nuclei in other solvent and solute molecules, with

paramagnetic impurities in the sample, and with the small inhomogeneities in the external magnetic. It is difficult to adjust quantitatively the Hamiltonians for these effects as it would require knowing a great deal of information about the spatial dynamics of the sample and the external magnetic field. Therefore, no direct attempt to account for these interactions is made and it is assumed that the nuclear spins experience no inhomogeneities in the magnetic field while they undergo linear diffusion, the additional interactions being accounted for in the random magnetic field Hamiltonian.

1.11.2.2 Vibrational Motion

For the vast majority of molecules the frequencies of the different vibrational modes corresponds to energies so far beyond that currently required in nuclear magnetic resonance spectroscopy that it is not possible for them to stimulate transitions within the sample. The exception to this occurs in large molecular systems, such as proteins, where certain modes of vibration do correspond to NMR frequencies. However, on the whole this need not be accounted for so it will be assumed that any spin system under consideration is held rigidly in place within the molecule.

1.11.2.3 Rotational Motion

Rotational motion modulates both intra- and inter-molecular spin interactions. This does occur at frequencies comparable to those found in nuclear magnetic resonance spectroscopy and it is predominantly through these interactions that relaxation of the NMR sample occurs. These interactions are, therefore, of some significance to the NMR experiment, requiring the rotation of Hamiltonians in the laboratory frame. Therefore, to facilitate this rotation the Hamiltonians should be constructed in the form of irreducible spherical tensors (Appendix 3.3).

1.11.3 The Hamiltonians of NMR.

Given the relevance of the above molecular motions it is possible to deduce a general format for a Hamiltonian [28]. The derivation of the general format for the Hamiltonians is given in appendix 2 and results in;

$$\mathcal{H} = C\sum_{l=0}^{2}\sum_{m=-l}^{l}(-1)^{m}A_{l}^{-m}X_{l}^{m} \qquad (2.50)$$

where C is a constant, A and X are the appropriate tensors describing the interaction and

A_l^m and X_l^m refer to the irreducible spherical tensors of A and X respectively.

Although this may be used as the general form of the Hamiltonians it is sometimes useful to factor out any constants in the tensors such that;

$$a(F_l^m) = A_l^m \tag{2.51}$$

$$b(T_l^m) = X_l^m \tag{2.52}$$

$$\xi = abC \tag{2.53}$$

which gives the Hamiltonian in the laboratory frame as;

$$\mathcal{H}_{(LAB,t)} = \xi \sum_{l=0}^{2} \sum_{m=-l}^{l} (-1)^m F_{l\,(LAB,t)}^{-m} T_{l\,(LAB)}^{m} \tag{2.54}$$

Thus, given the energetic description appropriate to an interaction it is possible to derive [28, 29], through a methodology similar to that in appendix 2, an appropriate Hamiltonian in a form similar to that of equation(2.54).

For the sake of simplicity, where the Hamiltonian has both isotropic and anisotropic components, only the isotropic Hamiltonian, the high resolution static Hamiltonian, is given.

1.11.4.1 The Zeeman Hamiltonian

The simplest of the NMR interactions is that between a nuclear spin and the static magnetic field of the spectrometer and is called the Zeeman interaction. The classical interaction energy of a magnetic dipole and a magnetic field is given by;

$$E_{Zeeman} = -\boldsymbol{\mu} \cdot \mathbf{B} \tag{2.55}$$

Normalisation of the magnetic field results in the removal of all magnetic field components from the xy plane. As a consequence of this all components of the irreducible spherical tensor which describe the context of the interaction are zero with the exception of the rank zero component, the resulting Hamiltonian being;

$$\mathcal{H}_{Z\,(LAB)} = \sum_{i}^{spins} \xi_i^Z F_{0\,(LAB)}^0 T_0^0(i)_{(LAB)} \tag{2.56}$$

where

$$\begin{aligned} \xi_i^Z &= -\hbar\gamma_i B_0 \\ F_{0\,(LAB)}^0 &= -\sqrt{3} \\ T_0^0(i)_{(LAB)} &= -\frac{I_z(i)}{\sqrt{3}} \end{aligned} \tag{2.57}$$

1.11.4.2 The Scalar Coupling Hamiltonian

This interaction accounts for the electron mediated, internuclear coupling of nuclei referred to as J or spin-spin coupling. The energy involved in scalar coupling between spins i and j at a distance r from each other is given by;

$$E_{J\,(ij)} = \frac{\boldsymbol{\mu}_i \cdot \boldsymbol{\mu}'_j}{r_{ij}^3} \tag{2.58}$$

Here $\boldsymbol{\mu}'_j$ is the effective magnetic moment of spin j after it has been adjust for the indirect 'through bond' interactions found in scalar coupling. Defining a scalar coupling tensor $\hat{J}'_{(ij)}$, such that;

$$\hat{J}'_{(ij)} \cdot \boldsymbol{\mu}'_j = \frac{1}{r_{ij}^3}\boldsymbol{\mu}'_j \tag{2.59}$$

then this interaction energy becomes;

$$E_{J\,(ij)} = \boldsymbol{\mu}_i \cdot \hat{J}'_{(ij)} \cdot \boldsymbol{\mu}'_j \tag{2.60}$$

The resultant Hamiltonian has an isotropic and anisotropic contribution with the isotropic Hamiltonian, which is included in the high-resolution static NMR Hamiltonian being defined as;

$$\begin{aligned} \mathcal{H}_{JI}(ij)_{(LAB)} &= \hbar \sum_{i}^{spins} \sum_{j>i}^{spins} J_{iso}(ij)\mathbf{I}(i) \cdot \mathbf{I}(j) \\ &= \hbar \sum_{i}^{spins} \sum_{j>i}^{spins} J_{iso}(ij)\left[I_z(i)I_z(j) + \frac{\left[I_+(i)I_-(j) + I_-(i)I_+(j)\right]}{2}\right] \end{aligned} \tag{2.61}$$

where

$$J_{iso} = \frac{J_{xx} + J_{yy} + J_{zz}}{3} \tag{2.62}$$

1.11.4.3 The Chemical Shift Hamiltonian

In the presence of the static magnetic field of the spectrometer the motion of the electron clouds around the nuclear spins generates a localized, inherently anisotropic magnetic field. Defining a chemical shift screening tensor $\hat{\sigma}$ such that;

$$\mathbf{B}_{Induced}(i) = -\hat{\sigma}(i) \cdot \mathbf{B}_0 \tag{2.63}$$

then the energy resulting from the interaction of this induced field and the nuclear spin is

$$E_{CS}(i) = \mu_i \cdot \hat{\sigma}(i) \cdot \mathbf{B_0} \tag{2.64}$$

Once again the resulting Hamiltonian may be sub-divided into an isotropic $\mathcal{H}_{CSI}$, and anisotropic $\mathcal{H}_{CSA}$ Hamiltonians with the isotropic Hamiltonian defined as;

$$\mathcal{H}_{CSI\,(LAB)} = \sum_{i}^{spins} \hbar\gamma_i B_0 \sigma_{iso}(i) I_z(i) \tag{2.65}$$

1.11.4.4 The Dipolar Hamiltonian

The classical interaction energy between two dipoles $\boldsymbol{\mu}_i$ and $\boldsymbol{\mu}_j$ separated by a vector $\mathbf{r}$ is given by;

$$E_{DIP} = \frac{\boldsymbol{\mu}_i \cdot \boldsymbol{\mu}_j}{r^3} - 3\frac{(\boldsymbol{\mu}_i \cdot \mathbf{r})(\boldsymbol{\mu}_j \cdot \mathbf{r})}{r^5} \tag{2.66}$$

The resulting Hamiltonian can be represented as the summation of six components, referred to as the dipolar alphabet;

$$\begin{aligned}
H_{DIP}(ij) &= \frac{\gamma_i\gamma_j\hbar}{r_{ij}^3}(A + B + C + D + E + F) \\
A &= -(3\cos^2\theta_{ij} - 1)\left[I_z(i)I_z(j)\right] \\
B &= \frac{1}{4}(3\cos^2\theta_{ij} - 1)\left[I_+(i)I_-(j) + I_-(i)I_+(j)\right] \\
C &= -\frac{3}{2}\sin\theta_{ij}\cos\theta_{ij}e^{-i\phi_{ij}}\left[I_+(i)I_z(j) + I_z(i)I_+(j)\right] \\
D &= -\frac{3}{2}\sin\theta_{ij}\cos\theta_{ij}e^{i\phi_{ij}}\left[I_-(i)I_z(j) + I_z(i)I_-(j)\right] \\
E &= -\frac{3}{4}\sin^2\theta_{ij}e^{-2i\phi_{ij}}\left[I_+(i)I_+(j)\right] \\
F &= -\frac{3}{4}\sin^2\theta_{ij}e^{+2i\phi_{ij}}\left[I_-(i)I_-(j)\right]
\end{aligned} \tag{2.67}$$

1.11.4.5 The Random-Field Hamiltonian.

Here the interaction is between a magnetic moment and a magnetic field as in the Zeeman interaction. However, in this case the magnitude and direction of the field varies randomly with time. The energy of such an interaction is given by;

$$E = -\boldsymbol{\mu}_i \cdot \mathbf{B}_{RDM}(t) \tag{2.68}$$

The Hamiltonian which applies to this relationship is;

$$\mathcal{H}_{RDM}(t) = \sum_{i}^{spins} \xi_i^{RDM}(t) \sum_{m=-1}^{1} (-1)^m Y_1^{-m}(t,i) T_1^m(i)$$

$$\begin{aligned} \xi_i^{RDM}(t) &= -\sqrt{\frac{4\pi}{3}} B_i^{RDM}(t) \hbar \gamma_i \\ T_1^m(i) &= I_1^m(i) \\ Y_1^m(t,i) &= \sqrt{\frac{3}{4\pi}} \left(\frac{B_1^m(t,i)}{B_i^{RDM}(t)} \right) \end{aligned} \qquad (2.69)$$

1.11.4.6 The Radio-Frequency Field Hamiltonian.

Once again concern is with the interaction of a magnetic spin and a magnetic field. The magnetic in this case is generated from an r.f. field of angular frequency Ω_{rf} at a phase ϕ applied along the positive x-axis and is denoted by $\mathbf{B}_{rf}(t)$. As a result of this the appropriate Hamiltonian is deduced to be;

$$\mathcal{H}_{RF}(t) = \sum_{i}^{spin} \xi_i^{RF} F_0^0 T_0^0(i)$$

$$\begin{aligned} \xi_i^{RF} &= -2\hbar\gamma_i B_{rf} \cos(\Omega_{rf} t - \phi) \\ F_0^0 &= -\sqrt{3} \\ T_0^0(i) &= -\frac{1}{\sqrt{3}} I_x(i) \end{aligned} \qquad (2.70)$$

1.11.4.7 The Quadrupolar Hamiltonian.

The interaction energy of a simple electric quadrupole moment Q consisting of two point dipoles back-to-back which are a distance s apart in an electric field **E**, of gradient dE/dz running perpendicular to **E** is;

$$E = -\frac{1}{2} \mu s \sin(2\Theta) \frac{dE}{dz} \qquad (2.71)$$

where the angle between the electric field and the electric dipole μ, is Θ. The interaction of the non-spherical distribution of charge in quadrupolar nuclei with an electric field is described in an analogous manor, resulting in the Hamiltonian for such systems being;

$$\begin{aligned} \hat{\mathcal{H}}_Q &= \frac{d^2V}{dz^2} eQ \frac{(3\hat{I}_z^2 - \hat{\mathbf{I}}^2)}{4I(2I-1)} \\ &= e^2 q Q \frac{(3\hat{I}_z^2 - \hat{\mathbf{I}}^2)}{4I(2I-1)} \end{aligned} \qquad (2.72)$$

where Q is the quadrupole moment of the nucleus, $\frac{d^2V}{dz^2} = eq$ is the electric field gradient, e is the elementary charge and q is the z component of the electric field gradient tensor.

1.11.5 The Motional Averaging of Hamiltonians and their Contribution to Relaxation in Liquid State NMR.

It is common to perform NMR spectroscopy on liquids or solutions of low viscosity. The rapid incoherent reorientation of molecules found in such samples results in the anisotropic interaction Hamiltonians being averaged to zero. As a result of this only the isotropic interactions from the scalar spin-spin coupling and the chemical shift survive which when taken into account with the Zeeman interaction gives the high resolution Hamiltonian and yields the classical liquid 'stick' spectrum.

Although the positioning of absorptions in the NMR spectrum of liquids is independent of the anisotropic Hamiltonians their influence is not entirely removed. The action of the random tumbling of the molecules on the anisotropic interactions causes the interaction energy to vary with time, effectively modulating the strength of the magnetic field at a particular nucleus. Although these perturbations average to zero over time, at any one instant in time they may be changing such that components of the magnetic field vary with the same frequency as the Larmor precessional frequency of the nucleus. When this does occur it enables the nucleus to relax. The anisotropic interactions, therefore, contribute to both the longitudinal relaxation allowing the nucleus to return to its Boltzmann equilibrium value, and to the transverse relaxational mechanisms giving width to the NMR absorptions. Thus the total relaxational rates has contributions from each of the anisotropic interactions such that;

$$\begin{aligned} R_1 &= R_{1\,(Dip)} + R_{1\,(CSA)} + R_{1\,(SR)} + R_{1(Q)} + R_{1(JA)} \\ \frac{1}{T_1} &= \frac{1}{T_{1(Dip)}} + \frac{1}{T_{1(CSA)}} + \frac{1}{T_{1(SR)}} + \frac{1}{T_{1(Q)}} + \frac{1}{T_{1(JA)}} \end{aligned} \qquad (2.73)$$

$$\begin{aligned} R_2 &= R_{2\,(Dip)} + R_{2(Q)} + R_{1(JA)} \\ \frac{1}{T_2} &= \frac{1}{T_{2(Dip)}} + \frac{1}{T_{2(Q)}} + \frac{1}{T_{2(JA)}} \end{aligned} \qquad (2.74)$$

These components are discussed below;

1.11.5.1 Relaxation via Dipolar Interactions.

If two nuclei i & j of nuclear spin I and S are at a separation r_{ij} then the contribution to the longitudinal relaxational rate R_1 of i is;

$$R_1 = \frac{1}{T_{1\,(Dip)}} = \frac{2\gamma_i^2\gamma_j^2\hbar^2 S(S+1)}{15r_{ij}^6}\left[\frac{3\tau_c}{1+\tau_c^2\omega_I^2} + \frac{\tau_c}{1+\tau_c^2(\omega_I-\omega_S)^2} + \frac{6\tau_c}{1+\tau_c^2(\omega_I+\omega_S)^2}\right] \quad (2.75)$$

while the contribution to the transverse relaxational rate R_2 is;

$$R_2 = \frac{1}{T_{2\,(Dip)}} = \frac{\gamma_i^2\gamma_j^2\hbar^2 S(S+1)}{15r_{ij}^6}\left[\begin{array}{r} 4\tau_c \\ +\dfrac{3\tau_c}{1+\tau_c^2\omega_I^2} \\ +\dfrac{\tau_c}{1+\tau_c^2(\omega_I-\omega_S)^2} \\ +\dfrac{6\tau_c}{1+\tau_c^2(\omega_I+\omega_S)^2} \\ +\dfrac{6\tau_c}{1+\tau_c^2\omega_S^2} \end{array}\right] \quad (2.76)$$

1.11.5.2 Relaxation via Chemical Shift Anisotropy.

If the chemical shift screen tensor is symmetrical then it is possible to define two quantities $\sigma^{\parallel}$ and $\sigma^{\perp}$ which refer to the components of the shielding tensor parallel and perpendicular to the axis of symmetry. The relaxational rate for such a system is then given by;

$$R_{1(CSA)} = \frac{2}{15}\gamma^2 B_o^2(\sigma^{\parallel} - \sigma^{\perp})^2\tau_c \quad (2.77)$$

1.11.5.3 Relaxation via Spin-Rotation Interactions.

For liquids undergoing isotropic molecular reorientation the relaxation rate induced by the motion of a *molecular* magnetic moment is;

$$R_{1(SC)} = \frac{2\pi MR^2kT}{h^2}C_{eff}^2\tau_J \quad (2.78)$$

where M is the mass of the molecule, R is the radius of the molecule, C_{eff}^2 is the average component of the spin-rotation tensor and τ_J is the *angular momentum* correlation time, which is a measure of time that a molecule spends in any given angular momentum state.

1.11.5.4 Relaxation via the Electric Quadrupole Interaction.

In tumbling molecules, the electric field that constituent quadrupolar nuclei experience is constantly fluctuating. As in the dipolar mechanism there may be frequency components of this fluctuation capable of inducing transitions between energy levels. Despite the fact that these transitions are now between nuclear quadrupole energy levels and caused by a fluctuating electric field it still remains a mechanism whereby the nucleus can relax. In the simplified case of a quadrupolar nucleus of spin I undergoing rapid molecular tumbling with axial symmetry of the molecular electric field the induced relaxational rates become;

$$R_{1(Q)} = R_{2(Q)} = \frac{3}{40}\frac{2I+3}{I^2(2I-1)}\left(\frac{e^2Qq}{\hbar}\right)^2\tau_c \qquad (2.79)$$

$\frac{e^2Qq}{\hbar}$ = quadrupolar coupling constant.

where
Q = nuclear quadrupole moment.
q = electric field gradinent.

1.11.5.5 Relaxation via Scalar Interactions.

Scalar or spin-spin coupling is discussed in section 1.10.2 . If two nuclei, I & S, are coupled I experiences a changing magnetic field as S relaxes. This may induce the relaxation of I when;

(a)$R_1^s \gg 2\pi J$ and $R_1^s \gg R_1^I$. This situation may be found when a quadrupolar nucleus S is coupled to a dipolar nucleus I with a relatively large J coupling constant. Because of the rapid relaxation of S the expected splitting of I is not observed. The affect this has on the rate constants is;

$$R_1^I = \frac{8\pi^2J^2}{3}S(S+1)\frac{T_1^S}{1+(\omega_I-\omega_S)^2(T_1^S)^2} \qquad (2.80)$$

$$R_2^I = \frac{4\pi^2J^2}{3}S(S+1)\left[T_1^S + \frac{T_1^S}{1+(\omega_I-\omega_S)^2(T_1^S)^2}\right] \qquad (2.81)$$

For this it can be seen that there is only a significant contribution to R_1 when the Larmor precessional frequencies of the two coupled nuclei are similar (For example as found in the coupling between ^{13}C and ^{79}Br in Bromoform). R_2, however, is more readily affected and it is this which leads to the broadening of the absorptions from nitrogen bonded protons.

(b) $R_1^s \ll 2\pi J$ and $R_1^s > R_1^I$. In this situation the spin-spin splitting is not effected nor is R_1, however R_2 is reduced. For example, in $^{13}CH_3COOCD_3$ J_{CH}=130Hz, $T_1(^1H)$=12.5 sec,$T_1(^{13}C)$=19.2 sec, while $T_2(^{13}C)$=6.1 sec. In this rapidly tumbling molecule it would be expected to find both the T_1 and the T_2 of ^{13}C to be equal in the absence of scalar coupling.

Although not all of the phenomena characterized above are of immediate relevance to the work described later, they have been dealt with in order to place in perspective those phenomena that do impinge directly on this work.

Chapter 2

Introduction to Fourier Transformation Nuclear Magnetic Resonance Spectroscopy.

2.1 Introduction

Initially nuclear magnetic resonance spectrometers were based on a continuous wave experiment. For this either the magnetic field or irradiation frequency of the spectrometer is scanned slowly, with the other fixed, while detecting the change in the absorption characteristics of the NMR sample.

In modern spectrometers the continuous wave method of detecting the NMR spectrum has been abandoned in favour of a more direct approach; i.e. by measuring the free induction decay (FID) of the e.m.f induced by the NMR sample in detector coils as a function of time. As it is difficult for the spectroscopist to identify frequency components in the time domain spectrum (which is the resultant of the superposition of any number of harmonically oscillating waves) their direct interpretation is almost impossible for all but the simplest of systems. However, there exists a transformation, called the Fourier transformation, that enables the time domain spectrum to be transformed into a frequency domain spectrum, equivalent to that produced in the continuous wave experiment. It was only after the 'digital revolution' that Fourier transform NMR spectroscopy[30 - 32] became possible as the scale of the calculations required by the Fourier transform necessitated its implementation on a micro-computer.

Although the Fourier transform (FT) initially appears to be a hindrance when implemented on NMR spectrometers it brings with it many advantages, not least of which, given that the signal to noise ratio (S/N) improves proportionally with (Number Scans)$^{1/2}$ [33], is the ease with which spectra of an acceptable signal to noise ratio can be obtained. The advantages are such that FT NMR spectrometers now dominate all aspects of NMR spectroscopy.

The following sections describe briefly the implementation and implications of FT NMR spectroscopy.

2.2 The Fourier Transformation

The Fourier transformation relates the time domain data f(t) to the frequency domain data f(ω). It is a continuous transform as it requires the integration of f(t) over all time, giving;

$$f(\omega) = \int_{-\infty}^{+\infty} f(t)e^{i\omega t}dt \qquad (2.82)$$

The use of micro-computers requires that the analogue signal from the spectrometer be transformed via digitization into a series of discrete values, being the average of the signal over small time periods. The rate and total time period over which this digitization occurs ultimately dictates the frequency width and resolution of the transformed spectrum and this readily allows the Fourier transform to be applied over a finite time period;

$$f(\omega) = \int_{-t}^{+t} f(t)e^{i\omega t}dt \tag{2.83}$$

Using the polynomial expansions of exponential, sine and cosine functions it becomes possible, with the aid of imaginary numbers, to relate the sine and cosine of an angle to an exponential such that;

$$e^{i\omega t} = \cos(\omega t) + i\sin(\omega t) \tag{2.84}$$

It now becomes apparent that the Fourier transform of the NMR signal has both a real (Re) and imaginary (Im) part; The real transform corresponds to the absorption mode of the NMR signal; The imaginary transform corresponds to the dispersion mode.

$$\mathrm{Re}[f(\omega)] = \int_{-t}^{+t} f(t)\cos(\omega t)dt \tag{2.85}$$

$$\mathrm{Im}[f(\omega)] = \int_{-t}^{+t} f(t)\sin(\omega t)dt \tag{2.86}$$

It is important to note that given the cosine and sine dependencies of the two separate parts of the Fourier transform the real and imaginary frequency domain spectra are symmetrical and anti-symmetric respectively. That is to say that given only one half of the inputs for the transform it is only possible to determine the magnitude of a component frequency, not its sign. Only when both transforms are combined is the true frequency domain spectrum produced.

For further reading on the Fourier transform a specialist text such as that published by Bracewell [34] is recommended.

2.3 Pulsed Fourier Transform NMR Spectroscopy.

2.3.1 The Basic Pulse FT-NMR Experiment

The major advantages of FT NMR over CW NMR stem from its ability to detect the whole NMR spectrum at once and that any number of time domain spectra can be added to each other prior to the Fourier transformation. These two factors alone allow a spectrum on a FT NMR spectrometer to be obtained more quickly for a given signal to noise ratio than on a CW NMR spectrometer, obtaining in seconds what would other wise have taken either minutes or hours.

The FT NMR method does, however, require that all nuclei in the spin system be stimulated simultaneously. This can be achieved by irradiating the sample with a short pulse of r.f. radiation the frequency of which is equal to the carrier frequency and is normally positioned so that it occurs in the centre of the NMR spectrum.

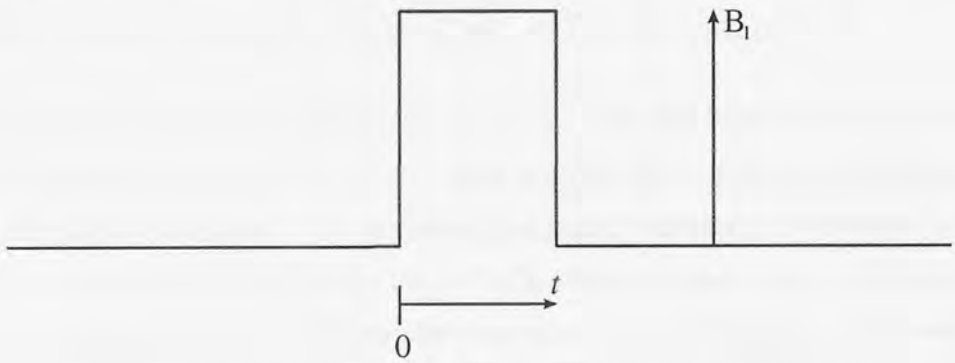

Figure 2.16 : A basic $\mathbf{B_1}$ pulse in a FT NMR experiment.

The frequency components relative to the carrier frequency induced by pulsing are determined by the Fourier transform of the pulse wave form. Assuming that the pulse is square, has an intensity B_1 and lasts from time=0 to time=*t* (as shown in figure 2.16) then ;

$$f(\omega) = \int_{-\infty}^{+\infty} f(t)e^{i\omega t}dt \qquad (2.87)$$

However, for the range t=-∞ to t=0 f(t)=0, for t=*t* to t=∞ f(t)=0 and for t=0 to t=*t* f(t)=B_1. So for a square pulse;

$$\int_{-\infty}^{+\infty} f(t)e^{i\omega t}dt \equiv \int_{0}^{t} B_1 e^{i\omega t}dt \qquad (2.88)$$

which leads to;

$$
\begin{aligned}
f(\omega) &= B_1 \int_0^t e^{i\omega t} dt \\
&= B_1 \left[\frac{1}{i\omega} e^{i\omega t} \right]_{t=0}^{t=t} \\
&= \frac{B_1}{i\omega} \left[\cos(\omega t) + i\sin(\omega t) \right]_{t=0}^{t=t} \\
&= \frac{B_1}{\omega} \sin(\omega t) + i \frac{B_1}{\omega} \left(1 - \cos(\omega t) \right)
\end{aligned}
\tag{2.89}
$$

This equation shows that the r.f. frequency components generated by the pulse vary in both intensity and phase relative to the carrier frequency. However, it is possible to approximate these variations to zero across the NMR spectrum, which typically has a frequency width of several thousand Hertz, by using very short pulses. Figure 2.17.a, 2.17.b and 2.17.c show the intensity and phases of the radio frequency components, defined by the real and imaginary Fourier transforms of the square wave B_1 pulse, generated by pulses of duration 0.01s, 100μs and 1μs respectively.

The angle by which the magnetization vector is nutated is dependent on both the length and intensity of the r.f. pulse. As these are specific to a spectrometer the nutation angle that the pulse induces rather than pulse intensity and duration is used when discussing the effect of pulses on the bulk magnetization vector. The nutation angle for a particular pulse width may be determined by performing a pulse-width calibration (section 2.3.2.3).

The basic pulsed FT-NMR experiment may be performed as follows:

The sample is prepared and placed into the NMR spectrometer where it establishes its Boltzmann magnetization. A 90° pulse is then applied to the sample bringing the magnetization vector into the x-y plane where the FID, generated by the Larmor precession of the individual magnetic moments, is detected, digitized and stored in a computer.

The sample may be pulsed and the FID detected any number of times with each FID being added to previous time domain spectra. Ideally sufficient time should be left between acquisition periods to allow the re-establishment of the Boltzmann magnetization. Once a sufficient number of time domain spectra have been acquired their resultant can be transformed by the Fourier transform giving the required frequency domain spectra. Figure 2.18

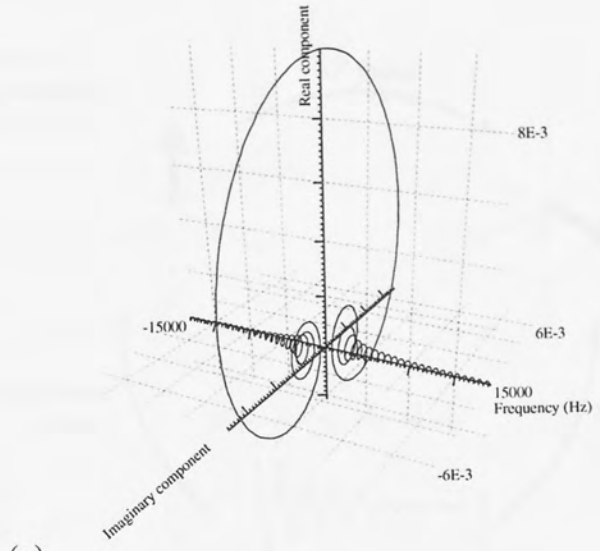

(a)

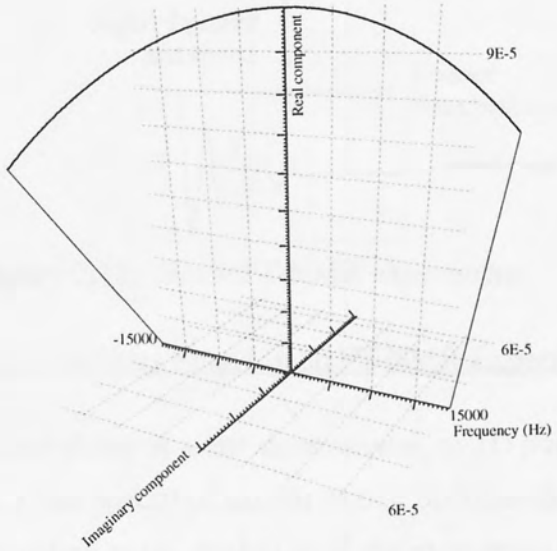

(b)

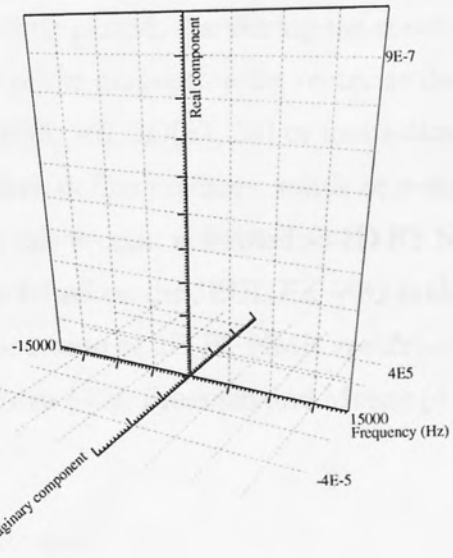

(c)

Figure 2.17 : Frequency components generated by pulsing B_1 for a duration of **(a)** 0.01s, **(b)** 100μs and **(c)** 1μs over a frequency width of 30000Hz.

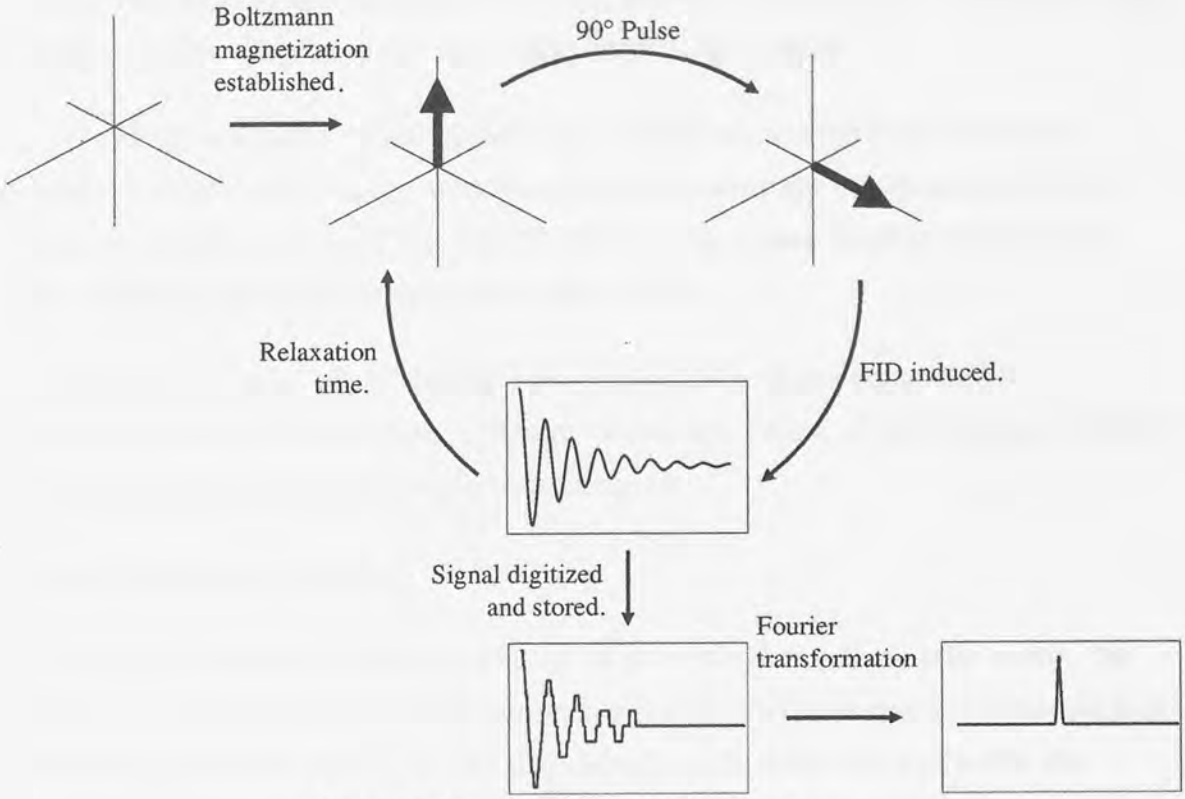

Figure 2.18 : Basic FT-NMR experiment.

2.3.2 The Common Parameters Found in an FT-NMR Experiment.

The experiment outlined above is a one dimensional, or 1D pulse FT-NMR experiment and results in a line spectrum similar to that obtained from a continuous wave experiment. It is so called as the evolution of the magnetization vectors is only monitored as a function of one time period, that during the spectral acquisition. It is possible to detect the evolution of the magnetization vector as the function of two, three or more time periods giving 2D[35, 36], 3D[37, 38] or multi-dimensional[39] FT-NMR spectroscopy, the outputs of which define surfaces, solids or n-dimensional space respectively. The discussion in this section is limited to 1D FT NMR spectroscopy, particularly to those parameters found on the JEOL FX-90Q multi-nuclear FT NMR spectrometer. For a concise discussion of 2D FT NMR spectroscopy the author recommends the reviews by Morris [40]; Freeman and Morris [41]; and Kessler, Gehrke and Griesinger [42].

2.3.2.1 Setting the Carrier Frequency.

The carrier frequency ultimately determines which nuclei in the NMR sample will eventually be detected as it defines the centre of the NMR spectrum. It is possible to

define this frequency explicitly. However, it has traditionally been set by using two values; the observation frequency (OBFREQ) and the offset frequency (OBSET) which together give the frequency of the centre of the NMR spectrum.

OBFREQ is usually defined in MHz and may be considered to be the coarse frequency control, determining which nucleus will eventually be detected. Having defined the band of nuclei of interest OBSET (usually quoted in kHz) acts as a fine tune, defining exactly where the pulse centre will be.

These frequencies can be obtained from calculations using equation(2.9). However, commonly used nuclei will have the suitable values of OBFREQ and OBSET defined in tables supplied by NMR manufacturers.

2.3.2.2 The Spectral Window.

It is also necessary to define a window of interest either side of pulse centre, the frequency range of which is called the spectral width. The final spectrum detected will cover a region which extends by half the spectral width above and half below the carrier frequency. On the JEOL spectrometer the spectral width is defined by FREQW and is limited to a maximum value of 30030Hz.

One problem with FT NMR spectroscopy is that signals that lie outside the spectral window can be folded back into the NMR spectrum giving false peaks in the spectrum (section 2.3.3.3). To alleviate this problem when the spectral width is set a frequency filter is also automatically configured to filter out frequencies outside the spectral window. This eliminates most folded peaks. However, due to imperfections in the filtering electronics, frequencies just outside the spectral window may still be folded onto the spectrum, albeit with reduced intensity.

2.3.2.3 Pulse width Calibration and Off-Resonance Effects.

The exact angles by which the magnetization vectors of the NMR sample are nutated is determined by the total power delivered to the sample during the pulse of r.f. radiation and the time for which it is applied. As it is usual for the pulsed r.f wave to be of fixed amplitude the nutation angle which the pulse induces is determined solely by the duration of the pulse. This duration, called the pulse width (PW1), is usually of the order of micro-seconds.

The Fourier transformation equations imply that as the duration of the pulse is increased so too do the amplitudes of the frequency components. However, when this increase is of the order of micro-seconds, the change in amplitude can be neglected and a linear dependence of the nutation angle on the pulse width is observed.

As the intensity of the detected signal is dependent on the transverse component of the bulk magnetic vector, the intensity of the signal produced from a NMR sample, which is initially at its Boltzmann equilibrium condition, should vary sinusoidally with pulse width. It is, therefore, possible from a plot of intensity against pulse width to determine the 90° pulse width (the first maximum in the curve) or the 180° pulse (the following null in the curve) and interpolate these pulse widths, neglecting pulse imperfections, to derive the pulse widths for all other nutation angles. Where a more accurate correlation between pulse width and nutation angle is required there exist more complex methodologies, such as that reported by Goez [43], which also account for pulse imperfections.

As shown in 2.3.1, when a square wave pulse of B_1 radiation is applied to the NMR sample the perturbation it induces is spread over a range of frequencies, centred on the frequency of B_1. It was also shown that the phase and relative magnitude of the induced perturbing field vary across the spectrum and that only the perturbation induced at the carrier frequency has constant phase with a change in pulse length. It is for this reason that any pulse width calibrations should be carried out 'on resonance', with the observed signal at the carrier frequency. Should the pulse width calibration be attempted off resonance then the phase changes in the perturbing field subject the signal under observation to an *off resonance effect.*

Classically the effect of the B_1 field on a magnetization vector is described by considering the magnetic vectors present in the rotating frame. For a signal which is off resonance there is a corresponding magnetic vector which rotates in the rotating frame. The frequency of this rotation in the rotating frame (ω_1) is the frequency difference between the reference frequency (i.e. the carrier frequency) (ω_{rf}) and Larmor precessional frequency (ω_0) of the off resonance nucleus;

$$\omega_1 = \omega_0 - \omega_{rf} \tag{2.90}$$

which corresponds to the nucleus rotating about an apparent magnetic field in the rotating frame of $B_{0'}$;

$$B_{0'} = -\frac{\omega_1}{\gamma} = \frac{\omega_{rf} - \omega_0}{\gamma} \tag{2.91}$$

When the B_1 field is applied to the sample it and the apparent magnetic field combine by vector addition to produce an effective magnetic field, B_{eff}, of magnitude

$$|B_{eff}| = \sqrt{B_1^2 + B_{0'}^2} \tag{2.92}$$

and tilted by an angle θ with respect to the z-axis such that;

$$\tan(\theta) = \frac{B_1}{B_{0'}} \tag{2.93}$$

Thus when a nutating pulse is applied to an off-resonance nucleus the magnetic vector nutates about B_{eff}, which does not lie in the x-y plane, by an angle β_{eff};

$$\beta_{eff} = \gamma B_{eff} \tau \tag{2.94}$$

Furthermore, the nutation angle for a given pulse duration increases with frequency offset. At exact resonance where B_{eff} is equal to B_1 equation(2.94) becomes;

$$\beta = \gamma B_1 \tau \tag{2.95}$$

The use of composite pulses [44] can curb off-resonance effects.

2.3.2.4 Relaxation Delay.

The time delay between successive pulses and spectral acquisitions is referred to the relaxation or pulse delay(PD). The effective implementation of FT NMR spectroscopy relies on setting this delay to an appropriate value to facilitate relaxation towards the Boltzmann equilibrium; a delay which is too short obliterating the NMR spectrum, while one which is too long needlessly adding to the length of the NMR experiment. (section 2.3.3.5)

2.3.2.5 Spectrometer Time Delays.

There are many other delays involved in the practical implementation of an FT NMR experiment. Some of these delays are common to all spectrometers. However, most of them are spectrometer specific. Those delays relating to a simple pulse sequence on the JEOL spectrometer are depicted in figure 2.19.

As can be seen even the most simple pulse experiment requires the setting of a number of delays, in addition to the pulse width and relaxation delay. Fortunately most of these delays are set automatically by the spectrometer and only on rare occasions do they need to be set manually.

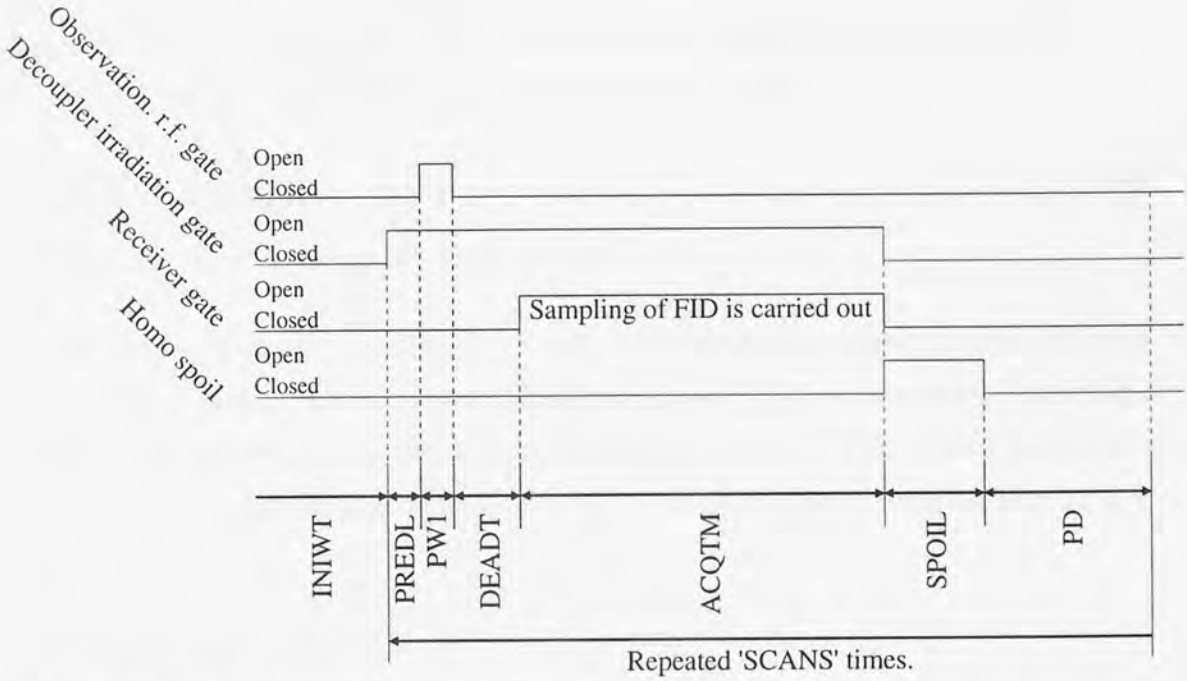

Figure 2.19 : The adjustable time delays of a simple pulse sequence as implemented on the JEOL FX-90Q NMR spectrometer.

2.3.2.5.1 INIWT : INItial WaiT.

This allows for there to be an initial delay between starting the NMR experiment and the execution of the first loop of the pulse sequence. It is often used to ensure that a sample has established its Boltzmann equilibrium magnetization prior to the NMR experiment.

2.3.2.5.2 PREDL : PRE-irradiation DeLay.

It is common in NMR spectroscopy to continuously irradiate a particular band of nuclei to remove their influence from the detected spectrum. As this does not occur instantaneously it is necessary to allow a delay between the start of irradiation and the rest of the pulse sequence during which the de-coupling occurs.

2.3.2.5.3 DEADT : DEAD Time.

If the FID is sampled too soon after the nutating pulse is applied it is possible to detect residual r.f. radiation which on Fourier transformation causes the distortion of the

resulting spectrum. The inclusion of a dead time allows any residual r.f. radiation to decay away prior to the acquisition of the FID.

2.3.2.5.4 ACQTM : ACQuisition TiMe.

During the acquisition period the FID is detected, sampled and stored. The acquisition time is dependent on both the number of data point (SAMPO) in the resultant spectrum and the frequency width of the spectrum:

$$\text{ACQTM} = \frac{\text{SAMPO}}{2.\text{FREQW}} \tag{2.97}$$

2.3.2.5.5 SPOIL : Homogeneity SPOILing pulse.

It may be necessary to artificially destroy any transverse magnetization within an NMR sample that remains after the acquisition period. This is achieved by applying a homogeneity spoiling pulse, the duration of which is set by SPOIL, which temporarily destroys the homogeneity of the magnetic field and all magnetic coherence in the x-y plane is rapidly lost.

2.3.3 Special Consideration.

2.3.3.1 Digital resolution

Of paramount importance to any NMR experiment is the resolution of the final frequency domain spectrum. Due to the digitization of the FID the resulting NMR spectrum is a number of connected data points and it is the distance between these points (the digital resolution) which limits the resolution of the final spectrum[45, 46]. The digital resolution, DR, measured in Hertz is inversely proportional to the acquisition time in seconds;

$$\text{DR} = \frac{1}{\text{ACQUM}} \tag{2.98}$$

It therefore follows that increasing the number of data points in a NMR spectrum improves the digital resolution and causes a proportional increase in the acquisition time. It is, therefore, of importance to have a sufficient number data points to obtain the required resolution, but not so many as to cause an unnecessary increase in the experimental time.

2.3.3.2 Truncation of the FID.

Sometimes the FID may persist after acquisition has stopped. When this occurs the FID is said to have been truncated and this results in a distortion of the resonant signals produced after Fourier transformation. Figure 2.20 shows the effect of truncating the FID.

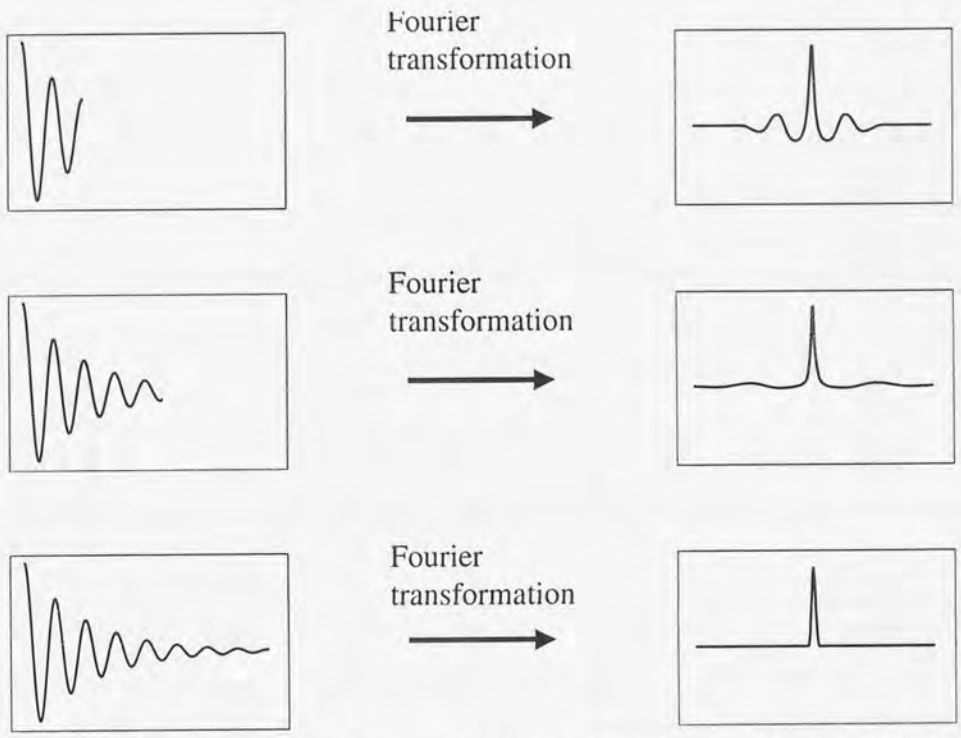

Figure 2.20 : The effect of truncating the FID on the resulting spectrum.

2.3.3.3 Folding

Despite frequency filtering, resonances that lie just outside the spectral window of the spectrometer may appear in the NMR spectrum. The positioning of such resonances makes the spectrum appear as if they have been folded about the edges of the spectral window and superimposed onto the NMR spectrum. Such folding continues about the edges of the spectrum until the resonance falls within the spectral window. Figure 2.21

2.3.3.4 Quadrature Detection

The FID measured by a detector aligned along the y axis of the rotating frame is composed solely of changes in the y component of the induced magnetic field, giving a signal which is the summation of a number of cosine waves. As discussed earlier the Fourier transformation of such a wave cannot distinguish between positive and negative frequency components relative to the carrier frequency, resulting in the spectrum being

mirrored about the carrier frequency. To alleviate this problem a second detector, aligned at 90° to the first is employed. Together the signals from these two detector provide the real and imaginary signal components required for the Fourier transformation, allowing the absolute frequency of the signals relative to the carrier frequency to be determined. The ability of the spectrometer to determine both the sign and the magnitude of the NMR signals in this way is know as quadrature detection[47-49].

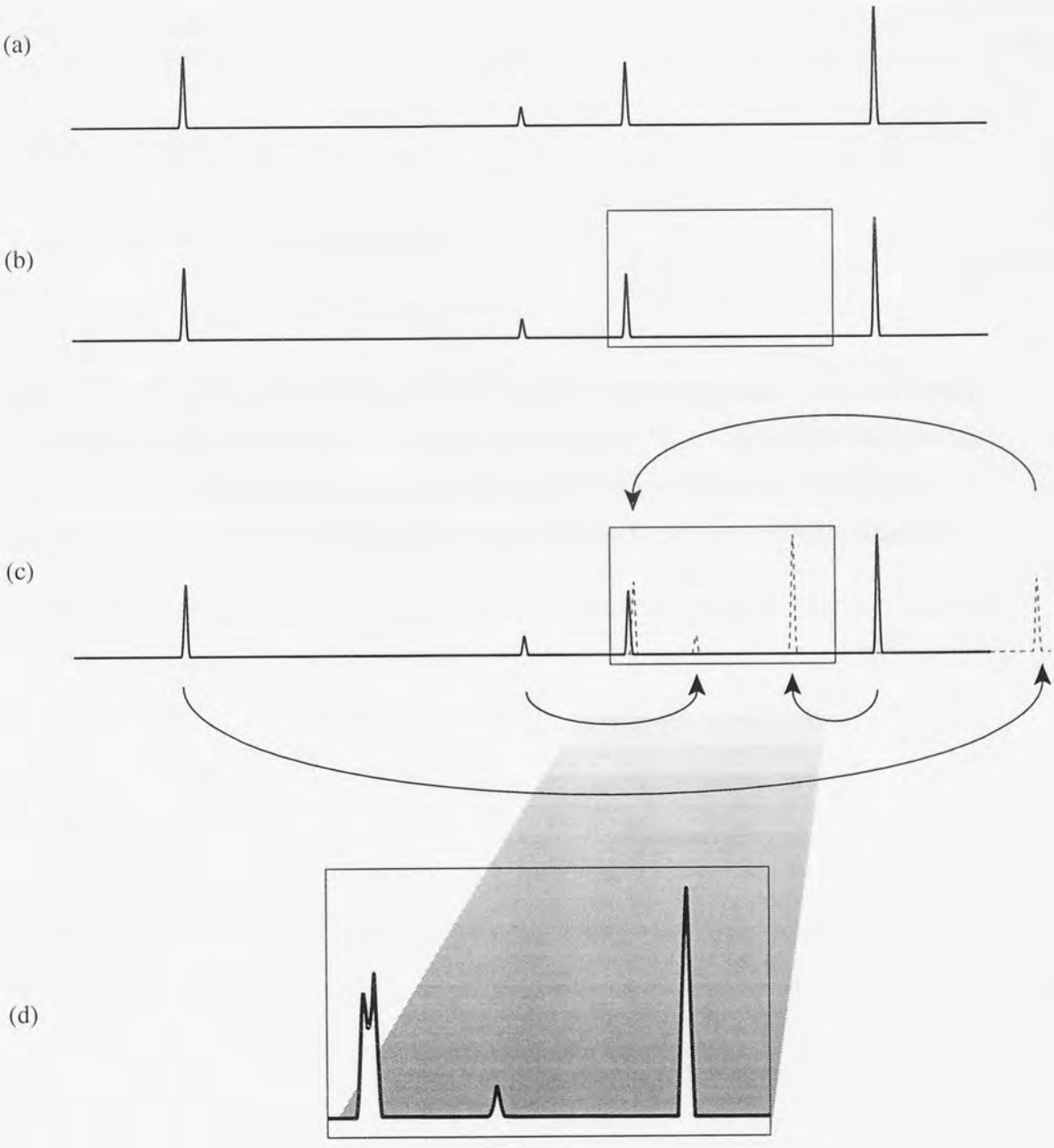

Figure 2.21 : Effects of folding on an NMR spectrum. **(a)** full spectrum, **(b)** spectral window imposed by spectrometer, **(c)** the folding of the peaks and **(d)** detected spectrum.

2.3.3.5 Inter-Sequence Delay.

2.3.3.5.1 Obtaining Quantitative Signal Intensities.

When a NMR experiment is conducted over a number of acquisitions the relaxation delay must be chosen so that an adequate amount of magnetization is re-established by relaxation. The relaxation of the z magnetization, M_z, of an ensemble of equivalent spins returning to its equilibrium magnetization, M_0, with a characteristic relaxation time of T_1 is governed by;

$$\frac{dM_z}{dt} = -\frac{M_z - M_o}{T_1} \tag{2.99}$$

which on integration gives;

$$\begin{aligned} \ln(M_0 - M_z) &= -\frac{t}{T_1} + \ln(M_0 - M_{zi}) \\ M_z &= M_0(1 - e^{-\frac{t}{T_1}}) - M_{zi}e^{-\frac{t}{T_1}} \end{aligned} \tag{2.100}$$

where t is the summation of all delays between consecutive pulses (predominantly comprised of the acquisition and relation delays) and M_{zi} is the initial value of the z magnetization after the nutating pulse. Figure 2.22 shows the recovery of the z-magnetization towards its Boltzmann magnetization from zero z-magnetization.

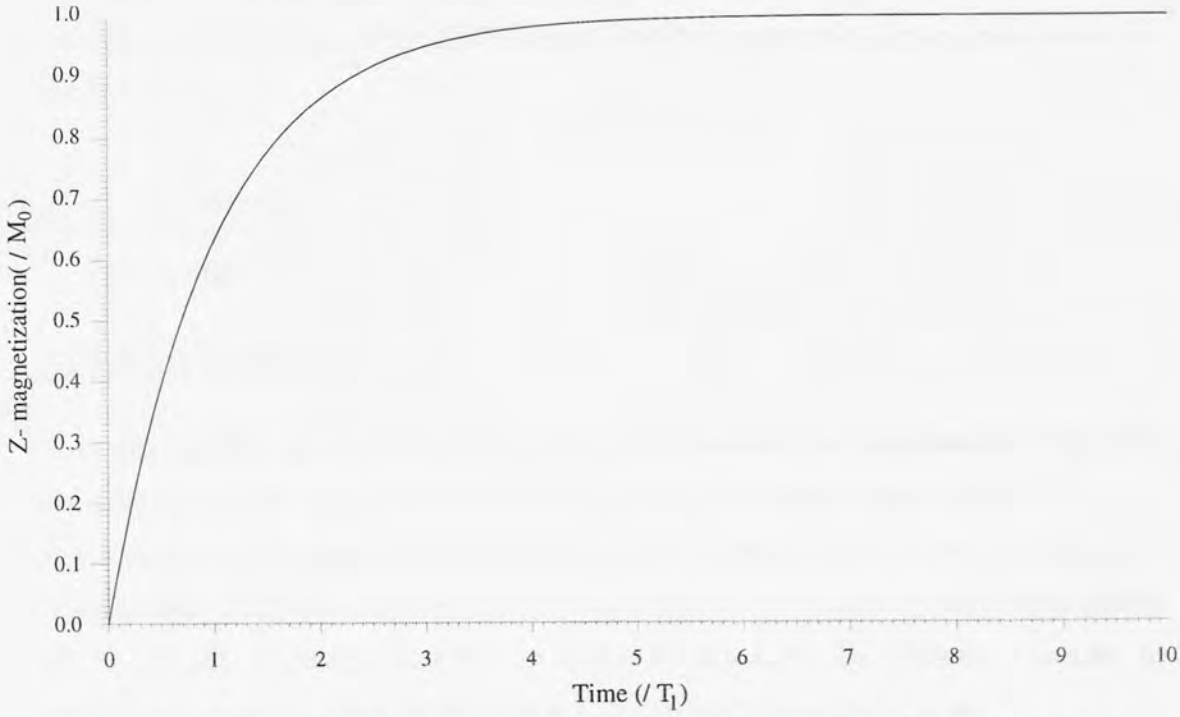

Figure 2.22 : Recovery of z-magnetization under T_1 relaxation after a 90° nutating pulse.

This implies that if quantitative signal intensities are required (by operating on M when it is within 0.05% of M_0) then a delay of 5.3 times T_1 should be used for the total relaxation delay. For a sample which consist of a number of magnetically different nuclei, quantitative spectra are obtained by employing a relaxation delay of 5.3 times the largest value of T_1.

2.3.3.5.2 Maximising Signal Intensity - Rapid Multi-pulsing.

When the relaxation delay is set to a value less than 5.3 T_1 M_0 is never re-attained during the experiment and, over successive scans, the z magnetization vector is driven to a new equilibrium. Although reducing the relaxation delay causes the intensity of the NMR signal detected on each transient to be reduced, more acquisitions can be achieved in a given time period. As the relationship between the signal intensity and relaxation delay is non-linear there exist optimum values of the pulse angle and relaxation delay which yields the optimum signal to noise ratio. For a given relaxation delay the optimum pulse angle is defined by the Ernst condition [50] such that;

$$\cos(\theta_E) = e^{\left(\frac{-t}{T_1}\right)} \tag{2.101}$$

Rapid multi-pulsing obtains the best signal enhancement when the relaxation delay is set such that t/T_1 has a value in the range of 0.1 to 0.5 and the pulse angle is set to the appropriate Ernst angle, θ_E. Under such conditions a signal enhancement of 56% is obtained over the same number of scans as in the classical 90° 5.3×T_1 experiment. The equilibrium intensity, I_{eq}, of the NMR signal detected under such driven conditions is given by;

$$\frac{I_{eq}}{M_0} \propto \frac{(1 - e^{-\frac{t}{T_1}})\sin(\theta)}{(1 - \cos(\theta)e^{-\frac{t}{T_1}})} \tag{2.102}$$

2.3.3.6 Phase Correction.

As discussed in section 2.3.2.5 there is a delay between the application of the pulse to the sample and the acquisition of the FID. During this delay, transverse magnetization which originally lay along one of the detector axes evolves in the x'-y' plane and each component of the magnetization acquires a frequency dependent phase shift. On transformation of the FID this frequency dependent shift can be overcome by computerised constant phase and frequency dependent phase corrections.

2.3.3.7 Special considerations for the observation of solids

The NMR resonances of solids have associated with them particularly short spin-spin relaxation times, the results of which are short-lived FID's and broad absorptions in the transformed spectra. A short FID does, however, present a problem for the NMR spectrometer as its rapid decay may cause it to be lost during any delays that occur between pulsing and spectral acquisition. To overcome this problem the dead time may be reduced to capture more of the FID. As discussed in section 2.3.2.5.3 a reduction in the dead time also increases the amount of r.f. break through from the pulse and results in the addition of base line role to the transformed spectrum.

Chapter 3

The NMR of Solids.

3.1 Introduction

The NMR spectra of particulate solids are usually broad and featureless, one absorption typically covering most of the isotropic chemical shift region for the nuclide under scrutiny. This simple absorption is not necessarily characteristic of the nuclei within the solid existing in simple chemical environments (although this may be the case) but is in fact caused by the spectrum being overloaded with additional information from the anisotropic Hamiltonians which, due to the lack of rotational and translational motion in the solid, are no longer averaged to zero.

In order to obtain 'solution-like' spectra of solids it, therefore, becomes necessary to artificially impart appropriate "molecular" motion to the solid sample, once again averaging the 'unwanted' Hamiltonians to zero. For all nuclei this involves averaging out the dipolar interactions and the chemical shift anisotropy while for the quadrupolar nuclei it also becomes necessary to average out the quadrupolar interactions.

It has long been commonplace in solution state NMR to spin the sample along either z or y axes as this averages out some of the inhomogeneities in the external magnetic field and improves resolution. This implies that unwanted interactions may be averaged out by rotating about a suitable axis. A number of techniques have successfully applied this basic idea to solids resulting in either the removal or reduction of unwanted interactions.

3.2 Magic Angle Spinning (MAS).

In a rigid lattice, as found in a solid, one can impart motion to the constituent nuclei by mechanically spinning the whole sample about some chosen axis. If the Hamiltonians are formulated under the principal axes system then it only becomes necessary to consider the effects of rotation on the second rank tensors as the first rank tensor becomes the null tensor and the zero rank tensor is unaffected by rotation.

It is possible to express the dipolar Hamiltonian, as with all the Hamiltonians, in a form as found in equation(2.54) using whichever coordinate basis is most appropriate to its manipulation. Previously this has been based on the laboratory axes but for this discussion it is easier if the Hamiltonian is left based in the principal axes (Axial bases are discussed in appendix 2);

$$\mathcal{H}_{D\,(PAS)} = \sum_{i}^{spins}\sum_{j>i}^{spins}\xi_{ij}^{Dip}\sum_{m=-2}^{+2}(-1)^{m}F_{2\,(PAS)}^{m}(ij)T_{2}^{m}(ij) \qquad (2.103)$$

The transformation of the dipolar tensor from the principal axes system to the laboratory frame by applying the appropriate Wigner rotational matrices [13, 51] (discussed in appendix 3) to transform it into the arbitrary internal axes system and then from the arbitrary internal axes system to the laboratory frame is given by;

$$\begin{aligned} F_{2\,(AAS)}^{m'}(ij) &= \sum_{m''=-2}^{2}\mathcal{D}_{m''m'}^{2}(\Omega_{ik})F_{2\,(PAS)}^{m''}(ij) \\ F_{2\,(LAB)}^{m}(ij) &= \sum_{m'=-2}^{2}\mathcal{D}_{m'm}^{2}(\Omega'_{ik})F_{2\,(AAS)}^{m'}(ij) \\ &= \sum_{m'=-2}^{2}\mathcal{D}_{m'm}^{2}(\Omega'_{ik})\sum_{m''=-2}^{2}\mathcal{D}_{m''m'}^{2}(\Omega_{ik})F_{2\,(PAS)}^{m''}(ij) \end{aligned} \qquad (2.104)$$

where $\mathcal{D}(\Omega_{ik})$ relates the principal axis system to the arbitrary internal axes and $\mathcal{D}(\Omega'_{ik})$ relates the arbitrary internal axes to the laboratory frame.

Spinning the sample at an angle β to the external magnetic field causes Ω' to become time dependent, the Euler angles taking the arbitrary internal axes to the laboratory frame being $(0, \beta, \omega_r t)$ where ω_r is the frequency of rotation about the axis. If the rotation is fast enough then the time average of $\mathcal{D}_{m'm}^{2}(\Omega'')$ (considering only the secular terms, m=0) becomes;

$$\overline{\mathcal{D}_{00}^{2}(0,\beta,\omega_r t)} = \frac{3\cos^2(\beta)-1}{2} \qquad (2.105)$$

allowing the effective secular dipolar Hamiltonian to be written as;

$$\mathcal{H}_{sec,\,eff}^{D} = -\frac{1}{2}\frac{h}{2\pi}\sum_{i}^{spins}\sum_{j>i}^{spin}\gamma_i\gamma_j\frac{(3\cos^2\beta-1)}{2}\frac{1}{r_{ij}^{3}}\left(3I_0(i)I_0(j)-\mathbf{I}(i)\cdot\mathbf{I}(j)\right) \qquad (2.106)$$

When β is chosen to be 54°44' (the magic angle) the term $3\cos^2\beta$-1 becomes zero, the effective dipolar Hamiltonian vanishes and the dipolar broadening interactions are removed.

Even if the dipolar terms are ignored the signal from a granular solid would not be entirely devoid of features. The signal would usually be shouldered either to the right or on both sides of the most intense part of the absorption. This shouldering is caused by the chemical shift anisotropy (CSA) and its shape is dictated by the chemical shift

screening tensor, depending on whether the tensor is symmetrical or asymmetrical (Figure 2.23).

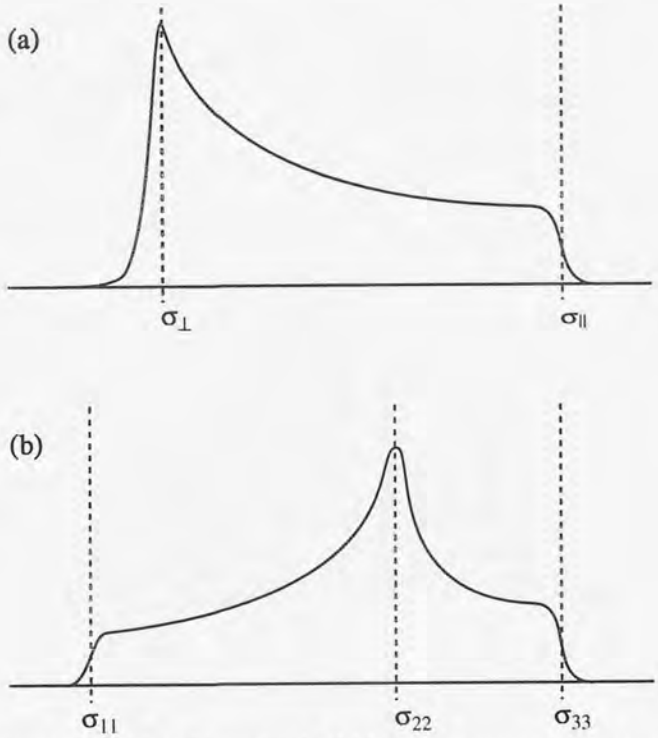

Figure 2.23 : Chemical Shift Anisotropy Patterns.
(**a**) with a symmetrical screening tensor
(**b**) with an asymmetrical screening tensors.

If the solid is spun at the magic angle the effect of CSA, like dipolar interactions, will be reduced. However, if the spinning frequency is less than the frequency width of the static solid then the absorption is split into a number of spinning side bands on either side of the isotropic chemical shift and separated by a frequency equal to that at which the solid is rotated. As the spinning sidebands follow the general shape of the chemical shift anisotropy pattern the most intense signal need not correspond to the isotropic chemical shift. Figure 2.24 shows the effect of spinning at the magic angle on solid glycine at various frequencies.

This technique used to minimize CSA and dipolar effects is referred to as magic angle spinning NMR (MAS NMR) and was first used independently by Andrew, Bradbury and Eades [1], and Lowe [52]. MAS NMR was initially much improved when it was combined with cross-polarization (CPMAS [53, 54]) enabling the detection of low magnetogyric ratio nuclei with subsequent improvements occurring when CPMAS was combined with multipulse proton decoupling [55] allowing the resolution of J-coupling of proton bound nuclei in solids.

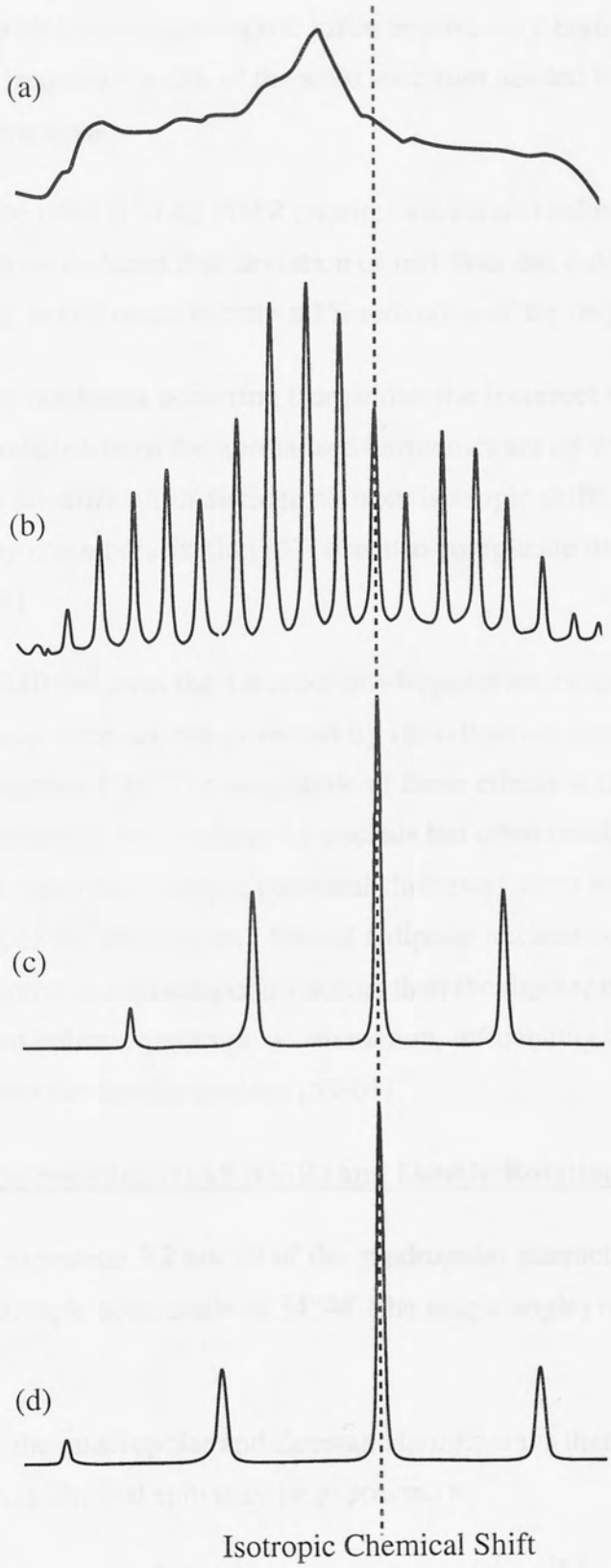

Figure 2.24 : ^{13}C NMR spectra of the carboxyl carbon of glycine in the solid state. (**a**) Static powder pattern. Spun at the magic angle at (**b**) 0.5 Hz, (**c**) 1.6 Hz and (**d**) 2.1 Hz

The problems with MAS include:

1. Nuclei with large magnetogyric ratios require very high spinning speeds to exceed the frequency width of the solid spectrum needed to totally remove the dipolar interactions.

2. The probe used in MAS NMR requires the careful calibration of the magic angle. Andrew deduced that deviation of less than one half a degree from the magic angle would result in only a 1% reduction of the original line width [56].

3. Spinning sidebands occurring from either the incorrect setting of the magic angle or produced from the normalised harmonics set up within the MAS experiment are difficult to distinguish from isotropic shifts. Intensity anomalies produced by cross-polarization [57] can also complicate the spinning sideband patterns [58].

4. MAS NMR removes the 1st order quadrupolar interactions, but not 2nd order interactions as these are not governed by Hamiltonians containing a factor of $3\cos^2\theta$-1 (section 3.3). The magnitude of these effects will depend heavily on the environment of the quadrupolar nucleus but often result in a 'quadrupolar shift' of the observed isotropic chemical shift away from its true value and also broadening of the absorptions. Should a dipolar nucleus be observed which is dipolar coupled to a quadrupolar nucleus then the dipolar nucleus may also be subject to an indirect quadrupolar interaction, influencing the line shape detected from the dipolar nucleus [59-61].

3.3 Dynamic Angle Spinning (DAS NMR) and Double Rotation (DOR NMR)

As mentioned in section 3.2 not all of the quadrupolar interactions are removed by spinning the solid sample at an angle of 54°44' (the magic angle) to the polarizing magnetic field.

If we consider the quadrupolar and Zeeman Hamiltonians then the combined Hamiltonian for an individual spin may be expressed as;

$$\mathcal{H}_{(Z+Q)(PAS)} = -\gamma\hbar\mathbf{B_0}\cdot\mathbf{I} + \frac{e^2qQ}{4I(2I-1)}\left[3I_{z'}^2 - I(I+1) + \frac{\eta(I_+^2 + I_-^2)}{2}\right] \qquad (2.107)$$

where the axes are the principal axes of the tensor V_{ij} that describes the electric field gradient and;

$$|V_{z'z'}| \geqslant |V_{y'y'}| \geqslant |V_{x'x'}|, \qquad eq = V_{z'z'}, \qquad \eta = \frac{V_{y'y'} - V_{x'x'}}{V_{z'z'}}, \qquad 0 \leqslant \eta \leqslant 1 \tag{2.108}$$

In the general case the Zeeman and quadrupolar interactions are of comparable size and to obtain the eigenstates and eigenvalues of equation(2.107) under such conditions requires a solution to a secular equation of order 2I+1 to be found. This, however, is rarely necessary and in most cases either the Zeeman or quadrupolar interactions dominate. As this text is concerned with the NMR spectrum of quadrupolar solids in high field spectrometers only the situation where the Zeeman interaction dominates is discussed.

Assuming that the quadrupole gradient has cylindrical symmetry equation(2.107) may be transformed instantly into the laboratory frame using the relationship;

$$I_z = I_{z'}\cos\theta + I_{x'}\sin\theta \tag{2.109}$$

resulting in;

$$\begin{aligned} \mathcal{H}_{(Z+Q)\,(LAB)} &= \mathcal{H}_{(Z)\,(LAB)} + \mathcal{H}_{(Q)\,(LAB)} \\ \mathcal{H}_{(Z)\,(LAB)} &= -\gamma\hbar B_0 I_z \\ \mathcal{H}_{(Q)\,(LAB)} &= \frac{e^2qQ}{4I(2I-1)}\left[\begin{array}{l} \dfrac{(3\cos^2\theta - 1)}{2}\left(3I_z^2 - I(I+1)\right) \\ +\dfrac{3\sin\theta\cos\theta}{2}\left(I_z(I_+ + I_-) + (I_+ + I_-)I_z\right) \\ +\dfrac{3\sin^2\theta}{4}\left(I_+^2 + I_-^2\right) \end{array}\right] \end{aligned} \tag{2.110}$$

The various energy levels of equation(2.110) can be written as;

$$E_m = E_m^0 + E_m^1 + E_m^2 + \ldots \tag{2.111}$$

where E_m^p represents the contribution to the energy, of the perturbation of order p, which using second order perturbation theory give

$$E_m^0 = -\gamma\hbar B_0 m \tag{2.112}$$

$$E_m^1 = \frac{3e^2qQ}{4I(I-1)}\mathcal{D}_{0,0}^2\left(m^2 - \frac{I(I+1)}{3}\right) \tag{2.113}$$

$$E_m^2 = -\left[\frac{3}{\hbar\gamma B_0}\left(\frac{e^2qQ}{4I(2I-1)}\right)^2\right]\left[\begin{array}{c}(\mathfrak{D}_{0,1}^2)^2(8m^2-4I(I+1)+1)\\+(\mathfrak{D}_{0,2}^2)^2(-2m^2+2I(I+1)-1)\end{array}\right] \quad (2.114)$$

From these it is evident that an angle of 54°44' is not 'magic' for the second order energy perturbations.

The inability to remove all quadrupolar interactions by MAS NMR lead to the development of Dynamic Angle Spinning [2] and Double Rotation NMR [3](DAS NMR and DOR NMR). The theoretical work of Llor and Virlet [62] in conjunction with Pines *et al* [3] showed that the 'magic' angles for the quadrupolar interaction could be found by solving the fourth order Legendre polynomials of cos(θ). The Legendre polynomial is given by;

$$P_n(x) = \sum_{m=0}^{M}(-1)^m\frac{(2n-2m)!}{2^n m!(n-m)!(n-2m)!}x^{n-2m} \quad (2.115)$$

where M=n/2 or (n-1)/2, whichever is an integer. This gives P_4 (cos θ) to be;

$$P_4(\cos(\theta)) = \frac{35\cos^4(\theta)-30\cos^2(\theta)+3}{8} \quad (2.116)$$

which has two solutions, θ = 30.56 and θ = 70.12.

DAS NMR uses a single rotor as in MAS NMR, but the angle that the axis of the rotor makes to the applied field is made time dependent. The sample is spun at the two angles corresponding to the solution to the 4th order polynomial. When the two spectra are superimposed, the point at which the absorptions cross is the isotropic shift position.

DOR NMR uses a double rotor system (one rotor inside another) with the inner and outer rotor set at 30.56° and 54.7° respectively to the applied magnetic field, with the inner rotor spinning at five time the frequency of the outer rotor. As the DOR technique combines the 'magic angles' for both dipolar and quadrupolar interactions the resultant NMR spectrum has these influences removed, giving a solution like spectrum. Combination of this technique with cross polarization has also been achieved giving a technique for quadrupolar nuclei analogous to CPMAS [63].

Problems with DAS and DOR NMR include;

1. The equipment required for the techniques is both complicated and expensive when compared to the standard MAS NMR experiment.

2. DAS NMR requires careful calibration of the rotor angle. Mueler and co-workers [2] achieved this by the use of a computerized pulley system which gave an angular resolution of 0.36°.

3. As the outer rotor in DOR is presently only capable of spinning at frequencies up to 900Hz, DOR NMR is more prone to spinning sidebands than MAS NMR although it is possible to analysis such sidebands as described by Sun et al [64] and increase their frequency spacing as described by Samoson and Lippmaa [65].

3.4 Multiple Pulse Experiments

Instead of causing the averaging of the dipolar interaction by mechanically manipulating the sample as in MAS NMR it is possible to use appropriate pulse sequences to average the dipolar interaction while keeping the sample static. Scheme 2.1 represents a pulse sequence which, if applied rapidly to the sample, is capable of causing such averaging.

$$\{90_{-y} - 2\tau - 90_{y} - \tau - 90_{x} - 2\tau - 90_{-x} - \tau - \}_{repeat}$$

Scheme 2.1: Pulse sequence capable of removing dipolar interactions in solids.

The pulse sequence moves the magnetization from one axis of the laboratory frame to the others in such a way that it spends an equal amount of time along each ordinate. If this occurs rapidly enough and the spectrum is acquired during the 2τ periods only the time average orientation, lying along the diagonal of a cube, is seen. Figure 2.25. As this diagonal makes the magic angle of 54°44' to $\mathbf{B_0}$ the dipolar interactions will be reduced to zero.

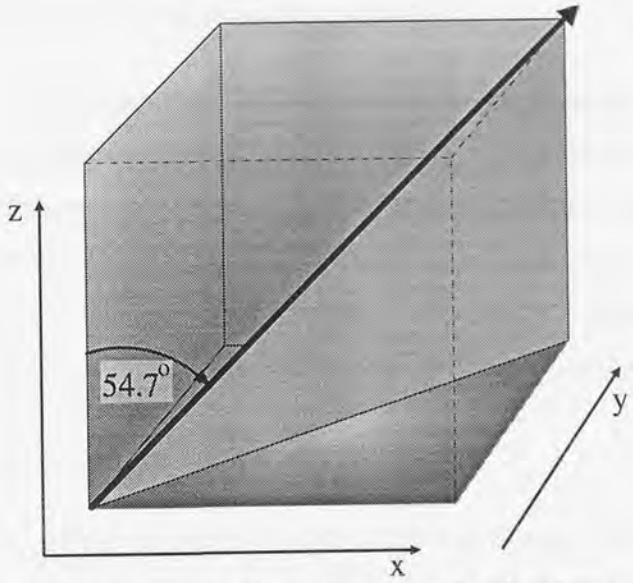

Figure 2.25 : Angle subtended from the z-axis by the diagonal of a cube.

The pulse sequence shown in scheme 2.1 is the WHH-4 or WAHUHA [66] experiment. It removes the dipolar interactions from the spectrum of the solid but as the sample is stationary within the field any chemical shift anisotropy remains (as the orientation between the constituent nuclei and the magnetic field remains constant). Pulse imperfection problems are inherent to the WHH-4 sequence [67] and to this end other cycles utilising a greater numbers of pulses have been developed. The greater number of pulses in these sequences (such as the widely used MREV-8 [68-72]) allows the utilization of other quadrants in the coordinate frame for the removal of pulse imperfections.

Due to the removal of the mechanical constraints from the averaging process such multiple pulse sequences are useful in the study of nuclei with large magnetogyric ratios, such as ^{1}H and ^{19}F whose MAS spectrum would otherwise require excessively high rotor frequencies. The natural development of such a multipulse experiment was to re-combine it with MAS spectroscopy to give a hybrid experiment, CRAMPS-combined rotation and multiple pulse spectroscopy [73, 74](initially using WHH-4 and MREV-8, more recently BR-24 [75-78] and TREV-8 [79]), which gives spectra with a greatly reduced dipolar interaction and chemical shift anisotropy for high magnetogyric ratio nuclei

Disadvantages with the multiple pulse sequences are:

1. Only high specification spectrometers (consequently high cost) are able to cope with the short time periods and intense pulses (while maintaining pulse shape) required to implement the sequence. e.g. To achieve effective averaging of the magnetization one cycle of WHH-4 (four 90° pulses and six time

periods) needs to been performed in circa 10μs.

2. The fact that the chemical shift anisotropy is not removed by multipulse sequences may be viewed as either an advantage or disadvantage, certainly its presence in the spectrum does not give a 'liquid-like' spectrum. However, such sequences are extensively used in the study of solid polymers where the residual chemical shift anisotropy is used to determine proportions of amorphous and crystalline regions; see e.g. Vega and English [80, 81].

3.5 Rotating Magnetic Fields.

Provided the solid sample is rotated relative to the magnetic field at the magic angle the dipolar interactions will be averaged. In MAS NMR this is achieved by rotating the sample in a fixed magnetic field. However, Andrew proposed that this may alternatively be achieved by rotating the magnetic field about a static sample [82]. This could be implemented by electrically rotating the magnetic field and has the advantage that, in principle, the upper frequency limit for cycling the magnetic field will by far exceed that obtained by mechanical manipulation of the sample. Despite the difficulty in generating and maintaining a large and uniform rotating magnetic field there is one report in the literature of causing averaging by this method [83].

This and the previous experiments have induced the narrowing of solid state spectra by imparting coherent motion on the broadening interactions found within the solid lattice. However, coherent rotation need not be the only mechanism by which such narrowing can be achieved and incoherent averaging, as used in the following two experiments, can also be employed.

3.6 Ultrafine Particle NMR (UFP NMR)

It has been reported that it is possible to obtain high resolution NMR spectra of solids in colloidal suspension utilizing only the Brownian motion of the molecules in the support liquid to average the unwanted interactions to zero. This technique is referred to as Ultrafine Particle (UFP) NMR. Using this technique Yesinowski [84, 85] has detected the narrowed ^{31}P absorption of calcium hydroxyapatite while Kimura and Satoh [86, 87] have detected the ^{27}Al absorption of AlF_3. Yesinowski stated that his result was produced with particle sizes in the order of 125 × 125 × 500Å while Kimura and Satoh stated that there result was obtained with particle sizes ranging from 1 - 3 nm. This technique has the obvious disadvantage of finding suitable support liquids

(ones in which the solid is totally insoluble) and of producing particles of sufficiently small dimensions.

3.7 Sonically Induced Narrowing of the Nuclear Magnetic Resonance Spectra of Solids (SINNMR).

Sonically induced narrowing nuclear magnetic resonance [4, 88] was proposed as a method for the narrowing of solid spectra by the ultrasonic irradiation of solid particles suspended in a liquid of suitable density. The narrowing of the spectra observed by this method is attributed to the ultrasound driving the particles into one another, causing tangential collision resulting in the rapid incoherent rotation of the particles and to the rapid reorientation of the particles caused by localised cavitational effects [88]. Although the phenomenon has only been observed in a limited number of samples it is hoped that investigation of the underlying mechanisms by which the incoherent motion of the particles is achieved will ease the current difficulty in applying the technique to a wider range of solid samples. To this end a section of this thesis is concerned with the cavitational effects of ultrasound at frequencies used in the SINNMR experiment.

Part 3

The Use of Ultrasound in Magnetic Resonance Spectroscopy.

Chapter 1

Introduction to Ultrasound.

1.1 Introduction.

Ultrasound is defined as any sound which is of a frequency beyond that to which the human ear can respond; the upper limit of human hearing being in the region of 16kHz. Ultrasound can be divided into two regions identified in terms of their frequency ranges and applications giving diagnostic ultrasound (2 - 10 MHz) and power ultrasound (20 - 100 kHz).

As ultrasound is nothing more than high frequency sound the theory of sound is also the theory of ultrasound. The remainder of this chapter, therefore, expands on certain aspects of the theory of sound while also including certain properties which are peculiar to ultrasound. A more comprehensive account of acoustics can be found in any standard acoustic text book [89] or in one of the excellent reviews of the subject [90].

1.2 Vibrations and Waves

Waves and vibrations can be classified into one of two categories; longitudinal waves, where the direction of particle (a particle being a constituent molecules or atom, see figure 3.1) displacement is co-linear to the direction of wave propagation; and transverse waves, where the particle displacements occur perpendicularly to the direction of wave propagation. All waves require a medium through which to propagate. However, not all media can support both categories of wave.

The propagation of a wave through a medium can be considered by assuming the medium to initially be represented by a regular array of particles, each column of particles representing a layer through the medium (Figure 3.1.a). It can be seen from this model that all materials can support longitudinal waves as the propagation of the wave relies on particles from one layer colliding with and recoiling from particles in the next layer, the oscillation of the source causing successive compressions and rarefactions to be progressively transmitted through the medium.(Figure 3.1.b).

For a transverse wave to propagate through a medium there must be an attractive association between particles in adjacent layers. Only through such an association can the vertical displacements of one layer (and initially the source) be transmitted horizontally through the medium to the next layer. Figure 3.1.c shows the associative bonds between particles of adjacent layers in a medium required to support transverse waves while figure 3.1.d shows a medium supporting a transverse wave (figure 3.1.d). As there is little or no attraction between layers in liquids and gases such media only

support longitudinal waves. Solids and some viscous liquids, however, support both transverse and longitudinal waves due to the high degree of association between their particle layers.

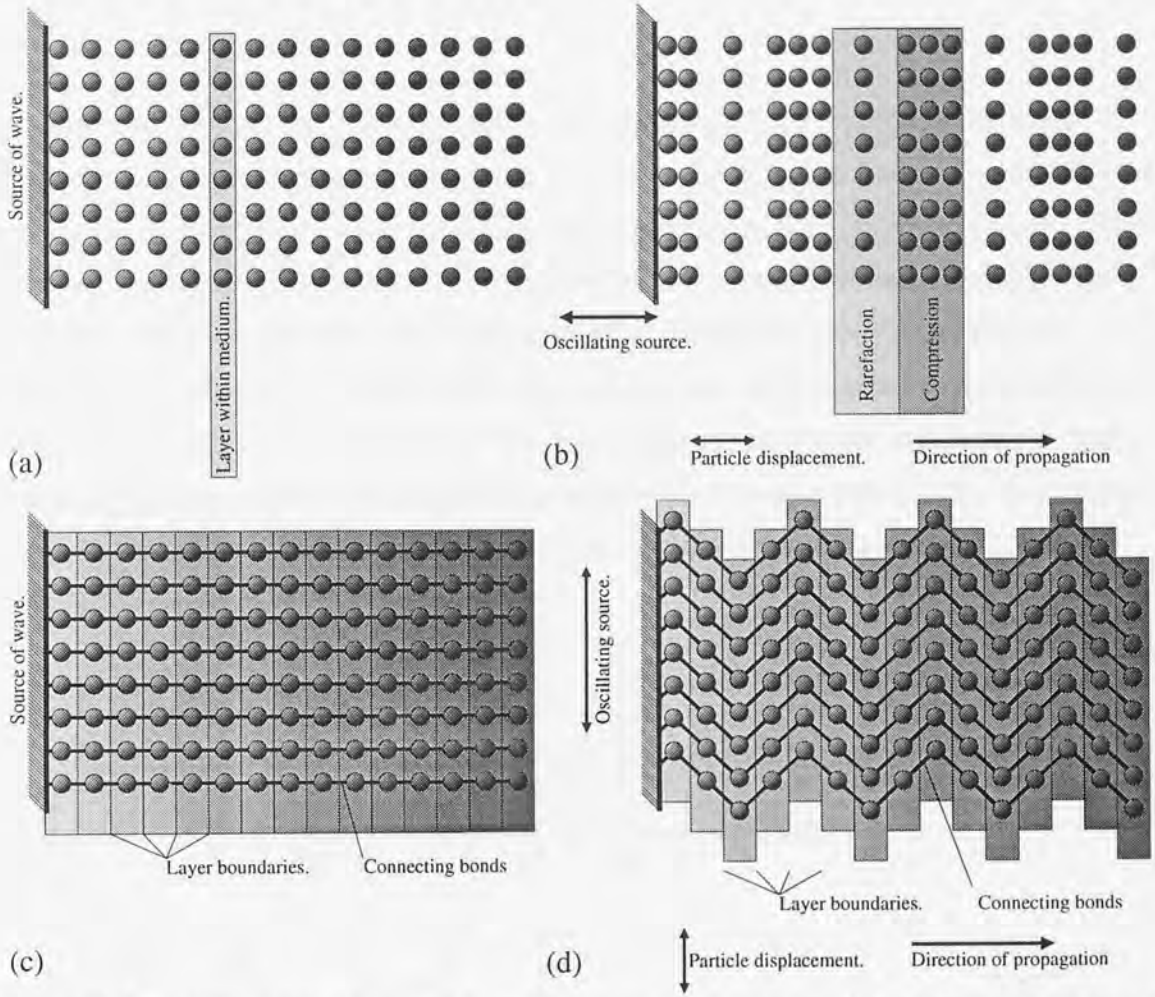

Figure 3.1 : (a) Particulate description of propagating medium, **(b)** layers propagating a longitudinal wave, **(c)** bonds required to support transverse waves and **(d)** layers propagating a transverse wave.

Sound occurs when a vibrational disturbance is allowed to propagate through some form of media as a pressure wave. This text is predominantly concerned with the transmission of sound (ultrasound) through non-viscous liquids necessitating the wave to be propagated as a longitudinal wave. The remainder of this section, therefore, concentrates on the characterization of longitudinal waves, although much of the theory is equally applicable to transverse waves.

A complex sound may always be shown to be the summation of a number of sinusoidally oscillating waves. These pure sinusoidal waves can be identified through the Fourier transform and may show the detected sound to contain any combination of individual frequencies, wide frequency bands or ranges of numerically related

frequencies. If the frequencies are numerically related then the lowest frequency is said to be the fundamental frequency with higher frequencies referred to as harmonics or partials. The second harmonic has a frequency which is twice that of the fundamental, the third harmonic has a frequency which is three times that of the fundamental, and so on.

For a pure sound the displacements of the particles which propagate the wave follow the y-component of a rotating vector of magnitude y_0 and frequency of rotation f which define the characteristic amplitude and frequency of the wave respectively (That is to say that the displacement of the particles follows simple harmonic motion). Two particles within in a medium may simultaneously experience two waves of equal frequency. If the two rotating vectors which define the displacement of the particles are not instantaneously co-linear then the two waves are said to be 'out of phase' and a phase angle, ϕ, can be defined equal to the instantaneous angle between the two vectors. Figure 3.2 shows two waves of frequency f and amplitude y_0 separated by a phase angle ϕ.

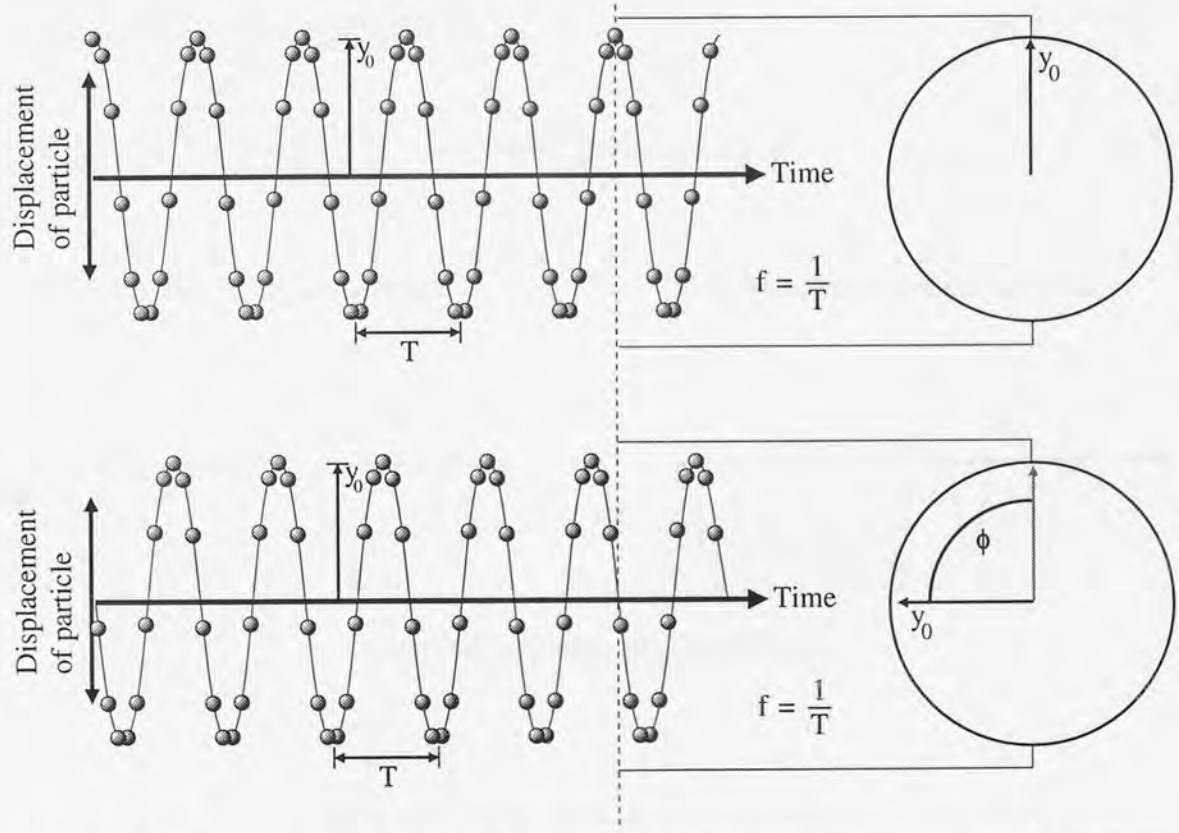

Figure 3.2 : Two wave of identical frequency,f , and amplitude, y_0, separated by phase angle of ϕ.

As stated above the displacement, y, induced in an individual particle by a wave away from its equilibrium position varies under simple harmonic motion which can be expressed mathematically as;

$$y = y_0 \sin\left(\frac{2\pi t}{T} + \phi\right) = y_0 \sin(\omega t + \phi) \tag{3.1}$$

where y represents the displacement of the particle from its equilibrium position, t is time, T is the time period of the oscillation defined as 1/f, ω is the angular frequency defined as $\omega = 2\pi f$ and y_0 is the maximum displacement of the particle from rest.

Similar expressions exist which define the variation of pressure with time, equation(3.2), and particle velocity with time, equation(3.3) in terms of the pressure amplitude, p_0, and the velocity amplitude, u_0, respectively. However, whereas the pressure (figure 3.3.b) and displacement (figure 3.3.a) waves are in phase with each other the velocity wave (figure 3.3.c) is out of phase with the displacement wave, leading it by a phase angle of $\pi/2$.

$$p = p_0 \sin\left(\frac{2\pi t}{T} + \phi\right) = p_0 \sin(\omega t + \phi) \tag{3.2}$$

$$u = u_0 \sin\left(\frac{2\pi t}{T} + \phi + \frac{\pi}{2}\right) = u_0 \sin\left(\omega t + \phi + \frac{\pi}{2}\right) = u_0 \sin(\omega t + \phi') \tag{3.3}$$

(a) Displacement of a particle with time.

(b) Variation of pressure with time.

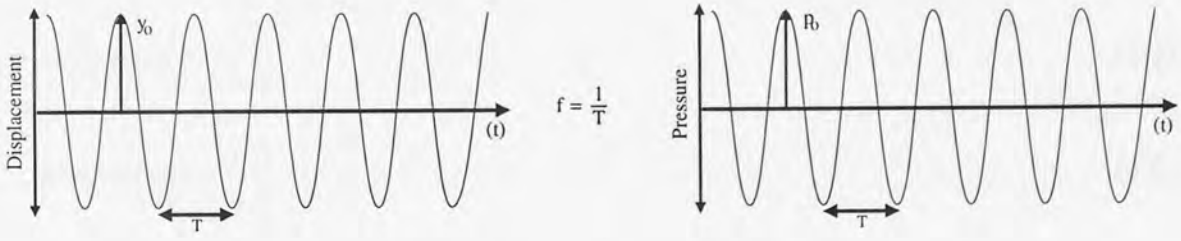

(c) Variation of particle velocity with time.

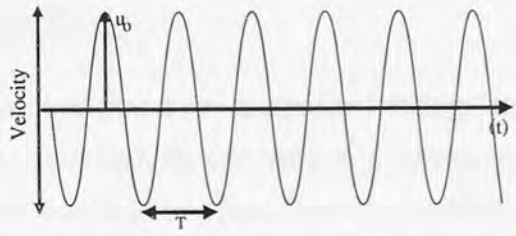

Figure 3.3 : The variation of an individual particles **(a)** displacement, **(b)** pressure and **(c)** velocity with time.

The source transmits vibrational energy to the particles within the first layer of the medium, these particles then, in turn, become the displacers for the particles in the next layer. Thus, in this manner, displacements are propagated through the medium. As it takes a small but finite time for the displacements to pass from one layer to the next, the phase of the vibration for each layer of particles differs from that of its neighbours by a small but finite amount. However, the velocity at which the wave propagates is constant for a specific homogeneous medium, depending upon the elastic modulus and density of the material. If one now considers a layer in the propagating medium situated at a distance x from a vibrating source, the time taken for the sound to reach this layer is equal to x/c, where c is the velocity of sound in the medium. Thus, it is possible to relate the phase of the vibrations in each layer at any time t to the phase of the source at a time (t - x/c). The displacement of the particles in a layer can, therefore, be found by substituting this quantity for t into equation(3.1) giving;

$$y = y_0 \sin\left(\omega\left(t - \frac{x}{c}\right) + \phi\right) \tag{3.4}$$

where the phase angle, ϕ, now relates the phase of a specific source to any other sources that may be causing displacements within the medium.

Thus, the principal characteristics of acoustic waves at a point in the medium are defined by particle displacement, y, particle velocity, u, and acoustic pressure (or stress), p, which, relative to the phase of the source, are given by equations(3.5), (3.6) and (3.7) respectively.

$$y = y_0 \sin\left(\omega\left(t - \frac{x}{c}\right)\right) \tag{3.5}$$

$$u = u_0 \sin\left(\omega\left(t - \frac{x}{c}\right)\right) \tag{3.6}$$

$$p = p_0 \sin\left(\omega\left(t - \frac{x}{c}\right)\right) \tag{3.7}$$

1.3 Attenuation of Plane Waves

So far it has been assumed that there is a perfect energy transfer from one layer of the propagating material to another, the intensity of a waves, whose wave front remains linear, remaining constant with distance from the sound source. In practice this perfect transfer of energy does not occur, resulting in the attenuation of the sound wave as it progresses through the medium. Assuming that there are no major defects in the

medium then the attenuation of the wave may be caused by diffraction, scattering, or absorption. Considering the passage of a wave through a homogeneous medium then diffractional and scattering effects can be neglected leaving only the absorption of energy by the medium to be accounted for. Given that the maximum amplitude of the wave at the source is A_0 then the maximum amplitude A, at a distance x from the source is given by an exponential relationship;

$$A = A_0 e^{(-2\alpha x)} \tag{3.8}$$

where 'α' is the attenuation or absorption coefficient which may be expressed in nepers per unit distance (e.g. Np mm^{-1}). The neper (also known as the napier) is a physical unit used for expressing the ratio of two analogous quantities; the number of nepers being the natural logarithm of this ratio. It is often more convenient to consider attenuation with wavelength, i.e. $\alpha\lambda$. This is the same as the attenuation per cycle, defined as the logarithmic decrement δ, for free vibrations, thus:

$$\alpha\lambda = \delta = \frac{\pi}{Q} \tag{3.9}$$

where Q is the quality factor as defined in the next section.

1.4 Specific Acoustic Impedance

An analogy can be drawn between the variations of sound wave characteristics and certain quantities used in electrical alternating current theory. Thus, regarding acoustic pressure as electrical voltage, particle velocity as electrical current, and particle displacement as electrical charge the acoustical equivalent of Ohm's law may be defined as;

$$Z_a = \frac{\text{p (accoustic pressure)}}{\text{u(particle velocity)}} \tag{3.10}$$

where Z_a, known as the specific acoustic impedance, is equivalent to electrical impedance.

As found in electrical impedance, Z_a is a complex quantity. However, for progressive plane waves the imaginary component disappears leaving a real quantity analogous to electrical resistance. This real quantity is referred to as the characteristic impedance (R_a) of the material and can be shown to be the product of the density, ρ, and speed, c, of sound in the medium:

$$R_a = \rho c \tag{3.11}$$

The value of R_a for a given material is only dependent on its physical properties and not on the properties of the wave.

1.5 Reflection and Transmission at a Boundary and the Quality of Resonance.

When a plane wave is normally incident on a boundary within the medium the wave is split with part of the wave continuing beyond the boundary and part of the wave being reflected. Figure 3.4

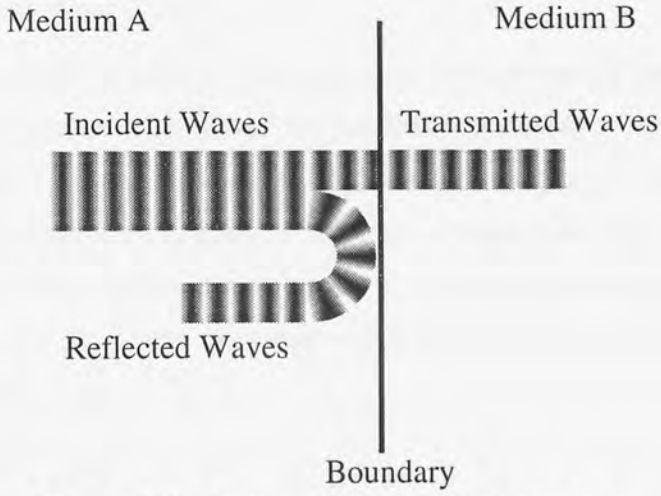

Figure 3.4 : Action of a wave at a boundary.

The relative amounts of reflected and transmitted intensities are expressed by the reflection and transmission coefficients;

$$\text{Reflection Coefficient} = \frac{\text{Intensity of Reflected Waves}}{\text{Intensity of Incident Waves}} \tag{3.12}$$

$$\text{Transmission Coefficient} = \frac{\text{Intensity of Transmitted Waves}}{\text{Intensity of Incident Waves}} \tag{3.13}$$

all measurements are taken at the boundary and expressed as either percentages or as a change in the number of decibels.

It can be shown that both coefficients can be expressed in terms of the characteristic impedances R_1 and R_2 of the media either side of the boundary giving;

$$\text{Reflection Coefficient} = \frac{(R_1 - R_2)^2}{(R_1 + R_2)^2} \tag{3.14}$$

$$\text{Transmission Coefficient} = \frac{4R_1R_2}{(R_1 + R_2)^2} \tag{3.15}$$

The best transmission of energy across a boundary occurs when the acoustic impedance of the media either side is similar. When this occurs the materials are said to be well matched or coupled.

When reflection coefficients are high and the absorption coefficient low 'resonance' occurs; the energy of the wave builds within the medium resulting in large displacement amplitudes. The degree to which resonance occurs by an ultrasonic source is indicated by a dimensionless number, called the Q (or Quality) factor, defined as;

$$Q = \frac{\text{Energy Supplied per Cycle}}{\text{Energy Dissipated per Cycle}} \tag{3.16}$$

Any object that can be used to transform one form of energy into sound waves is called a transducer (section 1.6). These too can be attributed Q values describing their resonant behaviour. Transducers with high Q values have specific frequencies at which resonance occurs, the velocity amplitude of the transducer reducing quickly as the frequency is moved from the resonant frequency. Transducers with a low Q value have a much flatter velocity amplitude response with the resonant frequency being less well defined. Figure 3.5.

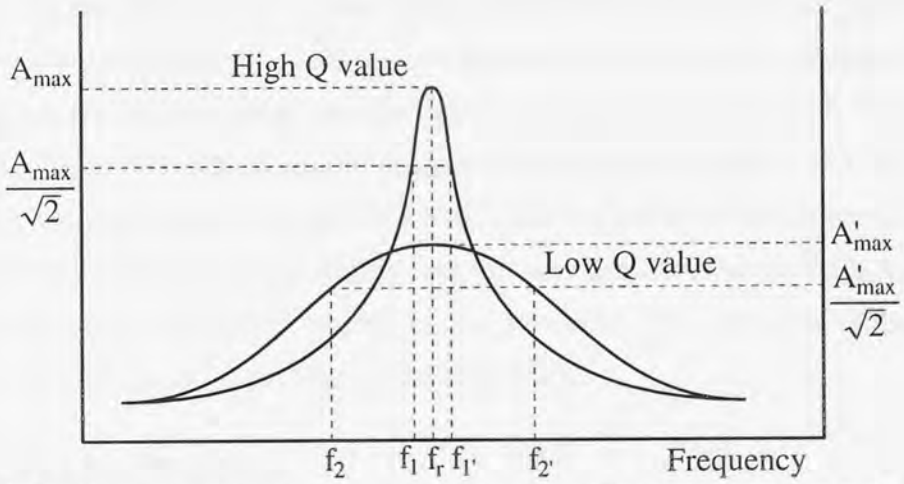

Figure 3.5 : Frequency response curves of two transducers one with a high and one with a low Q value both with the same resonant frequency.

Given the frequency response curve of a transducer an approximate value of Q can be obtained by reading off, from the curve, the values of the frequencies f_x and $f_{x'}$, on either side of the resonance frequency, f_r, where the maximum amplitude is reduced by $\sqrt{2}$. The Q values are given by;

$$Q \approx \frac{f_r}{f_{x'} - f_x} \tag{3.17}$$

This approximation is only valid where Q is greater than 3. The frequency difference $f_{x'} - f_x$ is known as the frequency bandwidth.

1.6 Progressive and Stationary Waves

A purely progressive wave is one in which the maximum displacement of all the particles which propagate the wave is the same. In a purely stationary wave the maximum displacement of the particles oscillates with distance from the source, varying from a maximum value to zero.

Stationary (or standing) waves result from the interference between the incident and reflected wave when a progressive wave is reflected at a plane boundary. If, after a single reflection, the maximum amplitudes of acoustic pressure or particle velocity at various distances from the reflecting surface are measured, an amplitude variation is obtained. The ratio of the maximum value to the minimum value of the amplitude variation is called the stationary (or standing) wave ratio (s.w.r).

1.7 The Generation Of Ultrasound.

The history of the generation of ultrasound dates back over 100 years to the work of Galton who was interested in establishing the threshold frequencies of hearing for both animals and humans. He produced a whistle with an adjustable resonance cavity which was capable of generating sound of known frequencies. With such an instrument he was able to determine the limit of human hearing as approximately 16 kHz. The whistle he produced was an example of a transducer - a device which converts energy from one form to that of another: in this case this was the conversion of gas motion into sound. A transducer can convert energy in one direction or be reversible whereupon the conversion in both directions is with equal efficiency.

1.7.1 Piezoelectric Transducers

Piezoelectric transducers are produced from materials displaying the piezoelectric effect, a phenomena discovered by Pierre and Jacques Curie in 1880 [91]. The effect occurs naturally in certain single crystals possessing polar axes such as quartz, tourmaline, lithium sulphate, cadmium sulphide and zinc oxide.

Materials of this nature can be machined into a disc or slab, and the plane faces coated with a thin metallic film to enable electrical contact. If a mechanical stress is applied to the coated surfaces, the crystal structure of the piezoelectric deforms and a

measurable voltage is generated across the electrical contacts. This is the direct piezoelectric effect. Conversely a mechanical stress is induced in the crystal when a voltage is applied across the contact plates. The application of an alternating voltage to the electrodes causes the induction of successive compressions and rarefactions within the crystal structure, causing the transducers surface to oscillate at the same frequency as the applied voltage. The amplitude of the oscillation is generally of the order of 10^{-6} times the transducers thickness but this may rise to the order of 10^{-4} times the thickness if the applied voltage has the same frequency as one of the transducers resonant frequencies. In practice piezoelectric crystals are operated at a resonant frequency for either 'thickness' or 'length' vibrations, depending on whether resonance occurs for the direction perpendicular to or parallel with the radiating faces. The natural resonant (fundamental) frequency for mechanical vibrations varies inversely with the dimension along which the oscillations occur.

1.7.2 Electromagnetic Transducers

Electromagnetic transducers are common in the generation of audible frequencies of sound with the vast majority of loudspeakers and microphones being based on such technology. Their application to ultrasonic frequencies is somewhat limited due to the rapid increase of inertial effects with frequency above the audible range. This has been somewhat alleviated with the application of thin film deposition techniques, lightweight electromagnetic transducers having been developed for use in a variety of low intensity applications.

1.7.3 Electrostatic Transducers

Electrostatic transducers may be considered to be a capacitor in which one of the plates is free to move perpendicularly to the other plate. A high resistance is placed in series with the plates and a direct potential difference of several hundred volts maintains steady charges on the plates. When this voltage is combined with a smaller oscillating electric voltage the electrostatic force between the plates varies causing the free plate to oscillate. Such devices are capable of acting as both a receiver and a transmitter at frequencies up to 300 kHz.

1.8 The Mechanical Amplification of Ultrasound

Where the sound generated by a transducer is caused by the oscillation of a solid surface, a solid horn can be used to amplify the displacement or particle velocity,

channelling it into the required environment while usually providing a more suitable impedance match between the transducer and the load to which it is to be coupled. Ultrasonic intensity is generally defined in terms of the power density at the radiating face of the ultrasonic transducer. The power density is defined as the electrical power delivered into the transducer divided by the surface area of the transducer: where a horn assembly is employed the surface area of the irradiation point is used. As there is a linear relationship between the power applied to a piezoelectric transducer and the amplitude of the induced oscillation the power delivered at the irradiating face is sometimes quoted as the peak-to-peak displacement amplitude, usually given in μm.

There are five designs of ultrasonic horn typically used; the stepped, the conical (or linear taper), the exponential, the catenoidal and the Fourier horn (Figure 3.6). For the most efficient operation of the horn it must be designed to resonate at the same frequency as the transducer which is driving it.

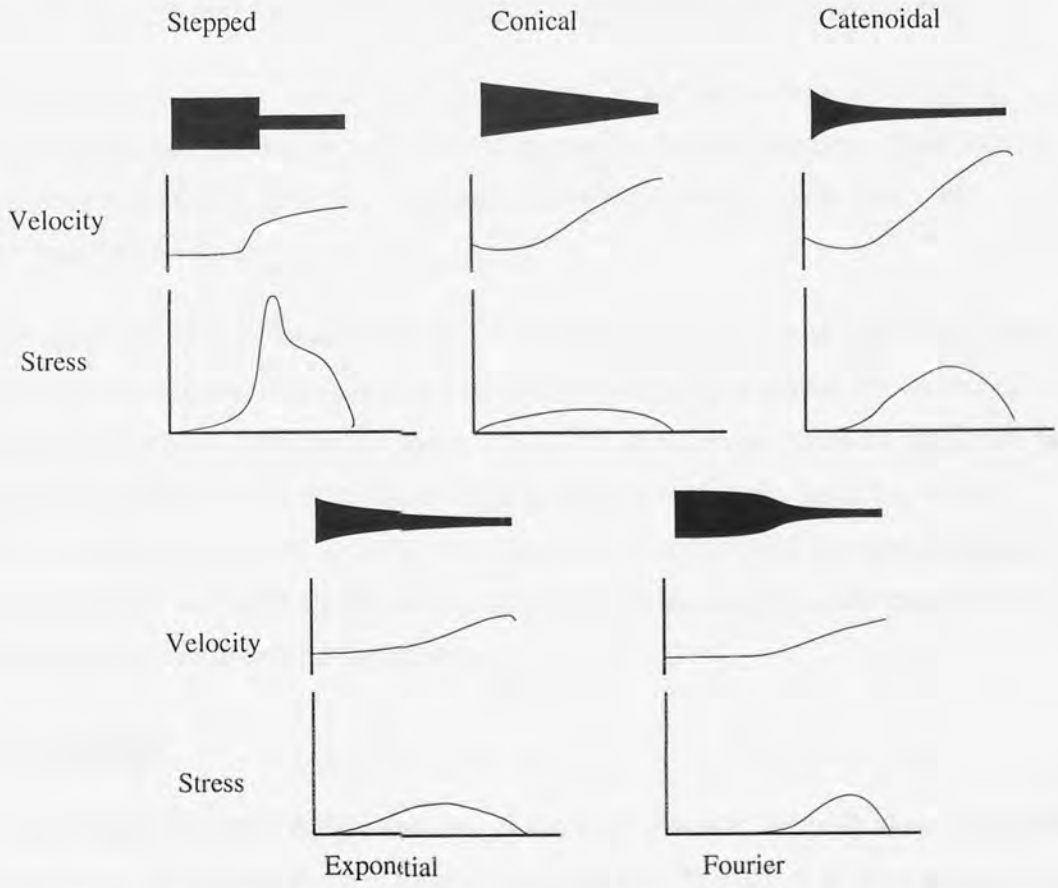

Figure 3.6 : Velocity and stress profiles of different ultrasonic horns.

As shear waves are not transferred from the horn to the liquid any energy used to excite shear waves in the horn is not accessible to the liquid. In order to avoid this energy loss the excitation of shear (transverse) modes within the horn can be suppressed

by restricting the maximum diameter of a horn to a value less than a quarter of the wavelength of the sound it propagates. As with all boundaries, that between the horn and the transducer will allow the most efficient transfer of energy when the acoustic impedances of the transducer and horn are matched. The transfer efficiency is further increased by grinding flat the two surface of the boundary to within 2.5 μm and by using a thin film of oil or grease to bridge any air pockets inherent in the boundary.

The amplification of ultrasound by the use of horns has several implications, the most pertinent of which being the concentration of energy at the horns tip. Not only can this cause the sonolysis of the solvent, generating a high concentration of chemically reactive species at the tip, but also may cause fatigue of the horns tip resulting in the surface becoming pitted and reducing transfer efficiency to the liquid.

1.9 The Effects Of Ultrasound On Liquids And Solids.

1.9.1 The Passage and Attenuation of Ultrasound Through Liquids and Solids.

As mentioned earlier (section 1.3) the passage of ultrasonic waves through a medium is accompanied by the exponential attenuation of the intensity of the wave. This energy loss occurs through the inelastic transfer of energy to the particles constituting the medium.

In liquids the degree of attenuation is dominated by its viscosity and temperature, the absorption of sound increasing with increasing viscosity and with the extent of thermal energy transfer within the liquid. In solids, density and physical form also play a role and generally losses occur at natural boundaries within the solid i.e. if it is polycrystalline or non-homogeneous. The intensity of ultrasound can also be reduced by the absorption of sound by the lattice, the sound stimulating specific transitions in electrons, nuclei or molecules themselves.

1.9.2 Streaming

Streaming, first observed by Faraday, is the term given to the bulk flow of fluid that results whenever a sound wave is present in a medium. The effect is most pronounced when using high intensity ultrasound in a contained environment.

1.9.3 Chemical Reactivity

The use of power ultrasound to accelerate and influence chemical reactions has expanded to the point that 'Sonochemistry' has become a complete subject in its own right [92, 93]. Many reactions utilise ultrasound for the production of radicals while in others its cavitational effect can be used to alter the surface characteristics of solid reactants.

1.9.4 Cavitation Occurring in the Bulk Sample

As an ultrasonic wave passes through a liquid a specific point within the liquid experiences the successive rarefactions and compressions. During the rarefaction the particles defining the liquid become more dispersed due to the creation of a region of low pressure. On the other hand, the compression cycle creates regions of high pressure, concentrating the particles. The intensity of the ultrasonic wave may be such that the forces generated during the rarefaction cycle, assisted by nucleation affects (section 1.8.6), are stronger than those holding the liquid together. At such intensities the liquid is effectively 'ripped' apart [94] creating a small void in the liquid which, on successive compressions and rarefactions, grows into a bubble. Eventually this bubble becomes unstable and the bubble implodes. The creation, growth, and implosive collapse of bubbles in this way is called acoustic cavitation.

The enhancement of chemical reactivity in sonochemistry is a feature of acoustic cavitation. However, currently, the theory describing the mechanism by which this occurs is contended. "Hot spot theory" attributes the enhancement to the generation of extreme temperatures and pressures caused by the implosion of the bubbles. "Electric field theory" attributes the enhancement to the generation of splinter bubbles with the proximity of the double layer at the constriction between the splinter and main bubble causing the dielectric breakdown of the liquid.

1.9.4.1 Hot Spot Theory

Simple theory predicts that more than 1000 atmospheres of negative acoustic pressure would be necessary to cavitate pure liquids. In practice, most liquids will cavitate at a negative pressure of a few atmospheres. A reduction in the required pressure in this manner is predicted by the Harvey model of microbubble stabilisation [95] which attributes the phenomenon to the existence of small solid particles in the sonicated liquid which have gas trapped in surface crevices that acts as a nucleation

centre for the formation of cavities.

Also found in a liquid is solvated gas. This gas is free to migrate into and out of the microbubble cavities: the rate of migration is limited by the surface area of the cavity, this restriction causing more gas to enter the microbubble during the rarefaction cycle than to leave during the compression cycle. Therefore, with each cycle of sound, the bubble expands slightly more than it shrinks and, over many cycles, its mean size will increase. Eventually the cavity reaches a size where the frequency at which it would naturally oscillate is equal to the frequency of the incident sound wave causing a resonant coupling between the sound wave and the microbubble. Under such conditions the efficiency of energy transfer from the wave to the bubble is greatly increased and large oscillation in the bubble are induced. At this point the bubble grows rapidly over a single cycle of sound with high-intensity ultrasound expanding the bubble so rapidly that the bubble does not shrink during the compressional cycle. Comparatively quickly a bubble size is reached which is no longer capable of the resonant adsorption of energy from the ultrasonic wave leaving the bubble relatively large and incapable of sustaining itself. Consequently the liquid rushes in and the cavity implodes. On collapse, the peak gas phase temperature and the surrounding liquid shell temperatures have been deduced by comparative rate thermometry to be ca. 5200 K and 1900 K respectively [96]. It is also thought that the instantaneous pressures produced on collapse could be of the order of 1000 atmospheres [97].

The critical size at which the resonant growth of the bubble occurs depends on the frequency of ultrasound [98];

$$R_r = \frac{1}{2\pi\nu}\sqrt{\frac{3\kappa P_0}{\rho}} \qquad (3.18)$$

where R_r is the critical cavity radius, ν is the ultrasound frequency, P_0 is the liquid ambient pressure, ρ is the liquid density and κ is the polytropic constant. The polytropic constant varies between the ratio of specific heats and unity, these being the limits for adiabatic and isothermal conditions, respectively.

1.9.4.2 Dielectric Breakdown

An alternative theory to the hot spot theory was developed by Margulis [99, 100]. This theory is based on the electric potential induced by an electrical (ionic) double layer about the cavitation bubbles and the electric field this generates as a splinter bubble is formed.

Initially an ionic double layer is set up at the bubble/liquid boundary due to the orientation of polar species and the migration of charged particles. The electrical potential φ, induced by this double layer decays exponentially away from the bubble. On the detachment of a fragment bubble these electric potentials are rapidly brought together effectively charging the liquid/gas interface. Margulis has calculated that the electric field generated by this action is in the order of 1.6×10^{11} Vm^{-1}, considerably greater than the critical electric field strength of 3×10^{6} Vm^{-1} required to produce di-electric breakdown in dry air at atmospheric pressure. The energy released by the ensuing electrical breakdown of the bubble is held to be responsible for many of the observations made in sonochemistry.

1.9.5 Cavitation Effects Occurring at a Solid Interface.

When cavitation occurs in a liquid near an extended solid boundary, the bubble does not collapse uniformly from all sides. As the liquid is more free to flow from the side of the bubble furthest from the solid, the non-uniform collapse of the bubble results in a jet of liquid, a microjet [101], crossing the cavity directed towards the solid surface at speeds in excess of $100ms^{-1}$.(Figure 3.7)

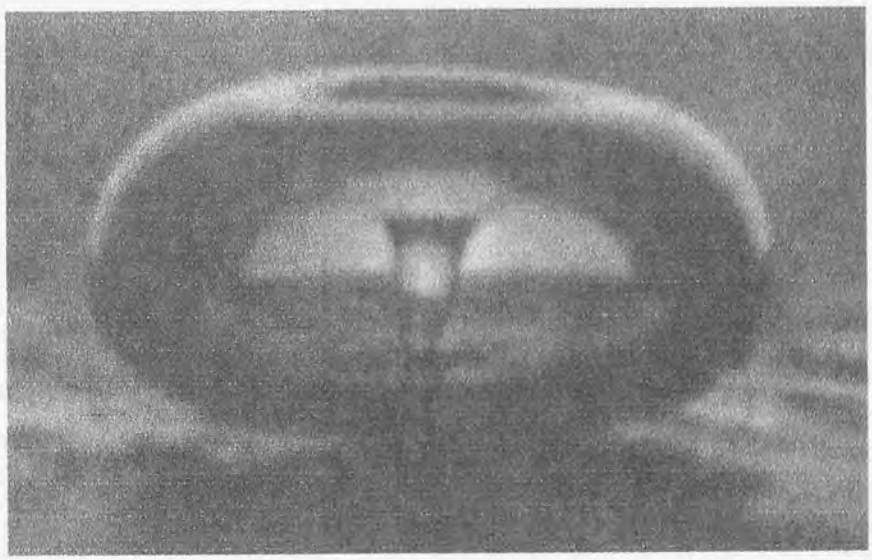

Figure 3.7 : A collapsing cavitation bubble showing a microjet of liquid directed at a solid surface.

The action of the microjet contributes to surface pitting, erosion and cleaning of the solid. Other contributions to these phenomena result from shock waves formed by the implosion of bubbles remote from the solid surface.

1.9.6 Factors Affecting the Induction of Cavitation.

The onset of cavitation is governed by a number of factors. Of these the most pertinent are ultrasonic intensity, physical properties of the liquid, temperature, presence of dissolved gases, the presence of particulate matter and ultrasonic frequency:

1.9.6.1 Ultrasonic power

There is a minimum ultrasonic power below which the forces induced during the rarefaction of the ultrasonic wave cannot induce cavitation. Above this cavitation threshold the extent of cavitation increases with ultrasonic power.

1.9.6.2 Physical properties of the liquid.

Neglecting nucleation, cavitation occurs when the ultrasonic force overcomes the intermolecular forces of the liquid medium. The cavitational threshold is, therefore, determined by the strength of these bonds; the greater the intermolecular forces in a liquid the greater its cavitational threshold.

1.9.6.3 Temperature.

Cavitation threshold drops as the temperature is increased towards the liquids boiling point, the intermolecular bonds being weakened by the increased thermal motion.

1.9.6.4 The Presence of Dissolved Gases.

The solubility of a gas in a liquid is related to the pressure exerted on the liquid. If a gas is dissolved in a liquid the reduction in pressure caused during the rarefaction of the ultrasonic wave may force the gas out of solution nucleating a cavity and effectively reducing the cavitational threshold. Naturally, the vapour pressure of the liquid impinges on this phenomenon.

1.9.6.5 The Presence of Particulate Matter.

The surface of a solid particle may trap pockets of air or gas when it is introduced to a liquid which, on subsequent sonication act as nucleation sites for microbubbles, reducing the cavitational threshold of the liquid.

1.9.6.6 Ultrasound frequency.

As the frequency of an ultrasonic wave is increased the time period in which the rarefaction acts on the liquid is reduced. In effect this increases the cavitational threshold as a higher ultrasonic intensity is required to induce a particular degree of cavitation. Conventionally, it is thought that at frequencies above a few megahertz it becomes impossible to induce cavitation and sonochemical reactions are not observable [102, 103]. However, experiments conducted in the authors laboratory suggest that cavitation is possible at frequencies up to 10 MHz [104].

Chapter 2

Experimental Equipment.

2.1 JEOL FX-90Q NMR Spectrometer.

In addition to the production of conventional NMR spectra, aspects of this work required the determination of the spin-lattice relaxation time of samples and the availability of a switchable, stable magnetic field. These facilities were afforded by a JEOL FX-90Q iron magnet FT-NMR spectrometer. When energised the electromagnet, which is central to the spectrometer, generates a stable 2.1 T magnetic field (corresponding to a resonant frequency for protons of 89.56 MHz). Any perturbations of the magnetic field are compensated for by a field frequency locking unit which can be locked onto a deuterium signal from the analyzed NMR sample or a lithium signal from a separate external reference held in close proximity to the detected sample. The detected spectra/FID may contain up to 32K data points over a maximum spectral window of 30030Hz. However, when used with the foreground/background unit the maximum size of the data array is limited to 8K.

The spectrometer allows exponential line broadening of the FID, FWHM measurements, peak intensity and integration, and basic pulse programming together with the facilities to output spectra to a chart plotter or to record the data using an integral tape cassette recorder.

A variable temperature unit was also available allowing the NMR probe to access temperatures in the range -100°C to +180°C. However, when this was not in operation the probe and electromagnet were held at a constant 28°C via the spectrometers water re-circulator and cooling system.

2.2 Brüker EMS 104 EPR Analyzer.

The detection of electron spin resonance (ESR) spectra was achieved using a Brüker EMS 104 EPR Analyzer, an electron paramagnetic resonance (EPR) spectrometer. This tabletop spectrometer is especially designed to be run as a dedicated EPR dosimetry system, monitoring the generation of radical species caused by ionizing radiation. The theory of ESR spectroscopy is analogous to that of NMR spectroscopy; the magnetic moments of unpaired electrons in ESR spectroscopy being manipulated in a similar way to the nuclear magnetic moments in NMR spectroscopy.

At the heart of the spectrometer is the microwave bridge. The EMS 104 uses a gunn oscillator at 9.8 GHz and a reference arm to provide suitable bias for the detector. The output can be varied from 50μW to 50mW in 1dB steps. The probe head has a

sample access of 5.2mm in diameter.

The magnetic field is provided by a permanent magnet with a 15mm air gap giving a magnetic field of 0.348T in the sample cavity. Sweep coils allow a maximum sweep range of 20 mT to be examined in time periods ranging from 0.67 seconds to 90 minutes.

2.3 The Kerry Ultrasonics & Chemsonics 20kHz Ultrasonic Apparatus .

The source of the ultrasound used in these experiments was either the commercially available Kerry Ultrasonics Apparatus or the Chemsonics apparatus provided by Professor Jacques Reisse (Universite Libre de Brusselles).

The Kerry apparatus consists of a 20kHz generator and power meter connected to a 20kHz quartz piezoelectric transducer. The Chemsonics unit consist of a 20kHz source with tracking unit, capable of compensating for small changes in the resonant frequency of the piezoelectric transducer; a pulsing unit, which can switch the ultrasound on and off in time periods in the range 10ms to 990s; and a power amplifier.

The 20kHz transducer can be attached to either ultrasonic source and can be used with a range of ultrasonic horns. For the work presented here two such horns were used; a 'long' titanium horn, 77cm in length, exponentially machined from a coupling surface of 19mm in diameter to a probe tip of 5mm in diameter, and a 'short' stainless steel horn, 250mm in length, machined from a 19mm diameter coupling surface to a 2mm diameter probe tip.

2.4 The Pye Unicam G.C.D Chromatograph.

The ultrasonic reactions were monitored using a Pye Unicam G.C.D Chromatograph employing a 10% Carbowax (20 M) on UNISORB (AW DMCS) column fitted with a flame ionization detection system connected to a Hewlett Packard HP3396A data logging console. For all analyses the injection temperature was set to 200°C, the column temperature to 170°C and the detector to 250°C.

Chapter 3

Investigation into the Nature of Cavitation.

3.1 Introduction.

It is now believed that cavitation, the ensuing shock wave and micro-jet of liquid caused by the collapse of the cavity near a solid surface is a major contributor to the mechanism whereby narrowing is achieved in SINNMR [4]. The micro-jets and shock waves are thought to be the cause of the rapid random motion of the suspended particles. It is, therefore, important that the exact nature of the cavities produced during sonication be ascertained together with any other effects that their collapse may have.

One aspect of cavitation that is currently contested is the mechanism by which radicals are produced. Currently there are two theories ascribed to their generation *viz* the 'hot spot theory' (section 1.8.4.1) and the 'electric field theory' [99, 100] (section 1.8.4.2). Essential to the electric field theory is the establishment of an ionic double layer, the movement of charge and eventually the dielectric breakdown of the medium surrounding the cavity. Clearly such electrical phenomena should be affected by the presence of a magnetic field, ultimately affecting the stability of any cavities generated by sonication. This has obvious implications for the SINNMR experiment as it has the potential not only to affect cavitational observations when moving in and out of a magnetic field but also to alter the cavitational mechanism when moving from one magnetic field strength to another.

3.2 The Effects of Magnetic Fields on Ultrasonically Induced Free Radical Isomerization of Diethyl Maleate to Diethyl Fumarate.

In order to establish the importance of electrical effects in cavitational behaviour the yield from an ultrasonically initiated free radical reaction in and out of a strong magnetic field was investigated.

The reaction chosen was the previously investigated ultrasonically induced isomerization of diethyl maleate to diethyl fumarate [105, 106] (figure 3.8). The experiments were performed in the probe of the JEOL FX-90Q FT spectrometer using the Kerry Ultrasonic apparatus to generate the 20kHz ultrasound and the long horn to deliver the ultrasound to the sample which was contained in a 10mm PTFE NMR tube. The effects on the degree of isomerization induced by the ultrasound were monitored using the G.C.D. chromatographic column, firstly while the NMR magnet was energised and secondly while de-energized. Using the standard condition (section 2.4) the GLC of the solution showed diethyl maleate to have a retention time of 3.8 minutes and diethyl fumarate to have a retention time of 5.3 minutes. As the isomerization is

photosensitive all light was excluded from the reaction prior to its analysis on the GLC.

All experiments were performed on 5 cm^3 of a stock solution prepared by adding 1.7cm^3 of bromoform to 50cm^3 of a 0.21 mol dm^{-3} solution of diethyl maleate in carbon tetrachloride. Once the sample was placed into the NMR spectrometer the tip of the long horn was positioned 2mm below the surface of the solution and the sample irradiated with 3μm ultrasound at 20kHz for 50 minutes. The variable temperature unit of the spectrometer was not used and the cooling system of the magnet was relied on to maintain a sample temperature of 28°C during the experiment. The experiment was repeated three times with the magnetic field on and three times with the magnetic field off with the products from each experiment normally analysed by GLC five times. The initial stock solution was analysed by GLC three times.

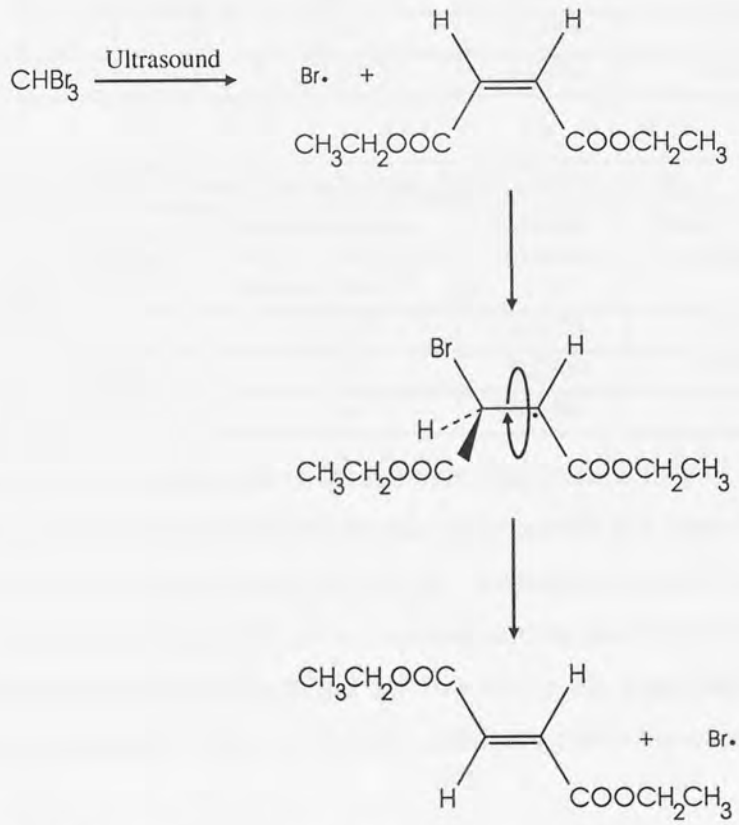

Figure 3.8 : The isomerization of diethyl maleate to diethyl fumarate.

3.3 Results and Discussion.

The results of these experiments are summarised in table 3.1.

It must be noted that the percentage conversion of the maleate form of the di-ester to the fumarate form of the di-ester achieved by sonication of the sample is comparable to the 25% conversion found elsewhere [105]. However, as the percentage conversion

obtained in and out of the magnetic field overlap the results fail to establish if an electrical phenomena lies at the heart of the cavitational process.

Table 3.1 : Summary of the GLC results for the sonically induced isomerization of diethyl maleate to diethyl fumarate.

Inititial Stock Solution				
Run	GLC's performed.	Mean percentage of the diester in the fumarate form.	Standard deviation.	Error to 90% confidence.
1	3	2.143	0.004911	±0.009

After 50 Minutes Sonication with the Magnetic Field Off.				
Run	GLC's performed.	Mean percentage of the diester in the fumarate form.	Standard deviation.	Error to 90% confidence.
1	5	26.9	0.1082	±0.1
2	5	26.4	0.1068	±0.1
3	5	27.51	0.0940	±0.09

After 50 Minutes Sonication with the Magnetic Field On.				
Run	GLC's performed.	Mean percentage of the diester in the fumarate form.	Standard deviation.	Error to 90% confidence.
1	5	27.2	0.2154	±0.2
2	5	17.32	0.0960	±0.09
3	2	29.4	0.0224	±1.4

What the results do demonstrate is the inherent irreproducibility of ultrasonic reactions [106]. The irreproducibility of the reactions occurs as a direct result of ultrasonically initiated reactions being, in general, exceedingly sensitive to the topography of their containing vessel. As the ultrasonic rig used in the experiment does not allow for the precise positioning of the horn tip within the sonicated sample the efficiency of the reactions in each run changes and thus adds to the overall experimental error.

Within the NMR research group, probes specifically designed for the introduction of ultrasound to an NMR sample are being developed. In such probes the source of the ultrasound and the NMR cell are directly bonded to each other and, as such, they would eliminate any positioning errors in the above experiment. It is, therefore, suggested that the above experiment be repeated using the completed ultrasound/NMR probe in an attempt to detect any change in conversion efficiency, which may have been previously masked by the experimental error introduced by the re-positioning of the ultrasound horn.

Chapter 4

Investigations into the Relationship Between Cavity Production and Line Narrowing in SINNMR.

4.1 Introduction.

The ability of SINNMR [4] to produce narrowed, liquid-like, spectra from solid suspensions is attributed to the collapse of cavities in the support media. Currently the rate at which cavities collapse can only be related to the difference between power delivered to the suspension and the cavitation threshold of the support liquid (the cavitation threshold for the support liquids used has been estimated to be ca. 16 Wcm^{-2} [107]). As neither of these quantities can be easily determined to any great degree of accuracy the rate of cavity implosion determined using this method is only approximate. Evidently what is needed is a method which can be used to accurately determine the rate of cavity production during the SINNMR experiment.

As the collapse of cavities also generates radical species, measurement of the steady state concentration of these radical species should be directly related to the rate of cavity collapse. The unpaired electrons in such radicals can cause an enhancement of NMR signals originating from the nucleus to which they are bound: this phenomenon is referred to as a 'chemically induced dynamic nuclear polarization' or CIDNP [108-111]. It was proposed, therefore, that measured CIDNP of the support media should directly relate to the radical concentration in the sample and this, in turn, should be related to the rate of cavitational collapse. An alternative approach is to monitor directly the acoustically produced radical concentration by EPR.

4.2 The Use of an EPR Spectrometer to Indirectly Detect the In-Situ Generation of Radicals.

4.2.1Experimental

Initially it was necessary to determine if it was possible to detect directly any radicals produced as a result of the cavitational process. To achieve this a Brüker EMS 104 EPR Analyzer was borrowed from Brüker Spectrospin Ltd, Coventry. Attempts were then made to detect directly any radicals formed by the action of ultrasound on chloroform and bromoform, the support media used in SINNMR. The Chemsonics apparatus was used to provide the ultrasound. Unfortunately, the limited tuning capabilities of the spectrometer prevented the adaptation of its cavity to a sufficient degree to allow the acquisition of EPR spectra. Eventually carbon tetrachloride was found to be a suitable sample for use with the EPR spectrometer and the following experiments were run using this as a solvent.

Attempts were made to detect an EPR spectrum from a carbon tetrachloride sample while it was simultaneously irradiated with ultrasound. For these experiments the EPR spectrometer was set to its maximum sweep width with a sweep time of 15 seconds. The EPR tube was filled with carbon tetrachloride to a depth of 6cm and then introduced into the EPR spectrometer where the tip of the small stainless steel ultrasonic horn was positioned 2mm below the original level of the liquid. An EPR spectrum of carbon tetrachloride was first obtained with the ultrasound turned off and then after 5 minutes irradiation with the 20kHz ultrasound. The sample was irradiated with ultrasonic powers set in the range 1μm to 10μm, but none of the spectra acquired showed an EPR signal.

Subsequent studies concentrated on the effects of ultrasound on 2,2,6,6-tetramethyl-1-piperidinyloxy,TEMPO, (RMM = 156.25gmol^{-1}) a stable organic free radical (figure 3.9), which gives a strong EPR triplet at low concentrations.

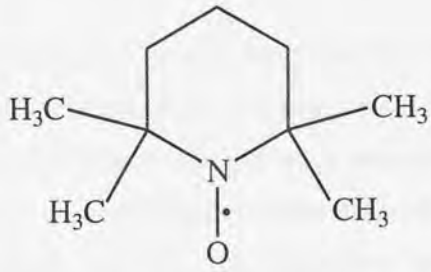

Figure 3.9 : The stable organic free radical TEMPO.

If free radicals can be formed in solution during irradiation with ultrasound it is expected that these would react with the stable free radical,TEMPO. The products of these reactions are not expected to yield an EPR spectrum and, so, the production of free radicals by the ultrasound will correspond to a reduction in the intensity of the TEMPO EPR spectrum. To investigate this reaction a solution of TEMPO and stearic acid (giving a supply of readily extractible protons, RMM = 284.48 gmol^{-1}) in carbon tetrachloride was made, the concentrations being 12mmol and 7mmol respectively: the EPR spectrum of this stock solution can be found in figure 3.10.

The EPR tube was filled with the solution to a depth of 6cm and the tip of the ultrasonic horn positioned 2mm below the original level of the liquid. Again the EPR spectrometer was set to its maximum sweep width, but with the sweep time reduced to 5 seconds. The small ultrasonic horn was used to deliver 20kHz ultrasound directly to the TEMPO/stearic acid sample. Prior to ultrasonic irradiation the EPR spectrum of the solution was was obtained.

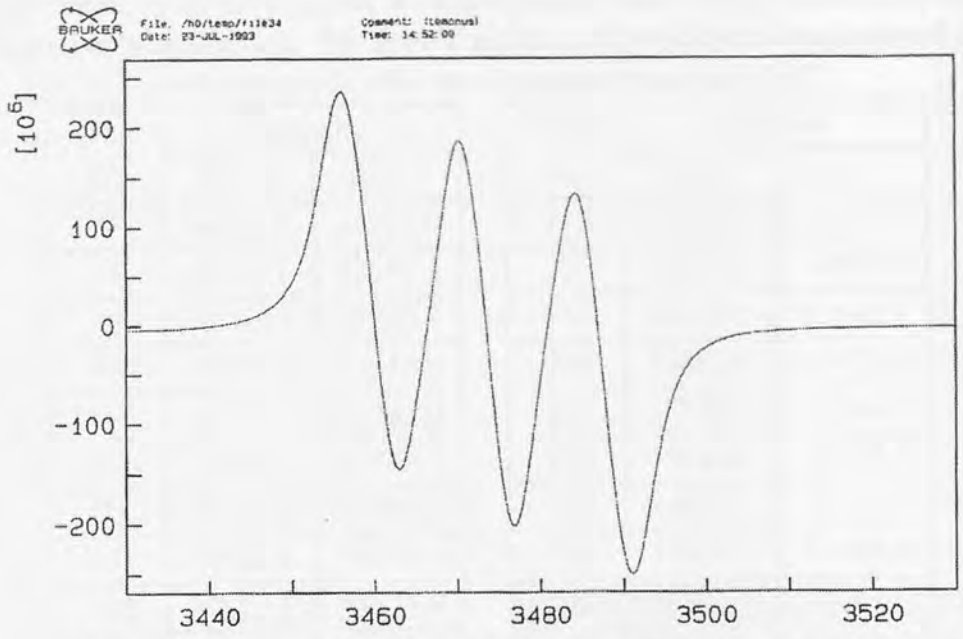

Figure 3.10 : EPR Spectrum of TEMPO/Stearic Acid stock solution in Carbon Tetrachloride.

The ultrasound was then turned on and the power set to 2μm. After an initial delay of 12.5 seconds 27 EPR spectra of the sample were obtained, each acquisition starting 15 seconds after the initiation of the previous acquisition. The ultrasound was active for the first 21 spectral acquisitions and inactive for the remaining six. This procedure was repeated a second time on a new sample of the TEMPO/stearic acid solution taken from the same stock solution as in the first run. The integral of each EPR spectra for each run was taken using the inbuilt facilities of the EPR spectrometer.

4.2.2 Results and Discussion.

The integral of the EPR spectrum obtained with the probe in place but with the ultrasound off was used as the intensity of the signal at zero time. Table 3.2 shows the integral values for the runs while figure 3.11 shows these results as a scatter plot.

As the attempts to directly observe the free electrons present in radicals generated by the sonication of carbon tetrachloride failed the lifetime of such radicals must be short. This is to be expected as the sample was not de-gassed and so contained solvated molecular oxygen, a di-radical, which can react rapidly with the simple radicals generated by the ultrasound to give an EPR neutral species.

Table 3.2 : Intensity of EPR signals obtained from a TEMPO/stearic acid solution while irradiated with ultrasound. The greyed region indicates intensities obtained from spectra acquired after the ultrasound was turned off.

Time	Intensity	
(s)	Run 1	Run 2
0	44283.0	44283.0
15	39797.1	37267.3
30	39543.7	37233.7
45	38976.2	36816.3
60	38390.7	36265.0
75	37848.1	35749.7
90	37439.8	35282.9
105	37125.9	34719.6
120	36823.1	34371.9
135	36457.8	34257.0
150	36311.5	33801.7
165	36060.7	33295.7
180	35810.5	32789.2
195	35836.8	32433.3

Time	Intensity	
(s)	Run 1	Run2
210	35880.9	32182.6
225	35917.6	31993.2
240	35904.0	31592.8
255	35882.0	31476.7
270	35839.8	31184.8
285	35843.0	31278.2
300	35851.3	31210.7
315	35867.3	31106.9
330	36564.1	31247.2
345	37334.1	31658.9
360	38209.4	32039.9
375	39421.3	33490.3
390	40494.9	34478.3
405	41479.7	35623.7

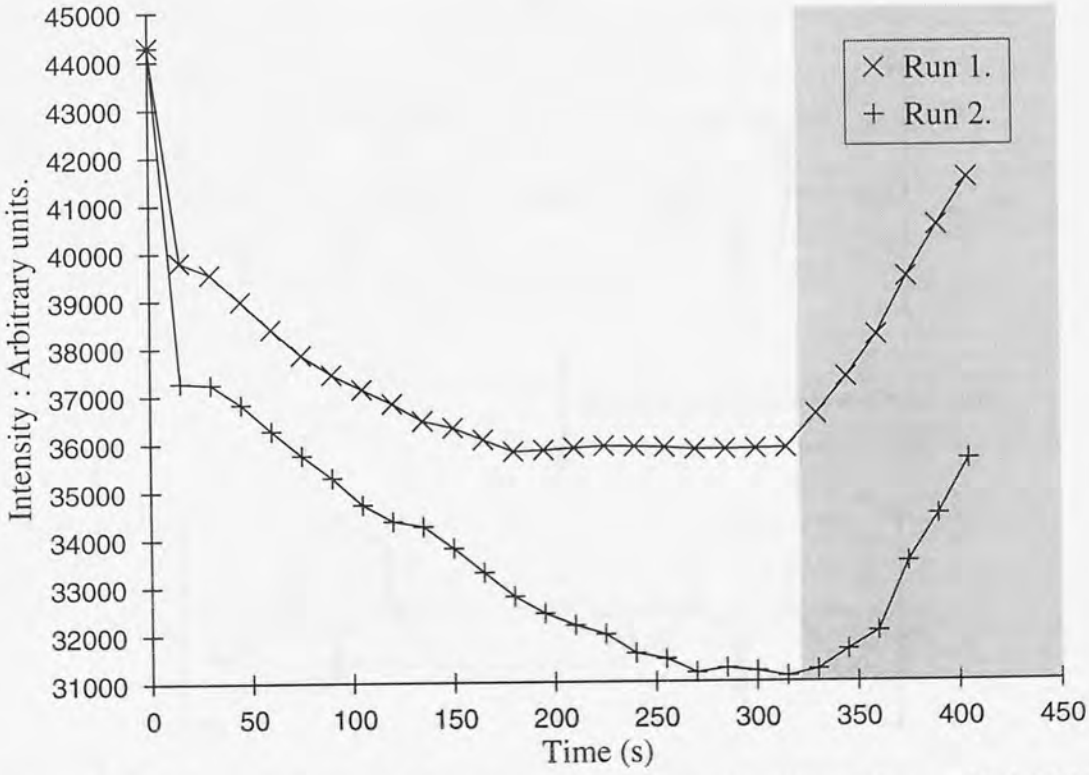

Figure 3.11 : Scatter plot of the intensity of EPR signals obtained from a TEMPO/ stearic acid solution in carbon tetrachloride while irradiated with ultrasound. Greyed region indicates intensities obtained from spectra acquired after the ultrasound was turned off.

Sonication of the TEMPO/stearic acid solution initially caused the expected decrease in signal intensity. However, in run 1 the decrease in signal intensity halts after 180 seconds and remains constant until the ultrasound is switched off. A similar trend is observed in run 2, a plateau in the signal intensity occurring after 285 second. When the ultrasound is turned off both runs show the signal intensities recovering towards their initial, pre-sonicated values. Such observations can only be accounted for if the reaction between TEMPO and the generated radical is reversible, or the reaction product is unstable, degrading to a molecular species which gives an identical ESR spectrum as TEMPO. A possible mechanism for this observation is shown figure 3.12.

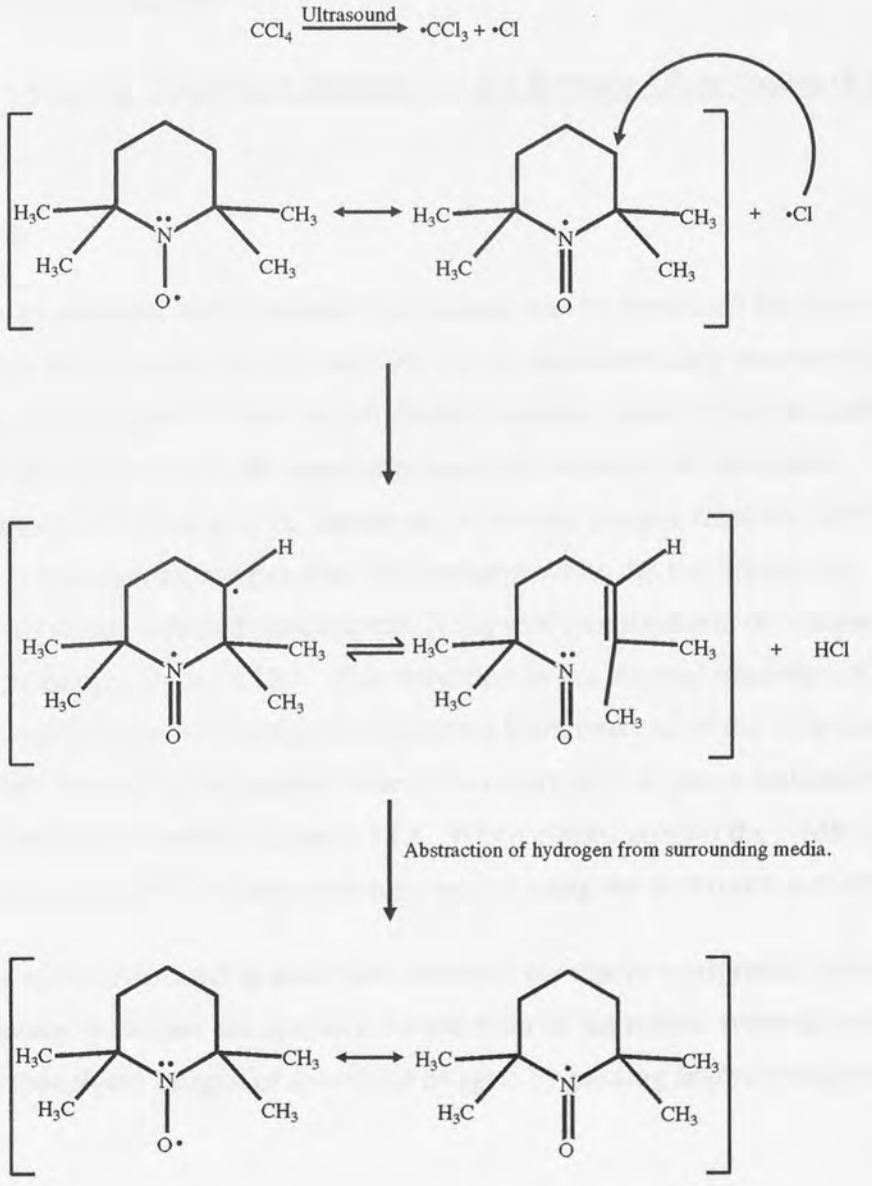

Figure 3.12 : Possible reaction mechanism for TEMPO.

One point of importance is the fact that, although both runs are performed 'identically' the plots of signal intensity with time are not coincident. This is attributed to two factors;

Firstly, that there are small positioning errors of the ultrasonic horn when moving from one experiment to another.

Secondly, every time an EPR sample is introduced to the spectrometer it was necessary to detach the ultrasonic horn from the ultrasonic transducer unit. It is, therefore, expected that the transmission efficiency of the horn varied from one experiment to another.

4.3 Attempts to Generate Conditions Suitable for the Routine Observation of a CIDNP.

4.3.1 Introduction.

The previous experiment demonstrated that radicals can be produced by ultrasonic irradiation, and that the presence of such radicals can be simultaneously monitored by magnetic resonance techniques. It also highlighted a possible problem for the routine observation of a CIDNP during NMR experiments *viz* the presence of molecular oxygen in the sample. The first goal is, therefore, to remove oxygen from the SINNMR liquids and then to maintain an oxygen free environment while the the liquids are sonicated. To achieve this a closed reaction cell [112] was modified and developed for use in NMR spectroscopy, figure 3.13.b. The reduction in the internal diameter of PVC tubing was achieved by removing triangular segments from one end of the tube and bringing the freshly formed faces together where they were held in place and sealed by a silicone rubber bathroom sealant, figure 3.13.a. When placed around the NMR tube any gaps remaining in the PVC tubing were also sealed using the bathroom sealant.

Experiments were performed to determine whether the above equipment, initially without the ultrasonic horn (nor the aperture for the horn in the rubber septum) could be used to purge a chloroform sample of dissolved oxygen by passing argon through the sample.

As molecular oxygen is paramagnetic it reduces the T_1 of any samples in which it is dissolved. Thus, measurement of the T_1 of the chloroform sample could both monitor the progress of the purging process and also be used to determine how well the apparatus could maintain an inert atmosphere.

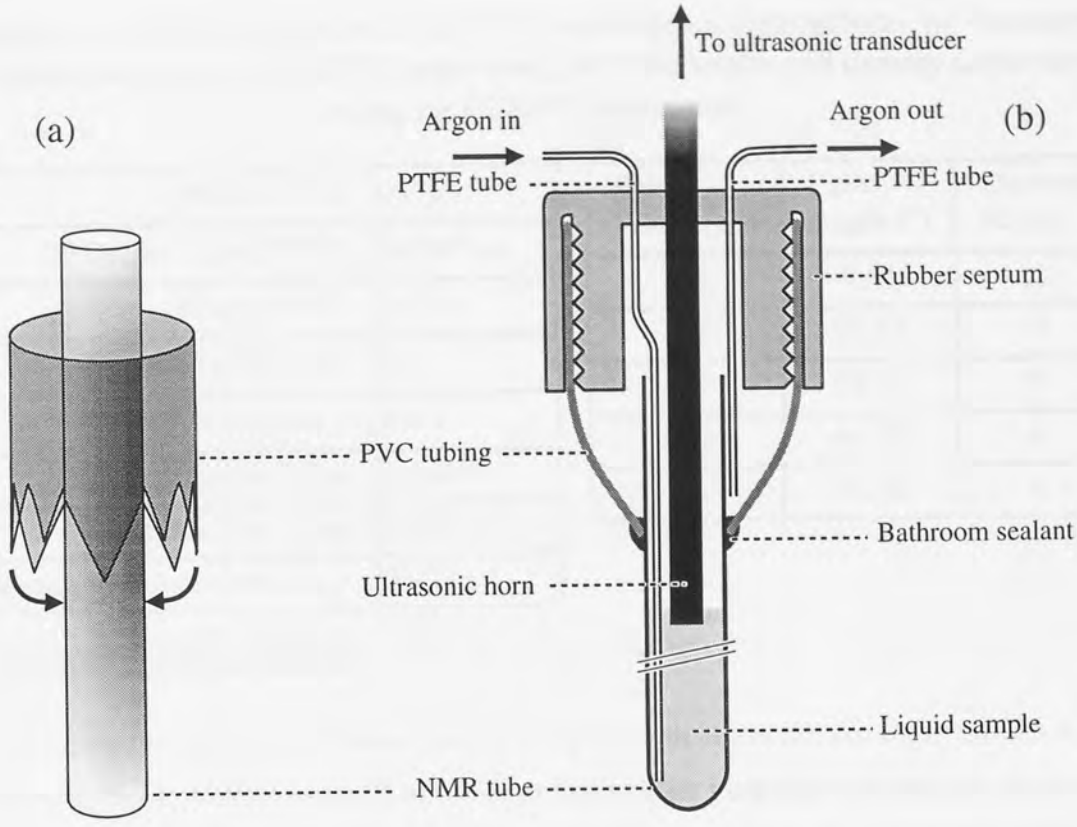

Figure 3.13 : **(a)** Formation of a PVC collar around a NMR tube and **(b)** collar positioned in a closed reaction cell adapted for use in NMR spectroscopy.

4.3.2 Experimental.

The adapted NMR tube was filled to a depth of 4cm with chloroform and placed into the JEOL NMR spectrometer. Prior to purging with argon a ^{13}C T_1 determination of chloroform was performed using the DESPOT [113-115] technique which found the spin-lattice relaxation time to be 8.8 seconds. The parameters for the experiment are shown in table 3.3.a and table 3.3.b.

Argon was allowed to bubble through the sample for 15 minutes after which the T_1 was determined using the same parameters as found in tables 3.3.a & 3.3.b. During the T_1 determination the long PTFE tube was re-positioned so that it delivered the argon to the surface of the chloroform, blanketing the sample with an inert atmosphere.

Table 3.3 : DESPOT determination of ^{13}C T_1 of oxygenated chloroform. **(a)** Parameters required to set up the DESPOT experiment. **(b)** Pulse widths and dummy scans used during the DESPOT experiment.

(a)

Pulse Offset	0.0 μs
90 Degree Pulse Width	16.865 μs
Estimated T_1	20.0 s
Required t_i/T_1 Ratio	0.2
Therefore Require t_i	4.0 s
Acquisition Time	1.024 s
Field Spoiling Time	0.001 s
Required Relaxation Delay	2.975 s

(b)

Pulse Width (μs)	Pulse Angle (°)	Dummy Scans
1.8	9.61	12
4.6	24.55	15
9.4	50.16	9
12.1	64.57	6
15	80.05	4

4.3.3 Results and Discussion.

The results of the experiment prior to purging with argon are shown in table 3.4 and figure 3.14, whilst the result of the experiment after purging with argon is shown in table 3.5 together with the corresponding scatter plot in figure 3.15. Despite repeated determinations scatter plots with poorly fitting lines prevented the accurate determination of T_1.

Table 3.4 : Results for the T_1 determination of oxygenated chloroform.

Pulse Angle (θ°)	N-Gain	Intensity	Absolute Intensity.(I)	I cos(θ)/ sin(θ)	I/ sin(θ)
9.60	1	5774	11548	68234.65	69204.94
24.55	2	5181	20724	45374.15	49882.84
50.16	2	9995	39980	33353.77	52066.06
64.57	2	8388	33552	15952.05	37151.10
80.05	2	6426	25704	4510.37	26096.72

Table 3.5 : Results for the T_1 determination of argon purged chloroform.

Pulse Angle(θ)	N-Gain	Intensity	Absolute Intensity(I)	Icos(θ)/sin(θ)	I/sin(θ)
9.60	1	2543	5086	30052.08	30479.42
24.55	2	2343	9372	20519.52	22558.48
50.16	2	9159	36636	30564.00	47711.16
64.57	2	8712	34848	16568.22	38586.13
80.05	2	9234	36936	6481.29	37500.34

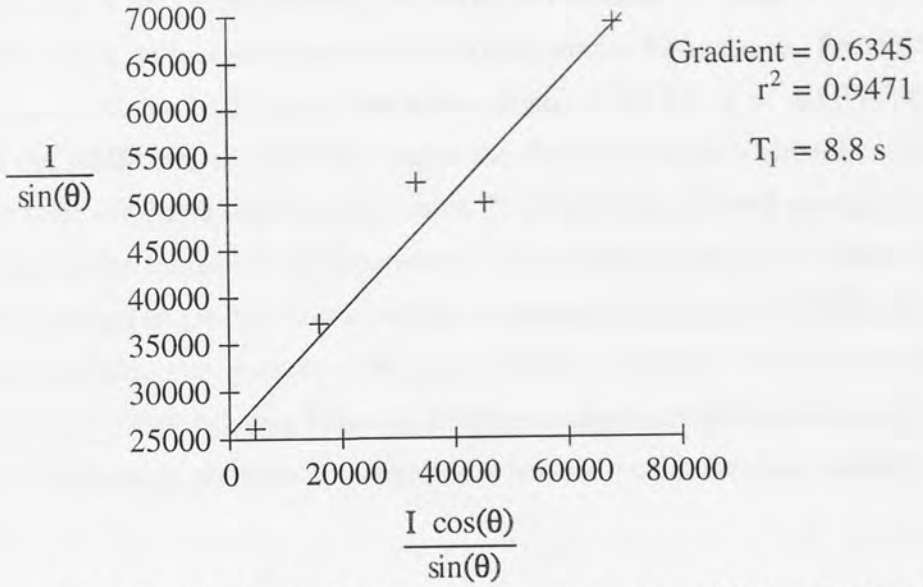

Figure 3.14 : DESPOT plot for the determination of the ^{13}C T_1 of oxygenated chloroform.

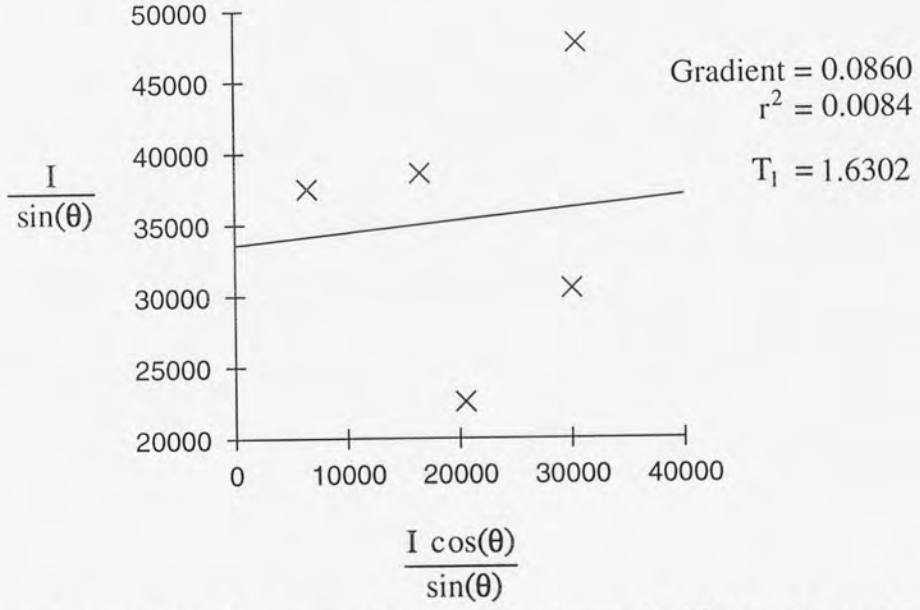

Figure 3.15 : DESPOT plot for the determination of the ^{13}C T_1 of argon purged chloroform.

The T_1 determination of the ^{13}C signal from the 'oxygenated' chloroform sample compares well to that found, independently, elsewhere in this thesis (part 5 : section 4.4). However, all attempts to determine the T_1 of the argon purged chloroform samples failed and produced almost random DESPOT plots. It is believed that this was caused by the failure of the adapted NMR tube to maintain an inert atmosphere above the chloroform sample, allowing oxygen to mix with the sample and causing the T_1 of the chloroform to change during the DESPOT experiment.

The design of the closed reaction cell took into account the need of the present SINNMR setup to deliver ultrasound to the NMR sample from above. Providing sufficient access to the NMR tube from above required the fitting of the PVC tube to the top of the NMR tube in order to increase the diameter of the NMR tube. However, the author believes that it was this very same PVC tube that allowed oxygen to re-enter the cell causing the failure of the experiment. Elimination of the PVC 'collar' is, therefore, expected to greatly reduce oxygen migration back into the NMR cell, allowing the purging experiments to be successfully completed. As the collar could easily be omitted from a design based on a bottom transducer SINNMR cell it is suggested that these experiments be repeated when such cells become available.

Chapter 5

Discussion of the Use of Ultrasound in Magnetic Resonance Spectroscopy.

5.1 Discussion of the Use of Ultrasound in Magnetic Resonance Spectroscopy.

The development of the SINNMR experiment has been hampered by the large number of variables of which account needs to be taken. The aim of this section was to throw light on the importance of some of these variables and to develop tools by which the importance of others could be investigated.

The investigation into the effect of magnetic field strength on a sonochemical reaction suggested that it had no discernible effect on the cavitational process. This important information implies that the next step in the evolution of the SINNMR experiment, where the SINNMR cell is transferred from an iron core magnet operating at 90MHz (proton) to a superconducting magnet operating at 250MHz, should be unaffected by the change in the magnetic field strength thereby allowing SINNMR experiments to be readily implemented at the higher field strength.

One of the phenomena associated with SINNMR is that of cavitation. However, the direct relationship between the rate of cavitation and the effectiveness of SINNMR is not accurately known. Attempts were, therefore, made to develop an experiment which could probe this relationship by utilizing the radicals formed during the implosion of the cavities. Initial experiments were concerned with detecting such radicals directly and witnessed the first experiment involving the *in situ* detection of the effects of ultrasound on a liquid via EPR spectroscopy. The encouraging results of the EPR experiments facilitated the development of an equivalent experiment in NMR spectroscopy whereby the CIDNP of the radicals generated in the support liquor used in SINNMR was to be measured. However, attempts to detect a CIDNP failed for the reasons given in the appropriate part of this thesis (section 4.3.3). Should the remedies suggested therein prove successful then detection of the CIDNP from the support liquids should become a valuable tool in the determination of ideal SINNMR conditions. As the CIDNP will hopefully give a direct measure of the rate at which the cavitational process occurs in the SINNMR cell, comparative measurement of the CIDNP between SINNMR experiments should allow the importance of size, shape and range of particles used in the SINNMR experiment to be more easily established.

Part 4

The Use of Fluidized Beds in NMR Spectroscopy

Chapter 1.

Introduction to Fluidization.

1.1 Introduction.

SINNMR is just one new method that is being developed to facilitate the routine detection of 'high resolution ' NMR spectra of solids. As explained earlier it is based on using ultrasound to cause suspended solid particles to move incoherently in a manner similar to large molecules in a liquid. Another way of achieving a similar end could be to pass air through a granular sample of the solid at sufficiently high velocities to support the granules and allow them to take on fluid-like properties. Hopefully, the interparticle collision would then cause the random motion needed to average out unwanted interactions within the solid resulting in the observation of high resolution, liquid-like spectra.

1.2 Fundamental Fluidized Bed Behaviour.

Fluid flowing through the spaces between particles in a powder bed exerts a drag force on the particles which may be large enough to disturb the arrangement of the particles. If the upward velocity of the fluid through the bed is increased progressively, a situation eventually arises where the fluid drag is sufficient to support the entire weight of the bed. The bed is then said to be 'incipiently fluidized' and exhibits fluid-like properties. The bed will flow, the free surface will remain horizontal if the container is tilted and low-density objects will float on or in the bed. (See figure 4.1)

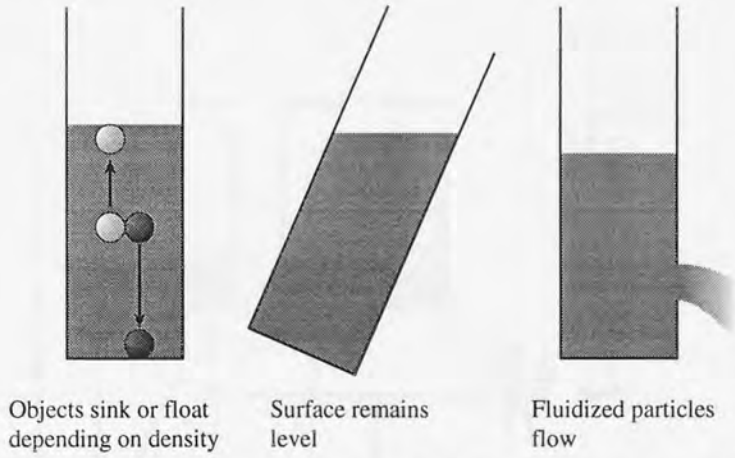

Figure 4.1 : The behaviour of incipiently fluidized particles.

The flow rate at which incipient fluidization occurs, the 'minimum fluidizing velocity', U_{mf}, is usually quoted as a velocity that is defined simply as;

$$U_{mf} = \frac{V_{mf}}{A} \qquad (4.1)$$

where V_{mf} is the volume flow rate and A is the cross sectional area of the vessel containing the bed.

Increasing the gas flow from zero causes the bed to take on various characteristics (figure 4.2): Initially the appearance of the bed does not change, the pressure drop across the bed rising with flow rate and reaches a maximum at the point of incipient fluidization. After this point the pressure drop remains constant. At first the particles accommodate the extra gas flow by rearranging themselves, resulting in an increase in the interstitial spacing (referred to as the bed voidage, ε) and the expansion of the bed to a greater depth. The extent to which this uniform expansion of the bed occurs depends on the nature of the particles being used. At some increased flow rate the fluidized bed becomes unstable and 'bubbles' of the fluidizing gas are formed. These bubbles rise through the bed, bursting when they reach the free surface, scattering particles into the region above the bed from which they fall back to the bed. The bubbling action causes the particles to mix and translate continuously. The bubbles continue to grow in size with gas velocity until the bubble occupies the whole cross section of the bed, one bubble following close behind the other. This stage is called slugging. As the velocity of the gas is further increased, some of the smaller particles become entrained in the gas flow and can be removed from the containing vessel. As the gas velocity further continues to increase more of the sample becomes entrained eventually resulting in the removal of all particles from the bed.

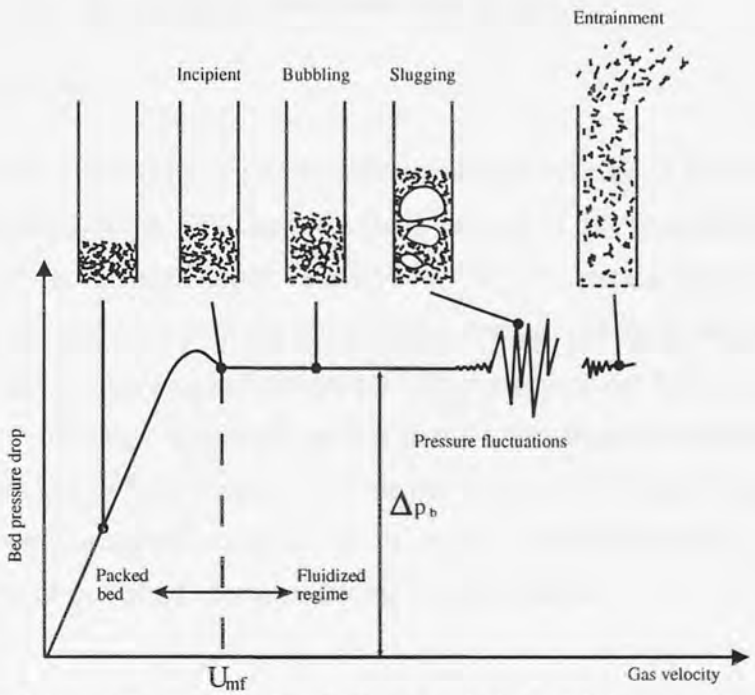

Figure 4.2 : Change in fluidized bed characteristics with increased gas velocity.

While in the fluidizing regime the pressure drop across the bed, Δp_b, can be related to the density and mass of the particles;

$$\Delta p_b = \frac{M}{\rho_p A}(\rho_p - \rho_g)g \qquad (4.2)$$

where M is the mass of particles, ρ_p is the particle density, ρ_g is the fluidizing gas density, 'A' is the cross sectional area of the bed and 'g' is the gravitational acceleration constant. Pressure drops across the bed predicted by equation(4.2) are usually greater than that found in practice as the equation makes no attempt to account for the interactions between the particles or for energy dissipated within the bed.

As depicted in figure 4.2 it is common to find a small 'hump' in the gas velocity/ bed pressure drop curve at gas velocities just below the minimum fluidizing velocity. This feature is especially prevalent on the first attempt to fluidize the bed and arises from the extra energy required to dislodge the particles from their original packed bed configuration.

1.3 Particle size and shape.

As the physical attributes of a particle are altered so does the nature of the bed formed during fluidization [116, 117]. Particles are, therefore, categorized into four main types, the category depending on the particles density and size. Each category of particles exhibits a different type of bed behaviour. Figure 4.3.

1.3.1 A-type particles.

A-type particles generally fall within the size range 20-100μm and have a particle density up to approximately 1400 kg m^{-3}. Beds formed of this type usually expand considerably with an increase in gas velocity when U_{mf} is first exceeded. Stable bed expansion usually continues until the gas velocity reaches two or three times that of U_{mf}. Any further increase in gas fluidization velocity causes the bed to collapse back to a magnitude of expansion comparable to that found at the minimum fluidizing velocity. Further increases in gas velocity results in the formation of bubbles. Because of this the gas velocity at which the bed collapses is termed the 'minimum bubbling velocity', U_{mb}. Prior to the onset of bubbling, particle mixing is very limited.

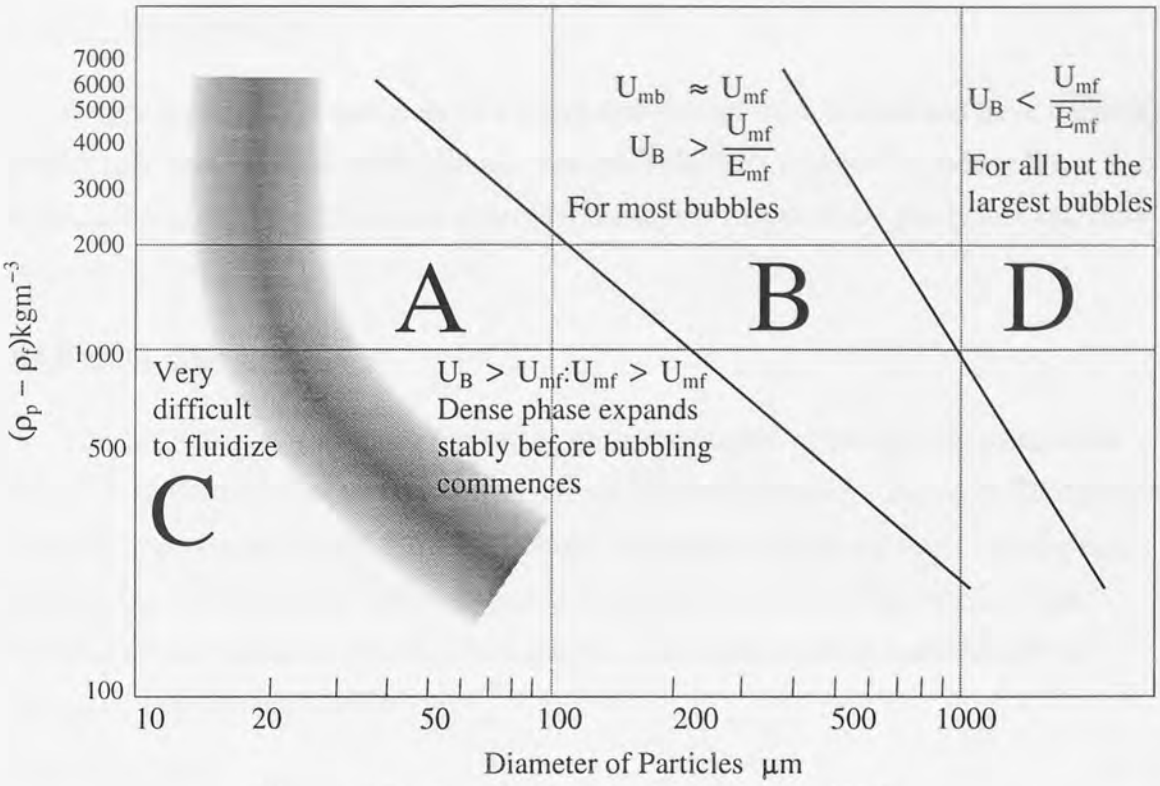

Figure 4.3 : Powder classification diagram [116].

1.3.2 B-type Particles.

B-type particles are generally classified as having a particle size range of 40-500μm and a density range of 1400-4500 kg m^{-3}. Their reaction to fluidization is very much like A-type particles. However, an increase in gas velocity above the minimum fluidizing velocity tends to result in the formation of bubbles in the bed rather than causing its uniform expansion. This implies that for B-type particle U_{mf} and U_{mb} are approximately equal.

1.3.3 C-Type Particles.

C-type particles are of low density and generally have a mean size of less than 30μm. The characteristics of fluidized beds formed from such particles are dominated by interparticle forces rather than gravity and this makes fluidization of the sample difficult. The particles in such beds preferentially rearrange themselves to result in the formation of low resistance channels in the powder, through which the fluidizing gas is channelled. Mechanical stirring of the sample close to the distributor can alleviate this situation but fluidization remains difficult and the sample is still prone to spontaneous de-fluidization.

1.3.4 D-Type Particles.

D-type particles are generally of a mean size greater than 600μm and have densities greater than that found in other groups. The gas velocities required to induce the fluidization of such particles is so great that the laminar flow of the gas is lost and flow becomes turbulent.

1.4 Bubble Rise and Shape.

The bubbling regime is a two phase system, the bubble phase and the particulate phase. It is assumed that all gas flow in excess of that required for incipient fluidization flows through the bed in the form of bubbles. Experimental results show that the rise velocity U_B, of an isolated bubble depends on the relative size of the bubble to the diameter of the fluidizing vessel. For a bubble isolated from other bubbles and the container wall then[117, 118];

$$U_B = 0.71\sqrt{gD_b} \tag{4.3}$$

and for a bubble diameter greater than 30% of the bed diameter then;

$$U_B = 0.35\sqrt{gD_c} \tag{4.4}$$

In a bubbling fluidized bed the bubble velocities are also affected by the velocity of the fluidizing gas giving the bubble rise velocity as;

$$U_B = k(U - U_{mf}) + 0.71\sqrt{gD_b} \tag{4.5}$$

In the above equations D_b is the diameter of the sphere having the same volume as the bubble, D_c is the diameter of the fluidized bed, g is the gravitational constant, k is a proportionality constant and U is the velocity of the fluidizing gas.

In most situations the fluidizing velocity is sufficiently greater than the minimum fluidizing velocity for the bubbles to be formed continuously. These bubbles are usually in such close proximity to each other that each bubble is influenced by its neighbouring bubbles, resulting in bubble growth, coalescence and splitting.

In type A and B particle systems it is possible to identify two types of bubbles *viz* those which rise slower than the fluidizing gas and those which rise faster. The slow bubbles give rise to a through flow of gas, as shown in figure 4.4.a, so that gas is exchanged between the bubble and particulate phases of the bed. If the bubble rises faster than the gas velocity through the voids, then the gas within the rising bubble stays with it, circulates with a surrounding particle cloud and never leaves the bubble/cloud

regime [119, 120](figure 4.4.b). The faster the bubble rises in relation to the fluidizing gas velocity the thinner this surrounding cloud becomes.

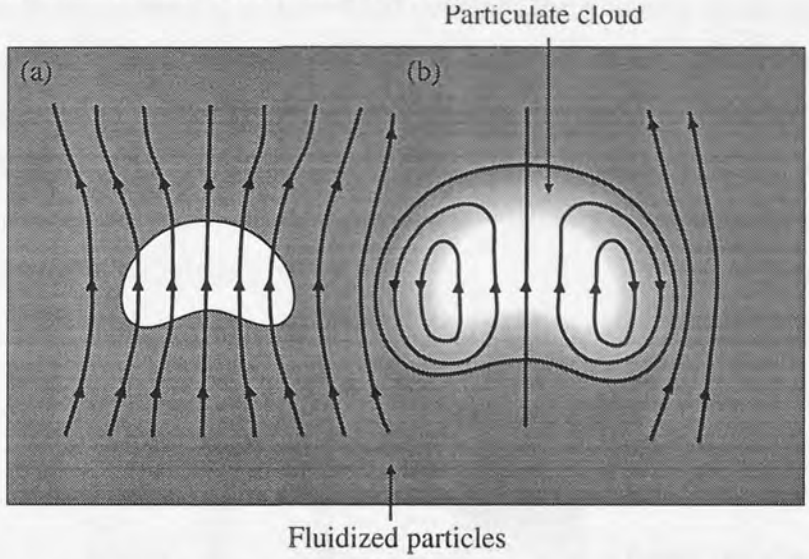

Figure 4.4 : Gas flow patterns between bubble and particulate phase.
(a) slow bubble, **(b)** fast bubble.

In type D particle systems the terms 'slow' and 'fast' rising bubbles lose their meaning as all bubble velocities are less than that of the gas passing through the particle voids, yet their velocity is still faster than the velocity of 'fast' rising bubbles in A- and B- type systems.

1.5 Bubble growth

Bubbles in group A particles tend to grow in size by coalescence and eventually reach a maximum stable size once an equilibrium between spontaneous bubble coalescence and bubble splitting is achieved. In B-type and D-type particle systems this equilibrium is not achieved and bubbles continue to grow as they progress up the bed, their only limit being the size of the containing vessel.

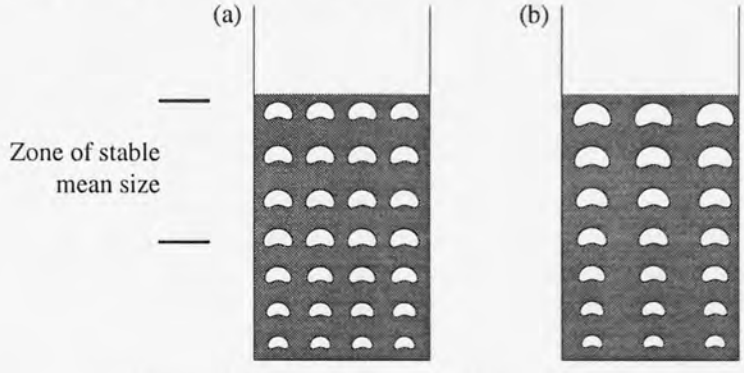

Figure 4.5 : Bubble growth in a bed consisting of
(a) A-type and **(b)** B-type particles.

1.6 Slugging

When the bubble grows to a size which occupies the majority of the cross sectional area of the containing area, the bed is said to be slugging. When this occurs the bubbles may either rise rapidly through the fluidized material or rise slowly while supporting a slug of de-fluidized particles which slowly unlock and fall through the bubble. Figure 4.6. The gas velocity at which slugging occurs is normally much smaller in small-diameter beds than in large-scale beds.

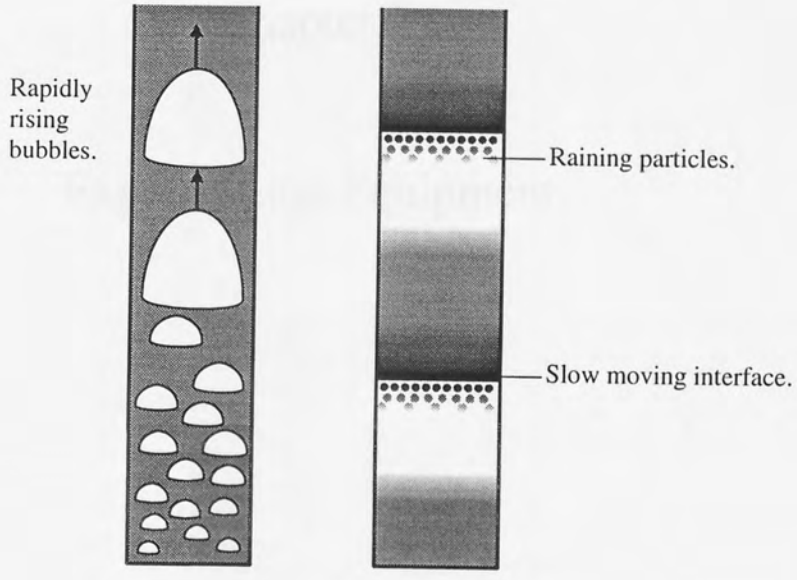

Figure 4.6 : Slugging behaviour.

Chapter 2

Experimental Equipment.

2.1 Fluidizing NMR tubes.

The effects of fluidizing particles within a NMR spectrometer were to be examined using the JEOL FX-90Q NMR spectrometer (part 3 : sections 2.1). In order to enable the fluidization of particles while they are contained within the probe region of the spectrometer it is necessary to cause air to flow up through the particles. Due to the restricted access around the NMR probe it was not possible to introduce a new air supply to feed the fluidized bed. It was, therefore, necessary to use one of the existing air supplies. Figure 4.7 shows a diagrammatic representation of the NMR probe when located in the NMR spectrometer together with air flows available to the probe.

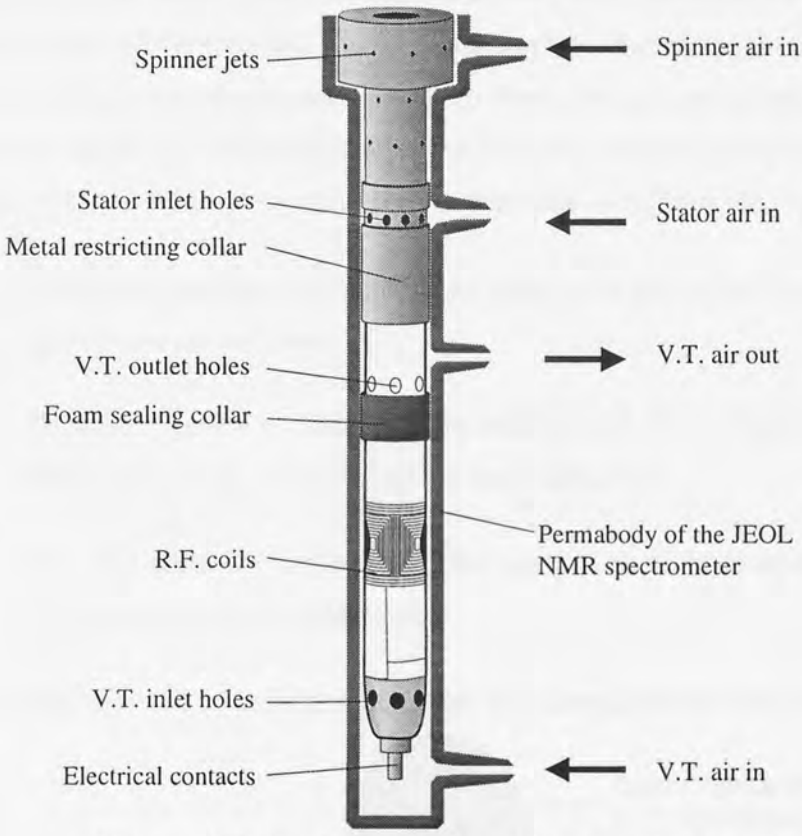

Figure 4.7 : The NMR probe while in position in the permabody of the spectrometer.

As can be seen the three air supplies to the probe are for the spinner air, the stator air and the variable temperature (V.T.) air supplies. When the probe is inserted into its housing (permabody) the metal restricting collar of the probe fits closely into the permabody of the NMR spectrometer, making the redirection of the spinner and stator air for use in a fluidizing NMR tube difficult.

During normal operation of the spectrometer the V.T. air enters the probe through the inlet holes at the bottom of the probes insert, passes over the surface of the NMR

tube and leaves through the V.T. exit holes. The V.T. air is prevented from flowing between the probe and permabody, directly from the 'V.T. air in' duct to the 'V.T. air out' duct, by a foam ring bonded to the exterior surface of the probe. Consequently, if the V.T. exit holes are blocked the V.T. air has nowhere to flow. However, if a NMR tube with a sintered bottom can be used instead of a standard NMR tube, the V.T. air would be forced through the sinter and pass up the inside of the NMR tube, fluidizing the contents of the NMR tube.

The initial design of the sample tubes was to replace the usually rounded bottom of a NMR tube with a glass sinter. However, there were several problems envisaged with this design which included the production of a sinter with the correct size, the bonding of the sinter to the NMR tube and the relatively high pressures required to force the air through the sinter at velocities great enough to cause the sample to fluidize. To overcome these problems a perforated paper diaphragm was used in place of the glass sinter. The fluidizing NMR tubes were, therefore, assembled as follows (see figure 4.8) ;

- A piece of ashless toughened filter paper was pierced with an approximate pattern shown in figure 4.8.
- The filter paper was bonded to the smooth end of an 10mm outer diameter NMR tube using 'Araldite' epoxy resin adhesive.
- Once the adhesive had set, the filter paper was cut back so that it was flush with the walls of the NMR tube.
- The rounded end of the NMR tube was scored and broken off.

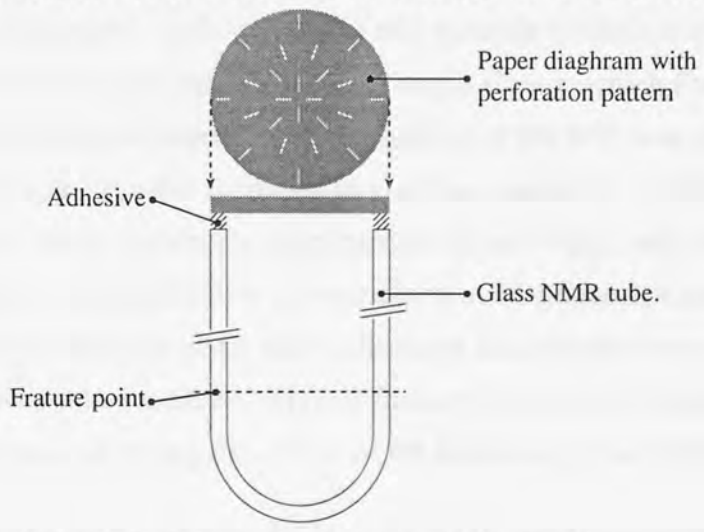

Figure 4.8 : Schematic diagram of sample tube.

2.2 Visual Inspection of the Fluidizing Sample Tubes.

A visual inspection of the fluidizing sample tube was made outside the NMR spectrometer using a separate air supply. To establish the rate of air flow through the fluidizing chamber a rotometer was placed in series with the air flow, between the fluidizing NMR tube and the air supply. The tube was then loaded with ungraded sodium orthophosphate dodecahydrate ($Na_3PO_4.12H_2O$) crystals to a depth of 17mm and the rate at which the gas flowed through the NMR tube gradually increased. This was repeated for a sample of 400-1000 μm aluminium granules. In general it was possible to observe each of the test powders progress through each of the fluidizing regimes from packed bed to entrainment. Both samples fully fluidized with gas flows of less than 2 litres/min with the beds expanding on their transformation from a static bed to a fluidized bed. The sodium orthophosphate dodecahydrate bed expanding by approximately 50% while the aluminium bed expanded by 100%. When comparing the aluminium and sodium orthophosphate dodecahydrate (TSP) experiments the particles of the TSP crystal were relatively difficult to fluidized and were more easily entrained at elevated gas velocities. The TSP sample was also prone to spontaneous de-fluidization, probably induced by the needle-like crystals locking together, forming a matrix able to resist the drag exerted by the fluidizing gas. The perforated paper diaphragm produced random particle motion through-out the whole of the sample although the portion of the sample that was visible near the bottom of the fluidizing tube appeared to be circulating less vigorously than the rest of the sample.

As the NMR V.T. air supply was capable of delivering measurable air flows of up to 20 litre/min, the fluidizing sample tube was first tested without blocking the V.T. outlet holes in the NMR probe. Although it was still possible to fluidize the samples using this configuration of probe and NMR tube, the gas flow at which fluidization occurred (determined by visual inspection of the surface of the bed) was raised from 2 litres/min to 10 litres/min. Further increases in gas flow caused the particles forming the fluid bed to agitate more vigorously, entrainment not occurring until a flow of 15 litres/min was reached. Above this flow rate entrainment of the particles occurred, all particles being removed from the NMR tube at flows of 18litres/min or above. As all stages of fluidization could be achieved with air flows of less then 20 litre/min the V.T. outlet hole were not blocked during the course of the following experiments.

Attempts to spin the fluidizing tube while in the NMR spectrometer were also successful having the potential advantage of not only adding additional rotational

motion to the fluidized particles but also of diffusing the air flow through the perforated diaphragm over the whole cross section of the NMR tube. It was, however, noted that if the rotational frequency of the sample tube was raised much over 7Hz then the centrifugal force threw the fluidized particles to the edge of the tube where they became immobilized.

Chapter 3

The Fluidization of Sodium Orthophosphate Dodecahydrate.

3.1 Introduction.

As the majority of successful SINNMR experiments have been performed using TSP [122] this was chosen as a sample to study in the fluidizing NMR tube. A benefit of using TSP is that crystals are relatively simple to grind and the dependence on particle classification (section 1.3) could also be easily investigated.

3.2 Investigation into the Effects of Particle Type on the NMR Spectra of Fluidized Sodium Orthophosphate Dodecahydrate.

3.2.1 Introduction.

Clearly the physical dimensions of particles determines their classification as proposed by Geldart [116, 117] (figure 4.3) and, consequently, will affect the dynamics of the fluidized beds they form. This, therefore, allows some control over the rate at which particle collision occur, the rate of bubble rise, the maximum bubble size as well as the susceptibility of the bed to particle entrainment and spontaneous de-fluidization. In an attempt to investigate this relationship between particle classification and the associated fluidized NMR spectra, samples of TSP of various particle-size ranges were examined.

3.2.2 Experimental

Commercially available TSP was lightly ground using a mortar and pestle and the resulting crystals sieved to produce samples with particle-size ranges of 1000μm-500μm, 500μm-210μm, 210μm-105μm, 105μm-90μm, 90μm-75μm, 75μm-53μm and <53μm.

Prior to the investigation of these samples a ^{23}Na NMR spectrum of the fluidizing NMR tube alone (figure 4.9, acquisition parameters A6.1) was obtained, enabling any ^{23}Na artifacts generated by the soda glass tube to be isolated from the ^{23}Na fluidized TSP spectra. The fluidizing NMR tube was then filled to a depth of 17mm with the 1000μm-500μm sample of TSP crystals and positioned within the NMR probe such that the surface of the static sample coincided with the middle of the 14mm active region of the probe. Prior to fluidization both ^{23}Na (figure 4.10, acquisition parameters A6.1)) and ^{31}P (figure 4.11, acquisition parameters A6.2)) NMR spectra of the static solid were obtained. The V.T. outlet holes of the NMR probe were left un-blocked in accordance with the findings of section 2.2 and the V.T. air supply was turned on and set to deliver 12litres/min of air to the NMR probe. Upon fluidization of the sample

both ^{23}Na (figure 4.12, acquisition parameters A6.1)) and ^{31}P (figure 4.13, acquisition parameters A6.2)) NMR spectra were obtained. This procedure was repeated for the remaining size ranges of TSP *viz* 500μm-210μm, 210μm-105μm, 105μm-90μm, 90μm-75μm, 75μm-53μm and <53μm.

3.2.3 Results and Discussion.

Table 4.1 outlines the nature of the fluidized bed produced during the experiments while table 4.2 summarizes any spectra obtained.

The static solid state ^{23}Na spectrum of 500-1000μm TSP (figure 4.10) features three broad peaks which, with decreasing screening constant, show a reduction in signal to noise ratio together with an increase in the frequency width at half maximum (FWHM) height. The comparable spectra of the fluidized sample (figure 4.12) shows only two of these peaks, the peak at the highest chemical shift presumable being lost under the baseline noise. On fluidization of the sample the spectrum obtained shows no significant line narrowing effects but does show a decrease in the signal to noise ratio of all peaks. This decrease in the signal to noise ratios is consistent with the expansion of the bed during fluidization, effectively reducing the concentration of the sample in the probe. The solid state ^{31}P spectrum (figure 4.11) of the 500-1000μm TSP sample features a single, broad peak with a FWHM of 5800Hz and, once again, shows no line narrowing effect on fluidization but does show the expected reduction in the signal to noise ratio.

As indicated in table 4.2 no spectra for the sub 500μm TSP samples were obtained as they did not remain fluidized for the duration of the NMR experiment.

The ^{23}Na static solid spectrum of TSP reported here does not correspond with that obtained elsewhere under similar conditions, reproduced in figure 4.14. This, together with the observation that some of the crystals of TSP appeared to have lost their luster after fluidization, suggested that the TSP crystals may be prone to a physico/chemical transformation and that the examined sample may no longer have been sodium orthophosphate dodecahydrate. Examination of this possibility is discussed in section 3.4. However, the source of 'TSP' which yielded ^{23}Na NMR spectra with three peaks was used for the remainder of this work as, not only did it give reproducible spectra but, the narrower sodium resonances implied smaller anisotropies of the nuclear interactions within the solid which should be more easily narrowed by the random motion induced by the fluidized bed.

Table 4.1 : Attempts to fluidize different particle ranges of TSP.

Particle range (μm)	Particle type	Description of the fluidized bed behaviour as viewed from the top of the fluidizing tube.
1000-500	B/D	When the V.T. air supply was delivering 12 litres/minute to the NMR probe the sample appeared to be fluidized and bubbling with few particles from the sample becoming entrained.
500-210	B	When the V.T. air supply was delivering 12 litres/minute to the NMR probe the sample appear to be fluidized, however the sample was prone to spontaneous de-fluidization. Elevating the gas flow to 15 litres/min prevented the spontaneous defluidization of the sample but resulted in the steady entrainment of the sample.
210-90	B/A	At a gas flow of 12 litre/minute the sample would not fluidize. Elevating the gas flow could not prevent the spontaneous de-fluidization of the sample, the sample becoming readily entrained in the air flow during periods of fluidization.
90-75 75-53 <53	A A A/C	Even at elevated gas flows the sample would not fluidize, the fluidizing gas forming stable channels through the sample matrix.

Table 4.2 : Summary of Fluidized bed NMR experiment performed on TSP in section 3.2.2

		^{23}Na				^{31}P		
TSP		Figure	Peak	FWHM (Hz)	S/N Ratio	Figure	FWHM (Hz)	S/N Ratio
1000 -500μm	Static solid	4.10	*i* *ii* *iii*	1400±200 1600±200 1900±300	6.9 2.7 1.7	4.11	5800±400	10.9
	Fluidized at 12 l/min	4.12	*i* *ii* *iii*	1400±200 1900±300 -	3.9 1.7 -	4.13	5800±400	4.7
All other ranges	Fluidized at 12 l/min	Samples would not remain fluidized throughout the NMR experiment, consequently no spectra were obtained.						
Fluidizing NMR Tube.		4.9		No Signal		-	-	-

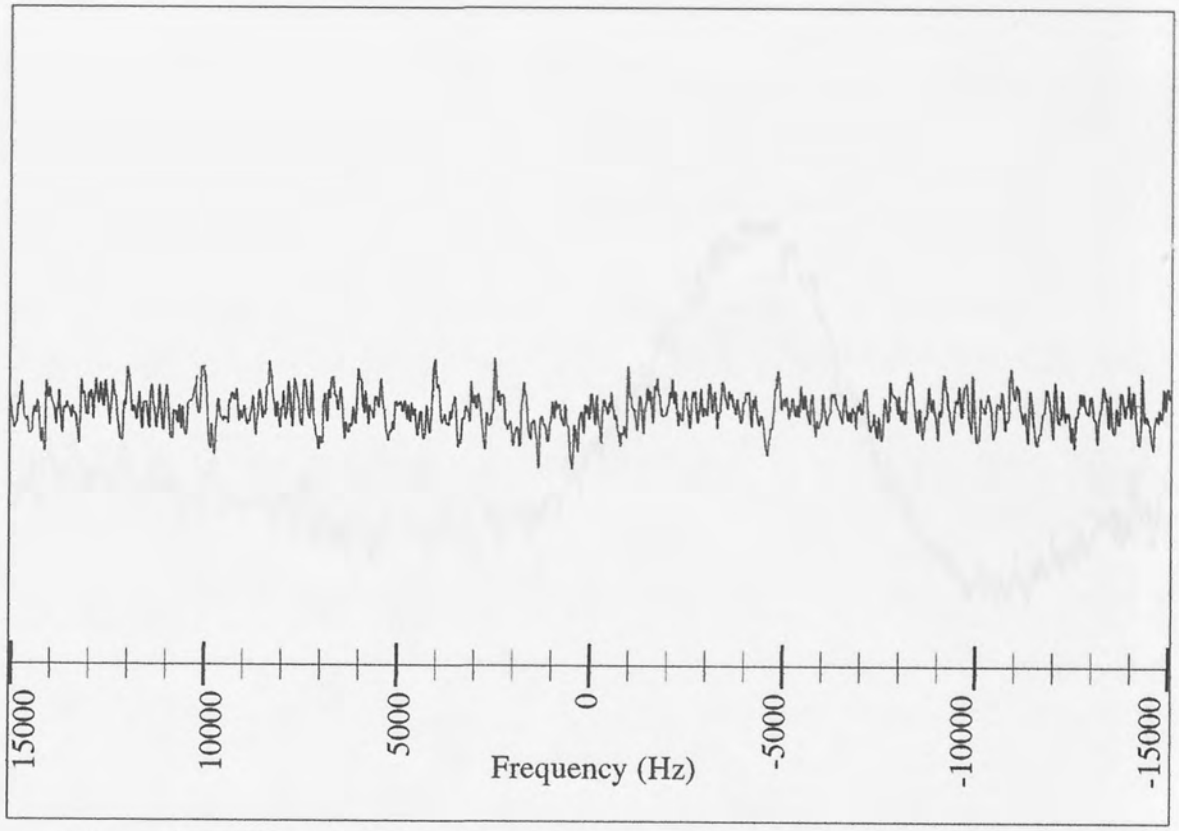

Figure 4.9 : ^{23}Na spectrum of empty fluidizing NMR tube. (Normal tube position)

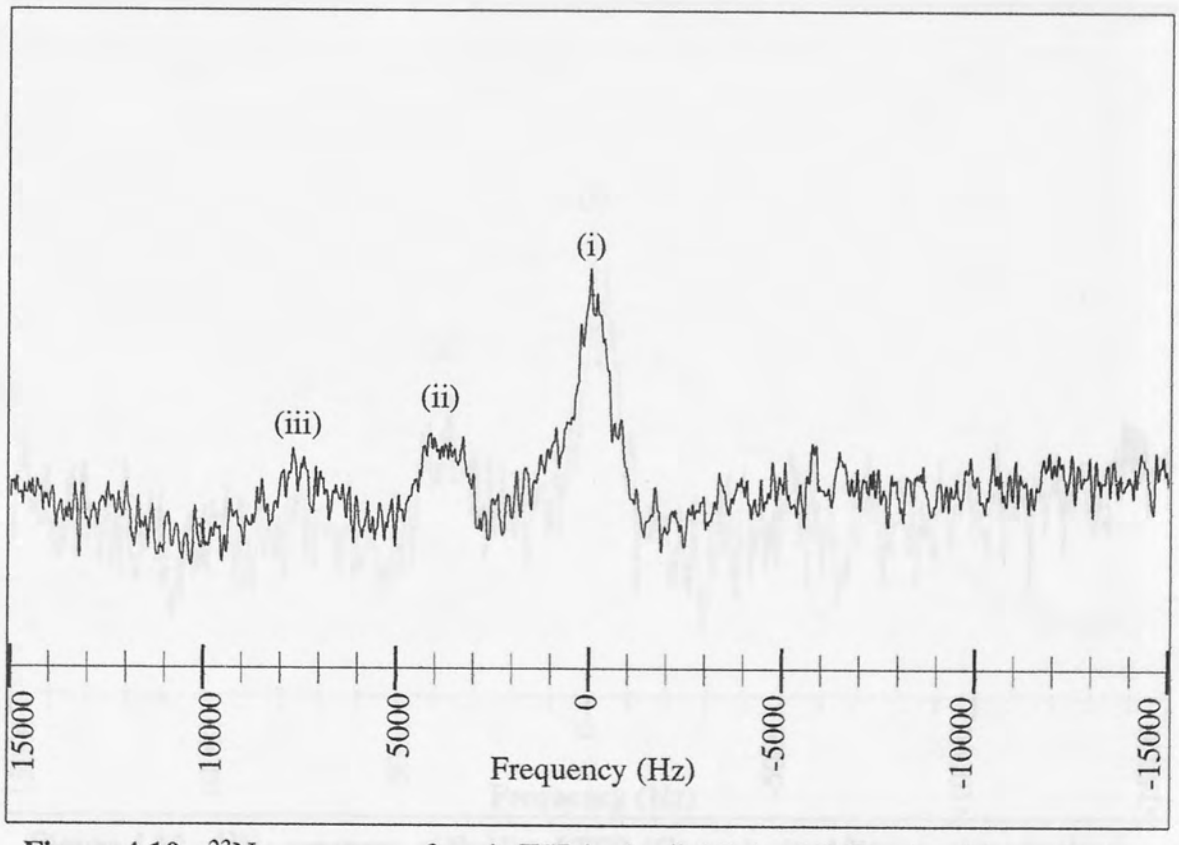

Figure 4.10 : ^{23}Na spectrum of static TSP in the fluidizing NMR tube. (Normal tube position)

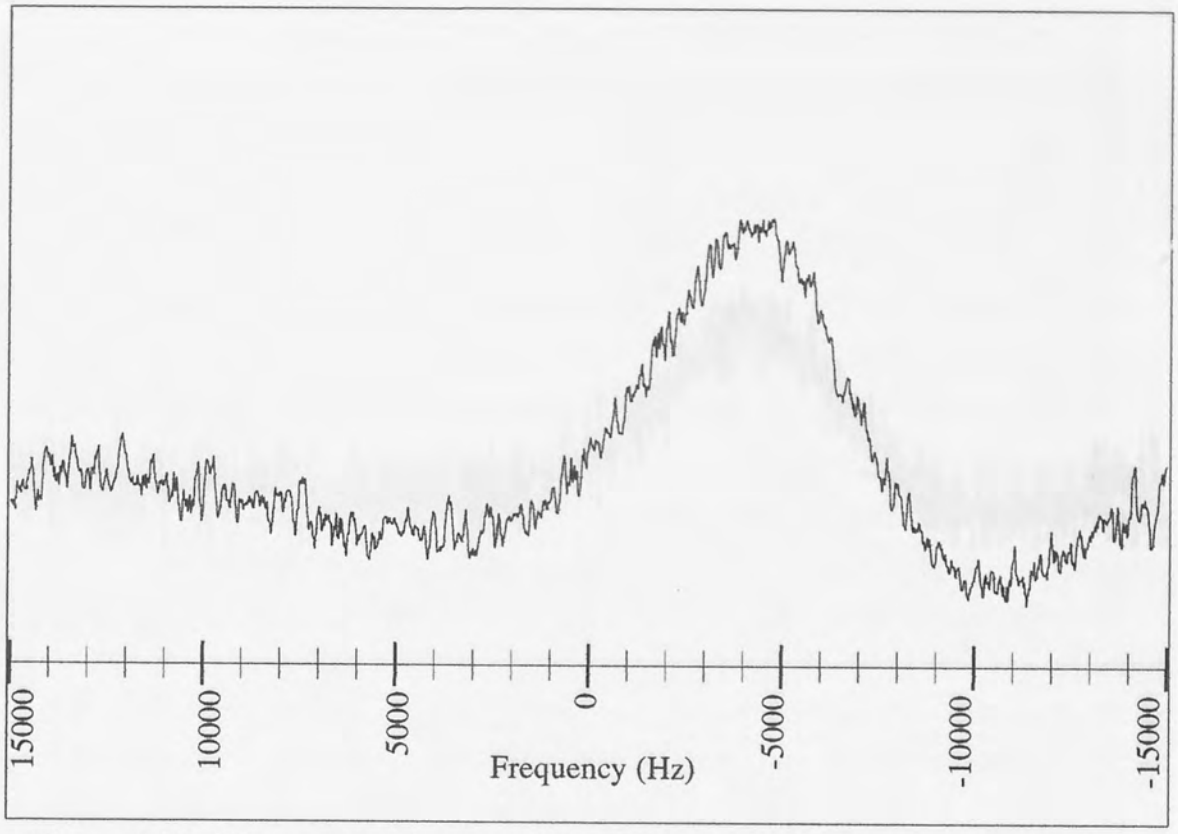

Figure 4.11 : ^{31}P spectrum of static TSP in the fluidizing NMR tube. (Normal tube position)

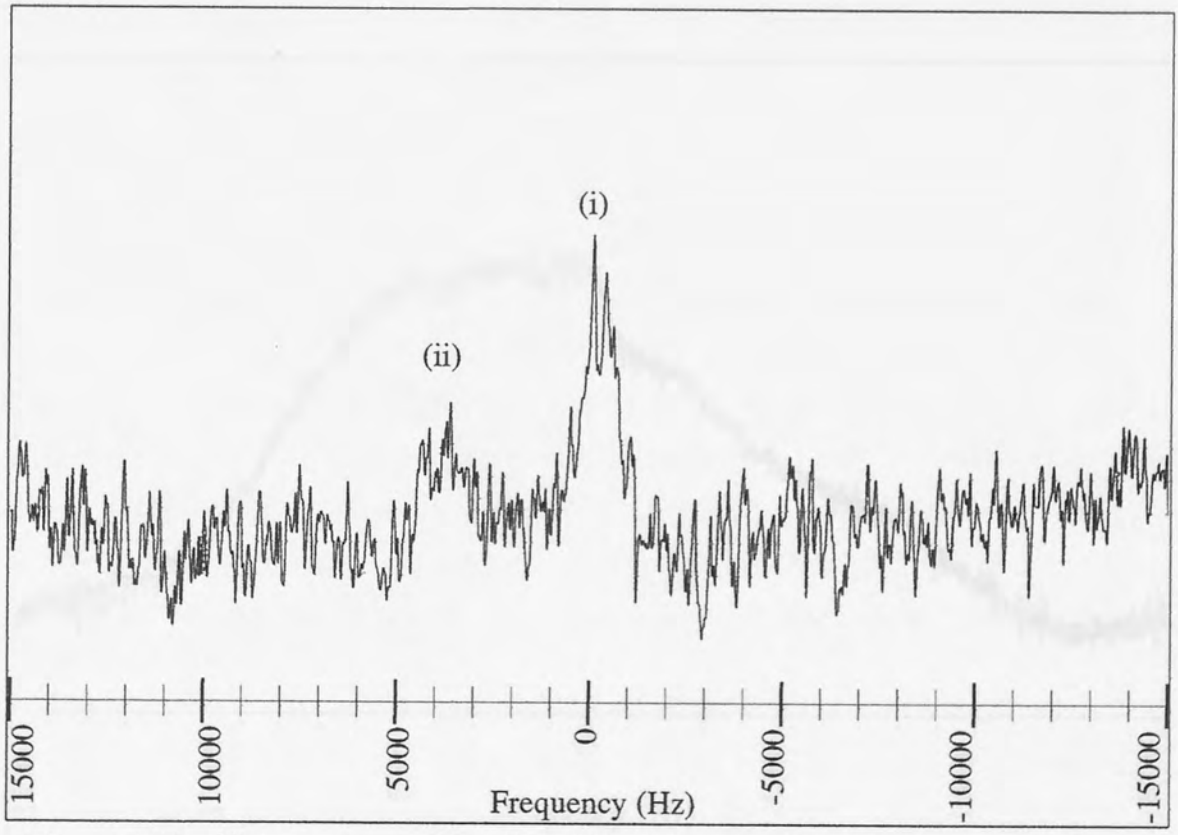

Figure 4.12 : ^{23}Na spectrum of fluidized TSP. (Gas velocity 12l/min, normal tube position)

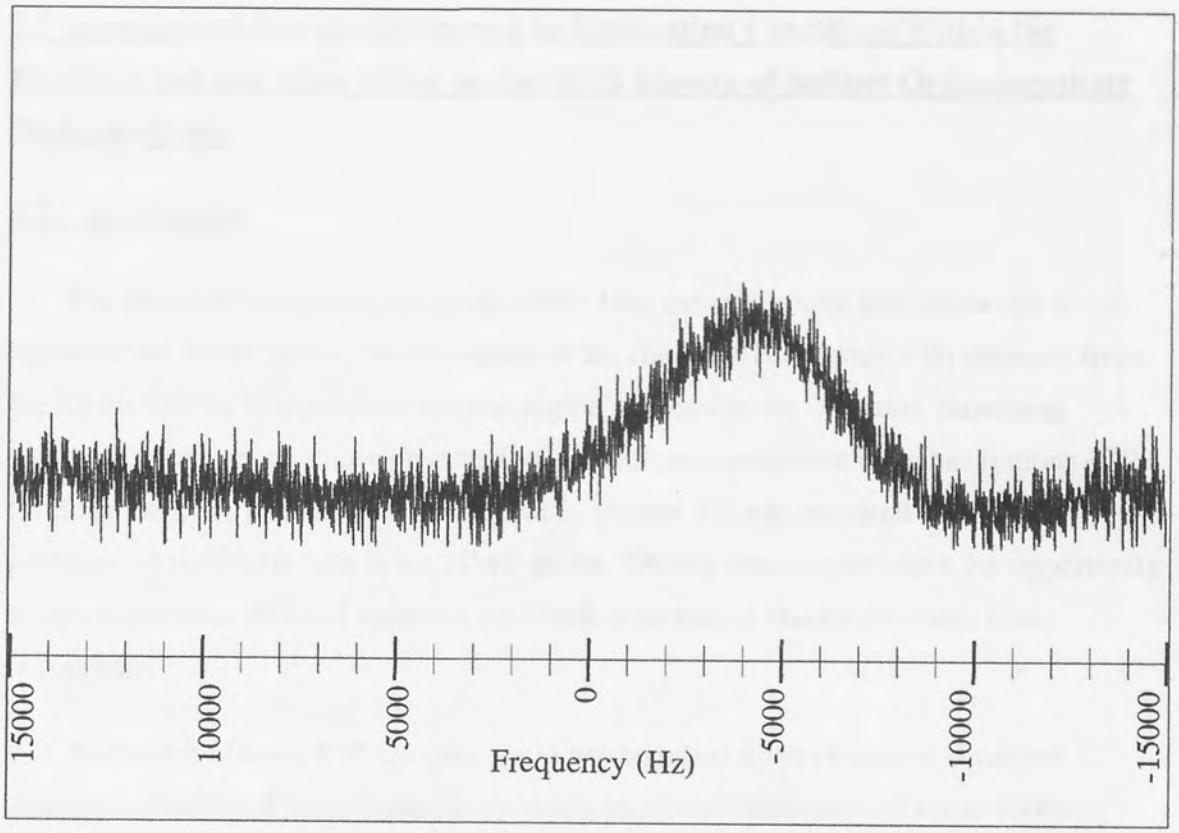

Figure 4.13 : ^{31}P spectrum of fluidized TSP. (Gas velocity 12l/min, normal tube position)

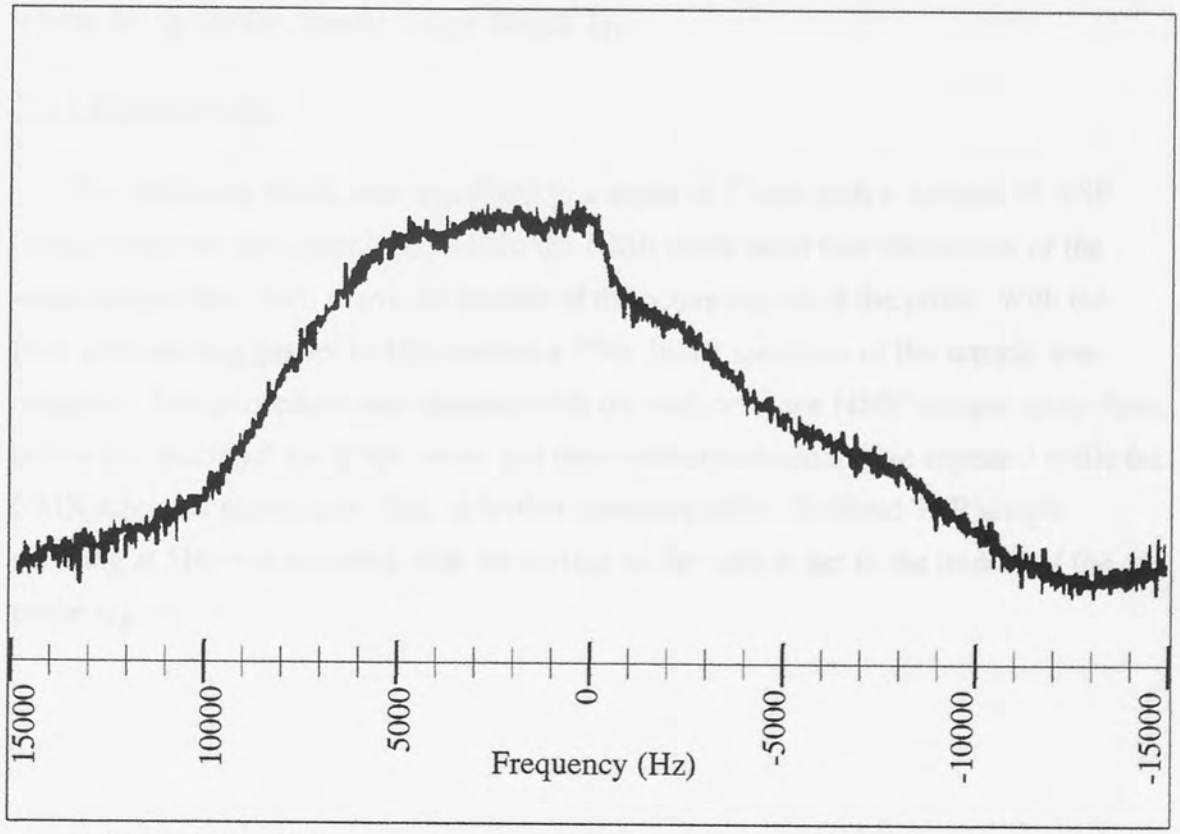

Figure 4.14 : ^{23}Na spectrum of static TSP as obtained by M. Howard [122].

3.3 Investigation into the Differences in Fluidization Conditions Within the Fluidized Bed and Their Effect on the NMR Spectra of Sodium Orthophosphate Dodecahydrate.

3.3.1 Introduction.

The fluidized bed produced in the NMR tube extends above and below the active region of the NMR probe. As the nature of the fluidized bed varies with distance from the air distributor it is possible that the region possessing the optimum fluidizing conditions may not be under observation. Therefore, to monitor the other regions of the fluidized bed, the fluidization experiment in section 3.2 was repeated for different positions of the NMR tube in the NMR probe. During these experiment the opportunity to investigate the effect of spinning the NMR tube during fluidization was also investigated.

As the sub 500μm TSP samples could not be relied upon to remain fluidized throughout the NMR experiment the investigation was limited to a 500μm-1000μm sample of TSP which, accounting for the findings of section 3.4, was replaced with a fresh sample from the TSP source after each NMR spectrum. Also the spectra obtained in this section were limited to ^{23}Na spectra which are more rapidly observed than ^{31}P which, being dipolar, has the longer longer T_1.

3.3.2 Experimental.

The fluidizing NMR tube was filled to a depth of 17mm with a sample of TSP crystals and was then positioned within the NMR probe such that the surface of the static sample was 7mm above the middle of the active region of the probe. With the flow of fluidizing gas set to 12litres/min a ^{23}Na NMR spectrum of the sample was obtained. This procedure was repeated with the surface of the NMR sample set to 7mm below the middle of the NMR probe and then both experiments were repeated while the NMR tube was spinning at 5Hz. A further spectrum of the fluidized TSP sample spinning at 5Hz was obtained with the surface of the sample set to the middle of the probe region.

3.3.3 Results and Discussion.

The spectra obtained during these experiments are summarised in table 4.3.

Table 4.3 : Summary of experiments performed on TSP in section 3.3.2. († by the end of the experiment the sample had de-fluidized).

		^{23}Na				
500-1000μm TSP		Figure	Peak	FWHM (Hz)	S/N Ratio	Acquisition parameters
Static Tube	Sample raised 7mm	4.15	*(i)* *(ii)* *(iii)*	1500±300 1300±300 2500±400	3.9 2.5 1.5	A6.1
	Sample lowered 7mm	4.16	*(i)* *(ii)* -	1400±300 1800±400 -	2.8 1.0 -	A6.1
Tube spinning at 5Hz	Sample raised 7mm	-	-	-	-	
	Sample at standard depth	4.17	*(i)* *(ii)* *(iii)*	1500±300 1600±600 2500±500	5.2 1.7 1.3	A6.1
	Sample lowered 7mm	-	-	-	-	

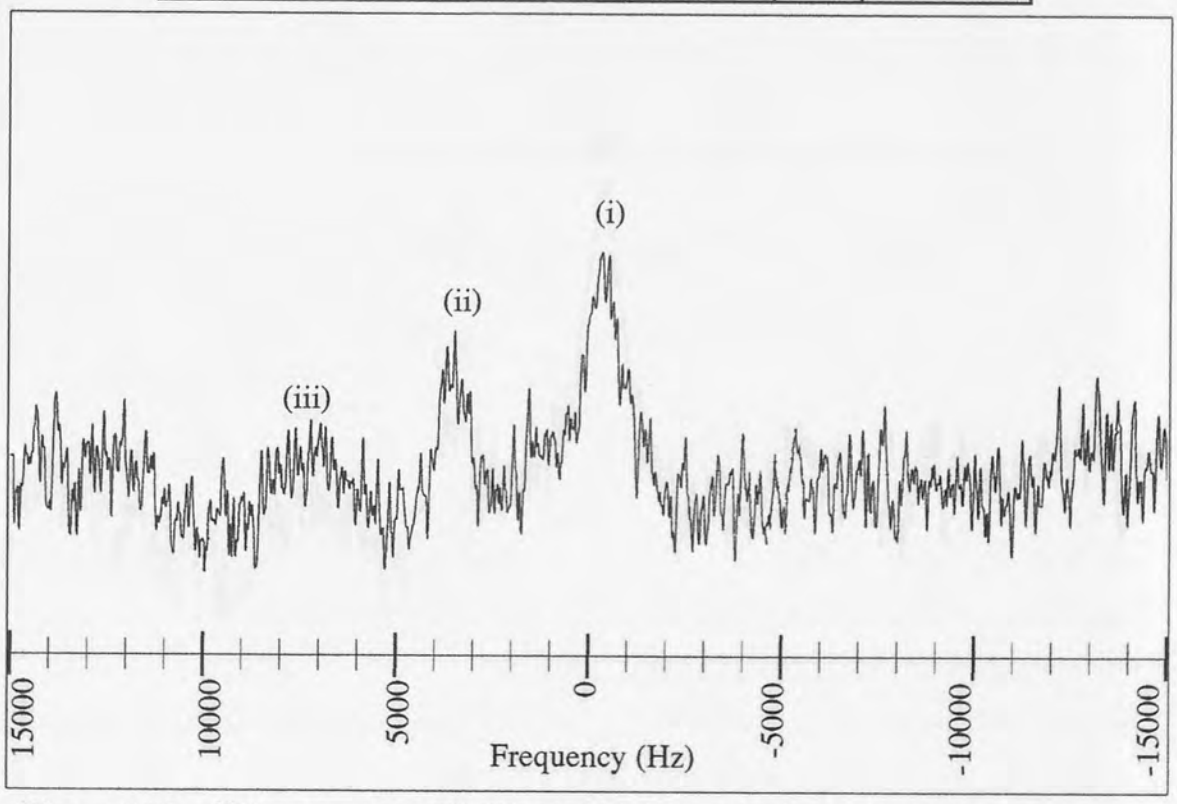

Figure 4.15 : ^{23}Na spectrum of fluidized TSP. (Gas velocity 12 l/min, tube raised 7 mm)

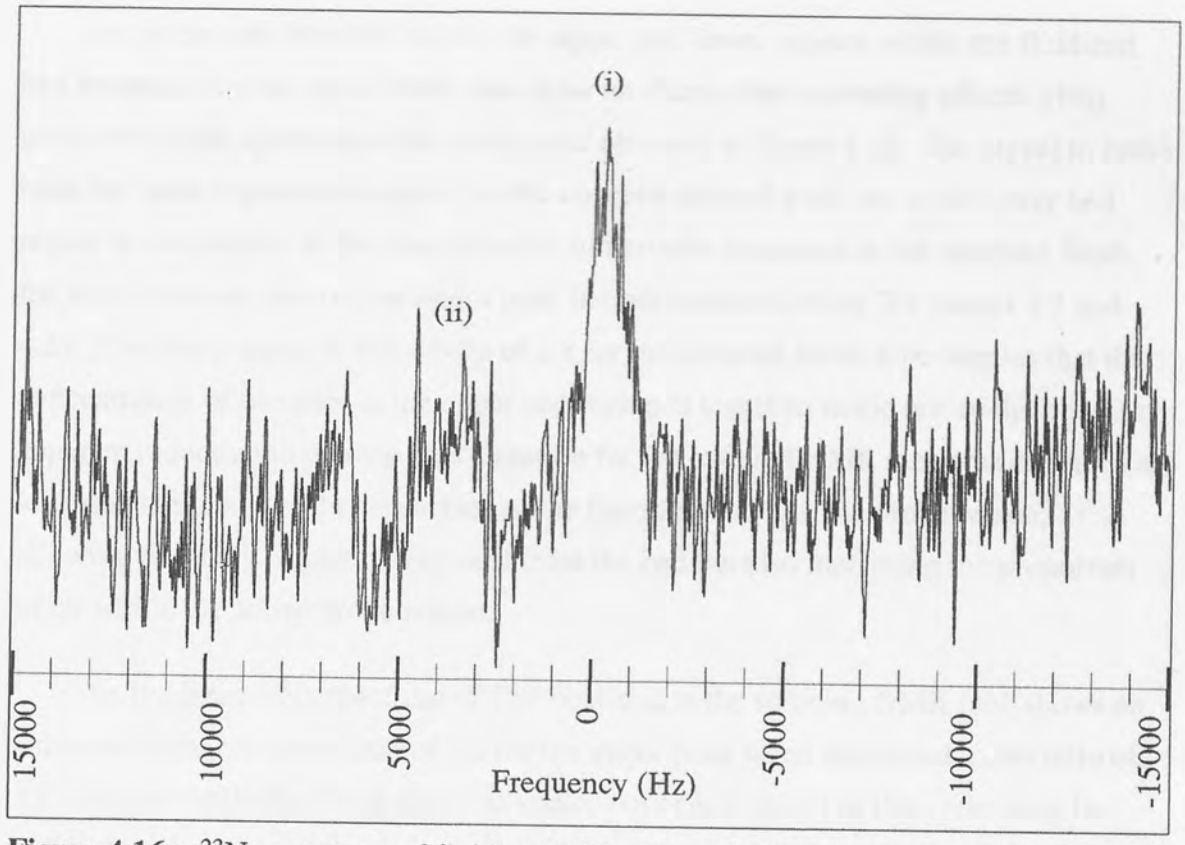

Figure 4.16 : ^{23}Na spectrum of fluidized TSP. (Gas velocity 12 l/min, tube lowered 7 mm)

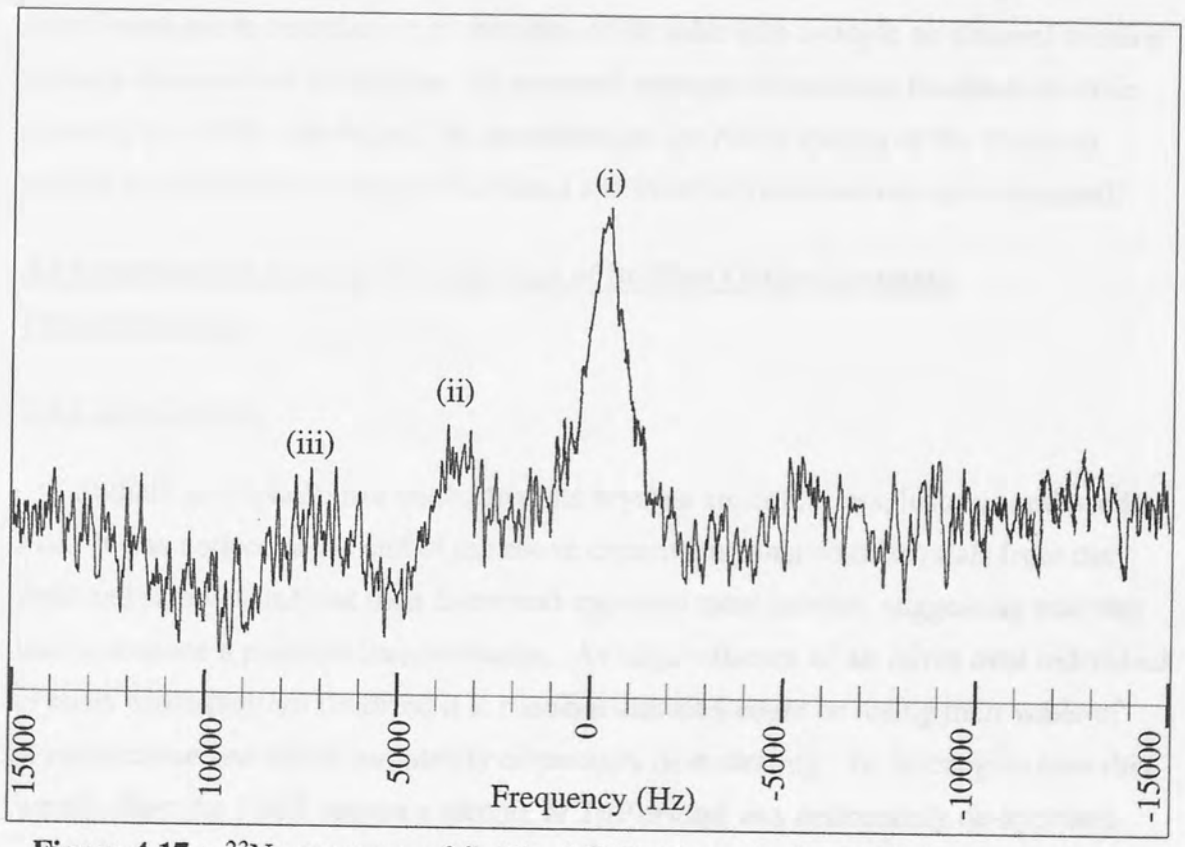

Figure 4.17 : ^{23}Na spectrum of fluidized TSP. (Gas velocity 12 l/min, standard tube position, tube spinning at 5Hz)

As can be seen from the results, the upper and lower regions within the fluidized bed generated by the static NMR tube show no discernible narrowing effects when compared to the spectrum of the static solid obtained in figure 4.10. The signal to noise ratio for these experiments show that the concentration of particles in the lower bed region is comparable to the concentration of particles measured at the standard depth, the signal to noise ratio of the major peak in both instances being 3.9 (tables 4.3 and 4.2). The lower signal to noise ratio of 2.8 for the lowered NMR tube implies that the concentration of particles in the upper bed region is less than in the rest of the bed. An apparent reduction in particle concentration for the lowered NMR tube was expected as lowering the tube bought the surface of the fluidized bed into the probe region, allowing the study of particles ejected from the bed but also increasing the proportion of air within the active probe region.

The fluidized ^{23}Na spectrum of TSP obtained in the spinning NMR tube shows an enhanced signal to noise ratio of 5.2 for the major peak when compared to the ratio of 3.9 obtained while the NMR tube was static. An enhancement of this order may be indicative of an emerging narrowing mechanism, any reduction in line width being masked by the superimposed spectral noise. However, on closer inspection of the spinning NMR tube, the TSP sample was found to have de-fluidized during the NMR experiment and to be adhering to the sides of the tube with a single air channel running through the centre of the sample. As repeated attempts to maintain fluidization while spinning the NMR tube failed, the acquisition of the NMR spectra of the fluidized sample with the tube rotating in the raised and lowered positions was not attempted.

3.4 Investigation into the De-hydration of Sodium Orthophosphate Dodecahydrate.

3.4.1 Introduction.

Sodium orthophosphate dodecahydrate crystals are colourless, lustrous and needle like. It was noticed at the end of the above experiments that some crystals from the fluidized samples had lost their lustre and appeared more opaque, suggesting that they had undergone a physical transformation. As large volumes of air move over individual crystals while they are fluidized it is possible that they could be losing their water of crystallization and either completely or partially de-hydrating. To investigate how this would effect the NMR spectra a sample of TSP crystal was deliberately de-hydrated.

3.4.2 Experimental.

A 2.276g sample of un-graded TSP crystals was placed on a watch-glass and left in a silica-gel loaded desiccator. After 24 hours the sample was removed from the desiccator, found to weigh 2.132g and then placed in a PTFE NMR tube where upon a ^{23}Na and a ^{31}P spectrum were obtained.

For comparison the ^{23}Na and ^{31}P spectra of commercially available anhydrous tri sodium phosphate were obtained under conditions identical to those used in the examination of the partially de-hydrated TSP sample. Under these conditions both the ^{23}Na and ^{31}P spectra of anhydrous tri sodium phosphate showed no discernible peaks, the resonances presumably being exceptional broad when compared to the spectral window.

3.4.3 Results and Discussion.

Table 4.4 summarises any spectra obtained in this section:

Table 4.4 : Summary of spectra of partially de-hydrated TSP.

^{23}Na			^{31}P		
Figure	FWHM (Hz)	Acquisition parameters	Figure	FWHM (Hz)	Acquisition parameters
4.18	250±40	A6.3	4.19	5300±600	A6.4

As stated above the mass of the TSP sample reduces from 2.276g to 2.132g. Assuming that this weight is lost from the TSP solely by the removal of water from the crystal lattice then this corresponds to a change in the empirical formula of the sample from $Na_3PO_4 \cdot 12H_2O$ (RMM = 380.12475) to $Na_3PO_4 \cdot (H_2O)_{10.6}$.

It can be seen in figures 4.10 and 4.11, that the ^{23}Na and ^{31}P solid state NMR spectra of the sample prior to de-hydration each show characteristically broad absorptions. Whereas dehydration appears to have no effect on the ^{31}P spectrum of the solid (figure 4.19), it has a dramatic effect on the ^{23}Na spectrum (figure 4.18) transforming the broad absorption into one that is narrow and well resolved, with no baseline distortion. As this narrowed line does not feature in the NMR spectra of anhydrous TSP this phenomena must be a feature of the partially de-hydrated sites within the lattice.

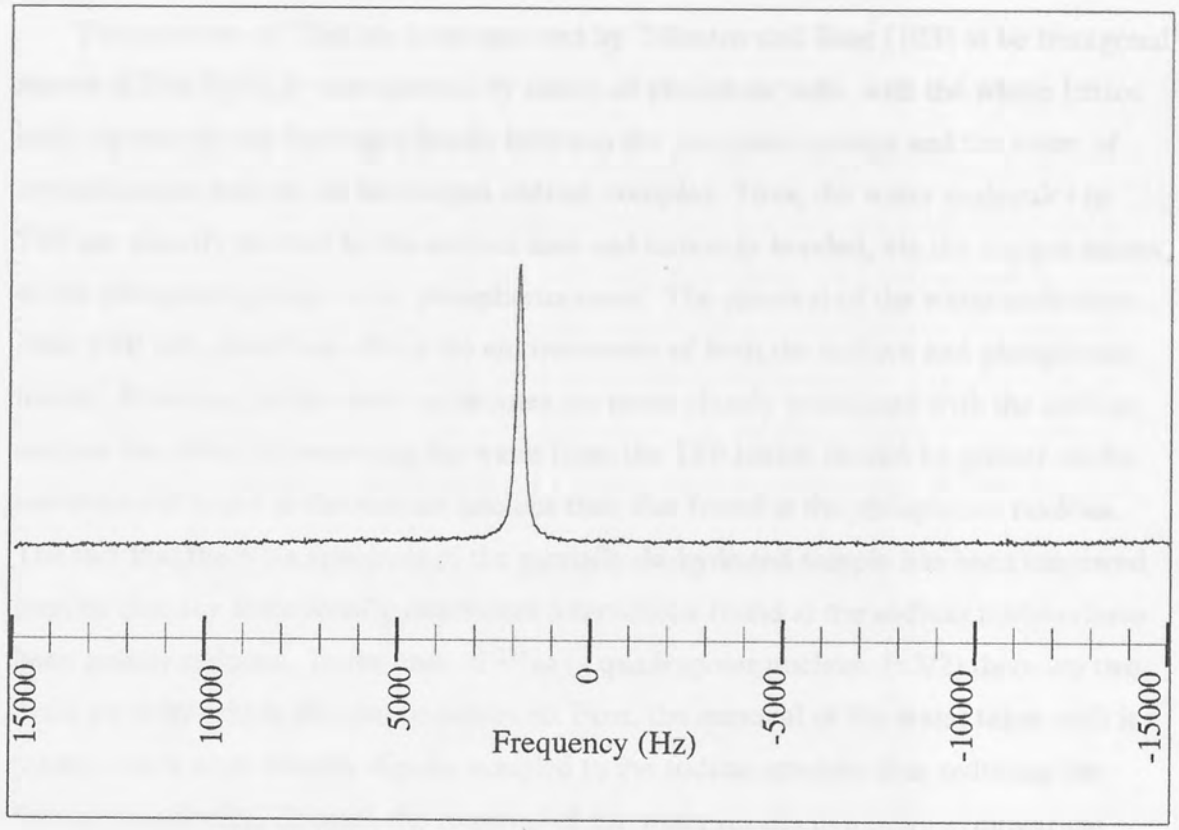

Figure 4.18 : ^{23}Na spectrum of partially dehydrated TSP.

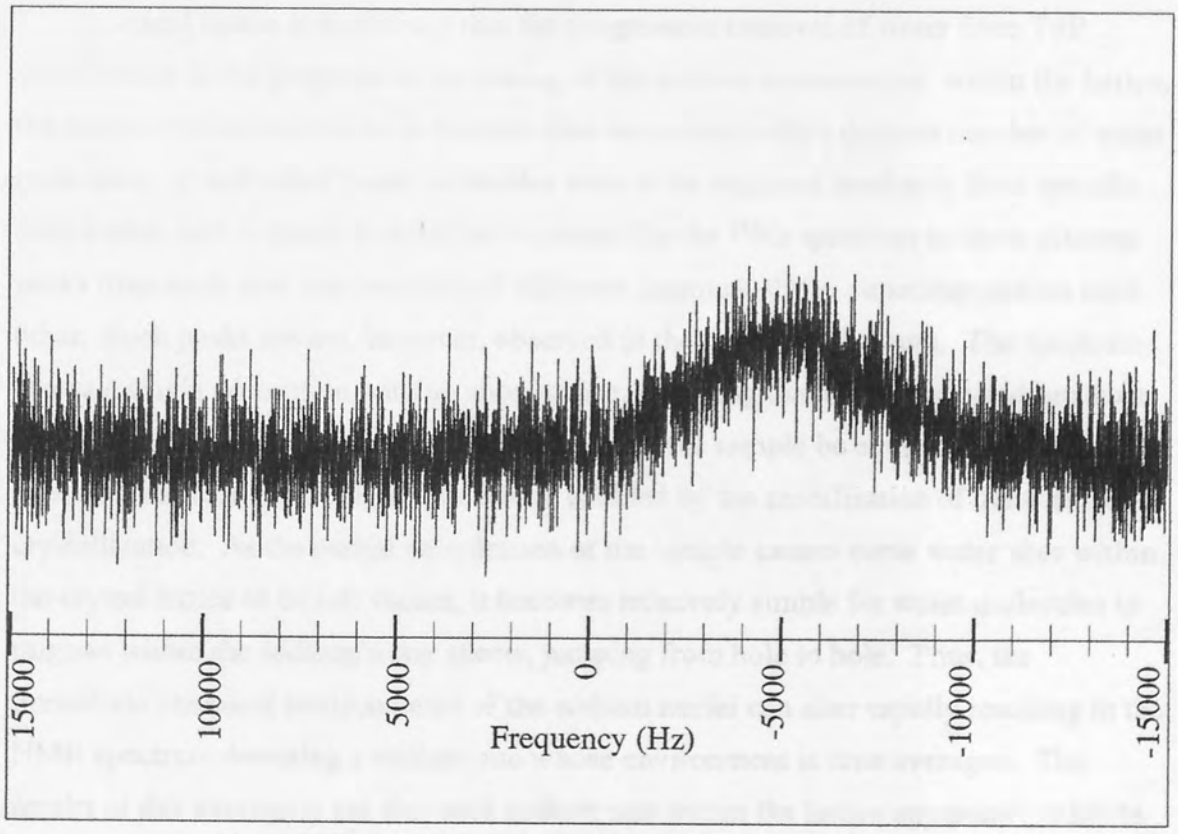

Figure 4.19 : ^{31}P spectrum of partially dehydrated TSP.

The structure of TSP has been reported by Tillmans and Baur [123] to be hexagonal sheets of $[Na(H_2O)_6]^+$ interspersed by sheets of phosphate ions, with the whole lattice held together by the hydrogen bonds between the phosphate groups and the water of crystallization held in the hexa-aqua sodium complex. Thus, the water molecules in TSP are directly bonded to the sodium ions and remotely bonded, via the oxygen atoms of the phosphate group, to the phosphorus atom. The removal of the water molecules from TSP will, therefore, affect the environments of both the sodium and phosphorus nuclei. However, as the water molecules are more closely associated with the sodium nucleus the effect of removing the water from the TSP lattice should be greater on the environment found at the sodium nucleus than that found at the phosphorus nucleus. The fact that the ^{23}Na spectrum of the partially de-hydrated sample has been narrowed implies that any directionally dependent interactions found at the sodium nucleus have been greatly reduced. In the case of ^{23}Na (a quadrupolar nucleus, I=3/2) there are two main ways by which this can be achieved. First, the removal of the water takes with it nuclei which were directly dipolar coupled to the sodium nucleus thus reducing the dipolar broadening. Second, the removal of the water results in a more symmetrical electric field gradient about the sodium nucleus, thus reducing any quadrupolar broadening.

In a rigid lattice it is unlikely that the progressive removal of water from TSP would result in the progressive narrowing of the sodium resonance as, within the lattice, the sodium nuclei must exist in discrete sites associated with a definite number of water molecules. If individual water molecules were to be removed randomly from specific sites within such a lattice it would be expected for the ^{23}Na spectrum to show discrete peaks from each new site, possibly of different chemical shifts, superimposed on each other. Such peaks are not, however, observed in the detected spectrum. The spectrum shows a single adsorption with no shouldering, requiring that the discrete sodium sites generated within the lattice by the dehydration of the sample be equivalent. It is possible that such an averaging process is enabled by the mobilisation of the water of crystallization. As the partial dehydration of the sample causes some water sites within the crystal lattice to be left vacant, it becomes relatively simple for water molecules to migrate within the sodium/water sheets, jumping from hole to hole. Thus, the immediate chemical environments of the sodium nuclei can alter rapidly resulting in the NMR spectrum detecting a sodium site whose environment is time averaged. The results of this averaging are that each sodium site within the lattice apparently exhibits the same chemical shift and that any anisotropic interactions between the sodium nuclei and the water molecules are approximated to zero. Thus, mobile water moieties within

the crystal lattice should result in an NMR spectrum composed of a single, relatively narrow adsorption.

The results, therefore, suggest that the partial dehydration of TSP results in a crystal lattice in which the water molecules are mobile and that the transition from a bound lattice to a mobile lattice is relatively easy to achieve. Furthermore, it is expected that dehydration of the sample does not cause a progressive narrowing of the solid peak, rather a narrowed peak forms which is superimposed on the broad peak. Thus, the dehydration of TSP induced by the action of the fluidizing gases should manifest itself as a new, narrow resonance superimposed on the static solid resonance.

The ^{23}Na signal from the de-hydrated TSP has a FWHM value of 250±50Hz. This value is similar to that of the 88Hz line width observed in the SINNMR experiment. It therefore raises the possibility that the line narrowing observed in the SINNMR of TSP occurs simply as a result of the de-hydration of the sample. Although this may be a contributory factor in the ^{23}Na SINNMR spectra of TSP the fact that de-hydration of the TSP sample has no effect on its ^{31}P spectra, whilst SINNMR reduces the line width by 99.5%, demonstrates that other mechanisms are in operation during the SINNMR experiment. Also it may be inferred that the other mechanisms in SINNMR are responsible for reducing the FWHM of the ^{23}Na resonance to 88Hz, either from 250Hz or from the static sample value. The ^{31}P T_1 measurements made by Howard strongly indicate that the 'other mechanisms' are indeed incoherent particle motion with a correlation time of ca. 10^{-7}s. The present work, therefore, lends support to the conclusion that SINNMR is a genuine phenomenon.

Chapter 4

The Fluidization of Aluminium Granules.

4.1 Introduction

Previously, apart from studies of TSP, other successful and most definitive SINNMR experiments have been performed through studies of aluminium particles [122]. In a typical SINNMR experiment the incoherent averaging imposed on the constituent particles is believed to be caused directly by ultrasonic phenomena. However, in SINNMR studies of aluminium particles, it was believed that in addition to ultrasonic contributions to incoherent averaging there existed a mechanism whereby eddy currents, generated in the aluminium particles by their motion through a magnetic field, caused particle re-orientations which contributed to the narrowing mechanisms. The possibility that such motions could also be generated in a fluidized bed lead, therefore, to the investigation of fluidized beds of aluminium particles. As grinding aluminium is difficult the investigation was limited to monitoring the behaviour of a fluidized bed composed of a single range of particle sizes by measuring the ^{27}Al spectra at different positions within the fluidizing NMR tube.

4.2 Investigation into the Differences in Fluidization Conditions Within the Fluidized Bed and their Effect on the NMR Spectra of Aluminium Particles.

4.2.1 Introduction.

In the SINNMR experiment it was first necessary to encapsulate the aluminium particles in a non-reactive resin to protect the aluminium from the reactive support liquid. As the support media used in SINNMR is redundant in gas fluidized beds this process was omitted and the aluminium particles were left un-coated. Consequently, a fluidized bed of aluminium particles was investigated in an analogous manner to the investigation of TSP in section 3.3.

4.2.2 Experimental.

Grading the sample of aluminium resulted in the production of a 500μm to 210μm fraction only. Using this sample the fluidizing NMR tube was filled to a depth of 17mm, positioned within the NMR probe such that the surface of the static sample coincided with the middle of the 14mm active region of the probe, and an ^{27}Al spectrum of the static solid obtained. The airflow to the probe was set to 12litres/min and two further ^{27}Al spectra were obtained, one with a stationary NMR tube and one with the tube spinning at 5Hz. Further ^{27}Al spectra of the fluidized bed were then obtained with the NMR tube raised and then lowered by 7mm, spectra being obtained

with the tube stationary and spinning at 5Hz in each instance.

4.2.3 Results and Discussion.

Table 4.5 documents the spectra obtained in this section.

Table 4.5 : ^{27}Al spectra of aluminium particles contained in the fluidizing NMR tube.

		Static tube		Tube spinning at 5Hz	
		Figure	Acquisition parameters	Figure	Acquisition parameter
Static solid	Sample at standard Depth	4.20	A6.5	-	
Fluidized bed (12 l/min)	Sample raised 7mm	4.23	A6.5	4.25	A6.5
	Sample at standard Depth	4.21	A6.5	4.24	A6.5
	Sample lowered 7mm	4.22	A6.5	4.26	A6.5

The ^{27}Al spectrum (figure 4.20) of the static solid aluminium powder shows a characteristically broad absorption which has a FWHM of 11,500 ± 400Hz. On fluidization the resulting ^{27}Al spectrum (figure 4.21) shows a distorted static-aluminium like resonance which appears to have a FWHM of 5700 ± 300Hz, an apparent reduction in line width of 50%. When the fluidized bed is then lowered by 7mm to allow investigation of the top of the fluidized bed, the resulting aluminium spectrum (figure 4.22) once again resembles the static solid aluminium spectrum (figure 4.20), but shows a FWHM of 5300 ± 200Hz corresponding to an reduction in linewidth of 54%.

The remaining spectra, which in practice were obtained after those already discussed (the exact order listed in table 4.6), show complex features which neither resemble the resonance obtained from the static solid or show any common features within themselves.

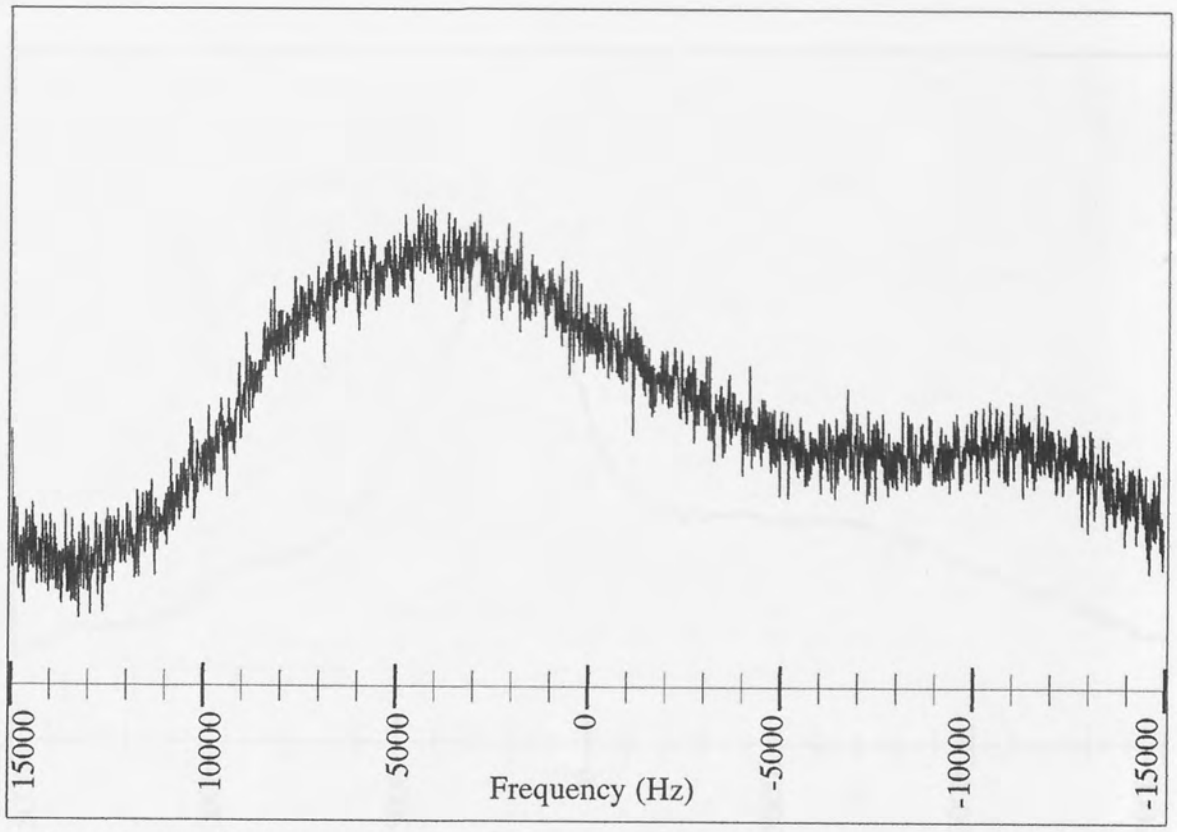

Figure 4.20 : ^{27}Al spectrum of static aluminium granules in the fluidizing NMR tube (Normal tube depth).

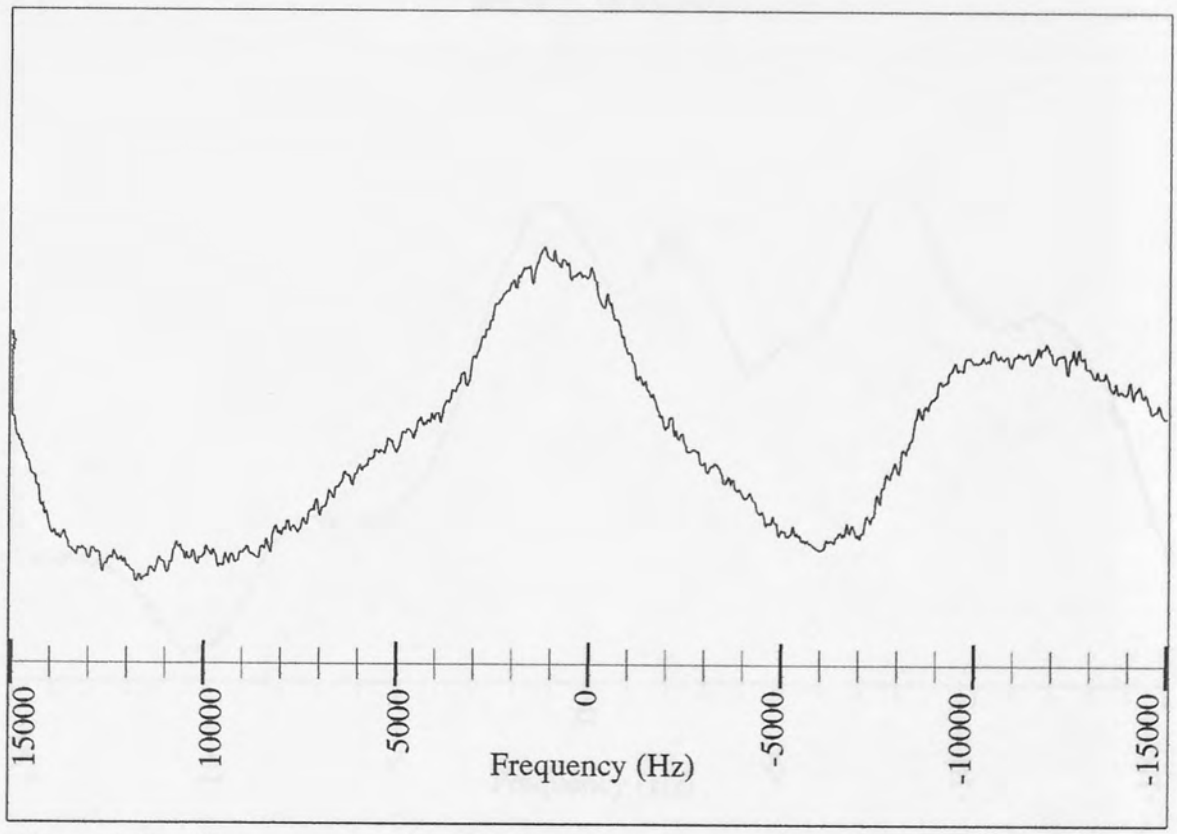

Figure 4.21 : ^{27}Al spectrum of fluidized aluminium granules. (Normal tube depth, gas flow 12 l/min)

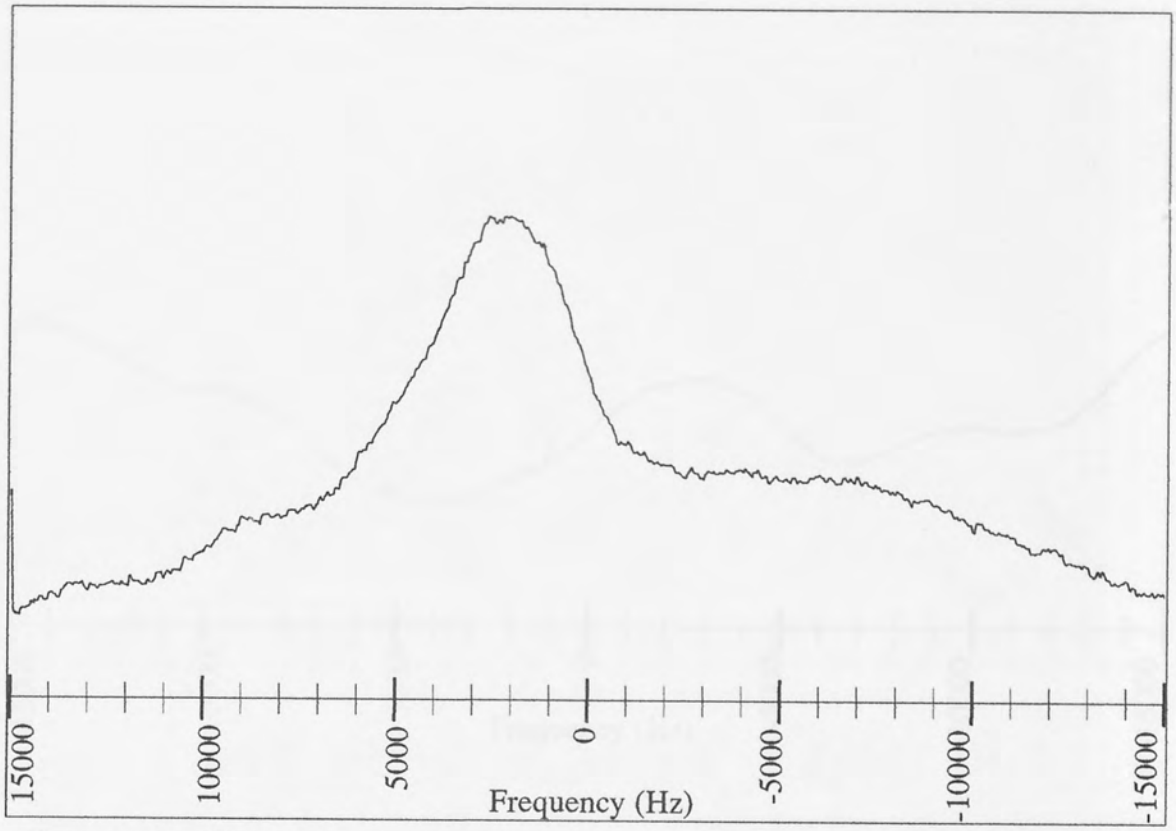

Figure 4.22 : ^{27}Al spectrum of fluidized aluminium granules. (Tube lowered by 7mm, gas flow 12 l/min)

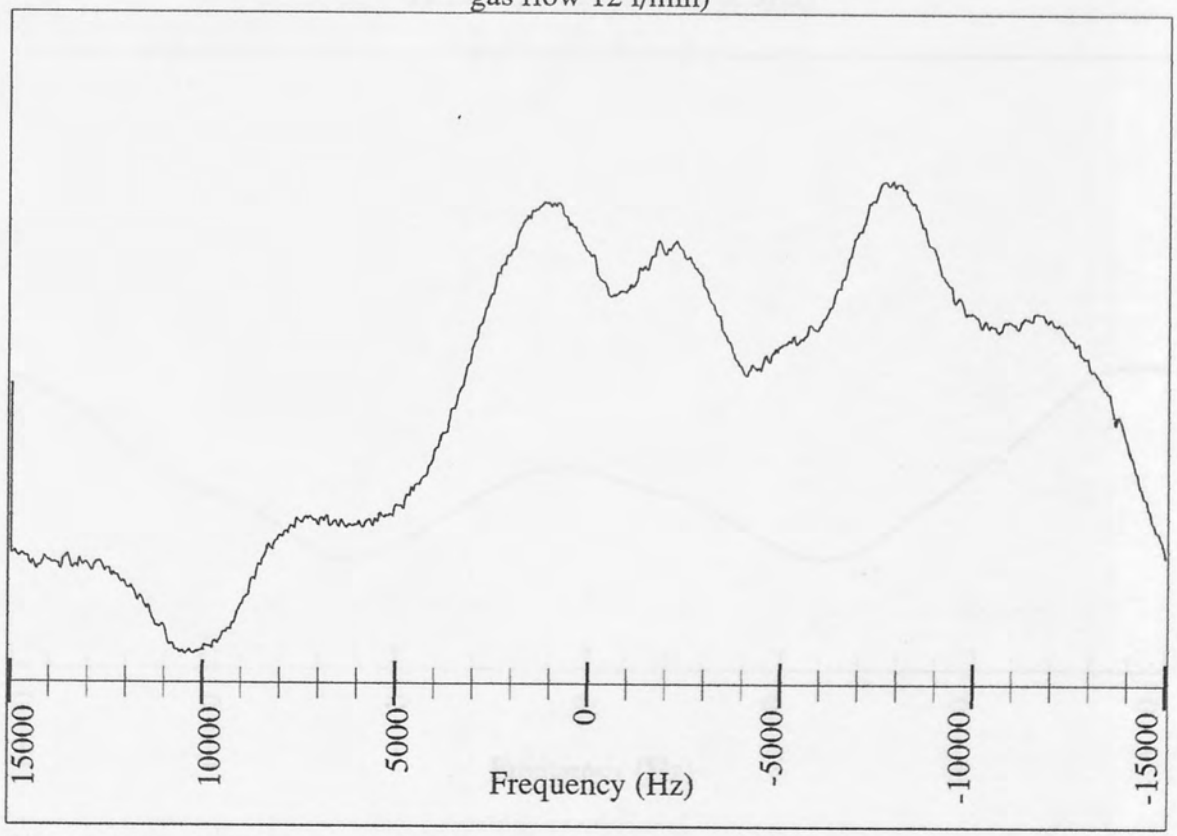

Figure 4.23 : ^{27}Al spectrum of fluidized aluminium granules. (Tube raised by 7mm, gas flow 12 l/min)

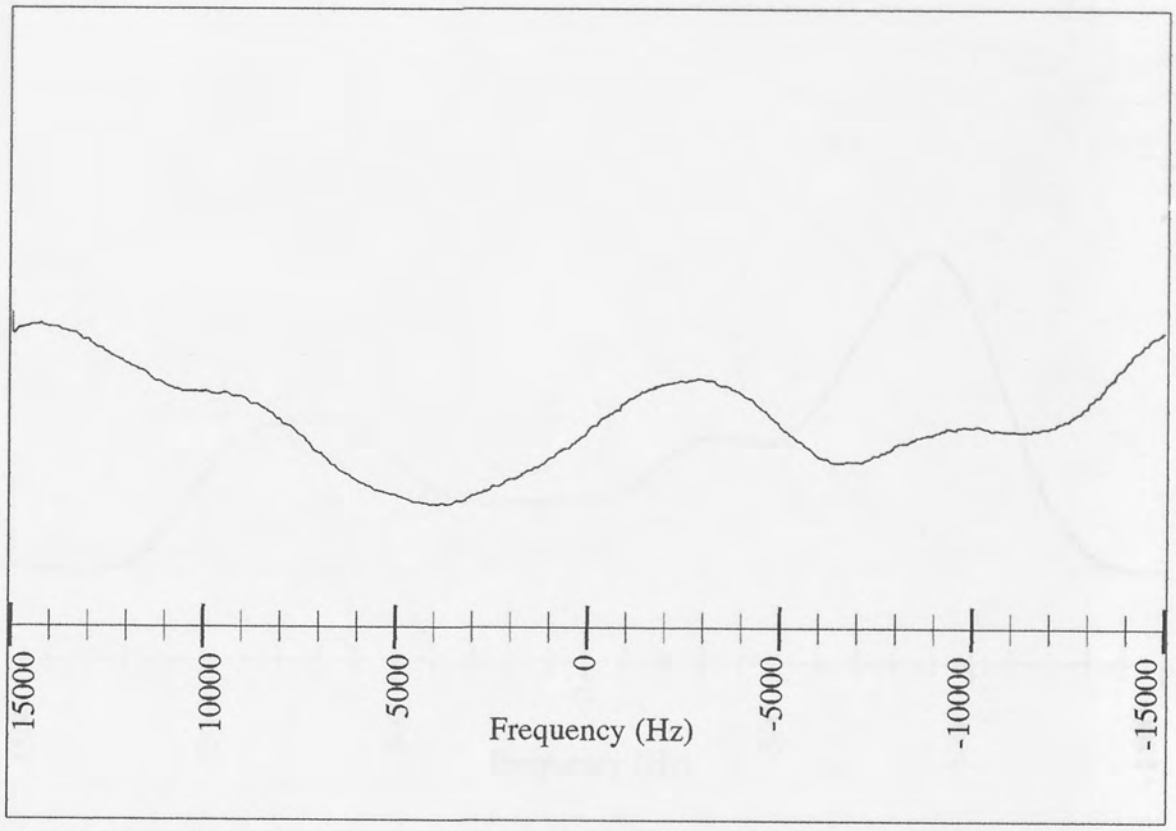

Figure 4.24 : ^{27}Al spectrum of fluidized aluminium granules. (Normal tube depth, flow 12 l/min, tube spinning at 5Hz)

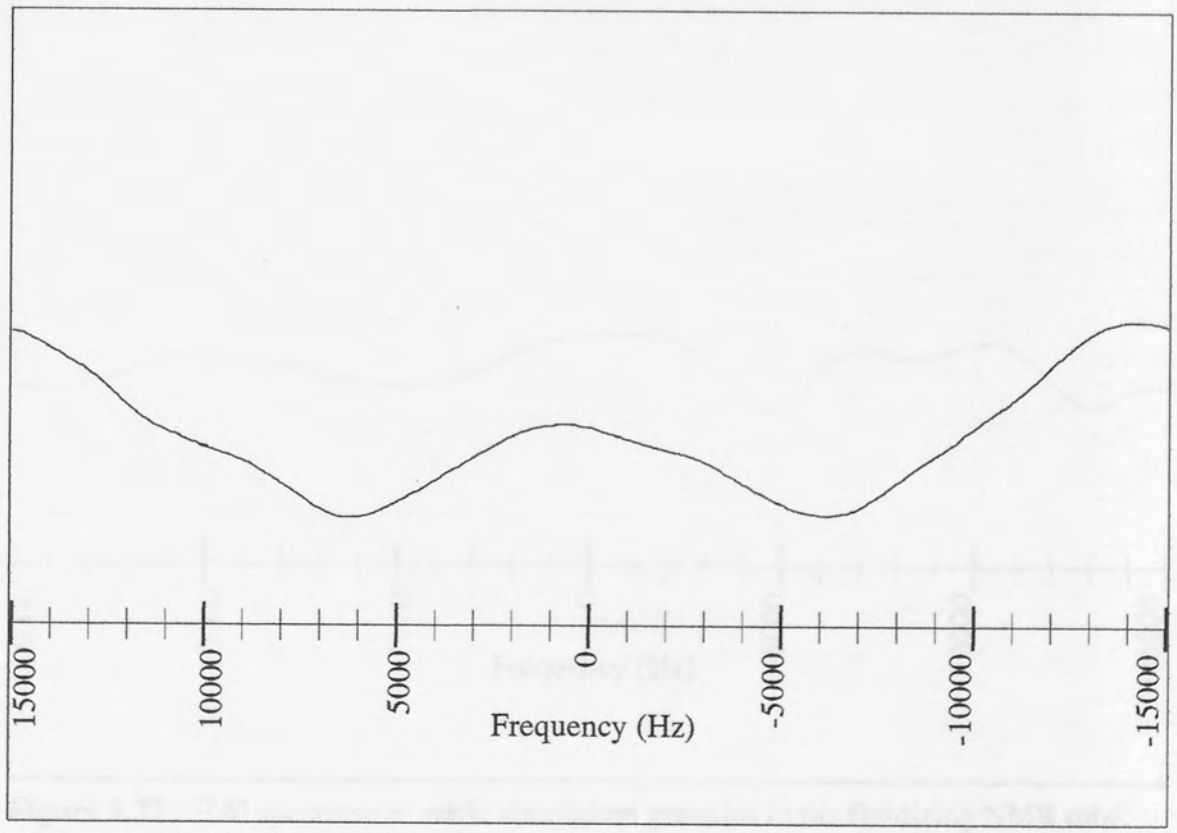

Figure 4.25 : ^{27}Al spectrum of fluidized aluminium granules. (Tube raised by 7mm, flow 12 l/min, tube spinning at 5Hz)

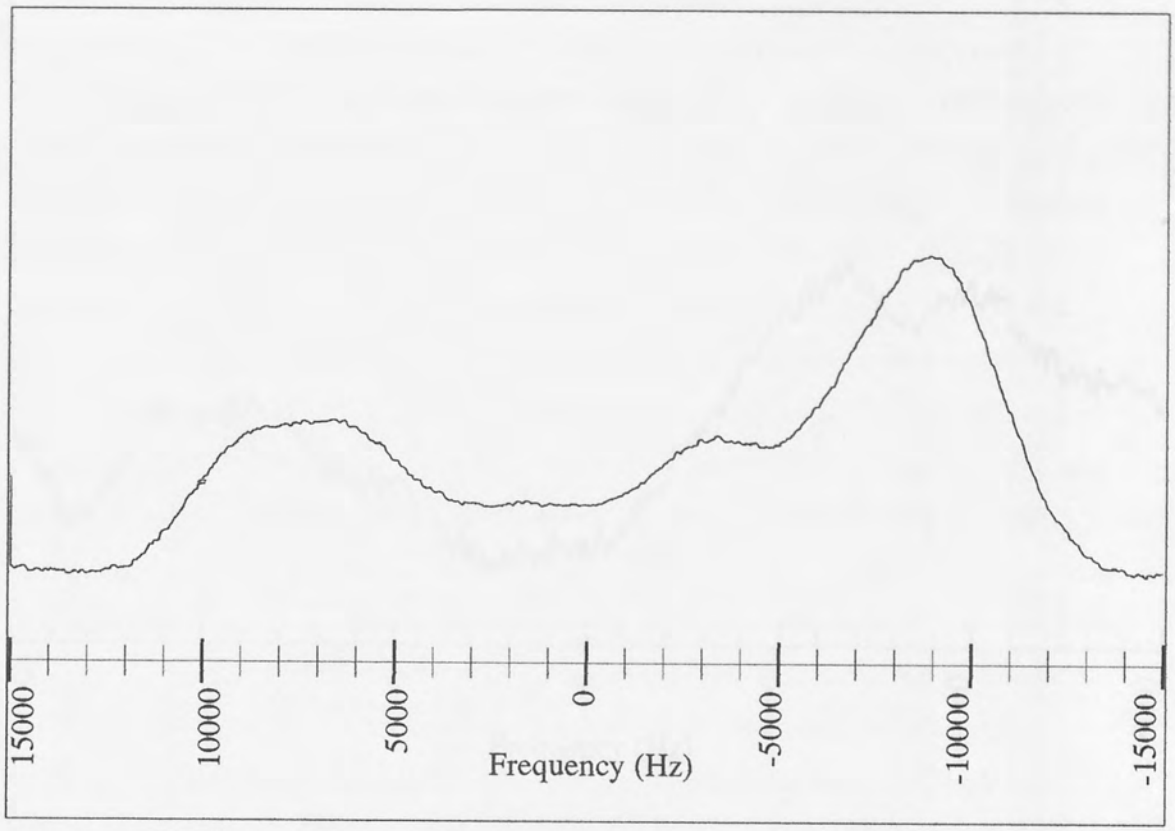

Figure 4.26 : ^{27}Al spectrum of fluidized aluminium granules. (Tube lowered by 7mm, flow 12 l/min, tube spinning at 5Hz)

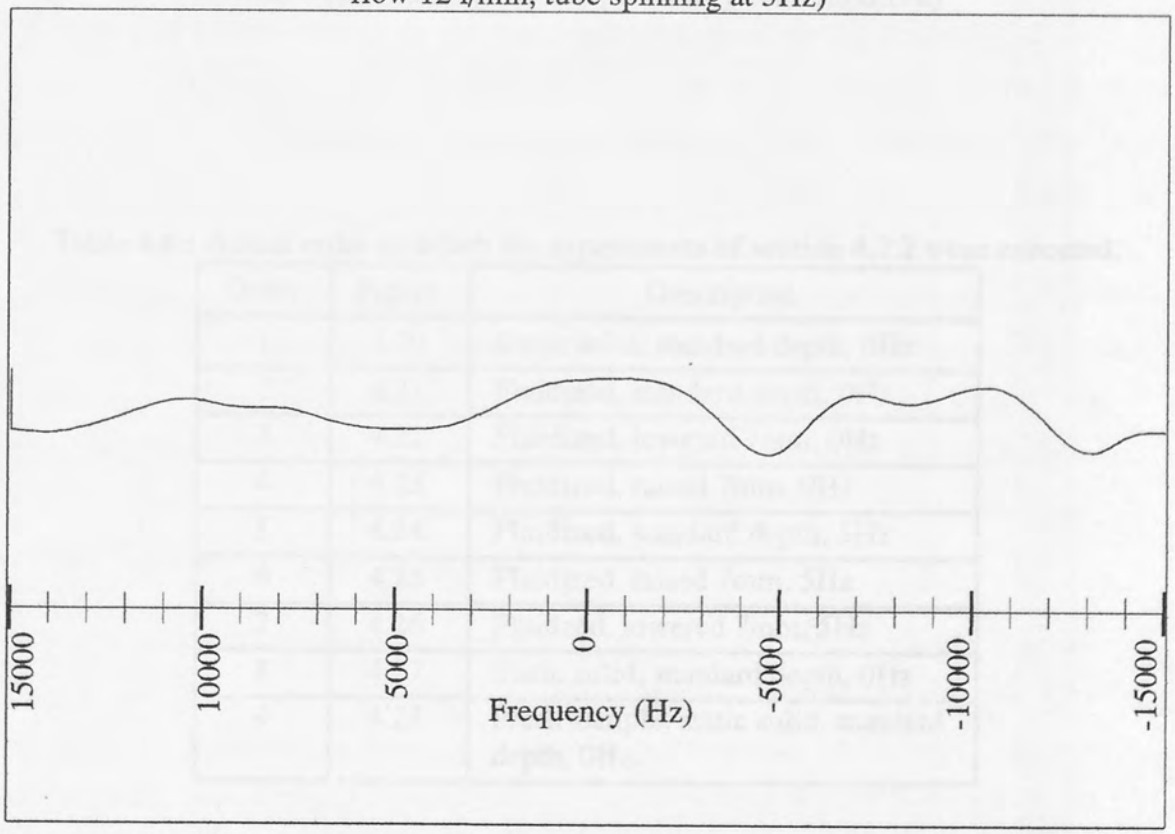

Figure 4.27 : ^{27}Al spectrum of static aluminium granules in the fluidizing NMR tube. (The sample was that used to obtain the spectra in figures 4.20 - 4.26)

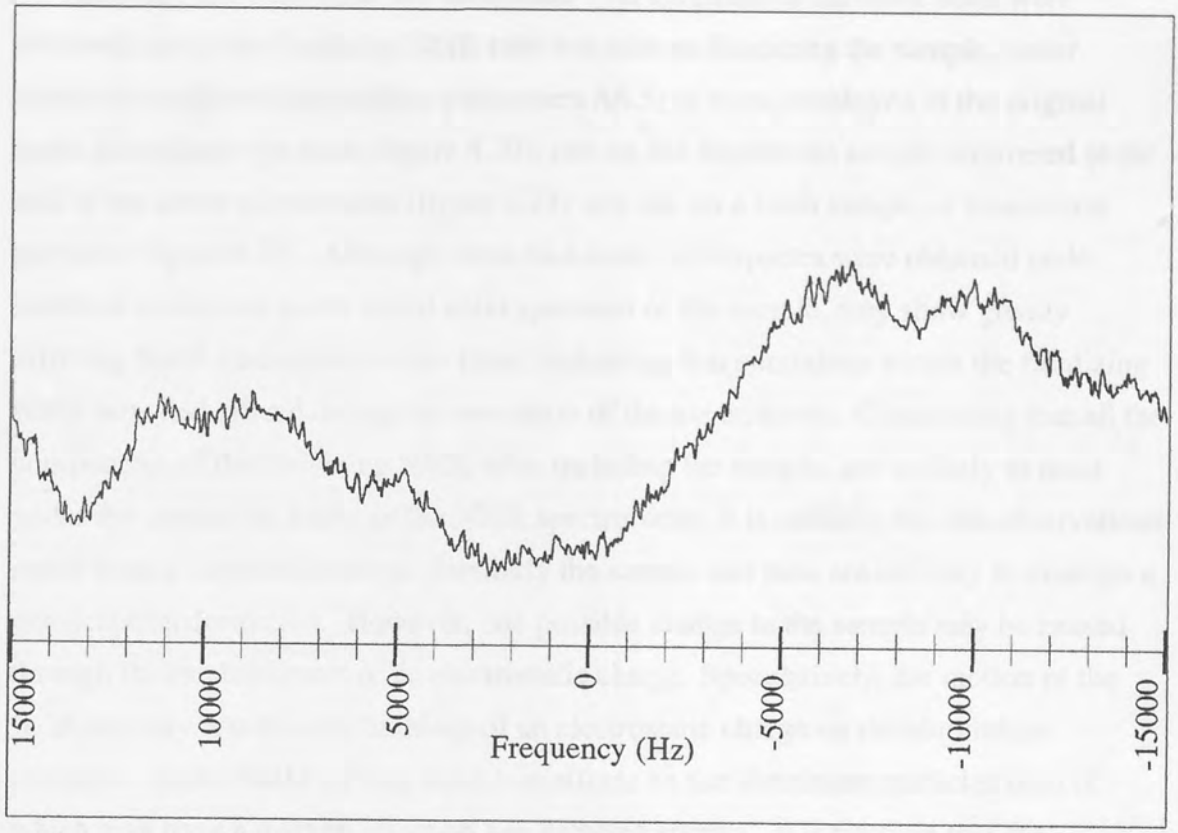

Figure 4.28 : ^{27}Al spectrum of fluidized aluminium granules in the fluidizing NMR tube. (The sample had not previously been fluidized)

Table 4.6 : Actual order in which the experiments of section 4.2.2 were executed.

Order	Figure	Description
1	4.20	Static solid, standard depth, 0Hz
2	4.21	Fluidized, standard depth, 0Hz
3	4.22	Fluidized, lowered 7mm, 0Hz
4	4.23	Fluidized, raised 7mm, 0Hz
5	4.24	Fluidized, standard depth, 5Hz
6	4.25	Fluidized, raised 7mm, 5Hz
7	4.26	Fluidzed, lowered 7mm, 5Hz
8	4.27	Static solid, standard depth, 0Hz
9	4.28	Fresh sample, static solid, standard depth, 0Hz.

To study this behaviour two additional ^{27}Al spectrum of the static solid were obtained, using the fluidizing NMR tube but without fluidizing the sample, under identical conditions (acquisition parameters A6.5) to those employed in the original static aluminium spectrum (figure 4.20); one on the aluminium sample recovered at the end of the above experiments (figure 4.27) and one on a fresh sample of aluminium particles (figure 4.28). Although these two static solid spectra were obtained under identical conditions to the initial solid spectrum of the sample, they show greatly differing NMR absorptions to the latter, indicating that conditions within the fluidizing NMR tube had altered during the execution of the experiments. Considering that all the components of the fluidizing NMR tube, including the sample, are unlikely to react under the conditions found in the NMR spectrometer, it is unlikely that the observations result from a chemical change. Similarly the sample and tube are unlikely to undergo a physical transformation. However, one possible change to the sample may be caused through the establishment of an electrostatic charge. Speculatively, the motion of the fluid bed may result in the build-up of an electrostatic charge on the aluminium particles. Such a build-up may have two effects on the aluminium particles both of which may have a marked effect on any detected spectra. It is possible that the population of electrons in the conductance band may change altering the Knight shift [24, 25, 124] contribution to the chemical shift. Alternatively the symmetry of any electric field gradients may change which, as aluminium has a nuclear spin of 5/2, alters the quadrupolar line broadening interactions. Attention must also be drawn to the fact that the NMR of aluminium granules is subject to skin depth effects, caused by the rapid dissipation of the investigative r.f. waves providing the $\mathbf{B_1}$ magnetic field during their passage into the aluminium granules, and results in only the surface 'skin' of the granules featuring in the detected spectra. Any electrostatic charge which forms on the aluminium granules will be associated mainly with the surface of the granules. It is, therefore, probable that due to the skin depth effects, the establishment of an electrical charge on the aluminium granules will have a disproportionately large effect on any detected spectra.

The static aluminium spectra taken after the above experiment on the original sample and on a fresh sample show similar line shapes, with the fresh sample showing a slightly poorer signal to noise ratio. One explanation for this would be for any electrostatic charge which formed on the initial aluminium sample to persist on the interior surface of the fluidizing NMR tube while the sample was changed. If this charge was transferred to the fresh aluminium sample when it was introduced to the NMR tube, a similar electrostatic interaction could be induced in the aluminium

granules and result in a ^{27}Al spectra similar to that produced by the sample previously subject to fluidization, albeit of reduced intensity.

Visual inspection of the spectra shows that as the experiments progress the distortion of the NMR signal increases slowly while the noise decreases. This suggests that electrical charges are established slowly on the aluminium granules over a number of experiments. If this is truly the case then any variations in the line shapes of the spectra detected during the initial fluidization experiments (subjectively the first two) are solely attributable to the motions imparted on the aluminium granules by the fluidized bed. Under such an assumption the comparison of the initial spectrum of the static aluminium granules (figure 4.20) and the first two spectra obtained from the fluidized bed (figures 4.21 and 4.22) is allowed and shows that the motional characteristics of the fluidized bed are such that the solid spectrum of the aluminium granules is narrowed by *ca.* 50%.

Chapter 5

Discussion of Fluidized Bed NMR Spectroscopy.

5.1 Discussion of Fluidized Bed NMR Spectroscopy.

The investigation into fluidized beds was initiated as it appeared to have the potential of overcoming some of the difficulties experienced in the SINNMR experiments, namely, solvent interaction with the solid suspension, matching the density of the support liquid to that of the solid, and the avoidance of reactive support liquids. All of these potential problems with SINNMR stem from its dependence on a support liquid to transfer the ultrasound from the ultrasonic transducer to the individual solid particles. In a gas fluidized bed such problems cannot normally occur as the 'support' media is simply air flowing through the sample. However, it is clear from the experiments reported in this section that the use of a fluidized bed in NMR brings with it unique problems; namely sample hydration/de-hydration and perhaps more seriously the possible establishment of an electrostatic charge.

Unfortunately both the ^{23}Na and ^{31}P spectra of TSP show no narrowing effects while fluidized. Given the difficulties encountered during the investigation of TSP this is probably indicative of a poorly fluidized sample rather than of the inability of the technique to narrow spectra.

The experiment involving the dehydration of TSP gave results which were of significant importance demonstrating that, through dehydration, the narrowing of TSP spectra could be achieved. Conceivably a sample of TSP investigated by SINNMR could undergo a similar dehydration to which the observed line-narrowing could be solely attributed. Although the dehydration of the sample in SINNMR may contribute to line-narrowing, the dehydration experiment demonstrated that such a phenomena could not solely account for the observed reduction in SINNMR line width. This observation lends further support to the contention that it is through the incoherent motion of the solid particles, induced by ultrasonic irradiation, that SINNMR achieves narrowed solid state spectra.

In contrast to the TSP experiment the results of section 4.2 for the aluminium fluidized beds do, however, imply that fluidized beds are capable of imparting motional characteristics to their constituent particles which can lead to a partial narrowing of their spectra. Although at *ca.* 50% this is a significant line width reduction, it is less than the *ca.* 98% line width reduction attained by SINNMR (resulting in a FWHM of 358Hz) on a similar sample.

Anticipating motional similarities between the particles in SINNMR and those in fluidized beds, gas flow replacing acoustic pressure, turbulence effects mimicking the action of cavities, interparticle collisions common to both, the investigation in this section was limited to those substances which are readily observed using SINNMR. Given that such similarities need not in fact exist it is suggested that investigation into fluidized beds continues, test samples being drawn from across the range of organic/ inorganic compounds, regardless of their amenability to the SINNMR technique. To assist in their fluidization appropriate samples should consist of particles that are relatively dense, not needle-like in form, which do not contain any water molecules and which are not hydroscopic. By limiting the NMR investigation to dipolar nuclei alone any effects caused by the build up of an electrostatic charge on the detected spectra should be avoided.

Part 5

New Pulse Sequences for NMR Spectroscopy.

Chapter 1

Introduction to Pulse Sequences.

1.1 Introduction

In part 2 : section 1.10 the factors influencing the frequency and amplitude of the characteristic absorptions found in nuclear magnetic resonance spectroscopy were discussed. The majority of these factors are determined by the nuclear and molecular properties of the NMR sample and cannot be influenced directly. However, one factor that is directly under the control of the NMR spectroscopist is the mode of application of the B_1 magnetic field to the NMR sample. By using pulses of r.f. radiation of appropriate intensity and duration, interspersed by suitably chosen time delays, the NMR spectrum may be manipulated in many different ways resulting in the enhancement, simplification, removal or phase changes of either specified or all absorptions in an NMR spectrum. The exact combination of these pulses and delays is referred to as a pulse sequence and, by the use of an appropriate pulse sequence, it is possible to deduce many of the physical properties of the sample from the interpretation of the resulting spectra. Often these pulse sequences rely on J-coupling and may appear to have little relevance to the study of solids. However, current indications are that many J-coupled based procedures may be translated to dipolar coupled sequences with similar outcome [7]. As in the solid state spectroscopy of dipolar nuclei slow relaxation may be a problem, a method of accelerating relaxation was sought. In the absence of appropriate hardware the approach was to develop an appropriate J-coupled liquid phase sequence in the hope that it might ultimately find use in solid state studies.

In the design and implementation of pulse sequences it is necessary to know the effect on each nuclei of each molecule in the sample caused by each r.f. pulse and time delay. The density operator formalism achieves this by determining the eigenfunctions of the NMR Hamiltonians to give the energy levels of the spin system in terms of a density matrix. By predicting the non-classical evolution of the density matrix using the Liouville-von Neumann equation the exact form of the NMR spin system at each stage of the pulse sequence can be deduced. The Liouville-von Neumann equation which describes the evolution of a density operator σ under the action of a Hamiltonian $\mathcal{H}$ with time is;

$$\frac{d\sigma}{dt} = -\frac{i}{\hbar}[\mathcal{H}(t),\sigma(t)] \qquad (5.1)$$

The density operator formalism is applicable to all NMR spin systems. However, it becomes cumbersome to implement when considering systems involving a large number of spins and, as it accounts for the states of the spin system irrespective of the

observables that will be finally detected, gives little insight into the workings of a pulse sequence. To overcome these problems a variety of other formalisms [125, 126], all approximations of the density operator method, have been developed which cope with specific aspects of the spin systems. Of these, the product operator formalism [42, 127-130] gives the most insight into the workings of pulse sequences while remaining relatively simple to implement.

The remainder of this chapter describes product operator formalism and its implementation in 1 and 2 dimensional NMR pulse sequences.

1.2 Product Operator Formalism

If we consider a spin ½ spin system each spin state can be characterized by the wave functions $|\alpha\rangle$ and $|\beta\rangle$, depending upon whether the spin is parallel or anti-parallel to the applied magnetic field. Considering a system of N spins as a whole, then there must be one wave function which describes the 2^N possible energy levels. (Figure 5.1)

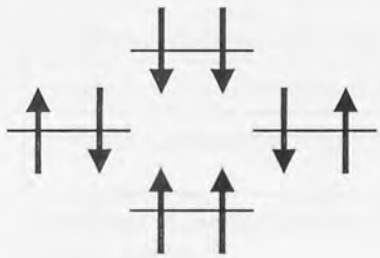

Figure 5.1 : The 4 energy levels of two spin ½ nuclei.

In the case of uncoupled or weakly coupled nuclei this system wide wavefunction is accurately represented by the product of the wavefunctions of the individual nuclei. Strongly coupled nuclei require more complicated wavefunctions.

A density operator σ can be expressed as a linear combination of a set of orthogonal base operators such that;

$$\sigma(t) = \sum_n c_n(t)U_n \qquad (5.2)$$

where U_n represents the orthogonal base operators and $c_n(t)$ the respective constant required to define the density operator. Using the product operators as the base operators the density matrix is split into sub-matrices all of which have a direct physical significance and, by limiting the spins systems to loosely coupled systems, the

relationships between these operators remains simple with no direct matrix manipulation being required. As a result of this, each of the product operators that form the basis of the density matrix are reduced to being no more than labels showing specific components of the spin magnetization. For a spin system involving N spins there are 4^N product operators which describe the whole system, this being all of the combinations of the N sets of four operators describing each spin (the identity, x, y and z operators). For a two spin system, using I and S to depict components from the two different spins (usually referring to a sensitive and insensitive nucleus respectively), these 16 operators and their physical significance are (excluding the identity operator);

Table 5.1 : Product operators for a spin system consisting of two spin ½ nuclei and their physical significance.

Product Operator	Physical Significance
I_z	Longitudinal magnetization of spin I.
I_x	In-phase x magnetization of spin I.
I_y	In-phase y magnetization of spin I.
S_z	Lontgitudinal magnetization of spin S.
S_x	In-phase x magnetization of spin S.
S_y	In-phase y magnetization of spin S.
$2I_xS_x / 2I_yS_y$ $2I_xS_y / 2I_yS_x$	Two-spin coherence of spin I and S.
$2I_xS_z$	antiphase X magnetization of spin I with repect to spin S.
$2I_yS_z$	antiphase Y magnetization of spin I with repect to spin S.
$2I_zS_x$	antiphase X magnetization of spin S with repect to spin I.
$2I_zS_y$	antiphase Y magnetization of spin S with repect to spin I.
$2I_zS_z$	Longitudinal two-spin order of spins I and S.

Where the product operator is made up from a combination of the cartesian operators (these are I_x, I_y and I_z for spin I and S_x, S_y and S_z for spin S) the order in which they are quoted is irrelevant. e.g. $2I_xS_z \equiv 2S_zI_x$.

When using product operator formalism to analyze the effect of a pulse sequence on a spin system, the sequence is first broken down into periods of r.f pulses and time delays. The appropriate transformations for each period in the pulse sequence are then applied to the product operators, the results from one section of the pulse sequence

feeding the transformations in the next section. In most cases the spin system will initially be described by the longitudinal spin operators alone as this represents the system in its Boltzmann equilibrium state. The different product operator transformation related to each period in the pulse sequence are described below.

1.2.1 The effect of R.F Pulses on the Product Operators.

Using the classical vector description of nuclear magnetic resonance spectroscopy it is possible to identify the x,y and z components of a bulk magnetization vector. The application of a B_1 field to the NMR sample causes the bulk magnetization vector to nutate by a specific angle about B_1.

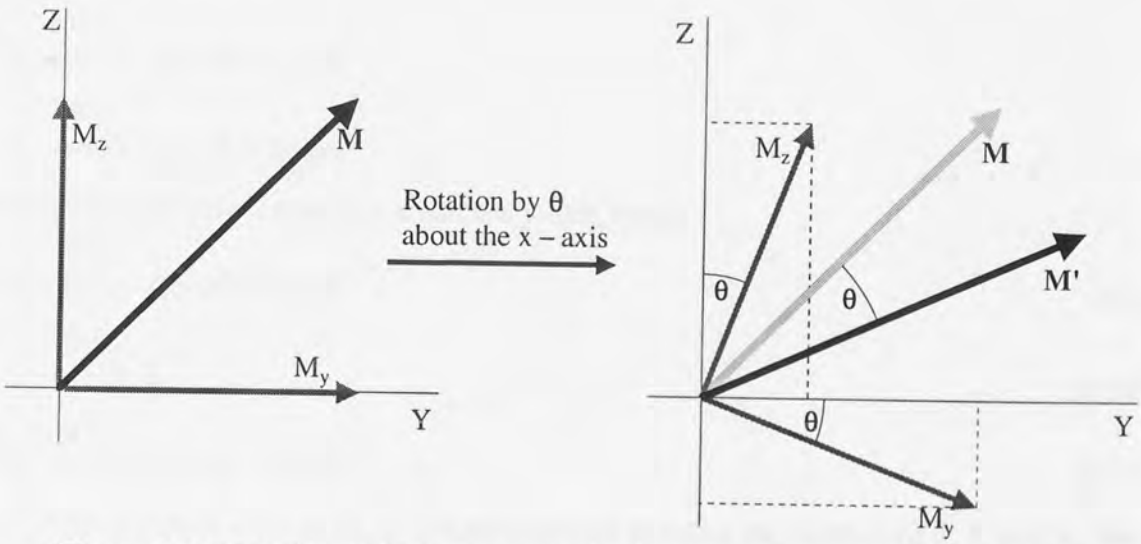

Figure 5.2 : Rotation of the bulk magnetization vector by an angle θ about the x-axis. **M** represents the initial position of the bulk magnetization vector with x and z components of magnitudes M_x and M_y respectively. **M'** represents the bulk magnetization vector after rotation .

Assuming that the bulk magnetization vector is instantaneously rotated by an angle θ about the x-axis then the components of the bulk magnetization vector are transformed such that; (Also see figure 5.2)

$$M_x \xrightarrow{\theta_x} M_x \tag{5.3}$$

$$M_y \xrightarrow{\theta_x} M_y\cos\theta - M_z\sin\theta \tag{5.4}$$

$$M_z \xrightarrow{\theta_x} M_z\cos\theta + M_y\sin\theta \tag{5.5}$$

The cartesian product operators may be consider to be no more than representations of these components of the magnetization vector and as such transform in an identical

manner. If the spin system is composed of spins from different isotopes (such as ^1H and ^{13}C nuclei) then it becomes possible to stimulate only one group of nuclei within the system. To indicate which nuclei are being nutated about which axis by a pulse, the pulse angle by which the nuclei are to be rotated is written followed by the alphabetical letter representing the spins which is subfixed by the angle that the (positive) rotational axis of the nutation makes to the x-axis. As most spectrometers only allow rotation about the x, -x, y and -y axes, it is common to replace the subscripts 0, 90, 180 and 270 with x,y,-x and -y. A rotation of spins 'I' by θ degrees about the y-axis is, therefore, indicated by '$\theta\ I_y$' allowing equations(5.3), (5.4) and (5.5) to be re-written for the product operators as;

$$I_x \xrightarrow{\theta\ I_x} I_x \tag{5.6}$$

$$I_y \xrightarrow{\theta\ I_x} I_y\cos\theta - I_z\sin\theta \tag{5.7}$$

$$I_z \xrightarrow{\theta\ I_x} I_z\cos\theta + I_y\sin\theta \tag{5.8}$$

with the appropriate rotations about the y-axis being;

$$I_x \xrightarrow{\theta\ I_y} I_x\cos\theta + I_z\sin\theta \tag{5.9}$$

$$I_y \xrightarrow{\theta\ I_y} I_y \tag{5.10}$$

$$I_z \xrightarrow{\theta\ I_y} I_z\cos\theta - I_x\sin\theta \tag{5.11}$$

As operators such as $2I_xS_x$ can be regarded as being the product of 2, I_x and S_x, the result of a rotational transformation can be found by applying the transform to each of these components and multiplying the results together. However, as the pulses are usually specific to one nucleus it may not affect all the components of a product operator. Thus applying the rotation '$\theta\ I_y$' to the product operator $2I_xS_x$ gives;

$$\begin{aligned} 2I_xS_x \xrightarrow{\theta\ I_y} \quad & 2S_x(I_x\cos\theta + I_z\sin\theta) \\ & = 2S_xI_x\cos\theta + 2S_xI_z\sin\theta \\ & \equiv 2I_xS_x\cos\theta + 2I_zS_x\sin\theta \end{aligned} \tag{5.12}$$

which for a 90° pulse simplifies to;

$$2I_xS_x \xrightarrow{90\ I_y} 2I_zS_x \tag{5.13}$$

Sometimes two or more nuclei are nutated simultaneously within a spin systems. The effect on the product operators can be determined by consecutively applying the appropriate rotation for each nucleus to the product operators, the results of one rotation

giving the starting operators for the remaining rotations. For example, the result of a simultaneous rotation on the product operator $2I_xS_z$, rotating spin I by α and spin S by β about the y and x axes respectively, is given by applying '$\alpha\ I_y$' to $2I_xS_z$ and then '$\beta\ S_x$' to the resultant product operators;

$$2I_xS_z \xrightarrow{\alpha I_y} 2I_xS_z\cos(\alpha) + 2I_zS_z\sin(\alpha)$$

$$2I_xS_z\cos(\alpha) + 2I_zS_z\sin(\alpha) \xrightarrow{\beta S_x} \begin{matrix} 2I_xS_z\cos(\alpha)\cos(\beta) + 2I_xS_y\cos(\alpha)\sin(\beta) \\ 2I_zS_z\sin(\alpha)\cos(\beta) + 2I_zS_y\sin(\alpha)\sin(\beta) \end{matrix} \qquad (5.14)$$

$\therefore$

$$2I_xS_z \xrightarrow{\begin{pmatrix}\alpha I_y \\ \beta S_x\end{pmatrix}} \begin{matrix} 2I_xS_z\cos(\alpha)\cos(\beta) - 2I_xS_y\cos(\alpha)\sin(\beta) \\ -2I_zS_z\sin(\alpha)\cos(\beta) + 2I_zS_y\sin(\alpha)\sin(\beta) \end{matrix}$$

1.2.2 Effect of Chemical Shift on the Product Operators.

During the delay periods of a pulse sequence, where there is no external influence on the spin systems, the nuclei are free to precess about the applied magnetic field. One contribution to this precession is from the chemical shift of the nucleus (part 2 : section 1.10.1).

The propagation of the product operators of the spin systems under the chemical shift of spin I affects only those operators which contain the transverse operators, I_x and I_y, and results in their rotation within the x-y plane. Given that the chemical shift of the spin in Hertz is Ω, corresponding to an angular frequency of Ω_I ($\Omega_I=2\pi\Omega$), then during a time period τ the angle of this rotation in the x-y plane is $\Omega_I\tau$. In a manner analogous to the B_1 induced rotation of the components of the bulk magnetization vector, figure 5.2 and equations(5.3), (5.4) and (5.5), the effects on the product operators are;

$$I_x \xrightarrow{\Omega_I\tau\ I_z} I_x\cos\Omega_I\tau - I_y\sin\Omega_I\tau \qquad (5.15)$$

$$I_y \xrightarrow{\Omega_I\tau\ I_z} I_y\cos\Omega_I\tau + I_x\sin\Omega_I\tau \qquad (5.16)$$

$$I_z \xrightarrow{\Omega_I\tau\ I_z} I_z \qquad (5.17)$$

where '$\Omega_I\tau\ I_z$' indicates that the transform is of spin I under its chemical shift.

During any delay period the propagation of the product operators by the chemical shifts for all the spins in the system must be implemented. This is achieved by applying

successive transformations to the product operators. For example, to allow for the evolution of chemical shifts in a 2 spin system composed of spins I and S where the chemical shifts are Ω_I and Ω_S respectively it would be necessary to firstly transform all 16 product operators under '$\Omega_I\tau\ I_z$' and then to transform the resulting operators under '$\Omega_S\tau\ S_z$', with all components of an operator not involved with a particular transformation acting as constants.

1.2.3 The Effect of Scalar Coupling on the Product Operators.

During the delay periods the effect of scalar coupling, described in part 2 : section 1.10.2, also needs to be accounted for. Given that spins I and S are coupled then the action of spin-spin coupling is to split the magnetization vectors of both I and S into two component vectors (I_α and I_β for spin I and S_α and S_β, for spin S) of equal but opposite frequency, centred about the chemical shift frequency. (Figure 5.3.a) . The classical vector model accounts for the propagation of these vectors separately. The product operator formalism, however, views these two vectors as a single entity and accounts for them as such. Assuming that the spin system is initially described solely by the operator I_x, then the action of scalar coupling causes a reduction in I_x while simultaneously generating anti-phase y-magnetization. This anti-phase magnetization is not detectable by NMR spectrometers and may be considered to be comprised of two vectors of equal intensity which are diametrically opposed to each other (the resultant of which is a null vector). (Figure 5.3.b.)

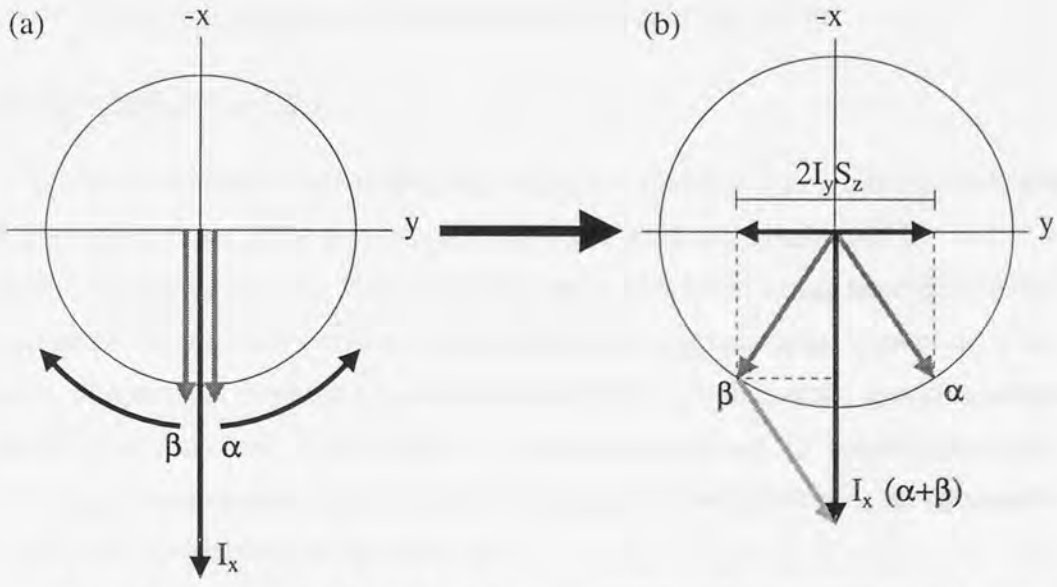

Figure 5.3 : Evolution of an I_x product operator under scalar coupling to a 'S' nucleus. **(a)** System prior to evolution with the component vectors 'α' and 'β'. **(b)** After evolution with the classical vector addition of 'α' and 'β' defining I_x alone while the product operator formalism also defines an anti-phase magnetization, $2I_yS_z$.

Despite the fact that on a macroscopic scale the anti-phase magnetization does not exist it is still accounted for. At its maximum, when I_x has been reduced to zero, the magnetization along the y-axis can be described as $I_y(I_\alpha - I_\beta)$. The relative populations of I_α and I_β are, of course, determined by the populations of S_α and S_β to which they are coupled. Thus, $(I_\alpha - I_\beta)$ reflects the population difference of the S spin and $(I_\alpha - I_\beta)$ can be replaced by $2S_z$ allowing the anti-phase magnetization of spin I to be described as $2I_yS_z$.

The evolution of scalar coupling between two spins, I and S, during a time period τ is indicated under product operator formalism as $\pi J_{IS}\tau 2I_zS_z$. Thus, if the coupling constant between two spins is J_{IS} the cartesian and anti-phase operators are transformed according to;

$$I_x \xrightarrow{\pi J_{IS}\tau 2I_zS_z} I_x\cos(\pi J_{IS}\tau) + 2I_yS_z\sin(\pi J_{IS}\tau) \tag{5.18}$$

$$I_y \xrightarrow{\pi J_{IS}\tau 2I_zS_z} I_y\cos(\pi J_{IS}\tau) - 2I_xS_z\sin(\pi J_{IS}\tau) \tag{5.19}$$

$$2I_xS_z \xrightarrow{\pi J_{IS}\tau 2I_zS_z} 2I_xS_z\cos(\pi J_{IS}\tau) + I_y\sin(\pi J_{IS}\tau) \tag{5.20}$$

$$2I_yS_z \xrightarrow{\pi J_{IS}\tau 2I_zS_z} 2I_yS_z\cos(\pi J_{IS}\tau) - I_x\sin(\pi J_{IS}\tau) \tag{5.21}$$

with a similar set of transformations existing for the component vectors of spin S. Where a product operator of the coupled nuclei contains transverse operators from both spins or longitudinal operators from both spins no evolution occurs.

1.2.4 Spin-Spin Decoupling

Spin-spin decoupling is a method by which the scalar coupling between two nuclei (usually heteronuclei in the present context) is removed and is achieved by continuously irradiating one of the coupled nuclei with either broad band or selective r.f. radiation. In product operator formalism the effect of spin-spin decoupling is to remove all operators from the spin system description which contain spin components of the irradiated nucleus. Thus, if spin 'I' was irradiated in an 'IS' spin system only those operators composed solely of spin 'S' component would remain, all composite 'IS' and pure 'I' operators being removed.

1.3 The Use of Product Operator to Describe One Dimensional Experiments.

The pulse sequences presented in this section are based on, or take their functionality from the 'Polarization Enhancement Nurtured During Attached Nucleus Test' or PENDANT pulse sequence [131, 132]. It is, therefore, of use to provide here the product operator formalism together with a vector description of the pulse sequence.

The product operator formalism for refocussed PENDANT is given in figure 5.5 while the PENDANT pulse sequence with vector representations of a CH and a quarternary unit at various points during the sequence are shown in figure 5.4. The representations of the CH spin system were generated by the freely available 'spin-sym' computer program and were calculated using the density operator method with all resonances set at pulse centre.

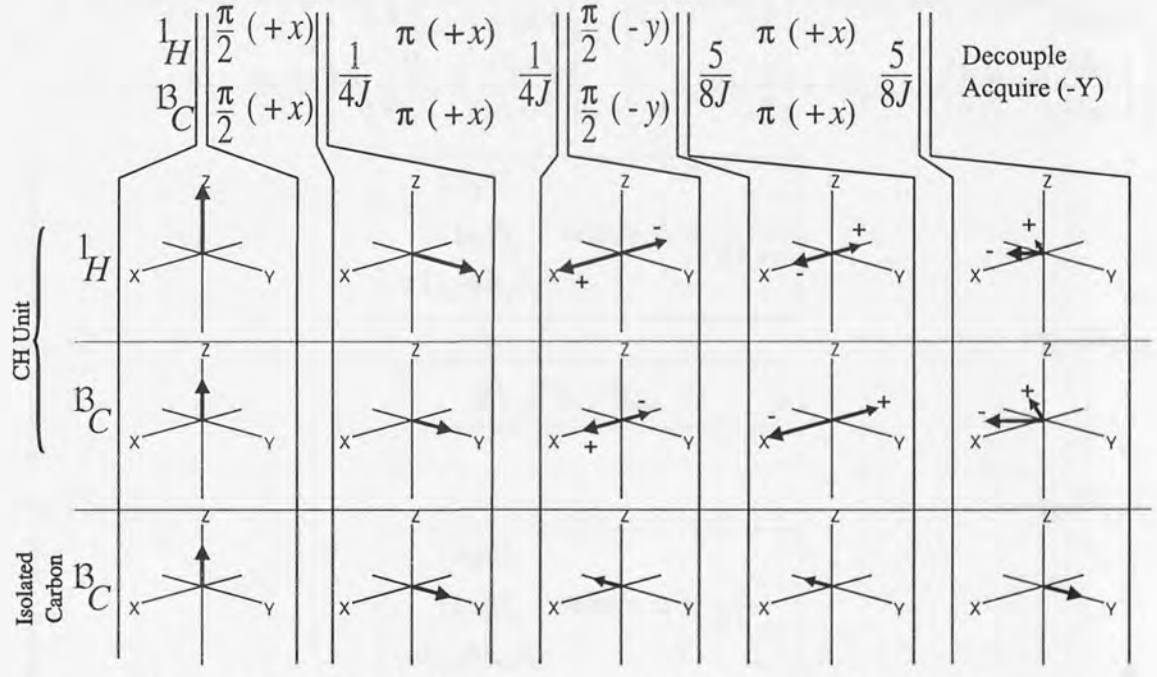

Figure 5.4 : Re-focused PENDANT with representation of a CH and quarternary spin systems.

1.4 Multi-Dimensional Experiments.

One dimensional NMR experiments are so-called as the NMR signal is detected as a function of one time evolution, requiring a single Fourier transformation to produce a spectrum. In the previous section the product operator formalism for PENDANT (figure 5.5) shows that, after de-coupling from ^1H, the signal on the carbon channel for

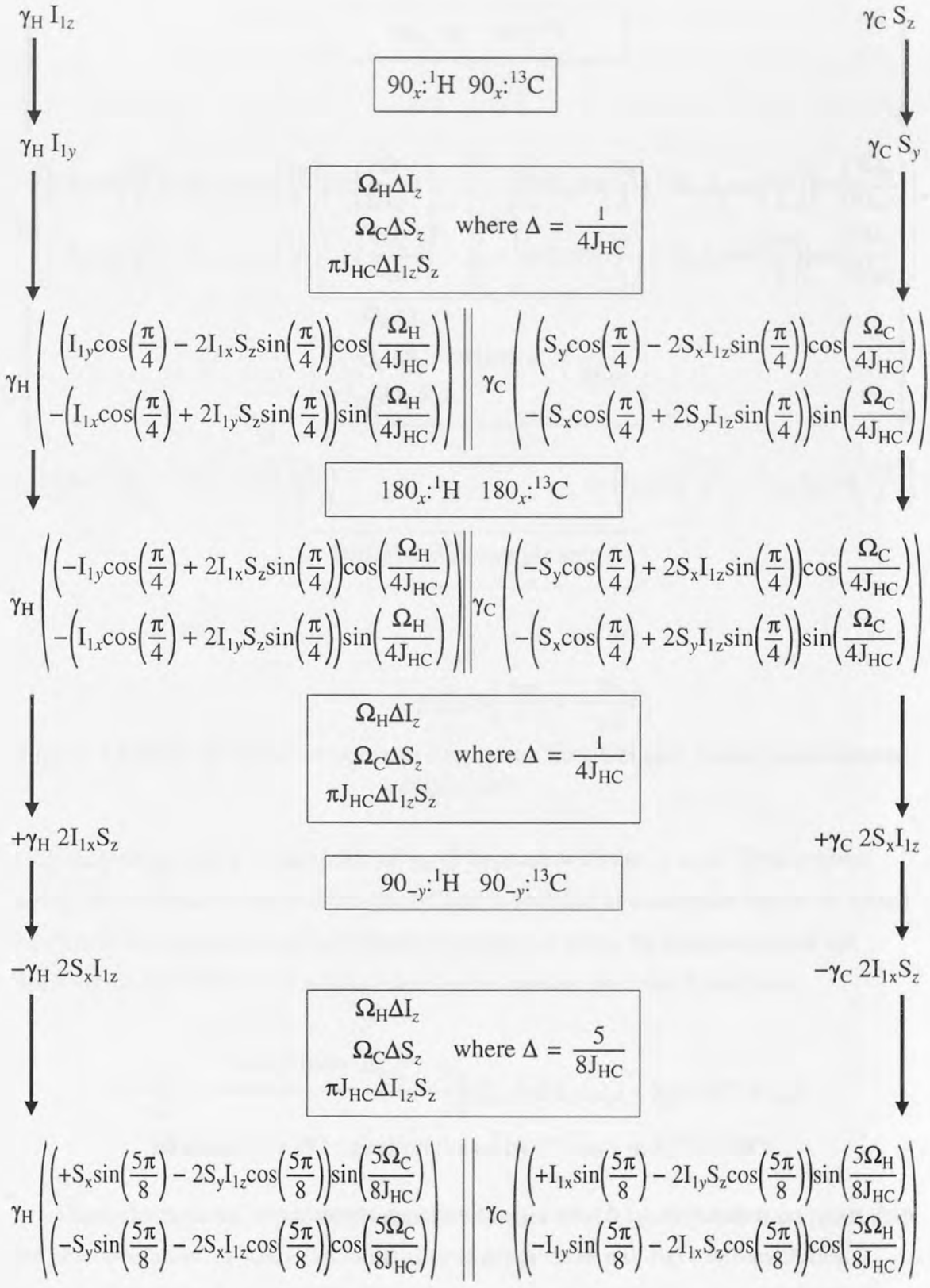

Figure 5.5 (Part 1) : Product Operator Formalism for a CH spin system in re-focused PENDANT.

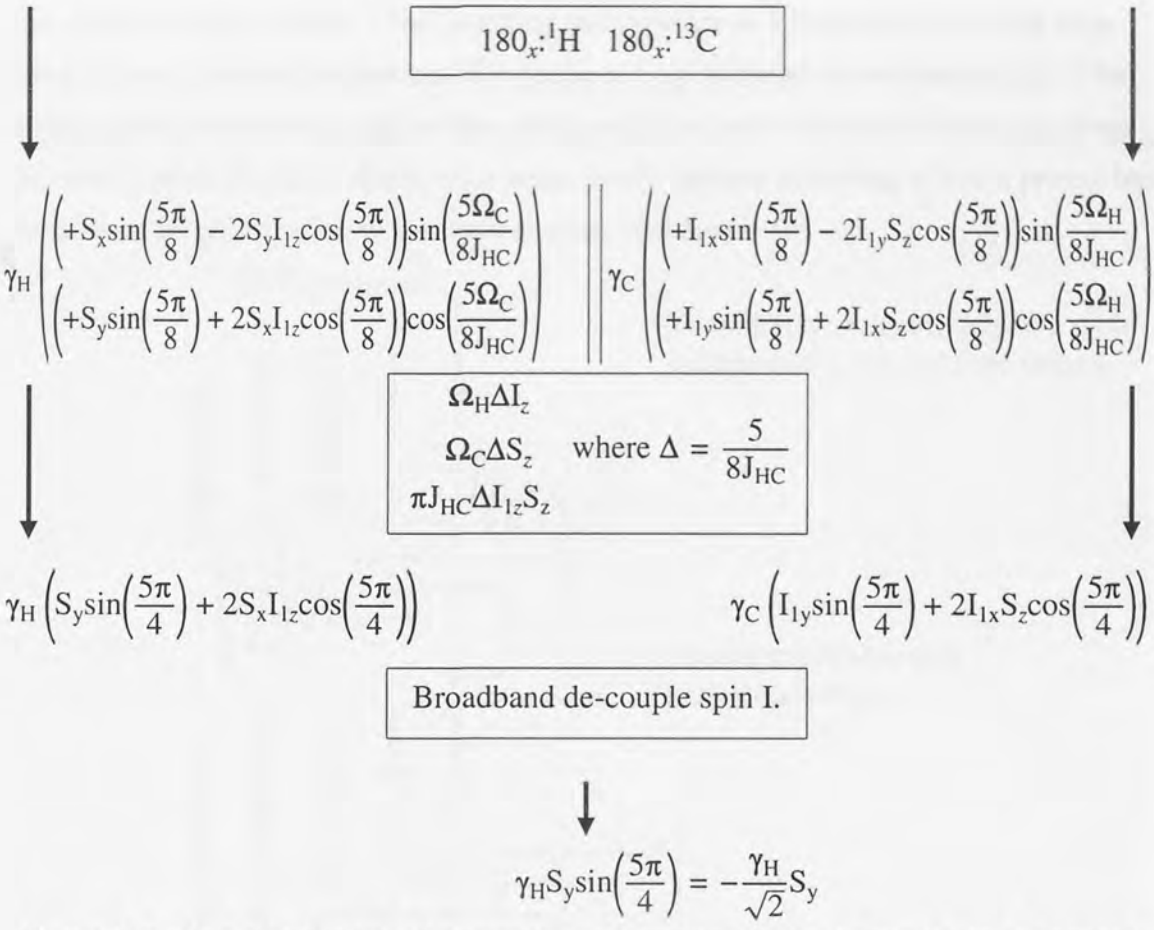

Figure 5.5 (Part 2) : Product Operator Formalism for a CH spin system in re-focused PENDANT.

a CH unit starts with a polarization of $\gamma_H/\sqrt{2}$ in phase with the -y axis. This evolves during the subsequent acquisitions period and is detected as a complex signal on which the Fourier transformation is performed. Scheme 5.1 gives the components of the NMR signal for PENDANT as predicted by the product operator formalism.

$$-\frac{\gamma_H}{\sqrt{2}} S_y \xrightarrow{\text{Acquitition } (\Delta_{Aq})} \frac{\gamma_H}{\sqrt{2}} \left(S_x \sin(\Omega_C \Delta_{Aq}) - S_y \cos(\Omega_C \Delta_{Aq}) \right)$$

Scheme 5.1 : ^{13}C signal produced by CH unit in PENDANT.

Multi dimensional experiments generate spectra which are dependent on more than one time evolution. Thus, a two dimensional experiment will have two evolution periods. For example, one where the polarization from a proton to carbon nucleus is varied and one where the carbon spectrum is acquired. As, in this example, the degree of polarization transfer from the proton to the carbon will be dependent on the chemical shift of the proton nuclei the detected carbon spectra will be composed of absorptions whose chemical shifts are those of carbon nuclei but whose intensities are governed by

the coupled proton nuclei. Thus, stacking such spectra as a function of the first time delay allows a second Fourier transformation to be performed across the spectra. The resulting two dimensional surface has along one axis carbon chemical shifts and along the other proton chemical shifts, with peaks on the surface occurring where a proton has transferred its polarization to a carbon nucleus. See figure 5.6

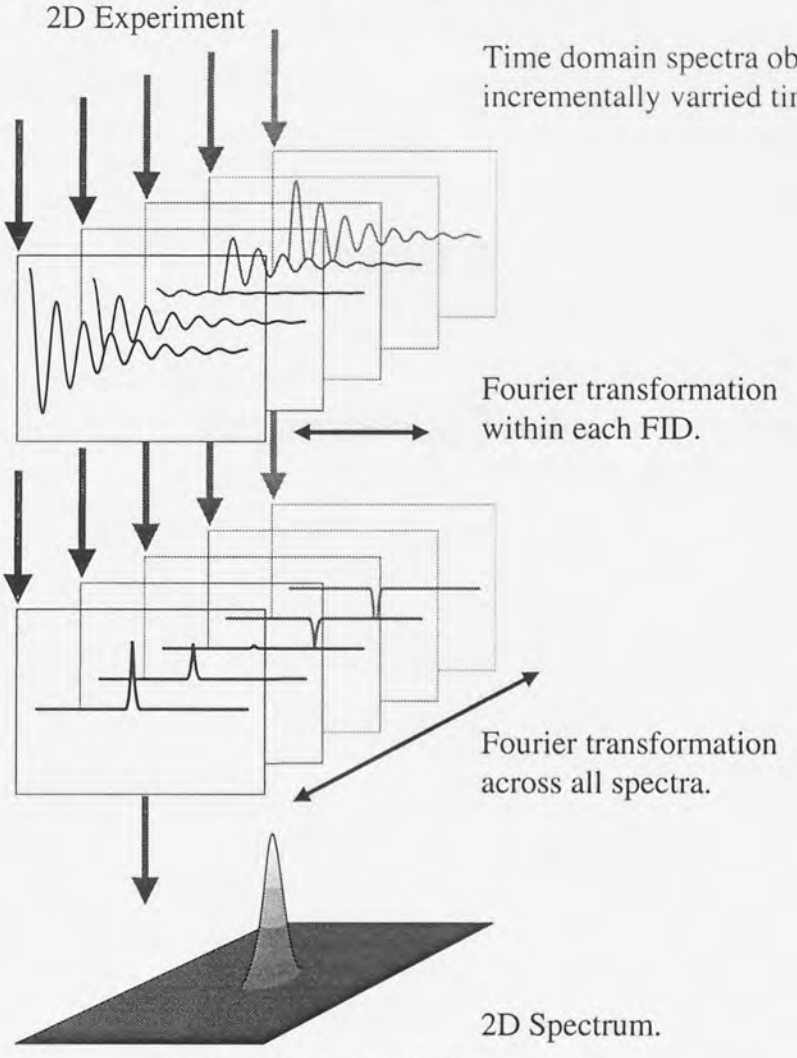

Figure 5.6 : A 2D NMR experiment.

Variable delays resulting in multi-dimensional NMR experiments are simply accounted for in product operator formalism by leaving the delay in terms of an arbitrary alpha-numeric rather than calculating the effects of the delay explicitly. Scheme 5.2 shows the product operators generated by a 2D NMR experiment where the NMR signal is governed by the carbon chemical shifts (Ω_C) during the acquisition time (Δ_{Aq}) but by the proton chemical shift (Ω_H) during the incremental delay(τ).

$$\frac{\gamma_H}{\sqrt{2}}\left(\sin(\Omega_H\tau) + \cos(\Omega_H\tau)\right)\left(S_x\sin(\Omega_C\Delta_{Aq}) - S_y\cos(\Omega_C\Delta_{Aq})\right)$$

Scheme 5.2 : Product operator formalism giving rise to a 2D spectrum.

Chapter 2

Experimental Tools.

2.1 Computer Program for the Numerical Evaluation of Product Operator Formalisms.

2.1.1 Introduction.

The development and refinement of new pulse sequences can require extensive spectrometer time. To assist in the optimisation of such pulse sequences a computer program, written in BBC Basic V [133, 134] running on an Acorn RiscPC, was developed which could simulate a spin system consisting of spin units chosen from quarternary carbons, CH, CH_2 and CH_3 units. Based on product operator formalism, the program generates numerical results allowing the search for the optimum conditions of a pulse sequence without the use of a spectrometer.

The search for optimum conditions requires a BBC Basic program to be written which calls the appropriate procedures from the main simulation program which is loaded as a library file at the start of the program. Thus to simulate the end states of the PENDANT pulse sequence the simulation program in figure 5.7 may be written.

```
LIBRARY SimLib

PROCInit(1)
AJ=140

PROCDefine(0,1000,  0,  0,  0,  0,  0, 0, 0, 0,0)
PROCDefine(1, 900,500,120,  0,  0,  0, 0, 0, 0,0)
PROCDefine(2, 800,400,300,130,135, 10, 0, 0, 0,0)
PROCDefine(3, 100,200,125, 50,160,150,10,75,12,9)

FOR Nucleus%=0 TO nnum%-1
 PROCpulse("H+X",90  ,Nucleus%)
 PROCpulse("C+X",90  ,Nucleus%)
 PROCdelay("1/(4*AJ)",Nucleus%)
 PROCpulse("H+X",180 ,Nucleus%)
 PROCpulse("C+X",180 ,Nucleus%)
 PROCdelay("1/(4*AJ)",Nucleus%)
 PROCpulse("H-Y",90,Nucleus%)
 PROCpulse("C-Y",90,Nucleus%)
 PROCdelay("5/(8*AJ)",Nucleus%)
 PROCpulse("H+X",180,Nucleus%)
 PROCpulse("C+X",180,Nucleus%)
 PROCdelay("5/(8*AJ)",Nucleus%)
NEXT

END
```

Figure 5.7 : Computer program corresponding to the PENDANT pulse sequence.

The remainder of this section describes the procedures made available by the simulation library together with its limitations, the library program (SimLib) itself is listed in appendix 4.

2.1.2 User Commands

2.1.2.1 Initialization Commands.

There are two initialization commands made available by the simulation library. The first informs the program of how many spin units are to be accommodated in the spin system, the second is used to define these spin units;

PROCInit(X) :
X=Integer.

This command initializes the arrays used by the simulation library. It causes space to be made for 'X' quarternary carbons, 'X' CH units, 'X' CH_2 units and 'X' CH_3 units.

PROCDefine(X,Val1, Val2, Val3, Val4, Val5 Val6, Val7, Val8, Val9, Val10) :
X=Integer : 'Val1'- 'Val10'=Real

This command is used to define the spin units which constitute the spin system studied by the simulation. The value of 'X' determines the type of spin unit defined; 0,1,2,3 defining C, CH, CH_2 and CH_3 respectively. The parameters defined by the variables 'Val1' to 'Val10' are dependent on spin unit as defined by 'X'. The definitions of 'Val1' - 'Val10' for the different spin units are given in table 5.2.

2.1.2.2 Pulse Sequence Commands

Pulse sequences are composed of pulses and delays. Consequently the simulation library provides two procedures for the manipulation of the spin systems, one for simulating the effects of pulses, the other for the effects of delays.

During the simulation it is necessary to nest the pulse sequence commands into a loop which runs from 0 to 'nnum%-1' in integral steps where nnum% is defined by the simulation library during initialization. The variable controlling this loop, referred to below as 'Nucleus', must be given as the last parameter when calling the pulse and delay procedures.

PROCPulse("Command", Angle, Nucleus) :
"Command" = Text : Angle = Real : Nucleus = Integer.

This command is used to pulse the spin system under study. The value of "Command" determines the nuclei to be stimulated together with the phase of the pulse, with 'Angle' defining the nutation angle (in degrees). Simultaneous stimulation of the protons and carbons is achieved by sequentially calling the pulsing procedure with the respective phases and pulse angles for each nucleus. Table 5.3 lists the acceptable value for the "Command" parameter together with their meaning.

PROCDelay("Command", Nucleus) :
"Command" = Text : Nucleus = Integer.

This command is used to allow the spin system to evolve during a period of time as defined by "Command". When evaluated, the content of "Command" must result in a real number which defines the delay period in seconds.

Table 5.2 : Parameter definitions for PROCDefine.
(All values should be given in Hertz)

	Spin Unit as Defined by X =			
	0	1	2	3
	C	CH	CH_2	CH_3
Val1	Chemical shift of carbon	Chemical shift of carbon	Chemical shift of carbon	Chemical shift of carbon
Val2	0	Chemical shift of proton	Chemical shift of proton1	Chemical shift of proton1
Val3	0	J Coupling between carbon and proton	Chemical shift of proton2	Chemical shift of proton2
Val4	0	0	J Coupling between carbon and proton1	Chemical shift of proton3
Val5	0	0	J Coupling between carbon and proton2	J Coupling between carbon and proton1
Val6	0	0	J Coupling between proton1 and proton2	J Coupling between carbon and proton2
Val7	0	0	0	J Coupling between proton1 and proton2
Val8	0	0	0	J Coupling between carbon and proton3
Val9	0	0	0	J Coupling between proton1 and proton3
Val10	0	0	0	J Coupling between proton2 and proton3

Table 5.3 : Parameters for PROCPulse.

Command	Meaning: Apply nutating pulse to the
"C+X"	carbon nuclei about the +X axis.
"C+Y"	carbon nuclei about the +Y axis.
"C-X"	carbon nuclei about the -X axis.
"C-Y"	carbon nuclei about the -Y axis.
"H+X"	proton nuclei about the +X axis.
"H+Y"	proton nuclei about the +Y axis.
"H-X"	proton nuclei about the -X axis.
"H-Y"	proton nuclei about the -Y axis.

2.1.2.3 Extraction of Information from Spin System.

The simulation library currently has no commands to extract data from the spin system. Rather it is left to the simulation program to access the spin system matrices directly. The exact method by which the matrices are referenced within the simulation library is not addressed here. However, ultimately each of the spin units making up the spin system is defined by a matrix whose dimentionality is equal to the number of nuclei in the spin unit. Each dimension of the matrix is of order four, these relating to the identity, x, y and z operator for each spin within the spin unit. Thus the 15 product (plus identity) operators for the CH unit are represented by the 4×4 matrix given in figure 5.8.

Proton Operators (I) \ Carbon Operators (S)	1	x	y	z
1	1	S_x	S_y	S_z
x	I_x	$2I_xS_x$	$2I_xS_y$	$2I_xS_z$
y	I_y	$2I_yS_x$	$2I_yS_y$	$2I_yS_z$
z	I_z	$2I_zS_x$	$2I_zS_y$	$2I_zS_z$

Figure 5.8 : Matrix representation of the product operators for the CH unit.

2.1.3 Limitations.

The simulation library fully implements the product operator formalism of spin systems consisting of C, CH, CH_2 and CH_3 spin units, allowing the chemical shift of each nuclei to be defined together with the coupling constants between all nuclei within

each spin unit. However, the following physical phenomena are not simulated;

- the T_1 and T_2 relaxation mechanisms.
- off resonance pulse effects.
- spin-spin decoupling.

2.2 Brüker WM-250 & AC-300 NMR spectrometers.

The pulse sequences discussed in this section were implemented on either the Brüker WM-250 or Brüker AC-300 NMR spectrometer which are based around vertical bore, superconducting solenoids operating at proton frequencies of 250MHz (5.88 Tesla) and 300MHz (7.05 Tesla) respectively. Any perturbations to the magnetic field that do occur are compensated for by a locking unit which monitors an in-situ deuterium signal from the NMR sample.

The detected spectra/FID may contain up to 256K data points over a maximum spectral window of 166,666Hz. The manipulation of the NMR data may be performed either on the spectrometer console or by downloading to IBM compatible personal computers running Brükers proprietary NMR packages; 1D-WINNMR and 2D-WINNMR.

The consoles of both spectrometer are based on the ASPECT3000 computer with control of the NMR probe occurring via a 'pulse programmer' in the WM-250 but via a 'process controller' in the AC-300. This makes little difference to the routine functionality of the spectrometers but does allow the AC-300 to execute more complex pulse sequences. The sequences presented here can, however, be executed on either the WM-250 or the AC-300.

A number of NMR probes are available for both spectrometers but for this work a 5mm $^{1}H/^{13}C$ dual nuclei probe was employed on the AC-300 and either a 5mm dedicated carbon probe or a 10mm high frequency (28.5MHz - 105MHz) broadband probe on the WM-250. All spectrometer probes are attached to variable temperature control units.

The operation of the NMR spectrometers and the use of the NMR packages are documented in the appropriate user manuals[135-137].

Chapter 3

Preliminary Investigations into the Extension of PENDANT to a Multi-Dimensional Experiment.

3.1 Introduction.

The PENDANT pulse sequence was developed to remedy one of the major failings of the DEPT [138, 140, 141] (Scheme 5.3.a) and INEPT[139] experiments *viz.* that being their inability to detect insensitive nuclei which are isolated from the sensitive nuclei such as quarternary carbons, at the same time as the insensitive nuclei bonded to the sensitive nuclei. PENDANT produces an enhanced NMR spectrum through polarization exchange giving CH, CH_2 and CH_3 signals of intensity equal to those found in the DEPT experiment together with a quarternary carbon signal which is slightly enhanced (through long range scalar coupling) when compared to a quarternary carbon detected directly in a 'normal' multi-pulse experiment. As with DEPT (and INEPT), PENDANT produces an NMR spectrum that shows spectral editing, both experiments showing CH_2 carbons with negative phase absorptions and with CH and CH_3 carbons as positive absorptions. The additional quarternary carbon in PENDANT spectra is detected as a negative phase absorption.

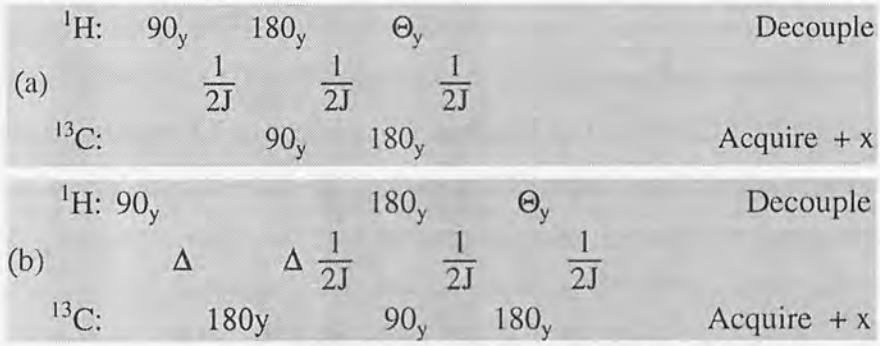

Scheme 5.3 : Pulse sequences for **(a)** the one dimensional DEPT experiment and **(b)** the two dimensional DEPT-COSY experiment, a two dimensional version of DEPT.

As DEPT provides signal enhancement through the transfer of polarization from the proton nuclei to the carbon nuclei, the technique is readily adapted to a 2 dimensional experiment. Such an experiment is that of DEPT-COSY[142-145] (Scheme 5.3.b), in which a proton spectrum is generated along one domain axis, a carbon spectrum along the other and where correlation peaks occur on the 2D surface where a proton nuclei is short-range scalar coupled to a carbon nucleus. As the enhancement of the NMR signal in PENDANT occurs through a similar mechanism it was suggested that PENDANT might be likewise adapted to a 2D experiment, giving the same spectra as generated by DEPT-COSY but with the addition of quarternary peaks on the 2D surface. As the quarternary carbons experience no short-range couplings it was believed that these peaks would show as correlations between the quarternary carbon and a 'phantom' proton absorption which would occur at zero Hertz in the referenced proton spectrum i.e. at pulse centre of the proton spectrum.

3.2 Theoretical.

A carbon-hydrogen 2D correlation spectrum is produced when the pulse program arranges for the hydrogens in a spin system to evolve independently of any carbon spin they may be coupled to, prior to the transfer of their polarization to the carbon nuclei. In the adaptation of DEPT to DEPT-COSY this is achieved by replacing the initial $^1H{:}90_y$ of the DEPT sequence with the sequence depicted in scheme 5.4, causing the proton nuclei to evolve under their chemical shift alone, independently of its scalar coupled carbon nuclei. The product operator formalism for a CH unit manipulated by this sequence is given in figure 5.9.

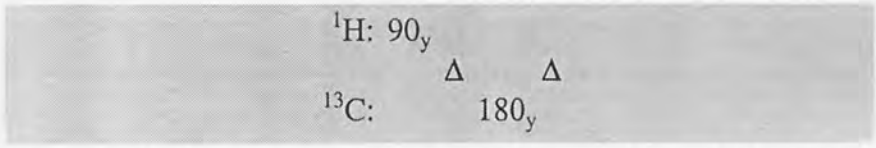

Scheme 5.4 : Sequence introduced to DEPT to obtain DEPT-COSY.

As an adaptation of PENDANT to a 2D technique (Dimensionally Enhanced PENDANT or DEPENDANT) will also require the independent evolution of protons, the sequence in scheme 5.4 should also be included in the PENDANT sequence, replacing the initial simultaneous 90° pulses on the proton and carbon channels with the sequence in scheme 5.4 followed by a 90° carbon pulse, taking into account the now inverted carbon spins. Scheme 5.5 shows the proposed DEPENDANT pulse sequence based on non-refocussed PENDANT while figure 5.10 shows the appropriate product operator formalism.

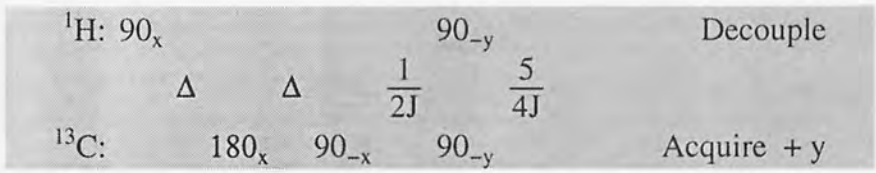

Scheme 5.5 : Proposed pulse sequence for DEPENDANT.

Thus, from the product operator formalism, the DEPENDANT experiment should show a DEPT-COSY like 2D spectrum with correlations showing between carbon and proton nuclei that are short range coupled, the correlation being centred on the chemical shift of the proton nuclei. As with PENDANT the DEPENDANT sequence arranges for the quarternary carbons to be detectable, the single quarternary vector being aligned along the y-axis.

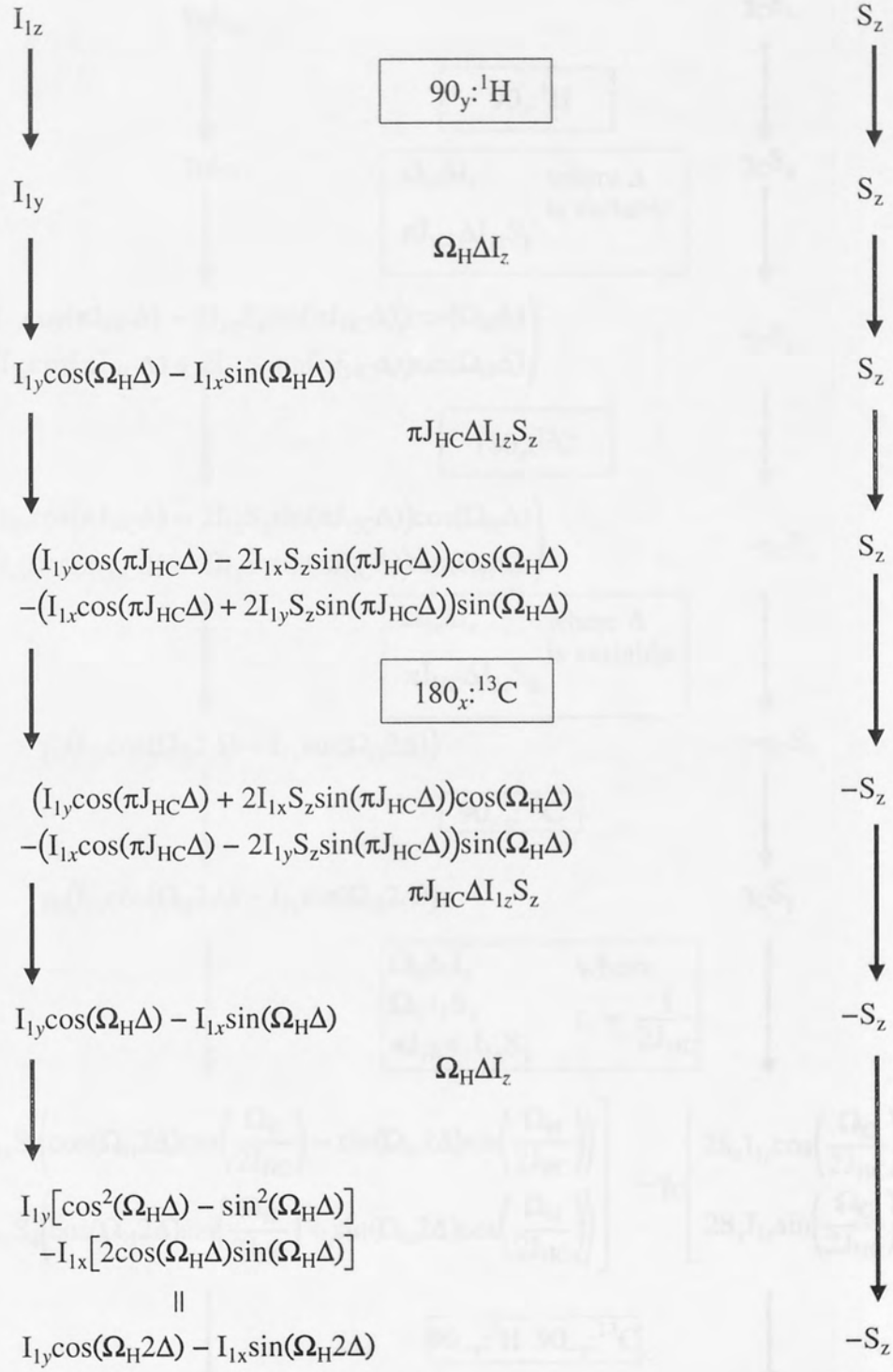

Figure 5.9 : Product operator formalism of a CH unit for the sequence; $^1H(90_y)\ \Delta\ ^{13}C(180_x)\ \Delta$.

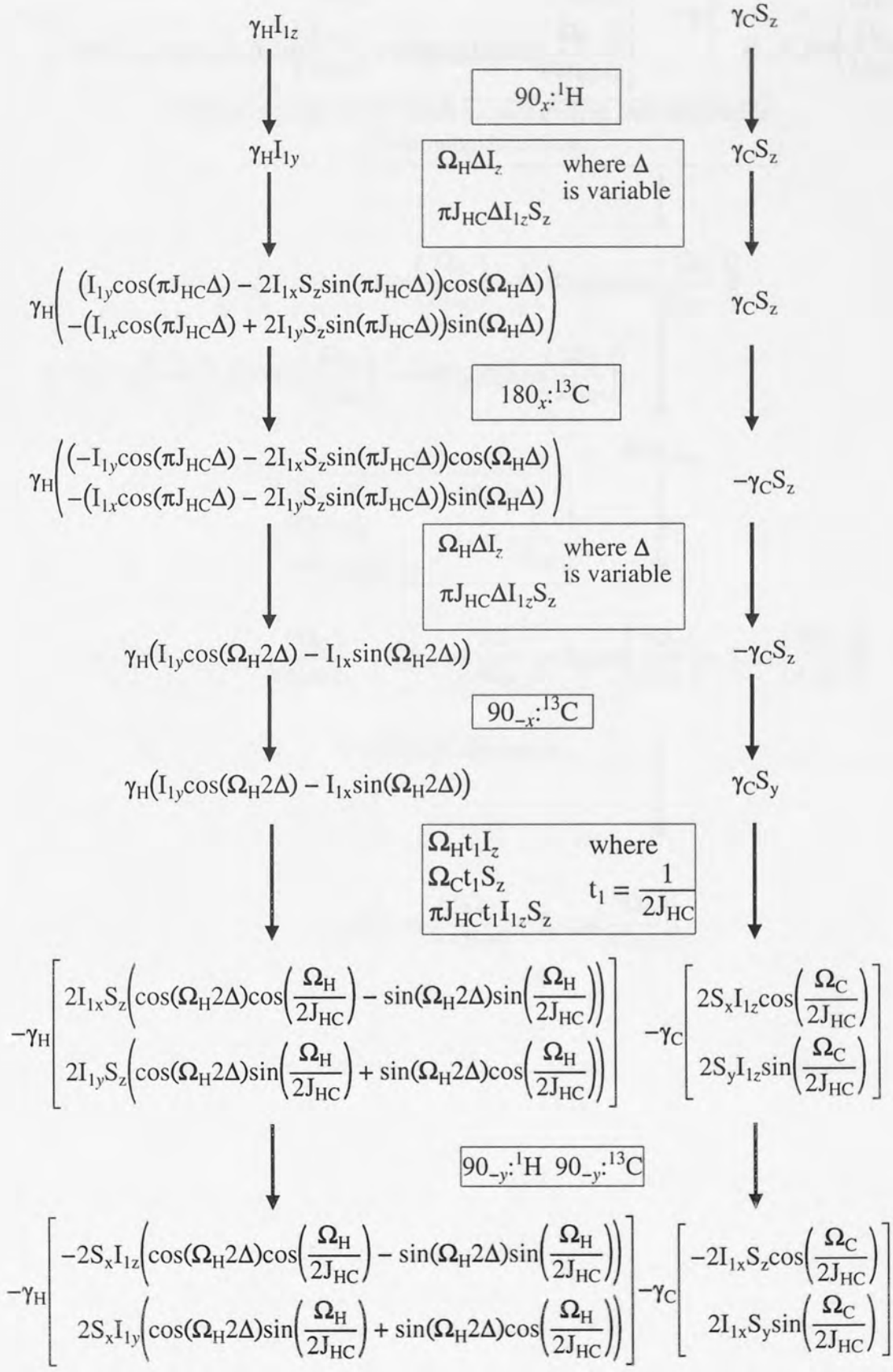

Figure 5.10 (Part1): Product operator formalism for the proposed DEPENDANT pulse sequence.

$$-\gamma_H\begin{bmatrix} -2S_xI_{1z}\left(\cos(\Omega_H 2\Delta)\cos\left(\frac{\Omega_H}{2J_{HC}}\right) - \sin(\Omega_H 2\Delta)\sin\left(\frac{\Omega_H}{2J_{HC}}\right)\right) \\ 2S_xI_{1y}\left(\cos(\Omega_H 2\Delta)\sin\left(\frac{\Omega_H}{2J_{HC}}\right) + \sin(\Omega_H 2\Delta)\cos\left(\frac{\Omega_H}{2J_{HC}}\right)\right) \end{bmatrix} \quad -\gamma_C\begin{bmatrix} -2I_{1x}S_z\cos\left(\frac{\Omega_C}{2J_{HC}}\right) \\ 2I_{1x}S_y\sin\left(\frac{\Omega_C}{2J_{HC}}\right) \end{bmatrix}$$

Neglecting operators which cannot evolve into detectable carbon magnetizations.

$$\gamma_H 2S_xI_{1z}\left(\cos(\Omega_H 2\Delta)\cos\left(\frac{\Omega_H}{2J_{HC}}\right) - \sin(\Omega_H 2\Delta)\sin\left(\frac{\Omega_H}{2J_{HC}}\right)\right)$$

$$\text{let } \Theta = \gamma_H\left(\cos(\Omega_H 2\Delta)\cos\left(\frac{\Omega_H}{2J_{HC}}\right) - \sin(\Omega_H 2\Delta)\sin\left(\frac{\Omega_H}{2J_{HC}}\right)\right)$$

$$\Theta 2S_xI_{1z}$$

$$\begin{array}{ll} \Omega_H t_2 I_z & \text{where} \\ \Omega_C t_2 S_z & \\ \pi J_{HC} t_2 I_{1z} S_z & t_2 = \dfrac{5}{4J_{HC}} \end{array}$$

$$-\frac{1}{\sqrt{2}}\Theta\left(2I_{1z}S_x\cos\left(\frac{5\Omega_C}{4J_{HC}}\right) + 2I_{1z}S_y\sin\left(\frac{5\Omega_C}{4J_{HC}}\right) + S_y\cos\left(\frac{5\Omega_C}{4J_{HC}}\right) - S_x\sin\left(\frac{5\Omega_C}{4J_{HC}}\right)\right)$$

Broad-band Decouple

$$\frac{1}{\sqrt{2}}\Theta\left(S_x\sin\left(\frac{5\Omega_C}{4J_{HC}}\right) - S_y\cos\left(\frac{5\Omega_C}{4J_{HC}}\right)\right)$$

Figure 5.10 (Part 2): Product operator formalism for the proposed DEPENDANT pulse sequence.

3.3 Experimental

The pulse sequence given in scheme 5.5 was converted into a pulse program (figure 5.11) that would run on the Brüker NMR spectrometers.

```
1   ZE
2   D1 S1 DO              ; S1 set so that P1=P2
3   P1:D PH1 D0           ; P1=90  degree proton
4   P2   PH2 D0           ; P2=180 degree carbon
5   P3   PH3 D1           ; D0 incremental delay
6   P1:D PH4 P3 PH5 D2    ; D1=1/(2J)
7   S2                    ; P3=90 degree carbon
8   GO=2 PH6 BB           ; D2=5/(4J)
9   D5 DO                 ; S2 set for decoupling
10  WR #1                 ; D5 decoupler switching time
11  IF #1
12  IN=1
13  EXIT

PH1=B0
PH2=A0
PH3=A2
PH4=B3
PH5=A3
PH6=R1
```

Figure 5.11 : DEPENDANT pulse program for Brüker NMR spectrometers running ASPECT 3000 computers.

Using the AC-300 NMR spectrometer fitted with a $^{1}H/^{13}C$ dual nuclei probe the pulse sequence given in figure 5.11 was set-up to to investigate a standard sample of 98% ethylbenzene in chloroform-d, maintained at 25°C by the variable temperature unit.

3.4 Results and Discussion.

The 2D spectrum resulting from the DEPENDANT pulse sequence is given in figure 5.12. Although the spectrum does show carbon/proton correlations, the spectrum is flawed in two major ways:-

- The spectrum contains axial peaks [146]; At the mid point of the proton projection of the 2D spectrum, corresponding to a referenced proton frequency of zero Hertz, there exist a row of correlations between all the carbons of ethylbenzene and a phantom proton nucleus.

- The spectrum has the carbon/proton correlations mirrored about the axial peaks.

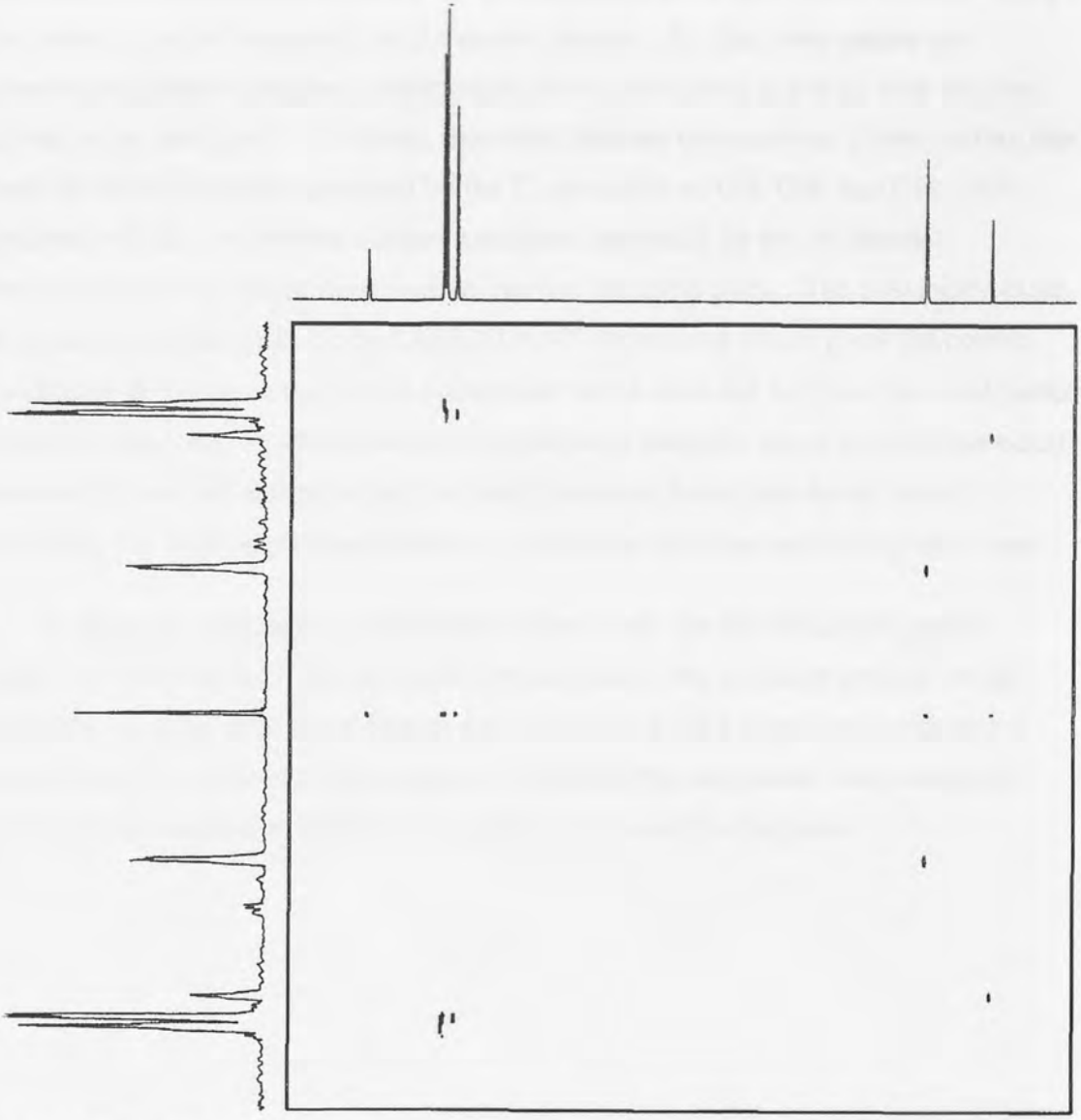

Figure 5.12 : 2D spectrum that results from the implementation of the DEPENDANT pulse sequence on a sample of ethyl-benzene.

The mirroring of the correlations is caused by either the real or imaginary component of the signal in the proton domain being omitted from the detected signal, leading to the inability of the Fourier transform to determine the absolute frequency of the correlation peak with regards to the 'carrier' frequency of the proton domain. Given correct phase cycling all the necessary components for the 2D fourier transformation can be provided. However, such a phase cycle would leave the axial peaks unaffected.

The axial peaks are caused by the T_1 relaxation of the carbon spins in the system during the delays in the pulse sequence, generating a bulk magnetization vector with a z component which is later made detectable by its rotation into the x-y plane. As the magnitude of this z component is invariant during the variable delay Δ, the Fourier

transformation gives the frequency of the component to be zero Hertz, corresponding to the central 'carrier' frequency for the proton domain. By their very nature the quarternary carbons are also unaffected by the variable delay Δ and as such they too appear as an axial peak. It is likely, therefore, that any conventional phase cycling that removes the axial peaks generated by the T_1 relaxation of CH, CH_2 and CH_3 spin systems will also remove the desired axial peak generated by the deliberate manipulation of the quarternary carbon into the detection plane. The possibility exists of creating a phase cycle for the DEPENDANT experiment which gives the correct quadrature detection in the proton domain but which does not suppress the axial peaks. However, the resulting spectra would be difficult to interpret where correlations occur between proton and carbon nuclei that have chemical shifts close to the centre frequency for their respective domains i.e. where the diagonal and axial peaks cross.

In summary, although it is possible to phase cycle the DEPENDANT pulse sequence removing both the axial and mirrored peaks, the resulting spectra would probably be identical to those obtained by the DEPT-COSY experiment and such a result does not warrant the time required to perform the additional work needed to produce a carbon/proton correlation spectrum with a single diagonal.

Chapter 4

Development of 'Sensitive Nucleus Accelerated Relaxation for Enhancement of Signal to Noise with Time' - SNARE.

4.1 Introduction.

One disadvantage of many NMR investigations is their time consuming nature that stems from lengthy relaxation delays. Few methods exist for the reduction of natural spin-lattice relaxation delays. The most popular depends on the addition of relaxation agents [147-149], but this may often be chemically undesirable. A more complex way is *via* the ultrasonic irradiation [150] of analytical samples, but the methodology of this approach remains complex. A different method of effectively reducing spin-lattice relaxation times may be possible by modifying the relaxation pathway of the sensitive nucleus (I), utilizing any magnetization which has developed on S during the acquisition time. One way by which this may be achieved is by utilizing a polarisation transfer technique, from S to I, inserted at the end of a pulse sequence, after the acquisition time, but prior to the relaxation delay thus enabling the 'Sensitive Nucleus Accelerated Relaxation for Enhancement of Signal to Noise with Time' - SNARE.

4.2 Theoretical

SNARE depends on polarisation transfer in the opposite sense (in a similar manner to that employed in the original version of inverse spectroscopy [151]) to that commonly employed [131, 138, 139], *viz*, from the insensitive to the sensitive nuclei. Necessarily, this imposes basic requirements on the spin system studied. These include the normal condition that the T_1 of I is shorter than that of S, and additionally that the relaxation time of S is reasonably short, for example, of the order of 3 times that of I. These conditions are often encountered in those air saturated samples, containing J-coupled ^{13}C-^{1}H spin systems, that are at the heart of many routine NMR investigations. SNARE, which may in principle replace the relaxation delay that precedes any conventional pulse sequences, also relies on the frequently used condition that the I nuclei are decoupled from S during acquisition. Consequently, to benefit from the nuclear Overhauser effect (nOe) [152, 153] the magnetogyric ratios of the sensitive and insensitive nuclei must be of the same sign: if they are not, gated decoupling of the sensitive nucleus during acquisition must be employed.

During the course of acquiring the spectrum of S while I is decoupled following a conventional pulse sequence, the situation is that while there should ideally be no I_z magnetisation, S_z develops with nuclear Overhauser enhancement (nOe, $\eta = \frac{\gamma^I}{2\gamma^S}$)

towards the maximum value of the enhanced magnetisation which is, $\eta = \frac{\gamma^I}{2\gamma^S} + 1$ times the normal S magnetisation M_o^S. The enhanced transient S magnetisation can be transferred to the I spin immediately after switching off the decoupler signal to I, and so accelerate the recovery of the I spin towards its equilibrium value. The situation may be summarized simply for a spin-½ only I-S system as in figure 5.13.

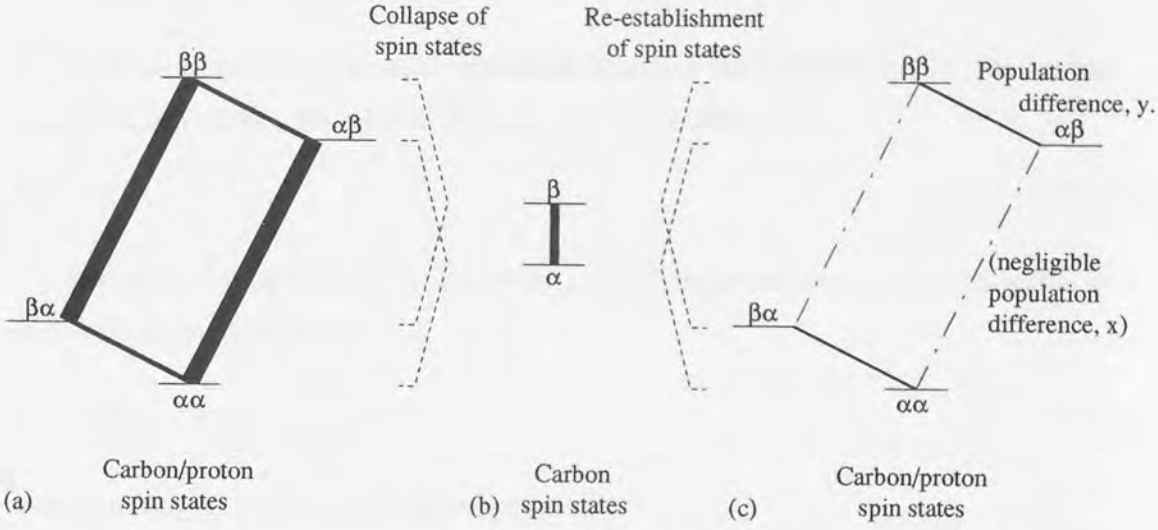

Figure 5.13 : Idealised energy levels in a CH spin system under various conditions. The relative population differences between the spin states is indicated by the thickness of the interconnecting transition lines.

Figure 5.13 specifically represents the principles implicit in SNARE as applied to a ^1H-^{13}C spin system: the populations of the four energy levels are idealised by assuming that the ^1H polarisation is 4 times that of ^{13}C, with each of the relevant spin states having equally increased or decreased populations relative to the zero magnetic field condition. Figure5.13.a represents the normal equilibrium situation. In figure 5.13.b it is assumed that decoupling is completely effective, but that Overhauser enhancement of the ^{13}C has not commenced, so that there is zero net population difference between the ^1H levels, but that between the ^{13}C levels is Boltzmann. Figure 5.13.c represents the situation immediately after ^{13}C acquisition in an appropriate investigative sequence, with the ^1H decoupling terminated: to accommodate switching times on stopping the decoupling process a small population difference, x, in the ^1H levels is assumed to have formed. During ^{13}C acquisition it is assumed that a ^{13}C population, y, has been generated under nOe condition resulting in z-phase magnetisations for ^{13}C, where, out of necessity, $y \leqslant |3|$.

The coherent z-magnetization formed on the ^{13}C nucleus can be rapidly manipulated, transforming it into z-phase ^{1}H magnetization, effectively step-jumping the proton relaxation along its normal pathway, thus facilitating a reduction in the relaxation delay necessary to obtain a chosen S/N that might be required under normal conditions. It must be emphasised that the advantage of using SNARE with a constant relaxation delay is only realized when x<y and is at a maximum when x=0 and y corresponds to the maximum nOe on S.

Assuming single exponential relaxation delays of the I (and S) nuclei, the normal relaxation of I during the relaxation delay, RD, is described by

$$M_z^I = M_o^I(1 - e^{-\frac{RD}{T_1}}) \tag{5.22}$$

Similarly, during the acquisition time t_{ac} the S magnetisation recovers towards its equilibrium value such that

$$M_z^S = M_0^S(\eta + 1)(1 - e^{-\frac{t_{ac}}{T_1}}) \tag{5.23}$$

corresponding to a recovery in polarisation of

$$\begin{aligned} \mu_z^S \Delta n_{t_{ac}}^S &= \mu_z^S \Delta n_o^S(\eta + 1)(1 - e^{-\frac{t_{ac}}{T_1}}) \\ \Delta n_{t_{ac}}^S &= \Delta n_o^S(\eta + 1)(1 - e^{-\frac{t_{ac}}{T_1}}) \end{aligned} \tag{5.24}$$

where Δn_o^S is the polarization of S under the Boltzmann equilibrium conditions, Δn_z^S is the polarization of S at time t_{ac} and μ_z^S is the z-component of the magnetic moment of S. If this polarisation is now inverse transferred to I as proposed in SNARE, the magnetization of I, given that

$$\begin{aligned} \frac{\Delta n_o^S}{\gamma_S} &= \frac{\Delta n_o^I}{\gamma_I} \\ \Delta n_o^S &= \frac{\gamma_S \Delta n_o^I}{\gamma_I} \end{aligned} \tag{5.25}$$

reaches

$$M_{zS}^I = M_o^I(1 - e^{-\frac{RD}{T_1^I}}) + \frac{\gamma_S}{\gamma_I} M_o^I(\eta + 1)(1 - e^{-\frac{t_{ac}}{T_1^S}})e^{-\frac{RD}{T_1^I}} \tag{5.26}$$

during an RD which is equivalent to that found in the 'standard' experiment, equation(5.22).

In general, the percentage increase (E) in I magnetisation that may be obtained using SNARE, relative to that achieved by normal relaxation of I, is

$$E = 100\frac{\gamma_S(\eta+1)(1-e^{-\frac{t_{ac}}{T_1^S}})}{\gamma_I(e^{\frac{RD}{T_1^I}}-1)} \qquad (5.27)$$

In the above equations M_o^S and M_o^I are the normal Boltzmann magnetisations of S and I respectively, M_z^S and M_z^I the corresponding relaxation dependent longitudinal magnetisations and M_{zS}^I that reached in SNARE, all after the delay RD, and T_1^S and T_1^I are the relaxation times of S and I respectively.

If, for an air saturated 1H-13C system, typical values of t_{ac}=RD =1s, T_1^S = 10s, T_1^I = 5s, $\eta = 2$ and $\gamma_o^I = 4\gamma_o^S$ are inserted into equation(5.27), it can be seen that the 1H z-magnetisation should be readily increased by 32%. This extra ^1H magnetisation that can be gained during RD is now available for polarisation transfer to the ^{13}C. Alternatively, the SNARE sequence can achieve the normal ^{13}C signal/noise ratio in 57% of the normal experimental time (deduced from equation(5.33)) .

To develop a general experimental procedure for SNARE it is necessary to characterizes the extent to which transferable anti-phase magnetization can be generated within a typical sample. It is, therefore, inappropriate to consider the IS system alone. Rather, an ensemble consisting of spin systems which are representative of typical molecular species should be considered. To establish how such an ensemble of spins generates transferable anti-phase z-magnetisation it is necessary to characterise how such a magnetization is formed within each of the spin systems constituting the ensemble.

Where SNARE is applied to organic molecules, utilizing carbon to proton transfer, a representative ensemble should contain IS, I_2S and I_3S spin systems. At the end of an acquisition period, where the proton nuclei have been decoupled from the carbon nuclei, such an ensemble will have developed a z-phase magnetization which is associated with the carbon spins alone. By applying a 90° y-phase pulse to the carbon nuclei the z-phase magnetization can be converted to x-phase magnetization, from which can be generated, through the action of I-S coupling, anti-phase magnetization. The transformation of the x-phase carbon magnetization (of magnitude ψ) into anti-phase magnetization is dependent on the spin system; For a CH system the formation of transferable anti-phase magnetization from the x-phase magnetization during an

evolution delay period, τ, with a coupling constant of J_{CH} is characterized by product operator formalism [42, 127-130] as

$$\psi S_x \longrightarrow \psi\left(S_x\cos(\pi J_{HC}\tau)+2S_yI_z\sin(\pi J_{HC}\tau)\right) \tag{5.28}$$

, for a CH_2 unit with coupling constant J_{CH2} as

$$\psi S_x \longrightarrow \psi\left(\begin{array}{l} S_x\cos^2(\pi J_{CH2}\tau) + \frac{1}{2}2S_yI_{2z}\sin(\pi J_{CH2}2\tau) \\ +\frac{1}{2}2S_yI_{1z}\sin(\pi J_{CH2}2\tau) - 4S_xI_{1z}I_{2z}\sin^2(\pi J_{CH2}\tau) \end{array}\right) \tag{5.29}$$

, and for a CH_3 unit with coupling constant J_{CH3} as

$$\psi S_x \longrightarrow \psi\left(\begin{array}{l} S_x\cos^3(\pi J_{CH3}\tau) \\ +\frac{1}{2}(2S_yI_{1z} + 2S_yI_{2z} + 2S_yI_{3z})\sin(\pi J_{CH3}2\tau)\cos(\pi J_{CH3}\tau) \\ -\frac{1}{2}(4S_xI_{1z}I_{2z} + 4S_xI_{1z}I_{3z} + 4S_xI_{2z}I_{3z})\sin(\pi J_{CH3}\tau)\sin(\pi J_{CH3}2\tau) \\ +8S_yI_{1z}I_{2z}I_{3z}\sin^3(\pi J_{CH3}\tau) \end{array}\right) \tag{5.30}$$

For the time being it will be assumed that some magnetisation evolution and pulse manipulation technique such as that implicit in the classical INEPT [139] or more recent PENDANT [131] sequences can be used to transfer the required anti-phase z-magnetizations implied in equations(5.28), (5.29) and (5.30). It is a fine decision as to whether to use an inverse process based on a true polarisation transfer sequence such as INEPT or to use a polarisation exchange sequence such as PENDANT as, after the accelerated relaxation of the I spins the condition of the S spins is not too important given that the subsequent I relaxation governs the recovery of the $S(I_n)$ systems towards equilibrium. However, the advantages of PENDANT are two-fold. Firstly, because this sequence is completely symmetrical, and, therefore, involves true polarisation exchange it is possible to return any residual S magnetisation components in phase along the z-axis. Secondly, PENDANT enables the manipulation of isolated S spins synchronously with those in $S(I_n)$ systems. In other words, despite the necessary manipulation of the IS systems it proves possible to leave essentially unaffected the isolated S spin z-magnetisation of quarternary carbons that has developed during the acquisition period.

The benefits of SNARE can be achieved by replacing the normal intersequence delay, that precedes conventional pulse sequences, by the symmetric PENDANT-type sequence;

^{1}H: 90_x 90_{+y} 90_{-x}
D_1 D_2 RD
^{13}C: 90_x 90_{+y} 90_{-x}

Scheme 5.6 : PENDANT-type sequence.

This sequence is phased to enable each repetitive cycle to start with multiplet components having the frequency labels appropriate to the equilibrium Boltzmann situation: for general use shift refocussing should be introduced by inserting simultaneous 180°(+x) pulses on S and I at the midpoint of each delay. Although the first 90°(+x) pulse to I might appear unnecessary because the initial value of I_z should be zero, it is included to accommodate any small value that might exist as a consequence of delays during switching periods. Thus, in product operator formalism the polarisation magnetisation exchange pathway is, neglecting the angular dependencies of J evolution, characterised as below, for n = 1 to 3.

$$S_z \xrightarrow{S:90_{+x}} S_y \xrightarrow{D_1} -\sum_{i=1}^{i=n} 2S_xI_{iz} \xrightarrow[S:90_y]{I:90_y} +\sum_{i=1}^{i=n} 2I_{ix}S_z \xrightarrow{D_2} +\sum_{i=1}^{i=n} I_{iy} \xrightarrow[S:90_{-x}]{I:90_{-x}} +\sum_{i=1}^{i=n} I_{iz} \quad (5.31)$$

while isolated S nuclei, such as quarternary ^{13}C, are returned to z-phase so that they relax normally;

$$S_z \xrightarrow{S:90_{+x}} S_y \xrightarrow{D_1} S_y \xrightarrow[S:90_y]{I:90_y} S_y \xrightarrow{D_2} S_y \xrightarrow[S:90_{-x}]{I:90_{-x}} S_z \quad (5.32)$$

The delays D_1 and D_2 have to be chosen to be compatible with the $S(I_n)$ system under study. For example, if only CH groups were studied, both delays would ideally be 1/2J. However, the simultaneous SNARE manipulation of an ensemble of spins means that all spins can neither be exactly on resonance nor D_1 and D_2 chosen to match the actual J values of each of the spin systems. Even if the ensemble is treated ideally the cyclic nature of the operators describing the spin systems results in multiple solutions for D_1 and D_2 where the transfer of magnetization from S to I is at a maximum. Reality dictates that some compromise value for D_1 and D_2 will have to be chosen to optimise the inverse polarisation of S over the whole ensemble.

4.3 Experimental

To determine the optimum, compromise values of D_1 and D_2 for use in a generally applicable SNARE sequence a computer program (appendix 5) was written which made use of the spin-library documented in section 2.1. The ensemble of spins used for this determination contained nine spin units; three S(I) units, with coupling constants of

140, 160 and 180Hz respectively; three $S(I_2)$ units, with coupling constants of 120, 130 and 140 Hz respectively; and three $S(I_3)$ spin units, with coupling constants of 120, 130 an 140Hz respectively. The states of the spin units within the ensemble were set so that in each spin unit the S spin had 1 unit of z-phase magnetization, while each of the I spins had no magnetization, thus mimicking the distribution of magnetization within a spin system immediately after an acquisition period where the proton nuclei had been decoupled from the carbon nuclei. The program then implemented the pulse sequence given in scheme 5.6, utilizing an average J coupling constant, <J>, of 145 Hz and varying the D_1 and D_2 values, allowing both to take values between 0 and 1/<J>. For each of these delay pairs the program generated three magnetization transfer values, one value for the total magnetization transferred from the S spins to the I spins over the three S(I) units, one for this value over the three $S(I_2)$ units and one for this value over the three $S(I_3)$ units. As the generated values are the result of summing three spin units which differ only in their S-I coupling constant, the generated transfer magnetization values relate to S(I), $S(I_2)$ and $S(I_3)$ spin units, each of which exhibit a typical distribution of S-I coupling constant. These transfer magnetization values were saved into three separate files (hereafter referred to as the 'transfer files') which defined the magnetization transferred by each different type of spin unit (a file for each of the S(I), $S(I_2)$ and $S(I_3)$ spin units) in terms of D_1 / D_2 pairs. It is possible to plot such transfer files as surfaces; the D_1 and D_2 values respectively defining the y and x ordinate of a point on the surface, with the transferred magnetization defining the height or z-ordinate of the surface. This has been done in figures 5.14.a, 5.14.b and 5.14.c showing the individual, transfer magnetization surfaces for the S(I), $S(I_2)$ and $S(I_3)$ spin units respectively. Examination of these plots in conjunction with the data found in the transfer files shows that, in the above ensemble, the maximum percentage transfer of magnetization from the S spins to the I spins in the S(I) units was 97.5%, in the $S(I_2)$ was 49.8% and in the $S(I_3)$ unit was 38.1%. Thus, the ratio of the maximum, absolute transfer of magnetization from the S spin to the I spin for the ensemble in the S(I), $S(I_2)$ and $S(I_3)$ spin units is 0.975 : 0.498 : 0.381 (where an ideal SI unit transfers 1 unit of magnetization onto the I spin)

The optimum values for D_1 and D_2 for a generally applicable version of SNARE can be found by the combination of the transfer files on a D_1/D_2 point-wise basis and searching the resulting surface for a global maxima. However, there are three search criteria by which the optimum values for D_1 and D_2 can be determined. The first criterion defines the optimum D_1 / D_2 pair as that which results in the maximum transfer of magnetization from the S spins onto the I spins in terms of the total units of

magnetization transferred summed over the whole ensemble. The second criterion defines the optimum D_1 / D_2 pair as that whereby each type of spin unit (the S(I), $S(I_2)$ and $S(I_3)$ units) contributes to the total transferred magnetization at a value as close to their respective maxima as possible. The third criterion acknowledges that S to I transfer in $S(I_2)$ and $S(I_3)$ units is significantly less efficient than in the S(I) unit. The optimum D_1/D_2 pair is, therefore, determined in an identical manner as for the second criterion but limits the search to a combination of the $S(I_2)$ and $S(I_3)$ transfer files, omitting the S(I) transfer file.

Selection via the first criterion requires the non-normalised transfer files to be directly combined and the D_1/D_2 surface searched for a maximum. Figure 5.15 shows the surface that results from such a combination. Analysis of this plot shows the optimum transfer value to occur when D_1 and D_2 take values of 0.31/<J> and 0.49/<J> respectively. Under such conditions the amount of magnetization transferred from the S spins to the I spins in the S(I), $S(I_2)$ and $S(I_3)$ systems is 0.848, 0.483 and 0.307 units respectively which, as percentages of their respective maxima, take values of 87%, 97% and 81% respectively.

The second criterion requires the magnetization transfer values held in the transfer files to be redefined from absolute values to values defined as a percentage of each files respective transfer maximum. The normalised transfer files that result from this procedure are then combined and the resultant D_1/D_2 surface searched for a maximum. Figure 5.16 shows the surface generated by this combination. Analysis of this plot shows the optimum transfer value to occur when D_1 and D_2 take values of 0.27/<J> and 0.52/<J> respectively. Under such conditions the amount of magnetization transferred from the S spins to the I spins in the S(I), $S(I_2)$ and $S(I_3)$ systems is 0.763, 0.493 and 0.357 units respectively which, as percentages of their respective maxima, take values of 78%, 98% and 93% respectively.

Selection via the third criterion requires the normalised transfer files for the $S(I_2)$ and $S(I_3)$ units, generated by the search under the second criterion, to be combined and searched for a maximum. Figure 5.17 shows the surface generated by this combination. Analysis of this plot shows the optimum transfer value to occur when D_1 and D_2 take values of 0.24/<J> and 0.56/<J> respectively. Under such conditions the amount of magnetization transferred from the S spins to the I spins in the S(I), $S(I_2)$ and $S(I_3)$ systems is 0.653, 0.483 and 0.377 units respectively which, as percentages of their respective maxima, take values of 67%, 97% and 99% respectively.

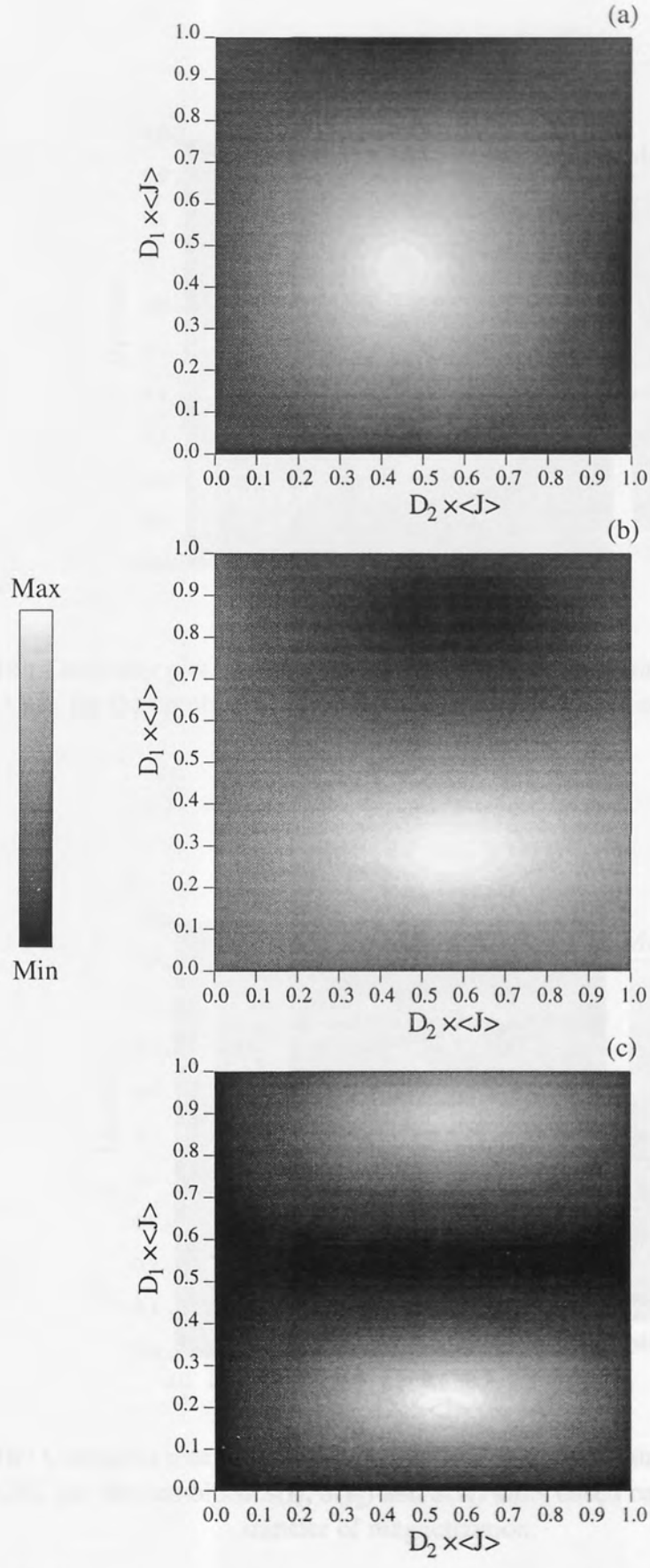

Figure 5.14 : Computer plots depicting transfer attained for D_1/D_2 pairs in the SNARE pulse sequence; **(a)** for S(I), **(b)** for $S(I_2)$ and **(c)** for $S(I_3)$ spin units.

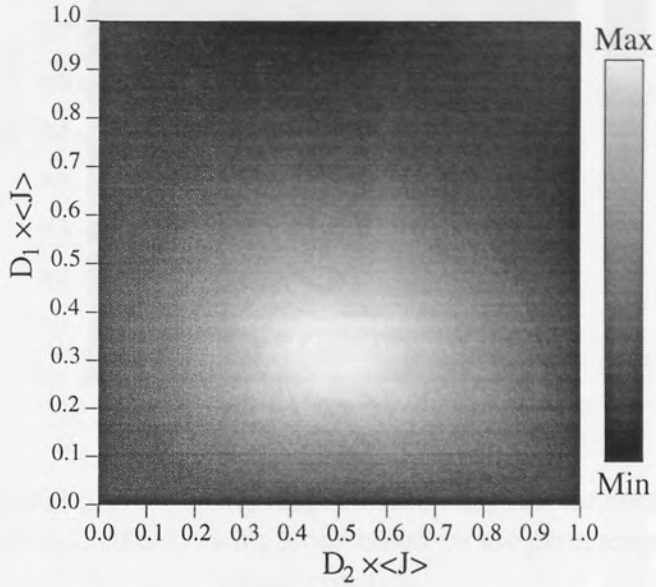

Figure 5.15 : Computer plot depicting magnetization transfer attained for D_1/D_2 pairs in SNARE for the combined S(I), $S(I_2)$ and $S(I_3)$ units based on the absolute transfer of magnetization.

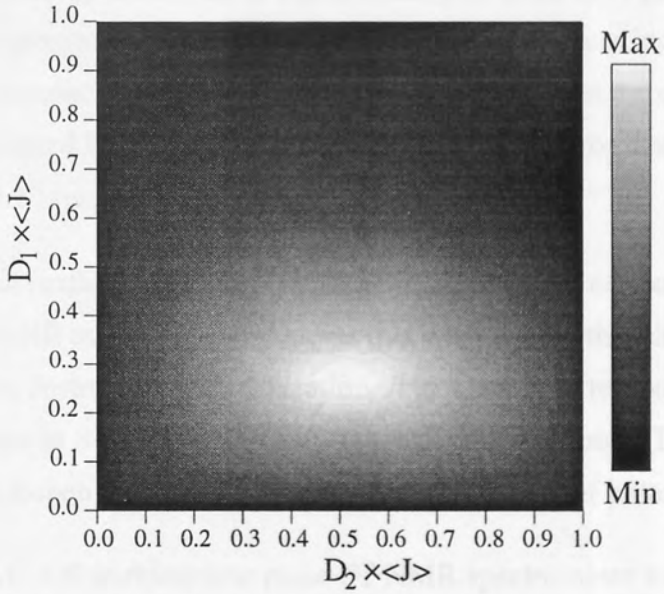

Figure 5.16 : Computer plot depicting magnetization transfer attained for D_1/D_2 pairs in SNARE for the combined S(I), $S(I_2)$ and $S(I_3)$ units based on the percentage transfer of magnetization.

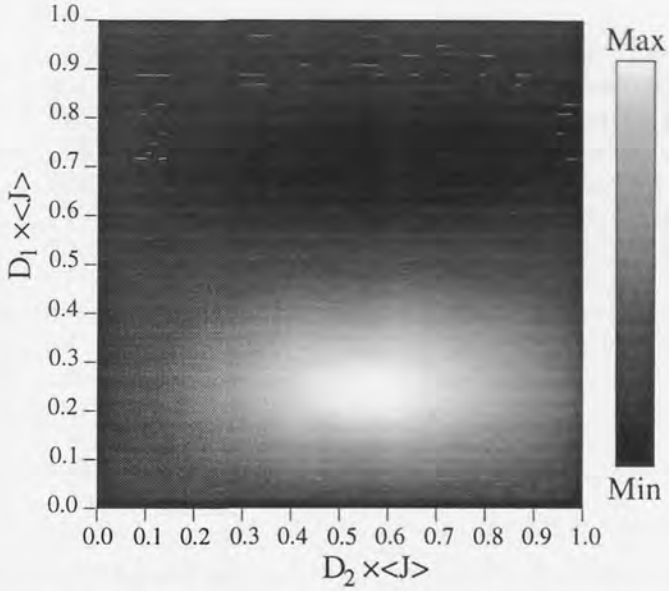

Figure 5.17 : Computer plot depicting magnetization transfer attained for D_1/D_2 pairs in SNARE for $S(I_2)$ and $S(I_3)$ units alone based on the percentage transfer of magnetization.

The various principles implicit in SNARE were examined initially through investigations of suitable air saturated samples by comparing the ^{13}C spectra obtained using PENDANT with those obtained with the relaxation delay in PENDANT replaced by SNARE (S-PENDANT). In order to facilitate the implementation of the pulse programs on the NMR spectrometer it was necessary to write the PENDANT and S-PENDANT pulse programs so that the SNARE sub-sequence was included at the beginning of the sequence with the relaxation delay occurring at the centre of the pulse sequences. The adapted PENDANT and S-PENDANT pulse programs are given in figures 5.18 and 5.19 respectively.

As can be seen neither sequences is phase cycled: there is, of course, little point in phase cycling SNARE as any I_{xy} components that exist during the actual relaxation part of the cycle will be destroyed by T_2 relaxation. It is interesting to note that the relevant coherence pathways in S-PENDANT (S»I»S) are opposite to those (I»S»I) proposed by Bodenhausen and Ruben [154] in the original double transfer of polarisation.

The Brüker AC 300 multinuclear pulse FT NMR spectrometer was used for the investigations. Comparative data were obtained using conditions of constant phase and amplitude. All spectra were obtained from samples thermostatted at 298 K in order to minimise variations in S/N due to temperature fluctuations. Where appropriate ^1H and ^{13}C T_1 data were obtained by the well-known inversion recovery method [155-157] and nOe's were measured under the conditions specified by Harris and Newman [158].

```
10   ZE
20   D5 S1 D0                    ; S1=set so that P1=P4
30   D0                          ; D0=incremental delay
40   (P1 PH1):D (P2 PH5) D2      ; P1=90 degree proton
50   (P3 PH1):D (P4 PH5) D2      ; P2=90 degree carbon
60   (P1 PH4):D (P2 PH8) D3      ; P3=180 degree proton
70   (P3 PH1):D (P4 PH5) D3 S2   ; P4=180 degree carbon
80   GO=20 PH9 BB                ; D2=1/(2J)
90   D7 D0                       ; D3=1/(2J)
100  WR #1                       ; S2 set power for decoupling
110  IF #1                       ; D7 decoupler switching time
120  IN=10
130  EXIT
PH1 = B0 B1 B2 B3
PH2 = B1 B2 B3 B0
PH3 = B2 B3 B0 B1
PH4 = B3 B0 B1 B2
PH5 = A0 A1 A2 A3
PH6 = A1 A2 A3 A0
PH7 = A2 A3 A0 A1
PH8 = A3 A0 A1 A2
PH9 = R1 R2 R3 R0
```

Figure 5.18 : The adapted PENDANT pulse sequence used for the investigation into SNARE theory.

```
10   ZE
20   D5 S1 D0                    ; S1=set so that P1=P4
30   (P1 PH1):D (P2 PH5) D4      ; P1=90 degree proton
40   (P3 PH1):D (P4 PH5) D4      ; P2=90 degree carbon
50   (P1 PH2):D (P2 PH6) D6      ; D4=1/(2J)
60   (P3 PH1):D (P4 PH5) D6      ; P3=180 degree proton
70   (P1 PH3):D (P2 PH7) D0      ; P4=180 degree carbon
80   (P1 PH1):D (P2 PH5) D2      ; D6=1/(2J)
90   (P3 PH1):D (P4 PH5) D2      ; D0=incremental delay
100  (P1 PH4):D (P2 PH8) D3      ; D2=1/(2J)
110  (P3 PH1):D (P4 PH5) D3 S2   ; D3=1/(2J)
120  GO=20 PH9 BB                ; S2 set power for decoupling
130  D7 D0                       ; D7 decoupler switching time
140  WR #1
150  IF #1
160  IN=10
170  EXIT
PH1 = B0 B1 B2 B3
PH2 = B1 B2 B3 B0
PH3 = B2 B3 B0 B1
PH4 = B3 B0 B1 B2
PH5 = A0 A1 A2 A3
PH6 = A1 A2 A3 A0
PH7 = A2 A3 A0 A1
PH8 = A3 A0 A1 A2
PH9 = R1 R2 R3 R0
```

Figure 5.19 : The S-PENDANT pulse sequence used for the investigation into SNARE theory.

The theory implicit in SNARE was tested by examining a pre-sealed, air saturated sample of chloroform, containing a small quantity of $CDCl_3$ for field frequency locking purposes.

The adapted PENDANT and S-PENDANT pulse sequences were configured so that both the ^{1}H and ^{13}C resonances of the chloroform sample were on-resonance for their respective channels and that the sequences gave both maximum polarisation transfer and detected signal intensity: the measured ^{1}H-^{13}C coupling constant of 209Hz was used and all evolution delays were set to 1/(2J). These pairs of experiments were then run using spectral sizes of 64K, 32K, 18430W and 4K corresponding to acquisition times of 1.9s, 0.95s, 0.534s and 0.11875s, examining relaxation delays of 0.0s to 3.0s in 0.2s increments. Due to the adaptation of the pulse sequences it is necessary precede each experiment with a number of dummy scans to drive the spin system to equilibrium.

4.4 Results and Discussion.

For the $CHCl_3$ sample, the ^{1}H (satellite) and ^{13}C T_1's were measured as 8.45 s and 23.4 s respectively and the $\{^{1}H\}$-^{13}C nOe was found to be 1.411. The relative intensities, measured by peak area, of the chloroform peak obtained in the adapted PENDANT and S-PENDANT experiments for the range of acquisition times and relaxation delays are listed in table 5.4. Computer analysis of these data resulted in the determination of quadratic lines of best fit which, together with their appropriate correlation coefficient, are listed in table 5.5.

Using the quadratic equations in table 5.5 the experimental signal intensity afforded by SNARE as a function of relaxation delay was calculated and plotted, together with the signal intensity as predicted by the SNARE theory, in figures 5.20, 5.21, 5.22 and 5.23 corresponding to the data acquired with acquisition times of 1.9s, 0.95s, 0.534s and 0.11875s respectively. Similarly, the actual and predicted signal enhancements attained by the use of the SNARE pulse sequence are given in figures 5.24, 5.25, 5.26 and 5.27

Table 5.4 : Relative intensity data for PENDANT and S-PENDANT for a range of spectral sizes and relaxation delays.
(Note : Intensities are comparable only between spectra of equal spectral sizes)

Relaxation Delay (s)	64K t_{ac} = 1.9s		32K t_{ac} = 0.95s		18430W t_{ac} = 0.534s		4K t_{ac} = 0.11875s	
	Normal	SNARE	Normal	SNARE	Normal	SNARE	Normal	SNARE
0.0	0.00	33.26	0.00	9.79	0.00	18.15	0.00	-
0.2	12.74	52.96	12.49	33.66	28.37	39.32	127.93	160.16
0.4	28.25	68.88	30.47	49.03	47.90	67.91	358.93	442.76
0.6	45.56	92.49	41.76	67.74	70.07	87.72	469.46	708.86
0.8	66.08	109.72	62.24	84.58	97.97	124.10	541.48	762.47
1.0	83.07	125.35	75.53	97.44	123.26	141.80	748.61	988.62
1.2	101.82	144.96	92.20	113.72	146.64	168.89	896.69	1061.64
1.4	120.9	163.08	108.57	130.17	167.35	196.55	1063.94	1039.13
1.6	133.82	179.68	119.57	144.92	183.86	213.13	1246.13	1340.87
1.8	152.95	198.56	135.36	164.04	213.65	239.75	1343.91	1454.62
2.0	164.46	208.68	149.04	170.55	232.00	261.05	1433.56	1642.15
2.2	175.79	232.00	156.96	182.60	252.45	284.78	1590.7	1652.75
2.4	198.18	241.43	170.61	199.74	268.34	304.72	1663.85	1834.04
2.6	212.43	259.68	186.59	212.41	291.07	322.15	1800.15	1996.00
2.8	228.10	271.40	196.46	228.90	312.84	346.79	1861.04	2049.00
3.0	235.38	287.71	207.89	234.13	323.01	361.53	2130.77	2354.10

Table 5.5 : Quadratic fits for intensity data.

		Quadratic fit ($y=Lx^2+Mx+C$)			
Spectral Size	Sequence	L	M	C	r^2
64K	PENDANT	-3.7693	+92.7136	-4.9149	0.9985
	S-PENDANT	-4.9989	+99.8917	+32.5239	0.9994
32K	PENDANT	-4.5984	+84.0748	-2.7482	0.9991
	S-PENDANT	-5.8752	+91.9329	+13.0275	0.9987
18430W	PENDANT	-6.6549	+129.1204	-0.6265	0.9993
	S-PENDANT	-6.8929	+137.2055	+14.2062	0.9993
4K	PENDANT	-41.3643	+811.05202	-8.6869	0.9957
	S-PENDANT	-47.9087	+865.2221	+68.3631	0.9867

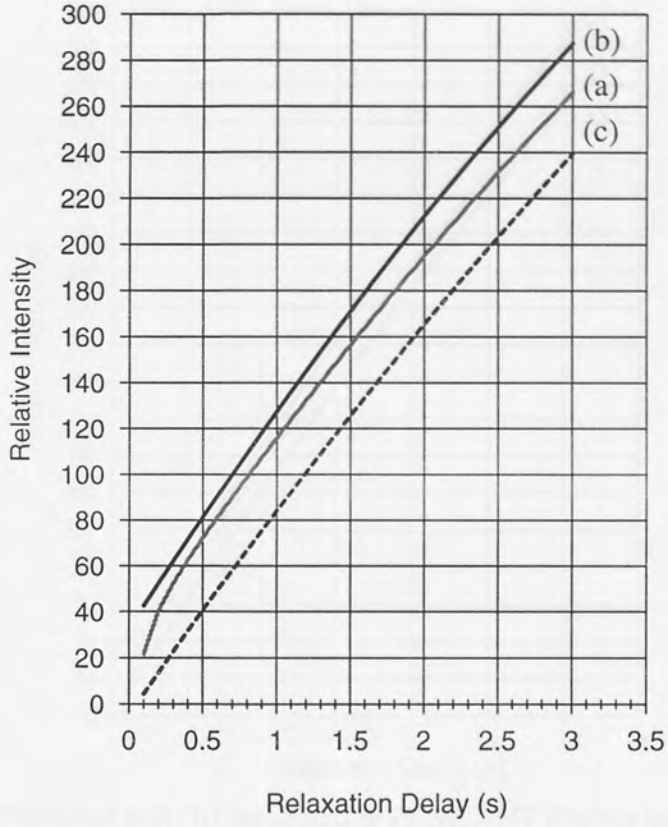

Figure 5.20 : (**a**) Predicted and (**b**) measured S-PENDANT intensities together with (**c**) normal PENDANT intensities for an acquisition time of 1.9s.

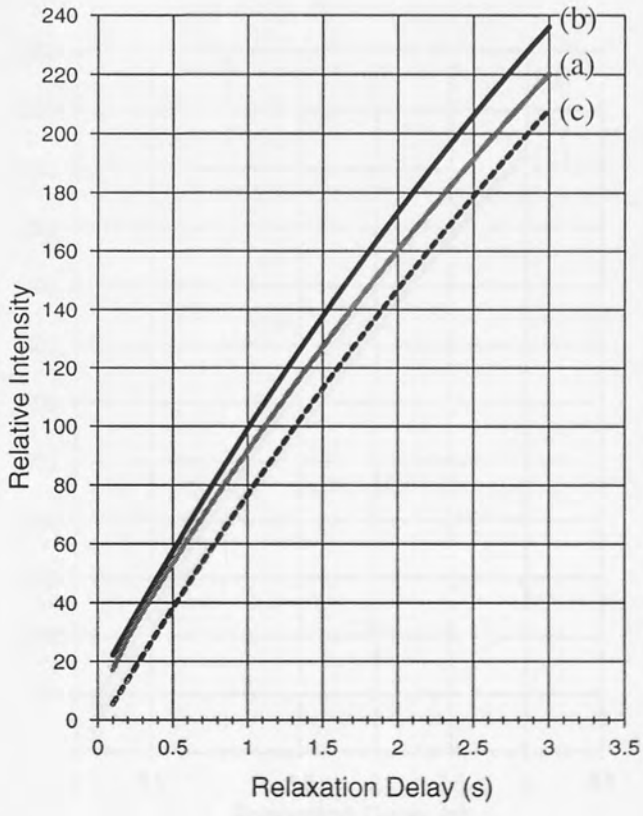

Figure 5.21 : (**a**) Predicted and (**b**) measured S-PENDANT intensities together with (**c**) normal PENDANT intensities for an acquisition time of 0.95 s.

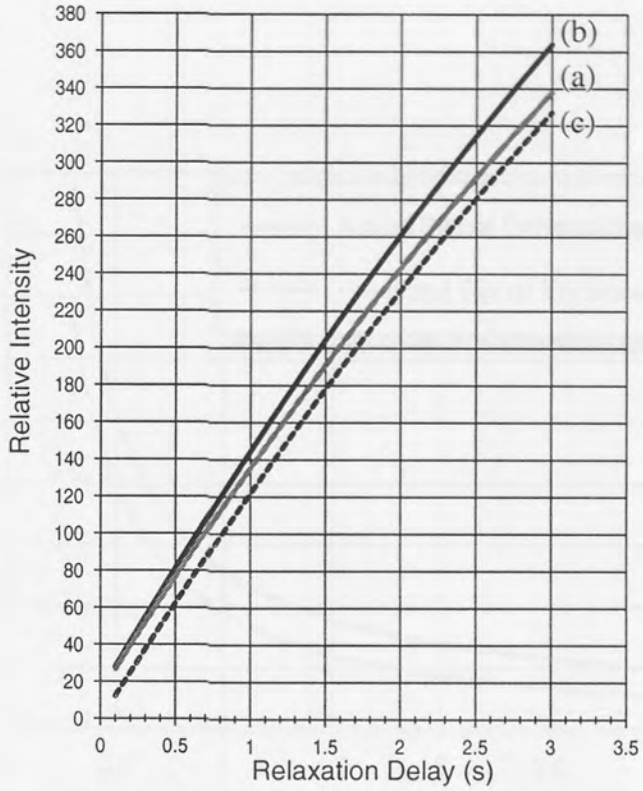

Figure 5.22 : (**a**) Predicted and (**b**) measured S-PENDANT intensities together with (**c**) normal PENDANT intensities for an acquisition time of 0.534 s.

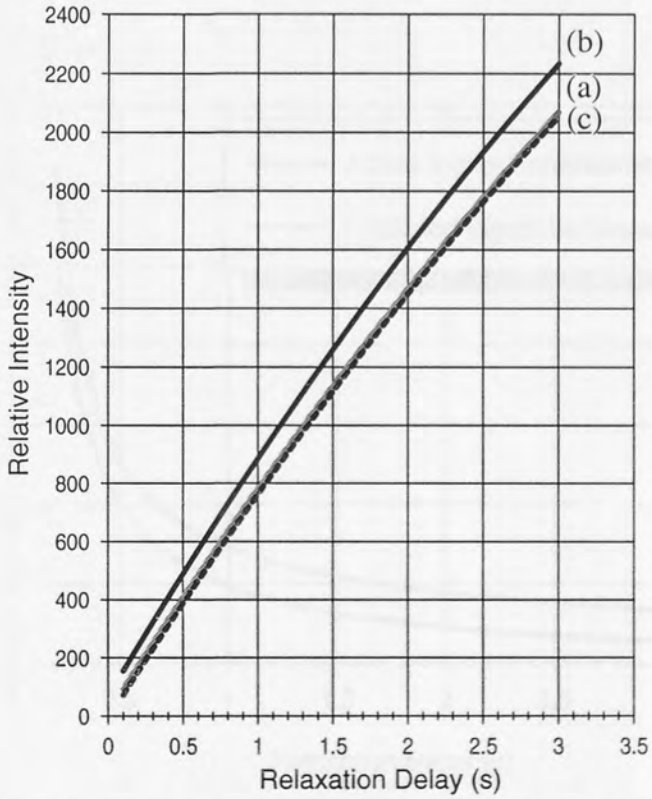

Figure 5.23 : (**a**) Predicted and (**b**) measured S-PENDANT intensities together with (**c**) normal PENDANT intensities for an acquisition time of 0.11875 s.

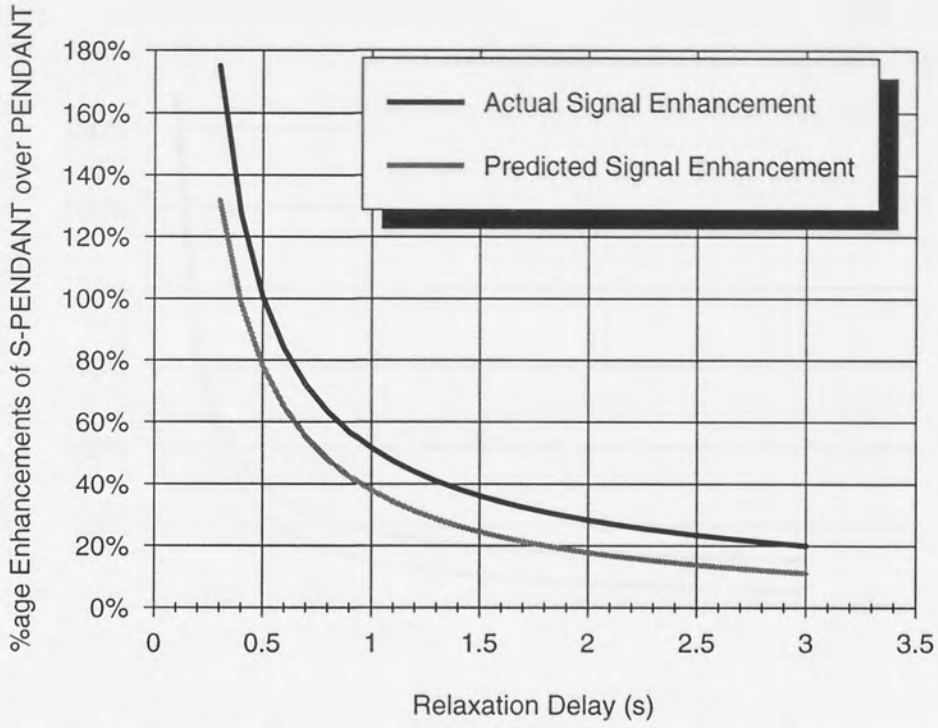

Figure 5.24 : Predicted and measured S-PENDANT percentage enhancements for an acquisition time of 1.9s.

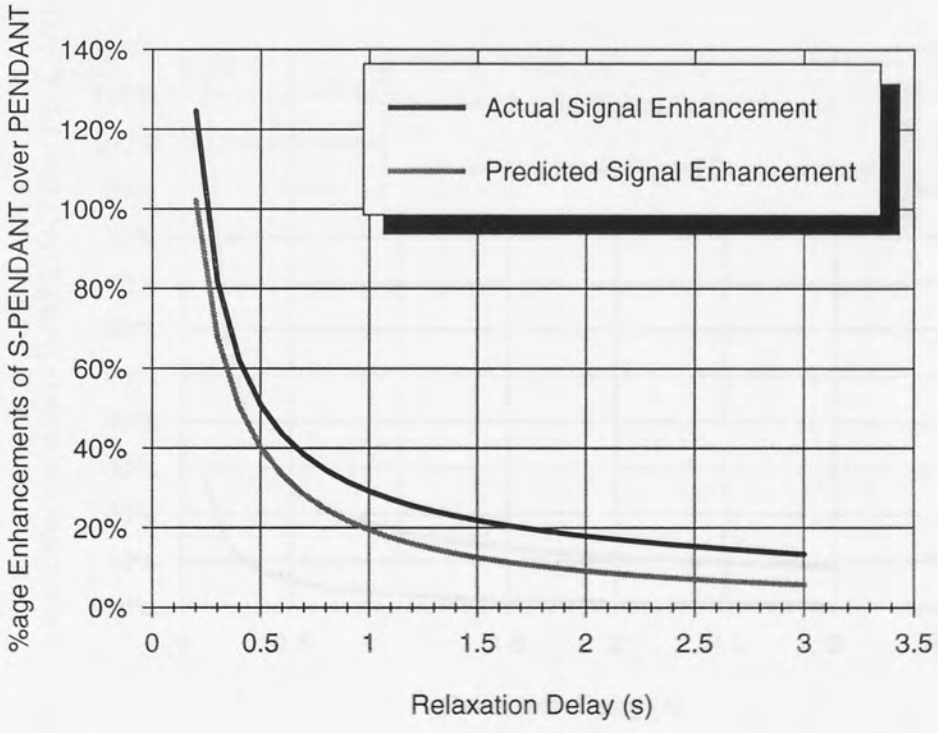

Figure 5.25 : Predicted and measured S-PENDANT percentage enhancements for an acquisition time of 0.95s.

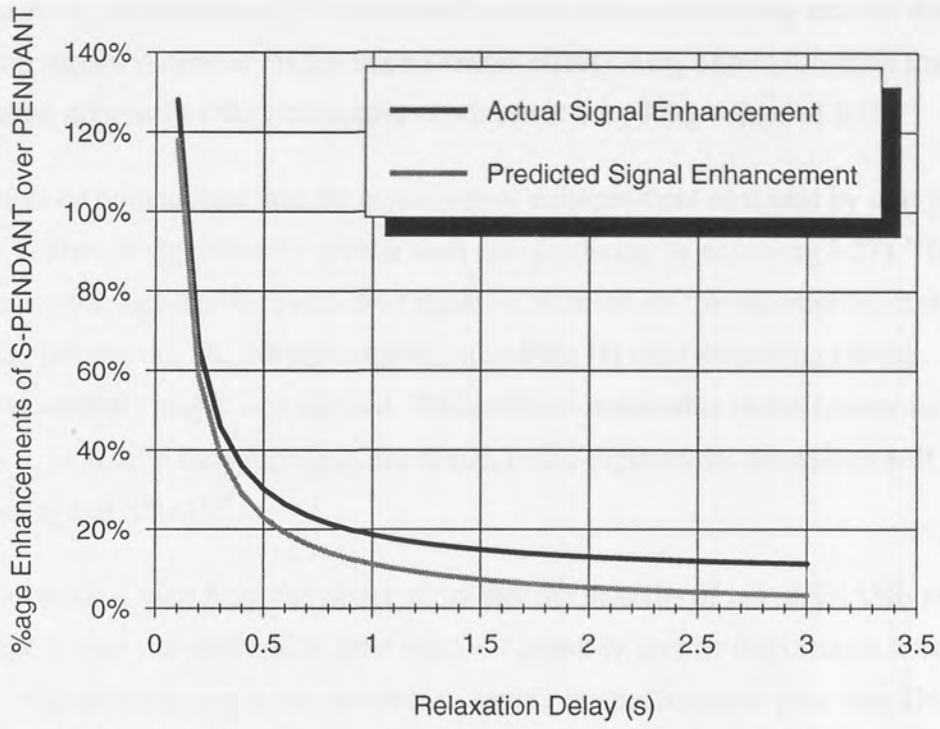

Figure 5.26 : Predicted and measured S-PENDANT percentage enhancements for an acquisition time of 0.534s.

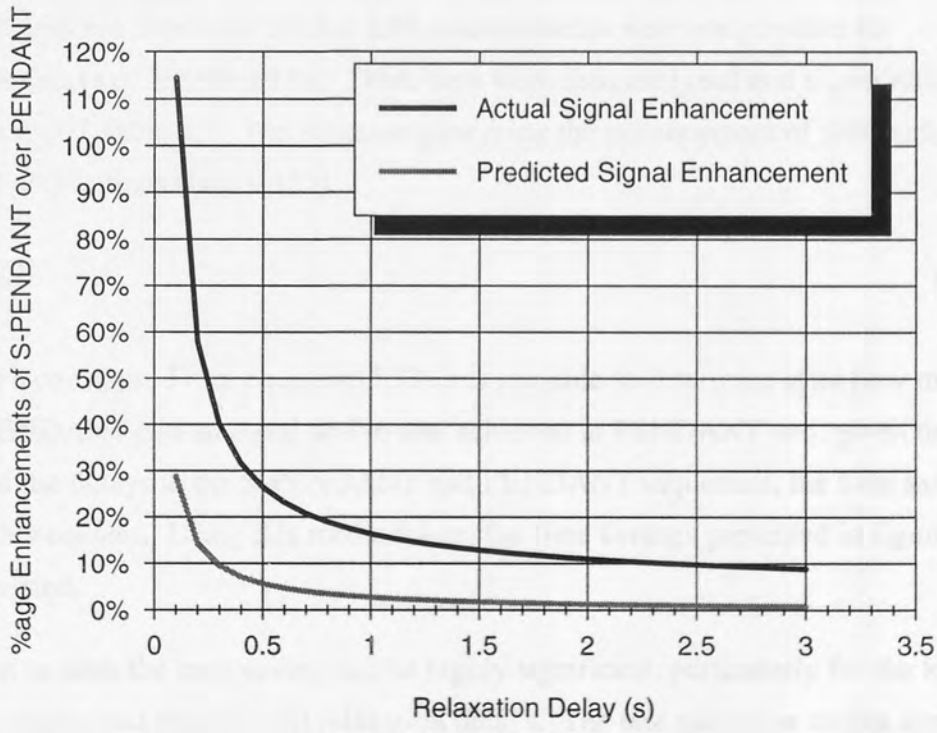

Figure 5.27 : Predicted and measured S-PENDANT percentage enhancements for an acquisition time of 0.11875s.

The experimental data in the above figures reveals that significant signal enhancements can be obtained by replacing a conventional relaxation delay by SNARE. It can be clearly seen that as RD increases the enhancements become smaller due to the step-jump repolarisation of ^{1}H having a smaller effect on the extent to which the ^{1}H polarisation approaches the Boltzmann condition at very long values of RD.

It must be emphasised that the actual signal enhancement obtained by using SNARE is always significantly greater than that predicted by equation(5.27). This is attributed to the fact that the predictive equation is based on the assumption that the relaxation of both the ^{13}C during acquisition and the ^{1}H after switching off the decoupler are truly single exponential. Whilst this is reasonable in the former case it is unlikely to be true in the latter case, for which multi-exponential behaviour will work to the advantage of SNARE.

It can also be seen from the above plots that the benefits of using SNARE are greater the longer the acquisition time used. Of possibly greater importance to routine use of NMR spectroscopy is the percentage saving in spectrometer time that SNARE enables in the achievement of a particular signal/noise ratio obtained by a standard pulse sequence with a conventional relaxation delay. The signal/noise ratio for the experimental data was calculated using the inbuilt facility on the NMR spectrometer and is presented in table 5.6. Due to the exceptionally poor signal levels in the 4K spectra (acquisition time = 0.11875 s) S/N measurements were not possible for relaxations delays of less than 1.0s. These data were then analysed and a quadratic fit to the data found, table 5.7. The equation governing the enhancement of S/N with the number of acquisitions (NS) is [33]

$$\frac{S}{N} = k\sqrt{NS} \qquad (5.33)$$

where k is a constant. From equation(5.33) it is possible to determine after how many scans S-PENDANT had an equal S/N to that achieved in PENDANT and, given the duration of the delays in the S-PENDANT and PENDANT sequences, the time saving to which this equates. Using this methodology the time savings presented in figure 5.28 were calculated.

As can be seen the time saving can be highly significant, particularly for the longer acquisition times and shorter total relaxation delays. The one exception to this appears to be for the 4K (0.11875 s) spectrum. However, this is attributed to errors induced by the poor signal/noise ratio of these spectra.

Table 5.6 : Signal/Noise data for PENDANT and S-PENDANT for a range of spectral sizes and relaxation delays.

Relaxation Delay	64K t_{ac} = 1.9s		32K t_{ac} = 0.95s		18430W t_{ac} = 0.534s		4K t_{ac} = 0.11875s	
	SNARE	Normal	SNARE	Normal	SNARE	Normal	SNARE	Normal
0.0	38.866	-	18.306	-	8.910	-	-	-
0.2	67.422	20.454	34.128	16.294	21.566	16.928	-	-
0.4	89.660	42.570	48.706	33.294	36.734	36.732	-	-
0.6	113.556	66.510	70.932	42.32	49.89	38.858	-	-
0.8	142.012	89.432	83.746	64.442	65.152	57.198	-	-
1.0	161.016	106.250	100.016	78.084	78.796	69.508	36.768	33.614
1.2	185.150	132.118	115.244	98.100	92.100	82.530	39.402	36.168
1.4	202.416	160.118	133.086	113.72	111.168	90.750	42.090	41.350
1.6	230.872	175.304	151.126	122.054	118.184	106.054	39.972	44.890
1.8	247.496	200.198	168.798	146.410	133.742	119.582	45.630	41.666
2.0	260.528	216.964	177.558	154.196	142.798	128.200	48.344	44.652
2.2	294.544	222.618	193.770	165.638	155.808	138.452	47.646	47.246
2.4	295.664	258.426	209.700	175.068	167.508	156.400	57.306	51.834
2.6	327.508	275.976	212.464	206.084	173.886	162.672	60.370	53.936
2.8	334.620	297.578	244.320	207.478	193.998	172.108	57.406	53.908
3.0	-	-	241.824	222.176	198.152	179.472	67.392	61.824

Table 5.7 : Quadratic fits for signal/noise data.

		Quadratic fit ($y=Lx^2+Mx+C$)			
Spectral Size	Sequence	L	M	C	r^2
64K	PENDANT	-2.8564	+113.5215	0	0.9977
	S-PENDANT	-8.9946	+131.5956	+39.53360	0.9978
32K	PENDANT	-2.8185	+82.8260	0	0.9930
	S-PENDANT	-4.3971	+90.1920	+16.0758	0.9967
18430W	PENDANT	-4.4838	+73.8678	0	0.9972
	S-PENDANT	-4.2356	+76.9275	+7.6927	0.9985
4K	PENDANT	-	+12.238	+21.987	0.9378
	S-PENDANT	-	+14.394	+20.515	0.9200

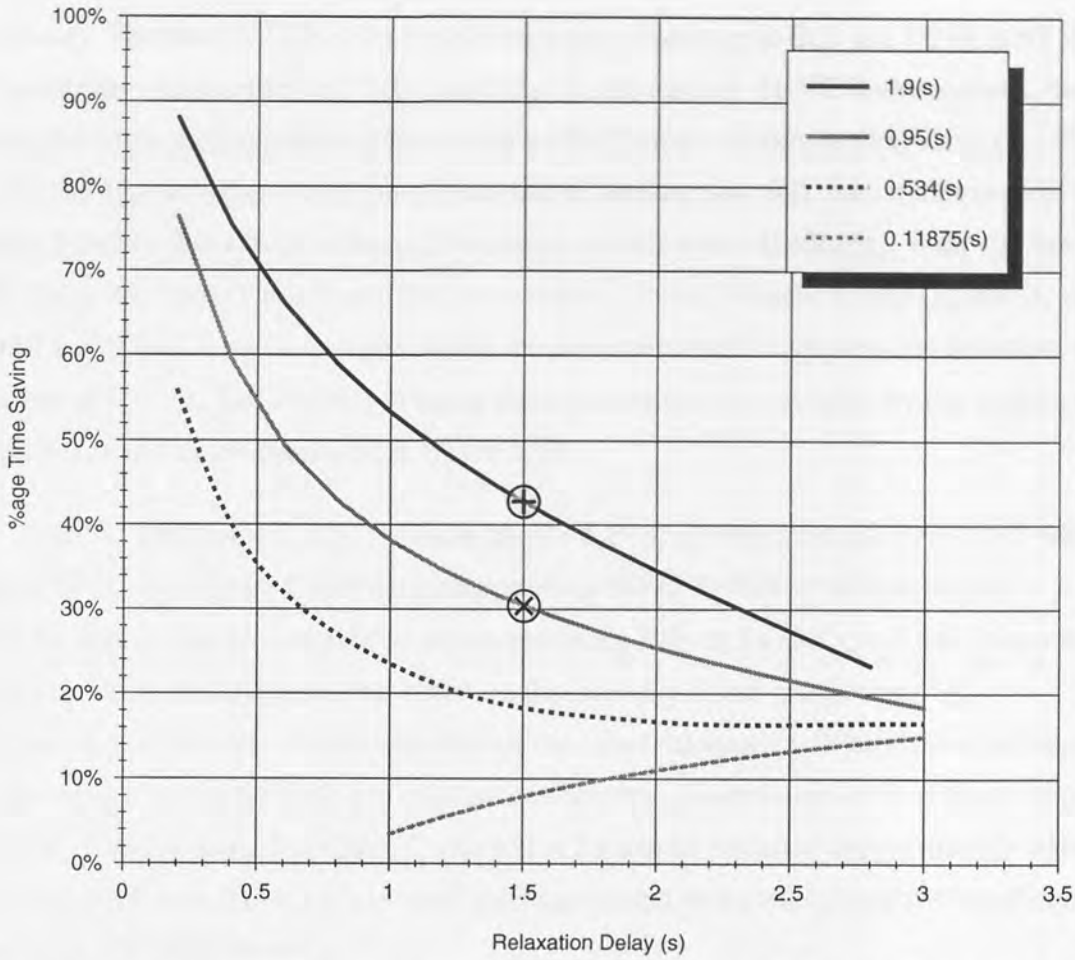

Figure 5.28 : Percentage time savings of S-PENDANT over PENDANT for acquisition times of 1.9s, 0.95s, 0.534s and 0.11875s.

In order to emphasise the conclusions drawn above, attention is drawn to data obtained under the commonly used routine conditions based on 32 K spectra obtained with an acquisition time of 0.95s and a relaxation delay of 1.5 s. These reveal that in a fixed investigative time requiring 48 transients S-PENDANT, relative to PENDANT, permits a percentage increase in signal intensity of 22%, or the achievement of a fixed S/N with a 30% time saving (marked by ⊗ on figure 5.28): the corresponding values for an acquisition time of 1.9 s are approximately 36% and 41% (marked by ⊕ on figure 5.28).

Turning now to the practicalities of using SNARE for studies of molecules containing S, S(I), $S(I_2)$ and $S(I_3)$ nuclear systems, it is evident from the earlier discussion that the inverse repolarisation of I will be largest for the S(I) group. Naturally, it will prove beneficial to equalise the repolarisation advantages across the range of S(I), $S(I_2)$ and $S(I_3)$ systems. The simulations indicate that this is possible to some extent by using $D_1 \approx 1/4J$ and $D_2 \approx 1/2J$. However, the advantages to the $S(I_3)$ systems are not greatly improved and an alternative method of compromise is

necessary. For this SNARE is set to maximise the advantage to S(I) and PENDANT set to favour the enhancement of $S(I_2)$ and $S(I_3)$. In the case of ^1H-^{13}C investigations, the latter condition can be achieved by reducing <J> from the recommended value of 145 Hz to 135 Hz (a further reduction is inadvisable because this will reduce the range of actual J-values that can be embraced to ensure reliable spectral editing). With <J> set at 135 Hz in PENDANT it is found that the value of <J> in SNARE, where D_1 and D_2 are 0.31/J and 0.49/J respectively (favouring the maximum total magnetization transfer), is best set at 160 Hz. The benefits of using these parameters are revealed by the spectra of ethyl benzene that are presented in figure 5.29.

The ^{13}C spectrum of ethyl benzene (figure 5.29.a) obtained using PENDANT with <J>=135 Hz is compared with the corresponding S-PENDANT spectrum (figure 5.29.b), obtained as recommended above and using RD= 0.5 s and t_{ac}= 1.84s. It can be seen that while SNARE has little effect on the intensity of the quarternary ^{13}C resonance, it effectively doubles the S/N of the other resonances. When RD is increased the benefits of using SNARE are reduced as expected. Nevertheless, it was found that the S/N obtained using PENDANT with RD = 2 s can be equalled approximately when S-PENDANT with RD = 1.5 s is used: the time-saving will evidently prove beneficial in routine ^{13}C NMR investigations.

The versatility of SNARE is illustrated through the comparison of the DEPT [138, 140, 141] (135°) and S-DEPT(135°) ^1H-^{13}C spectra of ethyl benzene in figure 5.29.c and 5.29.d. A detailed comparison of the figure 5.29.a and 5.29.b with the corresponding 5.29.c and 5.29.d reveal the two-fold benefits of using PENDANT rather than DEPT (135°). These are that isolated S nuclei can be detected simultaneously with $S(I_n)$ nuclei when using PENDANT, unlike DEPT which also reveals generally poorer S/N.

For pulse sequences that involve polarisation transfer, or exchange, with the sensitive nucleus decoupled during detection of insensitive nuclei, it is demonstrated that the dominant relaxation of the sensitive nuclei can be accelerated by inverse polarisation from the insensitive nuclei through the use of the magnetisation of the latter that develops under nOe conditions during the acquisition of the FID. In general the benefits of SNARE are greater the longer the acquisition time and the shorter the intersequence relaxation delay. SNARE should be capable of advantageously replacing the relaxation delay in many pulse sequences, including those that are designed to yield multi-dimensional spectra.

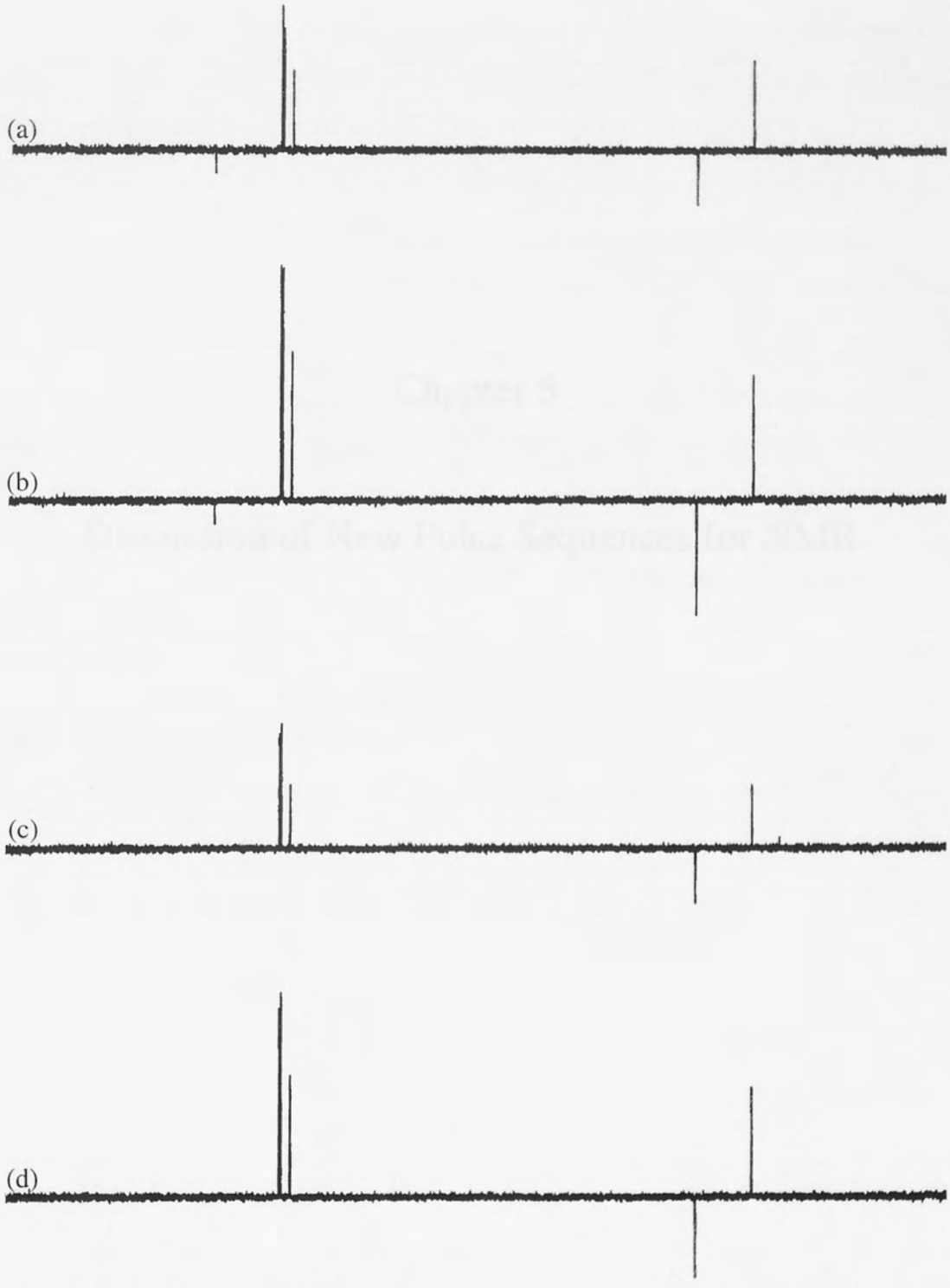

Figure 5.29 : ^{13}C Spectra of ethyl benzene obtained by using (**a**) PENDANT, (**b**) SNARE-PENDANT, (**c**) DEPT (135°) and (**d**)SNARE-DEPT (135°) : <J>=135Hz in PENDANT and DEPT(135°) and <J>=160Hz in SNARE.

Chapter 5

Discussion of New Pulse Sequences for NMR.

5.1 Discussion.

This section proposed two new pulse sequences for use in NMR spectroscopy; DEPENDANT, a 2D technique giving a proton/carbon correlation spectrum with the addition of quarternary carbons, and SNARE, a 'sub-sequence' for inclusion with standard pulse sequences which improves the S/N ratio.

While, as discussed in the relevant section, it was not possible to develop DEPENDANT into a usable technique, the performance of SNARE however, exceeded the theoretical expectation.

Currently the SNARE pulse sequence has to be physically written into existing pulse programs. It is, therefore, suggested that future work in this area not only continues the investigation into the applicability of SNARE to other pulse sequences, including multi-dimensional pulse sequences, but also includes work to re-write SNARE as a 'micro-program' that can be readily called by the use of a simple command from any other existing pulse sequence.

If J-based sequences can indeed be adapted to work with dipolar systems SNARE should be valuable in work on solids.

Part 6

Overall Conclusions

Conclusions.

The investigation into 'sonically induced narrowing of the NMR spectra of solids' conducted in part 3 was primarily concerned with elucidating the exact role of acoustic cavitation in the incoherent averaging process. Initial experiments concentrated on the nature of cavitation and how the cavitational process may be effected by a magnetic field. Attempts to determine these relationships were made by studying an ultrasonically initiated reaction, the conversion of diethyl maleate to its fumarate form, in separate experiments performed in and out of an intense magnetic field. Although it was not possible to confirm whether it is 'hot spot' theory or 'electric field' theory which more accurately accounts for the action of cavities, the results did show that an increase in magnetic field intensity of 2.1 Tesla had little, if any effect on the rate of cavitational collapse. It is, therefore, hoped that this information will facilitate the conduct of the SINNMR experiment in NMR spectrometers of different magnetic field strengths without dependence on magnetic field strength.

Further experiments in part 3 were conducted concerned with providing a method whereby the rate of cavitational collapse could be quantified. This was attempted through the study of radicals generated by the cavitation using EPR and NMR spectroscopy. The EPR experiments showed that it was possible to irradiate a sample with ultrasound while simultaneously monitoring the radicals induced by the sonication. To the authors knowledge this is the first time an experiment involving the *in situ* detection of radicals via a magnetic resonance technique has been conducted. The aim of the NMR experiments was to measure the CIDNP generated in the radicals by the unpaired electrons. Unfortunately it was not possible to maintain an environment amenable to such measurements.

One of the main hindrances to the experiments conducted in part 3 stems from the ultrasound assembly used in this work and the requirement that the ultrasound be introduced into a sample from above. Currently, co-workers in the author's laboratory are developing an ultrasonic cell which can introduce ultrasound to a sample from below. On successful completion of this project it is suggested that the experiments of part 3 be repeated, using the new equipment. The new equipment should benefit the reproducibility and accuracy of the experiments in two ways. Firstly, with respect to the study of ultrasonically initiated reaction, positioning errors and variable transmission efficiencies introduced by the use of a ultrasonic horn should be eliminated. Secondly, as the transducers will form an integral part of the new cells, it

will become relatively simple to seal the cell and control the environment of the sample.

At the heart of SINNMR lies the concept of incoherent averaging, which the technique induces through the action of ultrasound on a solid suspended in a liquid. This need not be the only method whereby incoherent motion of sufficient magnitude can be induced in solid particles in order to produce narrowed NMR spectra. Another method would appear to be through the utilization of gas fluidized solid samples. The investigations conducted in part 4 examined this possibility and, in particular, the effects of fluidization on granular samples of tri-sodium phosphate dodecahydrate (TSP) and of aluminium. The fluidization of TSP failed to show narrowing of the solid resonance. However, an incidental experiment concerned with granular TSP showed that it is possible to produced narrowed ^{23}Na spectra by partial de-hydration of the solid. This observation had profound implications for the SINNMR technique suggesting that the narrowed spectra it yields may not be caused through incoherent motion as originally reported. Further investigation of the data showed that this was not the case and thus added further weight to the hypothesis that the mechanism fundamental to the averaging mechanism induced by SINNMR is incoherent motion.

The investigations into fluidized samples of aluminium granules encounter problems associated with the establishment of electrostatic charges on the sample. Despite these electrostatic effects being exaggerated by skin depth problems some experiments suggested that the fluidization of the aluminium granules could result in the partial narrowing of the aluminium spectra, reducing the static peak width of the sample by 50%.

The results of part 4 therefore suggest that the investigation of fluidized samples is worth continuing. The investigations could be further assisted by the re-design of the fluidizing sample tubes with the aim of allowing greater fluidizing gas velocities to be used while preventing the entrainment of the sample. Possibly such requirements could be achieved by forcing the air through the sinter in such a way that it forms a vortex within the sample tube.

Part 5 was concerned with the development of two new pulse sequences. The first pulse sequence was to be a multi-dimensional version of PENDANT in which quarternary carbons as well as carbons short range coupled to protons were to feature. Unfortunately, an appropriate pulse program proved elusive. The second pulse sequence was designed to enable some existing pulse sequence (those where insensitive

nuclei are detected while the sensitive nuclei are decoupled and where the technique relies on any form of polarization transfer) to make more efficient use of magnetization, thereby increasing the signal intensity attained for a given experimental relaxation delay. This technique, entitled'Sensitive Nucleus Accelerated Relaxation for Enhancement' (SNARE), yielded excellent results when applied to liquids, in all cases exceeding the signal enhancements predicted by the theory. Under routine experimental conditions the signal enhancement afforded by the implementation of SNARE in PENDANT corresponded to a time saving of 30% over that required for the normal PENDANT experiment.

Due to the lack of progress towards narrow-line spectra the SNARE pulse program developed in part 5 was not adapted for solids. Future work on SNARE should, therefore, concentrate on this adaptation and address any problems that may arise as a consequence. Furthermore, the SNARE pulse program currently has to be manually written into existing pulse sequences. The further development of SNARE should, therefore, also focus on transforming the SNARE pulse program into a 'micro-program' which can be readily called from any other pulse program.

References

References

[1] E.R. Andrew, A. Bradbury and R.G. Eades, "Nuclear Magnetic Resonance Spectra from a Crystal rotated at High Speed.", Nature, 1958, **182**, p1659.

[2] K.T. Mueller, B.Q. Sun, G.C. Chingas, J.W. Zwanziger, T. Terao and A. Pines, "Dynamic-Angle Spinning of Quadrupolar Nuclei.", J. Magn. Reson., 1990, **86**, p470.

[3] A. Samoson, E. Lippmaa and A. Pines, "High Resolution Solid State NMR. Averaging of the Second Order Effects by Means of a Double Rotor.", Mol. Phys., 1988, **65(4)**, p1013.

[4] J. Homer, P.McKeown, W.R. McWhinnie, S.U. Patel and G.J. Tilstone, "Sonically Induced Narrowing of Solid-state Nuclear Magnetic Resonance Spectra: A Possible Alternative to Magic Angle Spinning Nuclear Magnetic Resonance", J. Chem. Soc. Faraday Trans., 1991, **87**, p2253.

[5] E.M. Purcell, H.C. Torrey and R.V Pound, "Resonance Adsorption by Nuclear Magnetic Moments in a Solid.", Phys. Rev., 1946, **69**, p37.

[6] F. Bloch, W.W Hansen and M. Packard, "The Nuclear Induction Experiment.", Phys. Rev., 1946, **69**, p127.

[7] Personal communication with Dr. C. Jaeger, University of Jena.

[8] W. Pauli, "Zuschriften und Vorläufige Mitteilungen", Die Naturwisschaften, 1924, p741.

[9] R.L. Liboff., "Introductory Quantum Mechanics.", Holden-Day Inc., San Francisco, 1980.

[10] R.C. Greenhow., "Introductory Quantum Mechanics : A Computer Illustrated Text.", Adam Hilger, Bristol, 1990.

[11] F. Mandl, "Quantum Mechanics.", John Wiley and Sons, Chichester, 1992.

[12] A.R. Edmonds.,"Angular Momentum in Quantum Mechanics.", Princeton, New Jersey, 1957.

[13] R.N. Zare, "Angular Momentum: Understanding Spacial Aspects in Chemistry and Physics.", Wiley, New York, 1987.

[14] F. Bloch, "Nuclear Induction", Phys. Rev., 1946, **70**, p460.

[15] G.A.Morris and P.B.Chilvers, "General Analytical Solutions of the Bloch Equations.", J. Magn, Res., 1994, **107**, p236.

[16] W. Heisenberg, "Uber den Anschaulichen Inhalt der Quantentheoretischen Kinematik und Mechanik.", Z. Phys., 1927, **43**, p172.

[17] W. Heisenberg, "The Physical Principles of Quantum Theory.", New York, 1930.

[18] N. Bloembergen, E.M. Purcell and R.V. Pound, "Relaxation Effects in Nuclear Magnetic Resonance Adsorption.", Phys. Rev., 1948, **73**, p679.

[19] G. Lindström, "An Experimental Investigation of the Nuclear Magetic Moments of Deuterium and Hydrogen.", Phys. Rev., 1950, **78**, p817.

[20] J.W. Emsley, J. Feeney and L.H. Sutcliffe, "High Resolution Nuclear Magnetic Resonance Spectroscopy: Vol 1.", Pergamon Press, Oxford, 1965, p4.

[21] H.A. Thomas, "The Diamagnetic Correction for Protons in Water and Mineral Oil.", Phys. Rev., 1950, **80**, p910.

[22] I.U.P.A.C, "Recommendations for the Presentation of NMR Data for Publications in Chemical Journals.", 1972, **29**, p627.

[23] I.U.P.A.C, "Presentation of NMR Data for Publication in Chemical Journals - B. Conventions relating to spectra from nuclei other than protons.", Pure Appl. Chem.,1976, **45**, p217.

[24] W.D. Knight, "Electron Paramagnetic and Nuclear Magnetic Resonace in Metals.", Solid State Phys., 1956, **2**, p1259.

[25] J. Winter, "Magnetic Resonance In Metals.", Oxford, London, 1971.

[26] H.S. Gutowsky and D.W. McCall, "Nuclear Magnetic Resonance Fine Structure in Liquids.", Phys. Rev., 1951, **82**, p748.

[27] W.G. Procter and F.C. Yu, "Nuclear Magnetic Resonace Fine Structure in Liquids.", Phys. Rev., 1951, **81**, p20.

[28] S.A. Smith, W.E. Palke and J.T. Gerig, "The Hamiltonians of NMR : Part 1.", Concepts Magn. Reson., 1992, **4**, p107.

[29] S.A. Smith, W.E. Palke and J.T. Gerig, "The Hamiltonians of NMR : Part 2.", Concepts Magn. Reson., 1992, **4**, p181.

[30] R.R. Ernst and W.A. Anderson, "Application of Fourier Transform Spectroscopy to Magnetic Resonance.", Rev. Sci. Instrum., 1966, **37**, p93.

[31] R.R. Ernst, "Sensitivity Enhancement in Magnetic Resonance.", Adv. Magn. Reson., 1966, **2**, p1.

[32] T.C. Farrar and E.D. Becker, "Pulse and Fourier Transform NMR.", Academic Press, New York, 1971.

[33] D.D.Traficante, "Time Averaging. Does the Noise Really Average Toward Zero?", Concepts Magn. Reson., 1991, **3**, p83.

[34] R. Bracewell, "The Fourier Transform and its Applications.", 2nd Edition, McGraw-Hill, New York, 1978.

[35] J.Jeener, Ampere Summer School, Basko Polje, Yugoslavia, 1971.

[36] W.P. Aue, E. Bartholdi, R.R. Ernst, "Two Dimensional Spectroscopy. Application to Nuclear Magnetic Resonance.", J. Phys. Chem., 1976, **64**, p2229.

[37] S.W. Fesik and E.P.R Zuiderweg., "Heteronuclear 3-Dimensional NMR Spectroscopy - A Strategy for the Simplification of Homonuclear 2-Dimensional NMR Spectra.", J. Magn. Reson., 1988, **78**, p588.

[38] L.E. Kay, M. Ikura, M. Tchudin and A. Bax, "3-Dimensional Triple-Resonance NMR Spectroscopy of Isotopically Enriched Proteins.", J. Magn. Reson., 1990, **89**, p496.

[39] L.E. Kay, G.M. Clore, A. Bax and A.M Gronenborn, "4-Dimensional Heteronuclear Triple-Resonance NMR Spectroscopy of Interleukin-1-beta in solution.", 1990, Science, **249**, p411.

[40] G.A.Morris, "Modern NMR Techniques for Structure Elucidation.", Magn. Reson. Chem., 1986, **24**, p371.

[41] R. Freeman, G. A. Morris, "Two-Dimensional Fourier Transformation in NMR, Bulletin of Magnetic Resonance.", 1979,**1(1)**, p5.

[42] H. Kessler, M. Gehrke and C. Griesinger., "Two-Dimensional NMR Spectroscopy : Background and Overview of the Experiments.", Angew. Chem., 1988, **27**, p490.

[43] M. Goez, "Flip Angle Calibration of NMR Pulses.", Magn. Reson. Chem., 1992, **30**, p958.

[44] R. Freeman, S. Kempsell and M.H. Levitt, "Radiofrequency Pulse Sequences Which Compensate Their Own Imperfections.", J. Magn. Reson., 1980, **38**, p453.

[45] J.W. Cooper, "The Computer in Fourier Transform NMR.", Top. Carbon-13 NMR Spectrosc., 1976, **2**, p391.

[46] S. Goldman, "Information Theory.", Practice Hall, Engle Cliffs, NJ, USA. 1953.

[47] D.I. Hoult., "The NMR Receiver : A Description and Analysis of Design.", 1978, Progr. NMR Spectr., **12**, p41.

[48] G. Bodenhausen, R. Freeman, G.A. Morris, R. Niedermeyer, D.L. Turner, "A Simple Approach to Single Channel Quadrature Detection.", J. Magn. Reson., 1977, **25**, p559.

[49] A.G. Redfield and S.D. Kunz., "Quadrature Fourier NMR Detection.", J. Magn. Reson., 1975, **19**, p250.

[50] R.R. Ernst, G. Bodenhausen and A. Wokaun, "Principles of Nuclear Magnetic Resonance in One and Two Dimensions.", Chapter 4.3.1.5, p153, 1990, Oxford Univ. Press, Oxford.

[51] D.M. Brink and G.R. Satchler, "Angular Momentum.", 1968, Clarendon Press, Oxford.

[52] I.J. Lowe, "Free Induction Decays of Rotating Solids.", Phys. Rev. Lett., 1959, **2(7)**, p285.

[53] X. Wu and K.W.Zilm, "Cross Polarization with High-Speed Magic-Angle Spinning.", J. Magn. Reson., 1993, Series **A 104**, p154.

[54] J. Schaefer and E.O. Stejskal, "Carbon-13 Nuclear Magnetic Resonance of Polymers rotating at the Magic Angle.", J. Am. Chem. Soc., 1976, **98(4)**, p1031.

[55] K.W. Zilm and D.M. Grant, "High-Resolution NMR Spectra with J Couplings in Solids.", J. Magn. Reson., 1982, **48**, p524.

[56] E.R. Andrew, "The Narrowing of NMR Spectra of Solids by High-Speed Specimen Rotation and the Resolution of Chemical Shift and Spin Multiplet Structures for Solids.", Prog. NMR Spectry., 1971, **8**, p1.

[57] A. Pines, M.G. Gibby and J.S. Waugh, "Proton Enhanced NMR of Dilute Spins in Solids.", J. Chem. Phys., 1973, **59**, p569.

[58] G. Jeschke and G. Grossmann, "Spinning-Sideband-Pattern Deviations in Cross-Polarization MAS NMR Spectra.", J. Magn. Reson., 1993, **103**, p323.

[59] R.K. Harris and A.C. Olivier, "Quadrupolar Effects Transferred to Spin-1/2 Magic-Angle Spinning Spectra of Solids.", Prog. NMR Spectry., 1992, **24**, p435.

[60] J.G.Hexem, M.H.Frey and S.J.Opella, "Molecular and structual information fro ^{14}N-^{13}C dipolar couplings manifested in high resolutuion ^{13}C NMR spectra of solids.", J. Chem. Phys., 1982, **77(7)**, p3847.

[61] A.C. Olivieri, "Dipolar and Scalar Coupling in Magic Angle Spinning Solid-State NMR Spectra of Spin 1/2 Nuclei Affected by Quadrupolar Nuclei with Large Quadrupole Coupling Constants.", J. Magn. Reson., 1993, **101**, p313.

[62] A. Llor and J. Virlet, "Towards High-Resolution NMR of More Nuclei in Solids: Sample Spinning with Time Dependent Spinner Axis Angle.", Chem. Phys. Lett., 1988, **152**, p248.

[63] Y. Wu, D. Lewis, J.S. Frye, A.R. Palmer and R.A. Wind, "Cross-Polarization Double-Rotation NMR.", J. Magn. Reson., 1992, **100**, p425.

[64] B.Q. Sun, J.H. Baltisberger, Y. Wu, A. Samosen and A. Pines, "Sidebands in Dynamic Angle Spinning (DAS) and Double Rotation (DOR) NMR.", Solid State NMR, 1992, **1**, p267.

[65] A. Samoson and E. Lippmaa,"Synchronized Double-Rotation NMR Spectroscopy.", J. Magn. Reson., 1989, **84**, p410.

[66] J.S. Waugh, L.M. Huber and U. Haeberlin, "Approach to High-Resolution NMR in Solids.", Phys. Rev. Lett., 1968, **20**, p180.

[67] U. Haeberlin,"High Resolution NMR in Solids, Selective Averaging.", Suppliment 1, 1976, Adv. Magn. Reson., Academic Press, New York.

[68] P. Mansfield, "Symmetrized Pulse Sequences in High Resolution NMR in Solids.", J. Phys. C: Solid State Phys., 1971, **4**, p1444.

[69] P. Mansfield, M.J. Orchard, D.C. Stalker and K.H.B. Richards, "Symmetrized Multipulse Nuclear Magnetic Resonance Experiments in Solids: Measurement of the Chemcial Shift Shielding Tensor in Some Compounds.", Phys. Rev., 1973, **B7**, p90.

[70] A.N. Garroway, P. Mansfield and D.C. Stalker, "Limits to Resolution in Multiple-Pulse NMR.", Phys. Rev., 1975, **B11**, p121.

[71] W.K. Rhim, D.D. Elleman and R.W. Vaughan, "Enhanced Resolution for Solid State NMR.", J. Chem. Phys., 1973, **58(4)**, p1772.

[72] W.K. Rhim, D.D. Elleman, R.W. Vaughan, "Analysis of Multiple Pulse NMR in Solids.", J. Chem. Phys., 1973, **59(7)**, p3740.

[73] R.E. Taylor, R.G. Pembleton, L.M. Ryan and B.C. Gerstein, "Combined Multiple Pulse NMR and Sample Spinning: Recovery of Proton Chemical Shift Tensors.", J. Chem. Phys., 1979, **71**, p4541.

[74] D.P. Burum,"Combined Rotation and Multiple Pulse Spectroscopy (CRAMPS).", Concepts Magn. Reson., **2**, p213

[75] D.P. Burum and W.K. Rhim, "Proton Anisotropic Chemical Shift Spectra in a Single Crystal of Hexagonal Water.", J. Chem. Phys., 1979, **71**, p3139.

[76] D.P. Burum and W.K. Rhim, "An Improved NMR Technique for Homonuclear Dipolar Decoupling in Solids: Application to Polycrystalline Ice.", J. Chem. Phys., 1979, **70(7)**, p3553.

[77] D.P. Burum and W.K. Rhim, "Proton NMR Study of Gypsum, $CaSO_4.2H_2O$, Using an Improved Technique for Homonuclear Dipolar Decoupling in Solids.", J. Magn. Reson., 1979, **34**, p241.

[78] G.E. Maciel, C.E. Bronnimann and B.L. Hawkins, "High-resolution 1H Nuclear Magnetic Resonance in Solids via CRAMPS.", Adv. Magn. Reson., 1990, **14**, p125.

[79] M.L. Buszko, C.E. Bronnimann and G.E. Maciel, "^{1}H CRAMPS Based on TREV.", J. Magn. Reson., 1993, **103**, p183.

[80] A.J. Vega and A.D. English, "Multiple-Pulse Nuclear Magnetic Resonance of Solid Polymers. Polymer Motions in Crystalline and Amorphous Poly(tetrafluoroethylene).", Macromol., 1979, **13**, p1635.

[81] A.D. English and A.J. Vega, "Multiple Pulse Nuclear Magnetic Resonance of Solid Polymers: Dynamics of Poly(tetrafluoroethylene).", Macromol., 1979, **12**, p353.

[82] E.R. Andrew and R.G. Eades, "Possibility for High-Resolution Nuclear Magnetic Resonance Spectra of Crystals.", Disc. Faraday Soc., 1962, **34**, p38.

[83] A. Bradbury, R.G. Eades and J.G. McCarten, "Nuclear Magnetic Resonance in a Rotating Magnetic Field.", Phys. Lett., 1968, **26A**, p405.

[84] J.P. Yesinowski, "High-Resolution NMR Spectroscopy of Solids and Surface Adsorbed Species in Colloidal Suspension: ^{31}P NMR Spectra of Hydroxyapatite and Diphosphonates.", J. Am. Chem. Soc., 1981, **103**, p6266.

[85] J.P. Yesinowski, "High-Resolution NMR of Solids and Surface-Adsorbed Species in Colloidal Susspensions: ^{31}P NMR of Hydroxyapatite and Diphosphonates.", 20th Experimental NMR Conference, Asilomar, California, USA, 1979.

[86] K. Kimura and N. Satoh, "High Resolution Solid State NMR of $^{27}AlF_3$ Particles Observed by a Conventional Fourier Transform Spectrometer.", Chem. Lett. (Jpn.), 1989, p271.

K. Kimura and N. Satoh., Errata : Chem. Lett. (Jpn.), 1989, p1317.

[87] N. Satoh and K. Kimura, "High Resolution Solid State NMR in Liquids. 2. ^{27}Al NMR Study of AlF_3 Ultrafine Particles.", J. Am. Chem. Soc., 1990, **112**, p4688.

[88] J. Homer and M.J. Howard, "Studies on the Origin of Sonically Induced Narrowing of Solid-state Nuclear Magnetic Resonance Spectra.", J. Chem. Soc. Faraday Trans., 1993, **89(16)**, p3029.

[89] R.W.B. Stephens and A.E. Bate, Acoustics and Vibrational Physics: 2nd Edition, London, 1966

[90] N. Serpone and P. Colarusso.,"Sonochemistry 1: Effects of Ultrasounds on Heterogeneous Chemical Reactions - A Useful Tool to Generate Radicals and to Examine Reaction Mechanisms.", Res. Chem. Intermed., 1994, **20**, p635.

[91] P. Curie and J. Curie, "Dévelopment, par Pression, de l'électricité Polaire dans les Cristaux Hémièdres à Faces Inclinéesé.", Compt. Rend., 1880, **91**, p294.

[92] Editor T. J. Mason, "Chemistry with Ultrasound.", Elsevier Applied Science, 1990.

[93] Editor G.J. Price, "Current Trends in Sonochemistry.", Royal Society of Chemistry, Cambridge., 1992.

[94] A. A. Atchley and L. A. Crum, "Acoustic Cavitation and Bubble Dynamics in, ultrasound: It's Chemical, Physical and Biological Effects.","Ultrasound : It's Chemical, Physical and Biological Effect.", Editor K.S. Suslick, VCH Publications, New York, 1988.

[95] E. N. Harvey, K. K. Barnes, W. D. McElroy, A. H. Whitely, D. C. Pease and K. W. Cooper, "Bubble Formation in Animals (1). Physical Factors.", J. Cell. Comp. Physiol., 1944, **24**, p1.

[96] K.S. Suslick, R.E. Cline Jr. and D.A. Hammerton, "The Sonochemical Hot-Spot.", J. Am. Chem. Soc., 1986, **108**, p5641.

[97] T.J. Mason, Chapter 1,"Introduction", "Chemistry with Ultrasound.", Elsevier Applied Science, 1990.

[98] R.E. Apfel, "Methods of Experimental Physics.", ed. P.D. Edmonds, Academic Press, New York, 1981, vol .19, ch.7.

[99] M.A. Margulis, "Study of Electrical Phenomena Related to Cavitation. I. Electrical Theories of Chemical and Physicochemical Action of Ultrasound." , Zh. Fiz. Khim., 1981, **55**, p154.

[100] M.A. Margulis, "Study of Electrical Phenomena Associated with Cavitation. II. Theory of the Development of Sonoluminescence in Acoustochemical Reactions.", J. Phys. Chem. (Russian), 1985, **59(6)**, p882.

[101] M. S. Plesset and R. B. Chapman, "Collapse of an Initially Spherical Vapour Cavity in the Neighbourhood of a Solid Boundary.", J. Fluid. Mech., 1971, **47**, p283.

[102] P. Renaud, "Hypothèse d'un Effet Réciproque de l'électrostriction Produit par l'ultrasonnation des Solvants Hydroides.", J. Chim. Phys., 1953, **50**, p135.

[103] R. O. Prudhomme, D. Picard and R. G. Busnel, "Sur l'utilisation Chimique de l'energie Acoustique émise par le Quartz dans les Réactions Ultrasonores.", J. Chim. Phys., 1953, **50**, p107.

[104] J. Homer, S. Reynolds and A.Weekes., unpublished work.

[105] J. Reisse, D-H Yang, M Maeck, J. Vandercammen and E.V. Donckt., "Sonochemistry : A systematic study of the maleate-fumarate isomerization in the presence of alkyl bromides.", Ultrasonics, 1992, **30(6)**, p397.

[106] L. Broeckbaert, T. Caulier, O. Fabre, C . Maerschalk, J. Reisse, J. Vandercammen and D.H. Yang, "Quantitative Homogeneous Sonochemistry : Scope and Limitation.", "Current Trends in Sonochemistry." Edited by G.J.Price, Royal Society of Chemistry, Cambridge., 1992, p8.

[107] B. Brown and J.E. Goodman, "High-Intensity Ultrasonics", London, 1965, Chapter 2.

[108] R. Kaptein., Biol. Magn. Reson., 1982, **4**, p145

[109] U.E. Steiner and T. Ulrich, "Magnetic Field Effects in Chemical-Kinetics and Related Phenomena.", Chem. Rev., 1989, **89**, p51.

[110] K.M. Salikhov, Yu.N. Molin, R.Z. Sagdeev and A.L. Buchachenko., "Spin Polarization and Magnetic Effects in Radical Reactions.", Elsevier, Amsterdam, 1984.

[111] V.F Tarasov and I.A. Shkrob, "Low-Field CIDNP in Intramicellar Radical Disproportionation. Violation of Equivalency in J-coupled Nuclear Spin Systems.", J. Magn. Reson., Series **A 109**, 1994, p65.

[112] for example see R.S. Davidson., "Ultrasonically Assisted Organic Synthesis.", "Chemistry with Ultrasound.", Editor T.J.Mason, Elsevier Applied Science, 1990, p82.

[113] J. Homer and J.K.Roberts,"Conditions for the Driven Equilibrium Single Pulse Observation of Spin-Lattice Relaxation Times.", J. Magn. Reson., 1987, **74**, p424.

[114] J. Homer and J. K. Roberts, "Routine Evaluation of M_o Ratios and T_1 Values from Driven-Equilibrium NMR Spectra.", J. Magn. Reson., **89**, p265.

[115] J. Homer and M.S. Beevers, "Driven-Equilibrium Single-Pulse Observation of T_1 Relaxation. A Reevaluation of a Rapid 'New' Method for Determining NMR Spin-Lattice Relaxation Times.", J. Magn. Reson., 1985, **63**, p287.

[116] D. Geldart,"Types of Gas Fluidization.", Powder Technol., 1973, **7**, p285.

[117] R.M. Davies and G. Taylor, "The Mechanics of Large Bubbles Rising Through Extended Liquids and Through Liquids in Tubes.", Proc. R. Soc., 1950, A **200**, p375.

[118] J.F. Davidson and D. Harrison, "Fluidized Particles.", 1963, Cambridge University Press, Cambridge.

[119] J.F. Davidson, Symposium on Fluidization, Trans. Inst. Chem. Eng., 1961, **39**, p230.

[120] R.N. Rowe, P.U. Foscolo, A.C. Hoffman and J.G. Yates, p53 in "Fluidization.", Editor D Kunii and R Toei, 1984, Engineering Foundation, New York.

[121] D. Geldart,"The Effect of Particle Size and Size Distribution on the Behaviour of Gas-Fluidized Beds.", 1972, **6**, p201.

[122] M.J. Howard., "Evaluation of the Sonically Induced Narrowing of Nuclear Magnetic Resonance Spectra of Solids.", Ph.D. Thesis, Aston University, 1994.

[123] E. Tillmanns and W.H. Baur, "On the Stoichiometry of Trisodium Orthophosphate Dodecahydrate", Inorg. Chem., 1970, **9**, p1957.

[124] E.R. Andrew, W.S. Hinshaw and R.S. Tiffen, "More Precise Determination of the Knight Shift of Aluminium.", Phys. Lett., 1973, **46A**, p57.

[125] P.B. Kingsley, "Coherence Pathways and Cartesian Product Operators. The C3PO Method.", J. Magn. Res.,1994, Series **A 107**, p14.

[126] S.A. Smith, W.E. Palke, J.T. Gerig, "Superoperator Propagators in Simulations of NMR Spectra.", J. Magn. Res., 1994, Series **A 106**, p57.

[127] O.W. Sørensen, G.W. Eich, M.H. Levitt, G. Bodenhausen and R.R. Ernst., "Product Operator Formalism for the Description of NMR Pulse Experiments.", Prog. NMR Spectry., 1983, **16**, p163.

[128] F.J.M. van de Ven and C.W. Hilberts., "A Simple Formalism for the Description of Multiple-Pulse Experiments. Application to a Weakly Coupled Two-Spin (I=1/2) System.", J. Magn. Reson., 1983, **54**, p512.

[129] K.J. Packer and P.E. Wright, "The Use of Single-Spin Operator Basis-sets in the NMR Spectroscopy of Scalar Coupled Spin Sytems.", Mol. Phys., 1983, **50**, p797.

[130] L.R. Brown and J. Bremer, "A Unified Product Operator Formalism. Application to Uniform Excitation in Heteronuclear Correlation 2D NMR.", J. Magn. Reson., 1986, **68**, p217.

[131] J. Homer and M.C. Perry., "New Methods for NMR Signal Enhancement by Polarization Transfer, and Attached Nucleus Testing.", J. Chem. Soc. Chem. Comm., 1994, **4**, p373

[132] J. Homer, M.C. Perry., "Enhancement of the NMR Spectra of Insensitive Nuclei Using PENDANT with Long-Range Coupling Constants.", J. Chem. Soc. Perkin Trans.2, 1995, p533.

[133] "The Archimedes Series. BBC Basic Guide.", Acorn Computers Ltd., Cambridge, 1988.

[134] Mike Williams, "Basis V. A Dabhand MiniGuide.", Dabs Press, Manchester, 1989.

[135] ASPECT 3000 User Manual, Brüker Spectrospin Ltd.

[136] 1D WINNMR, Brüker Spectrospin Ltd.

[137] 2D WINNMR, Brüker Spectrospin Ltd.

[138] M.R. Bendall, D.M. Dodrell and D.T. Pegg, "Editing of C-13 NMR Spectra, a Pulse Sequence for the Generation of Subspectra.", J. Am. Chem. Soc., 1981, **103**, p4603.

[139] G.A. Morris and R. Freeman, "Enhancement of Nuclear Magnetic Resonance Signals by Polarization Transfer.", J. Am. Chem. Soc.,1979, **101**, p760.

[140] D.T. Pegg, M.R. Bendall and D.M. Doddrell, "Proton Polarization Transfer Enhancement of a Heteronuclear Spin multiplet with Preservation of Phase Coherency and Relative Component Intensities.", J. Chem. Phys., 1982, **77**, p2745.

[141] D.M. Doddrell, D.T. Pegg and M.R. Bendall, "Distortionless Enhancement of NMR Signals by Polarization Transfer.", J. Magn. Reson., 1982, **48**, p323.

[142] M.H. Levitt, O.W. Sørensen and R.R. Ernst, "Multiplet Separated Heteronuclear 2-Dimensional NMR Spectroscopy.", Chem. Phys. Lett., 1983, **94**, p540.

[143] M.R. Bendall and D.T. Pegg, "H1 - C13 2-Dimensional Chemical Shift Correlation Spectroscopy using DEPT.", J. Magn. Reson., 1983, **53**, p144.

[144] D.T. Pegg and M.R. Bendall, "Two Dimensional DEPT NMR Spectroscopy.", J. Magn. Reson., 1983, **55**, p114.

[145] T.T. Nakashima, B.K. John, R.E.D. McClung, "Selective 2D DEPT Heteronuclear Shift Correlation Spectroscopy.", J. Magn. Reson., 1984, **59**, p124.

[146] A. Hammarstorm and G. Otting, "Axial-Peak Artifacts in Multipulse NMR Experiments.", J. Magn. Reson., 1994, Series **A109**, p246.

[147] O.A. Gansow & A.R. Burke, "A Shiftless Relaxation Reagent for Carbon-13 Magnetic Resonance of Organometallic Carbonyl Compounds.", J. C. S. Chem. Comm., 1972, p456.

[148] L.F. Farnell, E.W. Randall and A.I. White, "The Effect of Paramagnetic Species on the Nuclear Magnetic Resonance Spectra of Nitrogen-15.", J. C. S. Chem. Comm., 1972, p1159.

[149] O.A. Gansow, K.M. Triplett, T.T. Peterson, R.E. Botto and J.D. Roberts., "A 'Shiftless' Relaation Reagent for Metal Nuclide and Nitrogen-15 Magnetic Resonance in Aqueous Solution.", Org. Magn. Reson., 1980, **13(1)**, p77.

[150] J. Homer and S.U. Patel, "Preliminary Observations of High-Resolution Nuclear Magnetic Resonace for Liquids Subjected to Ultrasound.", J. Chem Soc. Faraday Trans., 1990, **86(1)**, p215.

[151] A.A. Maudsley and R.R. Ernst., "Indirect Detection of Magnetic Resonance by Heteronuclear Two Dimensional Spectroscopy.", Chem. Phys. Letters, 1977, **50**, p368.

[152] J.H. Noggle and R.E. Schirmer, "The Nuclear Overhauser Effect, Chemical Applications.", Academic Press, New York, 1971.

[153] A.W. Overhauser, "Polarization of Nuclei in Metals.", Phys. Rev., 1955, **92**, p411.

[154] G. Bodenhausen and D.J. Ruben, "Natural Abundance Nitrogen-15 NMR by Enhanced Heteronuclear Spectroscopy.", Chem. Phys. Letters, 1980, **69**, p85.

[155] G. Bodenhausen, "Multiple-Quantum NMR.", 1980, Progr. NMR Spectr., **14**, p137.

[156] R.L. Vold, J.S. Waugh, M.P. Klein and D.E. Phelps, "Measurement of Spin-Lattice Relaxation in Complex Systems.", J. Chem. Phys., 1968, **48**, p3831.

[157] R. Freeman and H.D.W. Hill, "High Resolution Studies of Nuclear Spin-Lattice Relaxation.", J.Chem. Phys., 1969, **51**, p3140.

[158] R.K. Harris and R.H. Newman, "Choice of Pulse Spacings for Accurate T_1 and NOE Measurements in NMR Spectroscopy.", J. Magn. Reson., 1976, **24**, p499.

Bibliography

Nuclear Magnetic Resonance Spectroscopy.

A. Abragam, "Principles of Nuclear Magnetism", Oxford, 1961.

E.D. Becker, "High Resolution NMR. Theory and Chemical Application", 2nd Edition, Academic Press, New York, 1980.

C. Brevard and P. Granger, "Handbook of High Resolution Multinuclear NMR", Wiley, New York, 1981.

A.E. Derome, "Modern NMR Techniques for Chemistry Research", Pergamon, Oxford, 1987.

J.W. Emsley, J. Feeney and L.H. Sutcliffe, "High Resolution Nuclear Magnetic Resonance Spectroscopy - Volume 1", Pergamon, Oxford, 1965.

J.W. Emsley, J. Feeney and L.H. Sutcliffe, "High Resolution Nuclear Magnetic Resonance Spectroscopy - Volume 2", Pergamon, Oxford, 1965.

R.R. Ernst, G. Bodenhausen and A. Wokaun, " Principles of Nuclear Magnetic Resonance in One and Two Dimensions", Oxford, 1987.

E. Fukushima and S.B. Roeder, "Experimental Pulse NMR, A Nuts and Bolts Approach", Addison-Wesley, USA, 1981.

R.K. Harris, "Nuclear Magnetic Resonance Spectroscopy. A Physicochemical View", Pitman, London, 1983.

J.W. Hennel and J. Klinowski, "Fundamentals of Nuclear Magnetic Resonance", 1993, Longman, England.

S.W. Homans, "A Dictionary of Concepts in NMR", Oxford, 1989.

Ed. G.C. Levy, "NMR Spectroscopy : New Methods and Applications", The American Chemical Society, Washington, 1982.

M.L. Martin, J.-J.Delpuech and G.J. Martin, "Practical NMR Spectroscopy", Heyden, London, 1980.

M. Mehring, "Principles of High Resolution NMR in Solids", 2nd Edition, Springer, New York, 1983.

C.P. Schlicter, "Principles of Magnetic Resonance", 3rd Edition, Springer, New York, 1990.

Ultrasonics

R.T. Beyer and S.V. Letcher, "Physical Ultrasoinics", Academic Press, New York, 1969.

J. Blitz, "Ultrasonics: Methods and Applications", Butterworths, London, 1971.

J. Blitz, "Fundamentals of Ultrasonics", Butterworths, London, 1967.

T.J Mason and J.P. Lorimer, "Sonochemistry, Theory, Application and Use of Ultrasound", Ellis Horwood Ltd, London, 1991.

T.J. Mason, "Chemistry with Ultrasound", Elsevier, Essex, 1990.

Fluidization.

Editors J.F. Davidson and D.Harrison; "Fluidization", Academic Press, London, 1971.

Editors J.F. Davidson, R.Clift and D.Harrison; "Fluidization", 2nd Edition, Academic Press, London, 1985.

Editor D. Geldart, "Gas Fluidization Technology", John Wiley and Sons, Chichester, 1986.

J.R. Howard, "Fluidized Bed Technology. Principles and Application", Adam Hilger, Bristol, 1989.

Appendices

Appendix 1

The Quantization of Angular Momentum.

A1.1 The Postulates of Quantum Mechanics

There is not a unique set of postulates in quantum mechanics, however the following six are commonly used, forming a self-consistent set [A1.1].

A1.1.1 The Wavefunction.

For any particle moving under the influence of an external potential there is an associated wavefunction. That wavefunction determines everything that can be know about the particle and is a single-valued complex function of the coordinates of the particle and time. The squared modulus of the function, evaluated at a particular point and time, is proportional to the probability density of the particle, at that point and time.

A1.1.2 The Schrödinger Equation.

The wavefunction Ψ, satisfies the time-dependent Schrödinger equation at all times, equation(A.1).

$$-\frac{\hbar}{i}\frac{\partial\Psi}{\partial t}(\mathbf{r},t) = -\frac{\hbar}{2m}\nabla^2\Psi(\mathbf{r},t) + V(\mathbf{r},t)\Psi(\mathbf{r},t) \qquad \left(\nabla^2 = \frac{\partial^2}{\partial x^2},\frac{\partial^2}{\partial y^2},\frac{\partial^2}{\partial z^2}\right) \qquad (A.1)$$

where $\mathbf{r}$ is the position vector of the particle, m is the rest mass of the particle and $V(\mathbf{r},t)$ is a function describing a potential which is imposed on a particle.

A1.1.3 Operators.

Every dynamic variable may be represented by a Hermitian operator, that is the matrix that forms the operator and the conjugate transpose of the matrix are identical;

$$\bar{\mathbf{A}}^T = \mathbf{A} \qquad (A.2)$$

The eigenvalues of these operators represent the possible results of measurements of the values of these variables. Immediately after such a measurement the wavefunction of a system will be that eigenfunction of the relevant operator which corresponds to the eigenvalue obtained as a result of the measurement.

Operators may be better exemplified by using a mathematical analogy, equation(A.3).

$$\frac{de^{2x}}{dx} = 2e^{2x} \qquad (A.3)$$

Here, the operator is $\frac{d}{dx}$ and the 'wavefunction' analogue is e^{2x} with the eigenvalue being 2.

A1.1.4 Position and Momentum Operators.

The operators representing the position **r** and momentum **P** of a particle are given by;

$$\hat{\mathbf{r}} = \mathbf{r} \tag{A.4}$$

$$\hat{\mathbf{P}} = -i\hbar\nabla \tag{A.5}$$

respectively. Operators representing other dynamical quantities are related to these operators in the same way that the classical quantities are related to the classical position and momentum variables.

A1.1.5 Expansion postulate.

The eigenfunctions of an operator form a complete set of linearly independent functions such that any acceptable wavefunction can be expressed as a linear superposition of them. If a measurement of the variable represented by the operator $\hat{Q}$ is performed on a system with normalised wavefunctions

$$\psi=\sum_n a_n\phi_n \tag{A.6}$$

where the ϕ_n are normalized eigenfunctions of $\hat{Q}$ with eigenvalue q_n, then the probability of obtaining the result q_n is $|a_n|^2$.

A1.1.6 Poisson Brackets

The commutators of the operators representing dynamical variables in quantum mechanics are proportional to the corresponding classical Poisson bracket. The constant of proportionality is $i\hbar$. For example,

$$[\hat{Q},\hat{R}] \Leftrightarrow i\hbar\{q,r\}. \tag{A.7}$$

A1.2 Quantization of Angular Momentum [A1.2-A1.5]

A1.2.1 Cartesian Components of Angular Momentum

Classically, the angular momentum, **L**, of a particle is a property that depends on a particle's linear momentum, **p**, and it position, **r**, from the designated origin of rotation, and is given by their cross (or vector) product, equation(A.8).

$$\mathbf{L} = \mathbf{r} \times \mathbf{p}$$

$$\mathbf{L} = \overbrace{(x\ y\ z)}^{r} \times \overbrace{\begin{pmatrix} p_x \\ p_y \\ p_z \end{pmatrix}}^{p} = \begin{pmatrix} yp_z - zp_y \\ zp_x - xp_z \\ xp_y - yp_x \end{pmatrix} \tag{A.8}$$

$$\begin{aligned} L_x &= yp_z - zp_y \\ L_y &= zp_x - xp_z \\ L_z &= xp_y - yp_x \end{aligned} \tag{A.9}$$

The quantum mechanical operators which correspond to observing these components of the angular momentum are $\hat{L}_x$, $\hat{L}_y$ and $\hat{L}_z$. Replacing **p** with its corresponding gradient operator (the fourth postulate of quantum mechanics) gives the quantum mechanical components of angular momentum, equations(A.10), (A.11) and (A.12).

$$\hat{L}_x = \hat{y}\hat{p}_z - \hat{z}\hat{p}_y = -i\hbar\left(y\frac{\partial}{\partial z} - z\frac{\partial}{\partial y}\right) \tag{A.10}$$

$$\hat{L}_y = \hat{z}\hat{p}_x - \hat{x}\hat{p}_z = -i\hbar\left(z\frac{\partial}{\partial x} - x\frac{\partial}{\partial z}\right) \tag{A.11}$$

$$\hat{L}_z = \hat{x}\hat{p}_y - \hat{y}\hat{p}_x = -i\hbar\left(x\frac{\partial}{\partial y} - y\frac{\partial}{\partial s}\right) \tag{A.12}$$

which when expressed in terms of the vector linear momentum operator, ∇, becomes

$$\hat{\mathbf{p}} = (\hat{p}_x,\hat{p}_y,\hat{p}_z) = -i\hbar\left(\frac{\partial}{\partial x},\frac{\partial}{\partial y},\frac{\partial}{\partial z}\right) = i\hbar\nabla \tag{A.13}$$

$$\mathbf{L} = -i\hbar\mathbf{r} \times \nabla \tag{A.14}$$

A1.2.2 Commutator Relations and their Implications.

If two operators do not commute then these operators do not have any common eigenfunctions. If, for example, $\hat{L}_x$ does not commute with $\hat{L}_y$, then these components of the angular momentum cannot be simultaneously specified in a single state.

The commutor relationship of two matrices, A and B, signified by enclosing the matrices in square brackets, is give in equation(A.15). Two operators are said to commute only if the commutator relation is zero.

$$[A,B] = AB - BA \tag{A.15}$$

$$\begin{aligned}[\hat{x},\hat{p}_x] &= \hat{x}\hat{p}_x - \hat{p}_x\hat{x} \\ &= x \cdot -i\hbar\frac{\partial}{\partial x} - -i\hbar\frac{\partial}{\partial x}x \\ &= i\hbar\end{aligned} \tag{A.16}$$

A1.2.2.1 Commutator Relation Between the Cartesian Components of Angular Momentum.

Given that the commutator of x and p_x is given in equation(A.16) the commutator relation between $\hat{L}_x$ and $\hat{L}_y$ can be deduced to be ;

$$\begin{aligned}[\hat{L}_x,\hat{L}_y] &= \hat{L}_x\hat{L}_y - \hat{L}_y\hat{L}_x \\ &= (\hat{y}\hat{p}_z - \hat{z}\hat{p}_y)(\hat{z}\hat{p}_x - \hat{x}\hat{p}_z) - (\hat{z}\hat{p}_x - \hat{x}\hat{p}_z)(\hat{y}\hat{p}_z - \hat{z}\hat{p}_y) \\ &= \hat{y}\hat{p}_z\hat{z}\hat{p}_x - \hat{y}\hat{p}_z\hat{x}\hat{p}_z - \hat{z}\hat{p}_y\hat{z}\hat{p}_x + \hat{z}\hat{p}_y\hat{x}\hat{p}_z - \hat{z}\hat{p}_x\hat{y}\hat{p}_z + \hat{z}\hat{p}_x\hat{z}\hat{p}_y + \hat{x}\hat{p}_z\hat{y}\hat{p}_z - \hat{x}\hat{p}_z\hat{z}\hat{p}_y \\ &= \hat{x}\hat{p}_y(\hat{z}\hat{p}_z - \hat{p}_z\hat{z}) - \hat{y}\hat{p}_x(\hat{z}\hat{p} - \hat{p}_z\hat{z}_z) \\ &= i\hbar(\hat{x}\hat{p}_y - \hat{y}\hat{p}_x) \\ &= i\hbar\hat{L}_z\end{aligned} \tag{A.17}$$

similarly yielding;

$$\begin{aligned}[\hat{L}_y,\hat{L}_z] &= i\hbar\hat{L}_x \\ [\hat{L}_z,\hat{L}_x] &= i\hbar\hat{L}_y \\ [\hat{L}_x,\hat{L}_y] &= i\hbar\hat{L}_z\end{aligned} \tag{A.18}$$

or

$$i\hbar\hat{\mathbf{L}} = \hat{\mathbf{L}} \times \hat{\mathbf{L}} \tag{A.19}$$

Following from these expressions it can be deduced that no two values of the Cartesian components of angular momentum can be simultaneously specified in a quantum mechanical state.

A1.2.2.2 Commutator Relation Between the Cartesian Components of Angular Momentum and the Total Angular Momentum.

Expressing the total angular momentum operator $\hat{\mathbf{L}}$ in terms of its cartesian components, equation(A.20), then the magnitude of the vector is given by the square of its coefficients, equation(A.21).

$$\hat{\mathbf{L}} = \mathbf{e}_x\hat{L}_x + \mathbf{e}_y\hat{L}_y + \mathbf{e}_z\hat{L}_z \tag{A.20}$$

$$\hat{L}^2 = \hat{L}_x^2 + \hat{L}_y^2 + \hat{L}_z^2 \tag{A.21}$$

The commutation between the magnitude of the total angular momentum and the z component of the angular momentum is thus found to be;

$$\begin{aligned}
[\hat{L}_z,\hat{L}^2] &= [\hat{L}_z,\hat{L}_x^2 + \hat{L}_y^2 + \hat{L}_z^2] \\
&= [\hat{L}_z,\hat{L}_x^2] + [\hat{L}_z,\hat{L}_y^2] + 0 \\
&= \hat{L}_x[\hat{L}_z,\hat{L}_x] + [\hat{L}_z,\hat{L}_x]\hat{L}_x + \hat{L}_y[\hat{L}_z,\hat{L}_y] + [\hat{L}_z,\hat{L}_y]\hat{L}_y \\
&= i\hbar[\hat{L}_x\hat{L}_y + \hat{L}_y\hat{L}_x - \hat{L}_y\hat{L}_x - \hat{L}_x\hat{L}_y] \\
&= 0
\end{aligned} \tag{A.22}$$

the full set of relationships being;

$$[\hat{L}_x,\hat{L}^2] = 0 \tag{A.23}$$

$$[\hat{L}_y,\hat{L}^2] = 0 \tag{A.24}$$

$$[\hat{L}_z,\hat{L}^2] = 0 \tag{A.25}$$

$$[\hat{\mathbf{L}},\hat{L}^2] = 0 \tag{A.26}$$

These commutators show that $\hat{L}^2$ and any one component $\hat{L}_x$, $\hat{L}_y$ or $\hat{L}_z$ are compatible observables, and that it must be possible to find simultaneous eigen-functions of the total angular momentum and any one of its components. In other words it is quantum mechanically allowed for the magnitude of the angular momentum and the size of one of it Cartesian components to simultaneously be known about a spin system.

A1.2.3 Eigenvalues of the Angular Momentum Operators.

As the angular momentum defined here is quantum it may take on only discrete values, the exact values being deduced by finding the eigenvalues of the angular momentum operators.

It is usual to use the symbol $\hat{\mathbf{J}}$ to describe angular momentum in general while

It is usual to use the symbol $\hat{\mathbf{J}}$ to describe angular momentum in general while reserving $\hat{\mathbf{L}}$ and $\hat{\mathbf{S}}$ to denote orbital and spin angular momentum respectively. Before determining the eigenvalues of the angular momentum operators it is useful to introduce the "ladder operators" . The ladder operators $\hat{J}_+$ and $\hat{J}_-$ are defined according to;

$$\hat{J}_+ = \hat{J}_x + i\hat{J}_y \tag{A.27}$$

$$\hat{J}_- = \hat{J}_x - i\hat{J}_y = \hat{J}_+^\dagger \tag{A.28}$$

Some of the relationships of these operators are defined in table A.1

Table A.1 : Relationships between ladder operators.

Relationship	Result	Equation Number
$[\hat{J}_z,\hat{J}_+]$	$\hbar\hat{J}_+$	(A.29)
$[\hat{J}_z,\hat{J}_-]$	$-\hbar\hat{J}_-$	(A.30)
$[\hat{J}_z,\hat{J}_\pm]$	$\pm\hbar\hat{J}_\pm$	(A.31)
$[\hat{J}^2,\hat{J}_+]$	0	(A.32)
$[\hat{J}^2,\hat{J}_-]$	0	(A.33)
$[\hat{J}^2,\hat{J}_\pm]$	0	(A.34)
$\hat{J}^2$	$\hat{J}_-\hat{J}_+ + J_z^2 + \hbar J_z^2$ $\hat{J}_+\hat{J}_- + J_z^2 - \hbar J_z^2$	(A.35a) (A.35b)
$\hat{J}^2$	$\hat{J}_\mp\hat{J}_\pm + J_z^2 \pm \hbar J_z^2$	(A.36)
$[\hat{J}_+,\hat{J}_-]$	$2\hbar J_z$	(A.37)

Now to determine the eigenvalues of $\hat{J}_z$ and $\hat{J}^2$ firstly let;

$$\hat{J}_z\varphi_m = E\varphi_m \tag{A.38}$$

where E represents the eigenvalues of the wavefunction φ_m. When the $\hat{J}_+$ ladder operator is applied to the wavefunction in equation(A.38) and $\hat{J}_z\varphi_m$ is substituted from equation(A.38) (utilising equation(A.29)) into the resultant expression, it is possible to re-arrange the resultant into a form similar to that in equation(A.38);

$$\hat{J}_z\hat{J}_+\varphi_m = \left([\hat{J}_z,\hat{J}_+] + \hat{J}_+\hat{J}_z\right)\varphi_m$$
$$= (\hbar\hat{J}_+ + \hat{J}_+\hat{J}_z)\varphi_m$$
$$= (\hbar\hat{J}_+ + E\hat{J}_+)\varphi_m$$
$$\hat{J}_z(\hat{J}_+\varphi_m) = \hbar\left(1 + \frac{E}{\hbar}\right)(\hat{J}_+\varphi_m) \qquad (A.39)$$

so substituting E=mħ into equation(A.38) and (A.39) gives equations(A.40) and (A.41) respectively.

$$\hat{J}_z\varphi_m = \hbar m\varphi_m \qquad (A.40)$$
$$\hat{J}_z(\hat{J}_+\varphi_m) = \hbar(m+1)(\hat{J}_+\varphi_m) \qquad (A.41)$$

When moving from equation(A.40) to equation (A.41), φ_m is replaced by $\hat{J}_+\varphi_m$ and m with m+1. If we now re-write equation(A.40) for m=m+1 we have;

$$\hat{J}_z\varphi_{m+1} = \hbar(m+1)\varphi_{m+1} \qquad (A.42)$$

Direct comparison of equation(A.40) with equation(A.42) implies that $\hat{J}_+\varphi_m$ is an eigenfunction of $\hat{J}_z$ corresponding to the eigenvalue ħ(m+1), and that;

$$\hat{J}_+\varphi_m = \varphi_{m+1} \qquad (A.43)$$

When applying $\hat{J}+$ a second time the new wavefunction becomes;

$$\hat{J}_+(\hat{J}_+\varphi_m) = \hat{J}_+\varphi_{m+1} = \varphi_{m+2} \qquad (A.44)$$

In a similar manner the effect of $\hat{J}_-$ on φ_m can also be deduced, resulting in;

$$\hat{J}_-\varphi_m = \varphi_{m-1}\,,\ \hat{J}_-\varphi_{m-1} = \varphi_{m-2} \qquad (A.45)$$

Thus a range of eigenfunctions for the z component of angular momentum are generated from a single eigenfunction φ_m, each one being found at integral increments or decrements of m i.e. the z component of the angular momentum is quantized with eigenvalues;

$$J_z = m\hbar = 0, \pm\hbar, \pm 2\hbar, \pm 3\hbar, \ldots \qquad (A.46)$$

The eigenvalues of $\hat{J}^2$ are found firstly by defining the eigenfunction of $\hat{J}^2$ to be governed by;

$$\hat{J}^2\varphi_m = \hbar^2K^2\varphi_m \tag{A.47}$$

As all eigenfunctions of $\hat{J}_z$ will be eigenfunctions of $\hat{J}^2$ it follows that the sequence of eigenfunctions in A.45 will also be eigenfunctions of $\hat{J}^2$, all corresponding to the same eigenvalue $\hbar^2K^2$. However, once the eigenvalue for $\hat{J}^2$ has been established the number of discrete eigenfunctions of $\hat{J}_z$ becomes limited. It is, therefore, possible to relate K to m by;

$$\begin{aligned} \langle J^2\rangle &= \hbar^2K^2 = \langle J_x^2\rangle + \langle J_y^2\rangle + \langle J_z^2\rangle \\ \hbar^2K^2 &= \langle J_x^2\rangle + \langle J_y^2\rangle + \hbar^2m^2 \end{aligned} \tag{A.48}$$

which must limit m such that;

$$\hbar^2K^2 \geq \hbar^2m^2 \tag{A.49}$$

$$|K| \geq |m| \tag{A.50}$$

This last inequality implies that for a given value of K>0, the possible values of m implicit in equation(A.46) must fall between +K and -K.

If the maximum and minimum values that m can assume for a given angular momentum are m_{max} and m_{min} respectively then;

$$\hat{J}_+\varphi_{m_{max}} = 0 \tag{A.51}$$

$$\hat{J}_-\varphi_{m_{min}} = 0 \tag{A.52}$$

Thus by combining these relationships with equation(A.35.a) or equation(A.35.b) the following is obtained;

$$\begin{aligned} \hat{J}^2\varphi_{m_{max}} = \hbar^2K^2\varphi_{m_{max}} &= \hat{J}_z^2\varphi_{m_{max}} + \hbar\hat{J}_z\varphi_{m_{max}} \\ \hbar^2K^2 &= \hbar^2m_{max}(m_{max}+1) \end{aligned} \tag{A.53}$$

$$\begin{aligned} \hat{J}^2\varphi_{m_{min}} = \hbar^2K^2\varphi_{m_{min}} &= \hat{J}_z^2\varphi_{m_{min}} - \hbar\hat{J}_z\varphi_{m_{min}} \\ \hbar^2K^2 &= \hbar^2m_{min}(m_{min}-1) \end{aligned} \tag{A.54}$$

This can only be true if;

$$\begin{aligned} m_{max}(m_{max}+1) &= m_{min}(m_{min}-1) \\ m_{max} &= -m_{min} \end{aligned} \tag{A.55}$$

This forces m to be symmetrically distributed about zero. Furthermore giving m_{max} the symbol *I*, then the requirement of m are only satisfied when *I* takes an integer or half integer value, resulting in the form of the eigenvalues of $\hat{J}^2$ becoming;

$$J^2 = \hbar^2 K^2 = \hbar^2 I(I+1) \qquad \text{(A.56)}$$

Thus we have derived two equation implying the quantization of angular momentum, one relating to the magnitude of the total angular momentum in terms of a quantum number *I* which may only take half integral values, and one relating to the z component of the angular momentum characterized by a quantum number m which is limited to values from *-I* to *+I* in integral steps;

$$|J| = \hbar\sqrt{I(I+1)} \qquad I = \left(0, \frac{1}{2}, 1, \frac{3}{2}, 2 \ldots\right) \qquad \text{(A.57)}$$

$$J_z = \hbar m \quad m = (-I, -I+1, -I+2, \ldots, +I-2, +I-1, +I) \qquad \text{(A.58)}$$

References for Appendix 1

[A1.1] R.C. Greenhow., "Introductory Quantum Mechanics : A Computer Illustrated Text.", Adam Hilger, Bristol, 1990. p294.

[A1.2] R.L. Liboff., "Introductory Quantum Mechanics.", Holden-Day Inc., San Fransisco, 1980.

[A1.3] F. Mandl, "Quantum Mechanics.", John Wiley and Sons, Chichester, 1992.

[A1.4] A.R. Edmonds.,"Angular Momentum in Quantum Mechanics.", Princeton, New Jersey, 1957.

[A1.5] R.N. Zare, "Angular Momentum: Understanding Spacial Aspects in Chemistry and Physics", Wiley, New York, 1987.

Appendix 2

A General Format for Hamiltonians.

A2.1 A General Format for Hamiltonians [A2.1, A2.2]

The Hamiltonians for a single spin system typically consist of many terms of the form;

$$\begin{aligned}\mathcal{H} = C(&I_xA_{xx}B_x + I_xA_{xy}B_y + I_xA_{xz}B_z + \\ &I_yA_{yx}B_x + I_yA_{yy}B_y + I_yA_{yz}B_z + \\ &I_zA_{zx}B_x + I_zA_{zy}B_y + I_zA_{zz}B_z\ )\end{aligned} \tag{A.59}$$

where C is a constant, I_u and B_u are components of the spin and magnetic field vectors, and A_{uv} is a component of a matrix. A more convenient way of writing this is as the dot product of a series of matrices, equation(A.60), which can be simplified to equation(A.61).

$$\mathcal{H} = C[I_x\ I_y\ I_z] \cdot \begin{bmatrix} A_{xx} & A_{xy} & A_{xz} \\ A_{yx} & A_{yy} & A_{yz} \\ A_{zx} & A_{zy} & A_{zz} \end{bmatrix} \cdot \begin{bmatrix} B_x \\ B_y \\ B_z \end{bmatrix} \tag{A.60}$$

$$\mathcal{H} = C\,\mathbf{I} \cdot \hat{A} \cdot \mathbf{B} \tag{A.61}$$

Expanding on equation(A.61), single spin interaction are thus represented as equation(A.62) and spin-spin interactions as equation(A.63);

$$\mathcal{H} = \sum_{i}^{\substack{All\\Spins}} \mathcal{H}(i) = \sum_{i}^{\substack{All\\Spins}} C_i\,\mathbf{I}(i) \cdot \hat{A}(i) \cdot \mathbf{B}(i) \tag{A.62}$$

$$\mathcal{H} = \sum_{i}^{\substack{All\\Spins}} \sum_{j>i}^{\substack{All\\Spins}} \mathcal{H}(ij) = \sum_{i,j}^{\substack{All\\Spins}} C_{ij}\,\mathbf{I}(i) \cdot \hat{A}(ij) \cdot \mathbf{I}(j) \tag{A.63}$$

which when written for the explicit summation over the coordinate axes becomes;

$$\mathcal{H}(i) = C_i \sum_{u}^{axes} \sum_{v}^{axes} \langle 1|\mathbf{I}(i)|u\rangle\langle u|\hat{A}(i)|v\rangle\langle v|\mathbf{B}(i)|1\rangle \tag{A.64}$$

$$\mathcal{H}(i) = C_i \sum_{u}^{axes} \sum_{v}^{axes} \langle 1|\mathbf{I}(i)|u\rangle\langle u|\hat{A}(ij)|v\rangle\langle v|\mathbf{I}(j)|1\rangle \tag{A.65}$$

where the three co-ordinate axes, u, v ={x, y, z}

For convenience the dot product in equations(A.64) and equation(A.65) is simplified by collecting the I_u and B_v factors into a single matrix, called a tensor $\hat{X}$;

$$\langle v|\hat{X}(i)|u\rangle = \langle v|\mathbf{B}(i)|1\rangle\langle 1|\mathbf{I}(i)|u\rangle \tag{A.66}$$

$$\langle v|\hat{X}(ij)|u\rangle = \langle v|\mathbf{I}(j)|1\rangle\langle 1|\mathbf{I}(i)|u\rangle \tag{A.67}$$

The Hamiltonian equation then has the form of a scalar product of two tensors (and is not a standard matrix multiplication);

$$\mathcal{H} = C\sum_{u}^{axes}\sum_{v}^{axes}\langle u|\hat{A}|v\rangle\langle v|\hat{X}|u\rangle = C\,\hat{A}\circ\hat{X} \tag{A.68}$$

$\hat{A}$ and $\hat{X}$ are rank 2 tensors, each of which has nine independent components and are in a reducible form. As a result of this there is no standard relationship between the tensor elements before and after rotation. To avoid this problem the rank 2 tensors can be broken up into three irreducible tensors of rank 0 through 2. If the rank of a tensor is l then it is made up from $2l+1$ components. Thus the zero rank tensor A_0, is composed of one component, the first rank tensor A_1, has three components and the second rank tensor A_2, contains five components. This gives a total of nine components spread over the three irreducible tensors, the same number of components as found in the original tensor. The advantage in doing this is that these three irreducible tensors transform under rotation in the same way as do the spherical harmonics of order 0, 1 and 2, and remain irreducible. That is, if a tensor is rotated by rotating its irreducible components the new elements are linear combinations of elements from their own rank.

$$\hat{A} = \begin{bmatrix} A_{xx} & A_{xy} & A_{xz} \\ A_{yx} & A_{yy} & A_{yz} \\ A_{zx} & A_{zy} & A_{zz} \end{bmatrix} = A_{iso}\overbrace{\begin{bmatrix} 1 & 0 & 0 \\ 0 & 1 & 0 \\ 0 & 0 & 1 \end{bmatrix}}^{A_0} + \overbrace{\begin{bmatrix} 0 & \alpha_{xy} & \alpha_{xz} \\ \alpha_{yx} & 0 & \alpha_{yz} \\ \alpha_{zx} & \alpha_{zy} & 0 \end{bmatrix}}^{A_1} + \overbrace{\begin{bmatrix} \delta_{xx} & \delta_{xy} & \delta_{xz} \\ \delta_{yx} & \delta_{yy} & \delta_{yz} \\ \delta_{zx} & \delta_{zy} & \delta_{zz} \end{bmatrix}}^{A_2} \tag{A.69}$$

$$A_{iso} = \frac{A_{xx}+A_{yy}+A_{zz}}{3} = \frac{Tr\{\hat{A}\}}{3}$$

$$\alpha_{uv} = \frac{A_{uv}-A_{vu}}{2}$$

$$\delta_{uv} = \frac{A_{uv}+A_{vu}-2A_{iso}}{2}$$

Every interaction will also include a second tensor, $\hat{X}$, which will either represent spin components or will involve both spin and magnetic field components. The complexity of these matrices can be greatly reduced by choosing an appropriate coordinate system for $\hat{A}$. There are a number of such axes commonly used and which particular set used depends on which time dependent molecular motions are to be accounted for.

Starting at the sub-molecular level, the first of these coordinate systems is based on *the principal axes* (PAS). Here the whole system is defined relative to the nuclear

interaction under scrutiny, such as relative to the interconnecting vector of a dipolar interaction between two nuclei. By allowing everything else to rotate and translate relative to this interaction the complexity of the matrices describing the interaction are greatly reduced.

Considering the NMR sample at a molecular level allows us to define a set of axes relative to a particular molecular orientation, *the arbitrary internal axes* (AAS). Now the rest of the molecules in the sample are allowed to rotate relative to this molecular orientation. The interaction in question is now defined in two coordinate systems (the one based on principal axes and the other on arbitrary internal axes) however these systems need not be normal to each other. It is , however, possible to convert from one axial system to the other by a simple rotation.

The next stage is to define the *principal axes of diffusion*. These axes allow for the molecular rotation, the molecule having components of its rotations about each of the ordinates. Once again, at any instant in time, a simple rotation will convert from this coordinate system to the others.

As we move from the principal axes to the arbitrary internal axes to the principal axes of diffusion we gradually increase the influence of time-dependent functions. Finally, when all time-dependent functions are being considered, the laboratory axes are used.

As mentioned earlier every interaction involving $\hat{A}$ will also have associated with it a second tensor $\hat{X}$ and the best choice of axes for $\hat{A}$ is dependent on the nature of $\hat{X}$. When $\hat{X}$ represents just spin components it is easier to compose $\hat{A}$ when using the principal axes as the coordinate base. When this occurs the interaction ends up being co-linear to the major axis of the ordinate system, greatly simplifying the resulting irreducible tensors and causing the second rank matrix A_2 to become a diagonal matrix, equation(A.70). Similarly, if $\hat{X}$ is dependent on both spin and magnetic components then a simplification is achieved if the coordinate system is chosen based on the laboratory axes, with magnetic field being co-linear with the z-axis of the laboratory axes.

$$\hat{A}_{(PAS)} = \begin{bmatrix} A_{xx} & 0 & 0 \\ 0 & A_{yy} & 0 \\ 0 & 0 & A_{zz} \end{bmatrix} = A_{iso}\overbrace{\begin{bmatrix} 1 & 0 & 0 \\ 0 & 1 & 0 \\ 0 & 0 & 1 \end{bmatrix}}^{A_0} + \overbrace{\begin{bmatrix} 0 & 0 & 0 \\ 0 & 0 & 0 \\ 0 & 0 & 0 \end{bmatrix}}^{A_1} + \overbrace{\begin{bmatrix} \delta_{xx} & 0 & 0 \\ 0 & \delta_{yy} & 0 \\ 0 & 0 & \delta_{zz} \end{bmatrix}}^{A_2} \qquad \text{(A.70)}$$

This formula expresses $\hat{A}$ in terms of its irreduceable Cartesian components. To facilitate the rotation of these matrices when moving from one co-ordinate system to another it is easier to use a spherical coordinate system.

The nine irreducible spherical tensors of a reducible rank 2 Cartesian tensor are given in appendix 3. When the irreducible spherical tensors of a Cartesian tensor which uses the principal axes system are determined five of the components are zero, the full set of components being, $A^{J}_{M\,(PAS)}$

$$A^{0}_{0\,(PAS)} = -\frac{Tr\{\hat{A}\}}{\sqrt{3}} \tag{A.71}$$

$$A^{0}_{1\,(PAS)} = 0 \tag{A.72}$$

$$A^{\pm1}_{1\,(PAS)} = 0 \tag{A.73}$$

$$A^{0}_{2\,(PAS)} = \frac{\left[3A_{zz} - Tr\{\hat{A}\}\right]}{\sqrt{6}} \tag{A.74}$$

$$A^{\pm1}_{2\,(PAS)} = 0 \tag{A.75}$$

$$A^{\pm2}_{2\,(PAS)} = \frac{(A_{xx} - A_{yy})}{2} \tag{A.76}$$

Although this is a much simpler representation of $\hat{A}$ it is now uses the wrong coordinate basis for the final Hamiltonian. To transform these components into the laboratory frame they are first transformed so that they use the arbitrary internal axes using a fixed rotation Ω, equation(A.77). and then they are rotated from this basis to the laboratory frame by using a time dependent rotation $\Omega(t)$, equation(A.78).

$$A^{m}_{l\,(AAS)} = \sum_{m=-l}^{l} D^{l}_{mm'}(\Omega) A^{m'}_{l\,(PAS)} \tag{A.77}$$

$$A^{m}_{l\,(LAB)} = \sum_{m=-l}^{l} D^{l}_{mm'}\left[\Omega(t)\right] A^{m'}_{l\,(AAS)} \tag{A.78}$$

The rotation element $D^{l}_{mm'}(\Omega)$ is briefly discussed in appendix 3.

As mentioned earlier the basis of the irreducible spherical tensors for $\hat{X}$ depends on whether it refers to a spin-spin interaction or a spin-field interaction. Assuming that $\hat{X}$ is measured using the laboratory axes then;

$$X^{0}_{0\,(LAB)} = -\frac{(X_{xx} + X_{yy} + X_{zz})}{\sqrt{3}} \tag{A.79}$$

$$X^{0}_{1\,(LAB)} = i\frac{(X_{xy} - X_{yx})}{\sqrt{2}} \tag{A.80}$$

$$X^{\pm 1}_{1\,(LAB)} = \frac{\left[X_{zx} - X_{xz} \pm i(X_{zy} - X_{yz})\right]}{2} \tag{A.81}$$

$$X^{0}_{2\,(LAB)} = \frac{\left[3X_{zz} - (X_{xx} + X_{yy} + X_{zz})\right]}{\sqrt{6}} \tag{A.82}$$

$$X^{\pm 1}_{2\,(LAB)} = \mp\frac{\left[X_{xz} + X_{zx} \pm i(X_{yz} + X_{zy})\right]}{2} \tag{A.83}$$

$$X^{\pm 2}_{2\,(LAB)} = \frac{\left[X_{xx} - X_{yy} \pm i(X_{xy} + X_{yx})\right]}{2} \tag{A.84}$$

Previously, equation(A.68), the scalar product of two tensors was defined. For the scalar product of two irreducible tensors of rank l this becomes;

$$A_l \circ X_l = \sum_{m=-l}^{l} (-1)^m A_l^m X_l^{-m} = \sum_{m=-l}^{l} (-1)^m A_l^{-m} X_l^m \tag{A.85}$$

so for all the components of a rank two tensors this is;

$$\hat{A} \circ \hat{X} = \sum_{l=0}^{2} A_l \circ X_l = \sum_{l=0}^{2} \sum_{m=-l}^{l} (-1)^m A_l^{-m} X_l^m \tag{A.86}$$

This can now be substituted directly into equation(A.68) giving the Hamiltonian in terms of nine distinct components which are now indexed by components of angular momentum rather than by the ordinates of the laboratory frame;

$$\mathcal{H} = C \sum_{l=0}^{2} \sum_{m=-l}^{l} (-1)^m A_l^{-m} X_l^m \tag{A.87}$$

Although this may be used as the general form of the Hamiltonians it is usual to factor out any constants in the tensors such that;

$$a(F_l^m) = A_l^m \tag{A.88}$$

$$b(T_l^m) = X_l^m \tag{A.89}$$

$$\xi = abC \tag{A.90}$$

which gives the Hamiltonian in the laboratory frame to be;

$$\begin{aligned} \mathcal{H}_{(LAB,t)} &= \xi \sum_{l=0}^{2} \sum_{m=-l}^{l} (-1)^m F_{l\,(LAB,t)}^{-m}\, T_{l\,(LAB)}^{m} \\ &= \xi \sum_{l=0}^{2} \sum_{m=-l}^{l} (-1)^m \left[\sum_{m'=-l}^{l} D^{l}_{m,m'}\left[\Omega(t)\right] F_{l\,(AAS)}^{-m} \right] T_{l\,(LAB)}^{m} \end{aligned} \tag{A.91}$$

References for Appendix 2.

[A2.1] S.A. Smith, W.E. Palke and J.T. Gerig, "The Hamiltonians of NMR: Part 1", Concepts Magn. Reson., 1992, **4**, p107.

[A2.2] S.A. Smith, W.E. Palke and J.T. Gerig, "The Hamiltonians of NMR: Part 2", Concepts Magn. Reson., 1992, **4**, p181.

Appendix 3

Spherical Co-Ordinates and Tensors.

A3.1 Spherical Polar Coordinates & Euler Angles. [A3.1]

The spherical polar coordinate system is another basis for describing three dimensional space, a particular point being described by two angles and a distance rather than as some product of three orthogonal unit vectors as used in the Cartesian system. The angular dependence of the spherical system has particular advantages over the Cartesian system when used to describe the interactions in NMR; rotation of the interaction tensors becomes relatively easy, and integration and averaging of interactions over all directions becomes simpler.

The three ordinates used to describe a point in space under the spherical polar coordinate system are the distance from the origin r, the angle that the interconnecting vector between the origin and the point in space makes to the z axis θ, and the angle that the projection of the interconnect on the x-y plane makes to the x-axis ϕ (Figure A.1).

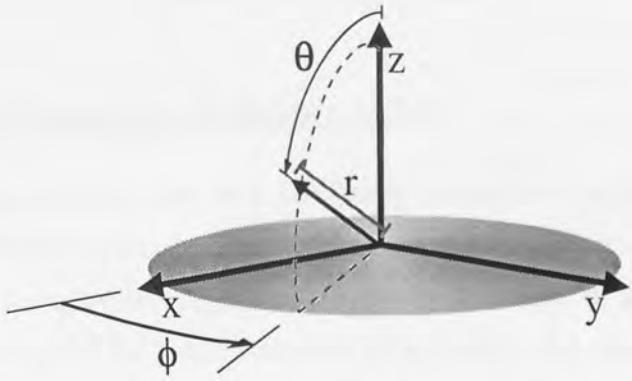

Figure A.1 : The Spherical Coordinate System.

Coordinates in the two systems are, therefore, related to each other by;

$$\begin{aligned} x &= r\cos\theta\sin\phi \\ y &= r\sin\theta\sin\phi \\ z &= r\cos\phi \end{aligned} \qquad (A.92)$$

The rotation of one Cartesian coordinate system to another (x,y,z to x''',y''',z'') is achieved by rotating the axes by the three Euler angles ϕ, θ and χ. The first two of these angle are the same as in the spherical polar coordinate system, relating to a rotation about the z axis by ϕ to give the axes x', y' and z' followed by a rotation about the y' axis by θ to give the axes x'', y'' and z''. The final angle χ, relates to the rotation of the coordinate system about the z''-axis, the axes now in their required orientation x''', y''', z'''. Figure A.2

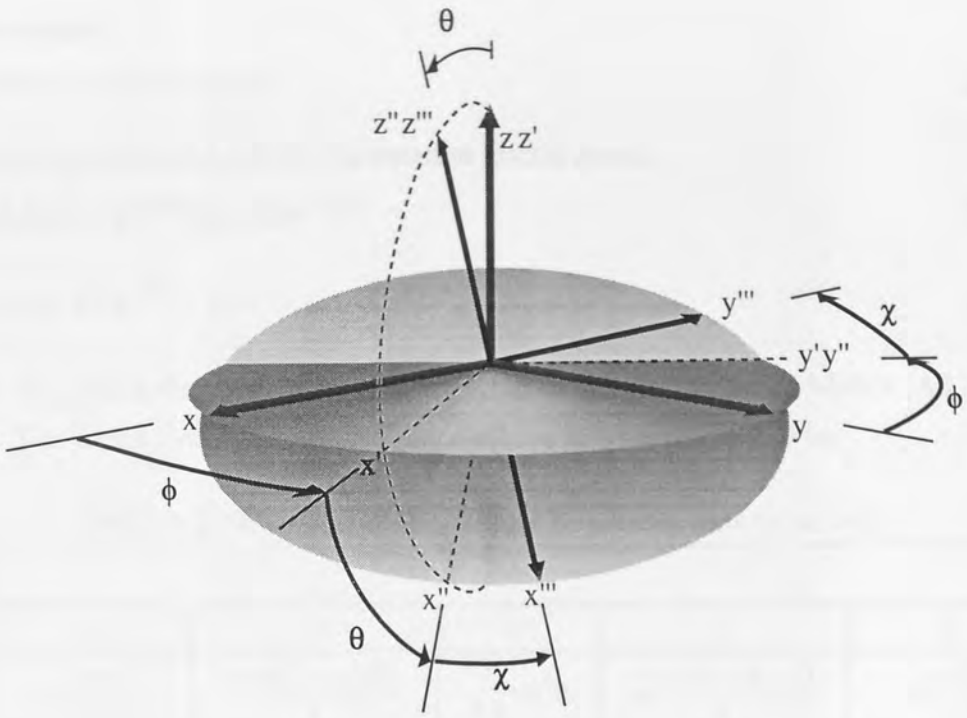

Figure A.2 : Euler Angles.

A3.2 Rotation of Eigenstates and Tensors. [A3.1]

The rotation as described above is needlessly complex to implement as the rotations are related to a number of sets of axes. The same rotation can be achieved while still only relating to the original set of axes by a rotation of χ about the z axis then a rotation of θ about the y axis followed by a rotation of ϕ once again about the z axis. The rotation R_v about an axis denoted by the unit vector **v** by an angle α is given by;

$$R_v(\theta) = e^{-i\theta(J \cdot v)} \tag{A.93}$$

when this is applied to the series of rotations (ϕ, θ and χ collectively being referred to as Ω) needed to transform on set of co-ordinates to another this become;

$$\begin{aligned} R(\phi,\theta,\chi) &= R_{z''}(\chi)R_{y'}(\theta)R_z(\phi) \\ R(\Omega) &= R_z(\phi)R_y(\theta)R_z(\chi) = e^{-i\phi J_z}e^{-i\theta J_y}e^{-i\chi J_z} \end{aligned} \tag{A.94}$$

When this rotation is applied to a particular eigenstate $|J\ M\rangle$ of $\mathbf{J}^2$ it transforms $|J\ M\rangle$ into a linear combination of other m values:

$$R(\Omega)|J\ M\rangle = \sum_{M'} D^J_{M'M}(\Omega)|J\ M'\rangle \tag{A.95}$$

where the rotation coefficients $D^J_{M'M}$ is the respective element of the (2J+1) by (2J+1)

rotation matrix;

$$D^J_{M'M}(\Omega) = \langle J,M'|R(\Omega)|J,M\rangle \tag{A.96}$$

substituting equation(A.94) for the rotation matrix gives;

$$D^J_{M'M}(\phi,\theta,\chi) = e^{-i\phi M'}\mathcal{D}^J_{M'M}(\theta)e^{-i\chi M} \tag{A.97}$$

$$\mathcal{D}^J_{M'M}(\theta)=\langle J\ M'|e^{-i\theta J_y}|J\ M\rangle \tag{A.98}$$

where $\mathcal{D}^J_{M'M}(\theta)$ is the appropriate element from the Wigner Rotation Matrix [A3.2, A3.3]. For a rank two tensor these elements have been calculated to be;

Table A.2 : Elements of the Wigner Rotational Matrix for J=2.

$\mathcal{D}^2_{M,N}$	N				
M	-2	-1	0	1	2
-2	$\cos^4\left(\frac{\theta}{2}\right)$	$\frac{\sin\theta(1+\cos\theta)}{2}$	$\sqrt{\frac{3}{8}}\sin^2\theta$	$\frac{-\sin\theta(\cos\theta-1)}{2}$	$\sin^4\left(\frac{\theta}{2}\right)$
-1	$\frac{-\sin\theta(1+\cos\theta)}{2}$	$\frac{(2\cos\theta-1)(\cos\theta+1)}{2}$	$\sqrt{\frac{3}{2}}\sin\theta\cos\theta$	$\frac{(2\cos\theta+1)(1-\cos\theta)}{2}$	$\frac{-\sin\theta(\cos\theta-1)}{2}$
0	$\sqrt{\frac{3}{8}}\sin^2\theta$	$\sqrt{\frac{3}{2}}\sin\theta\cos\theta$	$\frac{(3\cos^2\theta-1)}{2}$	$\sqrt{\frac{3}{2}}\sin\theta\cos\theta$	$\sqrt{\frac{3}{8}}\sin^2\theta$
1	$\frac{\sin\theta(\cos\theta-1)}{2}$	$\frac{(2\cos\theta+1)(1-\cos\theta)}{2}$	$\sqrt{\frac{3}{2}}\sin\theta\cos\theta$	$\frac{(2\cos\theta-1)(\cos\theta+1)}{2}$	$\frac{\sin\theta(1+\cos\theta)}{2}$
2	$\sin^4\left(\frac{\theta}{2}\right)$	$\frac{\sin\theta(\cos\theta-1)}{2}$	$\sqrt{\frac{3}{8}}\sin^2\theta$	$\frac{-\sin\theta(1+\cos\theta)}{2}$	$\cos^4\left(\frac{\theta}{2}\right)$

When operators are rotated they must first be expressed as irreducible spherical tensor operator, $\hat{T}$, these then rotate according to;

$$R(\Omega)T^M_J R^{-1}(\Omega) = \sum_{M'=-J}^{J} D^J_{M'M}(\Omega)T^{M'}_J \tag{A.99}$$

A3.3 Spherical Tensor Components from Cartesian Components[A3.4]

The components of an irreducible spherical tensor are represent by T^J_M where J represents the order of the tensor and M takes value of +J to -J in integral steps. These components may be determined directly from the reducible Cartesian matrix;

$$A^0_0 = -\frac{(A_{xx}+A_{yy}+A_{zz})}{\sqrt{3}} = -\frac{Tr\{\hat{A}\}}{\sqrt{3}} \tag{A.100}$$

$$A^0_1 = -i\frac{(A_{xy}-A_{yx})}{\sqrt{2}} \tag{A.101}$$

$$A^{\pm1}_1 = -\frac{[A_{zx}-A_{xz}\pm i(A_{zy}-A_{yz})]}{2} \tag{A.102}$$

$$A_2^0 = \frac{\left[3A_{zz} - (A_{xx} + A_{yy} + A_{zz})\right]}{\sqrt{6}} = \frac{\left[3A_{zz} - \mathrm{Tr}\{\hat{A}\}\right]}{\sqrt{6}} \quad \text{(A.103)}$$

$$A_2^{\pm 1} = \mp\frac{\left[A_{xz} + A_{zx} \pm i(A_{yz} + A_{zy})\right]}{2} \quad \text{(A.104)}$$

$$A_2^{\pm 2} = \frac{\left[A_{xx} - A_{yy} \pm i(A_{xy} + A_{yx})\right]}{2} \quad \text{(A.105)}$$

When the spherical components of the rank 2 tensor $\hat{X}$, formed by the dyadic product of 2 vectors, are required it is necessary to alter the sign of the rank 1 components so;

If,

$$[\vec{I} \cdot \vec{S}]_{dy} = \begin{bmatrix} I_x \\ I_y \\ I_z \end{bmatrix} \cdot \begin{bmatrix} S_x & S_y & S_z \end{bmatrix} = \begin{bmatrix} I_xS_x & I_xS_y & I_xS_z \\ I_yS_x & I_yS_y & I_yS_z \\ I_zS_x & I_zS_y & I_zS_z \end{bmatrix} = \hat{X} \quad \text{(A.106)}$$

then the irreducible spherical components of this will be;

$$X_0^0 = -\frac{(I_xS_x + I_yS_y + I_zS_z)}{\sqrt{3}} = \frac{\vec{I} \cdot \vec{S}}{\sqrt{3}} \quad \text{(A.107)}$$

$$X_1^0 = i\frac{(I_xS_y - S_yI_x)}{\sqrt{2}} \quad \text{(A.108)}$$

$$X_1^{\pm 1} = \frac{\left[I_zS_x - I_xS_z \pm i(I_xS_y - I_yS_z)\right]}{2} \quad \text{(A.109)}$$

$$X_2^0 = \frac{\left[3I_zS_z - (I_xS_x + I_yS_y + I_zS_z)\right]}{\sqrt{6}} = \frac{\left[4I_zS_z - (I_+S_- + I_-S_+)\right]}{2\sqrt{6}} \quad \text{(A.110)}$$

$$X_2^{\pm 1} = \mp\frac{\left[I_xS_z + I_zS_x \pm i(I_yS_z + I_zS_y)\right]}{2} = \mp\frac{I_zS_\pm + I_\pm S_z}{2} \quad \text{(A.111)}$$

$$X_2^{\pm 2} = \frac{\left[I_xS_x - I_yS_y \pm i(I_xS_y + I_yS_x)\right]}{2} = \frac{I_\pm S_\pm}{2} \quad \text{(A.112)}$$

References for Appendix 3

[A3.1] S.A. Smith, W.E. Palke and J.T. Gerig, "The Hamiltonians of NMR: Part 1", Concepts Magn. Reson., 1992, **4**, p107.

[A3.2] R.N. Zare, "Angular Momentum: Understanding Spacial Aspects in Chemistry and Physics", Wiley, New York, 1987.

[A3.3] D.M. Brink and G.R. Satchler, "Angular Momentum", 1968, Clarrendon Press, Oxford.

[A3.4] S.A. Smith, W.E. Palke and J.T. Gerig, "The Hamiltonians of NMR: Part 2", Concepts Magn. Reson., 1992, **4**, p181.

Appendix 4

Listing of the Computer Program for the Numerical Analysis of Pulse Sequences

```
REM SymLib Library Functions For Pulse program simulator

REM ————————————————————

DEFPROCInit(nuc%)
nuclei%=nuc%-1: REM arrays start at zero so reduce nuclei by 1
REM nucleus counter
nnum%=0

REM Array to hold system definition
REM System(x,0)=0,1,2,3 : For QC CH CH2 OR CH3
REM System(x,11) identifies which member of specific array the nucleus
    is.
REM
REM System(x,0)=0 Then System(x,1)=Ch.Sh. of QC
REM                    System(x,2:10) should be set to zero
REM
REM System(x,0)=1 Then System(x,1)=Ch.Sh. of C
REM                    System(x,2)=Ch.Sh. of H
REM                    System(x,3)=J CH
REM                    System(x,4:10) should be set to zero
REM
REM System(x,0)=2 Then System(x,1)=Ch.Sh. of C
REM                    System(x,2)=Ch.Sh. of H1
REM                    System(x,3)=Ch.Sh. of H2
REM                    System(x,4)=J CH1
REM                    System(x,5)=J CH2
REM                    System(x,6)=J H1H2
REM                    System(x,7:10) should be set to zero
REM
REM System(x,0)=3 Then System(x,1)=Ch.Sh. of C
REM                    System(x,2)=Ch.Sh. of H1
REM                    System(x,3)=Ch.Sh. of H2
REM                    System(x,4)=Ch.Sh. of H3
REM                    System(x,5)=J CH1
REM                    System(x,6)=J CH2
REM                    System(x,7)=J H1H2
REM                    System(x,8)=J CH3
REM                    System(x,9)=J H1H3
REM                    System(x,10)=J H2H3

DIM System((nuclei%+1)*4,11)
System()=0

REM Arrays to hold the P.O. of each nuclear system.
DIM C(nuclei%,3)          ,TC(3)
DIM CH(nuclei%,3,3)       ,TCH(3,3)
DIM CH2(nuclei%,3,3,3)    ,TCH2(3,3,3)
DIM CH3(nuclei%,3,3,3,3),TCH3(3,3,3,3)
C()=0:  TC()=0
CH()=0: TCH()=0
CH2()=0:TCH2()=0
CH3()=0:TCH3()=0

REM counters for each nuclear system type
DIM counters%(3)
```

```
counters%()=0

REM Fill Arrays with Z magnetization
FOR Nucleus%=0 TO nuclei%
C(Nucleus%,3)=1
:
CH(Nucleus%,3,0)=1
CH(Nucleus%,0,3)=4
:
CH2(Nucleus%,3,0,0)=1
CH2(Nucleus%,0,3,0)=4
CH2(Nucleus%,0,0,3)=4
:
CH3(Nucleus%,3,0,0,0)=1
CH3(Nucleus%,0,3,0,0)=4
CH3(Nucleus%,0,0,3,0)=4
CH3(Nucleus%,0,0,0,3)=4
NEXT

REM Array to transfer Definitions into.
DIM Def(10)
REM return nuclei% to original 'number of nuclei' value.
nuclei%+=1
ENDPROC

DEFPROCpulse(Action$,Angle,Nucleus%)
REM Action$,   ACTION   , PARAM
REM H+X, Proton  X Pulse, Angle in degrees
REM H+Y, Proton  Y Pulse, Angle in degrees
REM H-X, Proton -X Pulse, Angle in degrees
REM H-Y, Proton -Y Pulse, Angle in degrees
REM C+X, Carbon  X Pulse, Angle in degrees
REM C+Y, Carbon  Y Pulse, Angle in degrees
REM C-X, Carbon -X Pulse, Angle in degrees
REM C-Y, Carbon -Y Pulse, Angle in degrees

CASE Action$ OF
WHEN "H+X"
PROCHx(Angle,Nucleus%)
WHEN "H+Y"
PROCHy(Angle,Nucleus%)
WHEN "H-X"
PROCHx(-Angle,Nucleus%)
WHEN "H-Y"
PROCHy(-Angle,Nucleus%)
WHEN "C+X"
PROCCx(Angle,Nucleus%)
WHEN "C+Y"
PROCCy(Angle,Nucleus%)
WHEN "C-X"
PROCCx(-Angle,Nucleus%)
WHEN "C-Y"
PROCCy(-Angle,Nucleus%)
OTHERWISE
VDU 20

CLS
```

```
CLG
PRINT''
PRINT "Unknown Pulse Command :";Action$;":"
STOP
ENDCASE
PROCClearTemp
ENDPROC

DEFPROCDefine(Def(0),Def(1),Def(2),Def(3),Def(4),Def(5),Def(6),Def(7)-
     ,Def(8),Def(9),Def(10))
IF counters%(Def(0))=nuclei% THEN
PRINT "Maximum number of nuclei have been defined of type ";Def(0);"."
PRINT "Please re-initialize for more nuclei"
ELSE
FOR pointer%=0 TO 10
System(nnum%,pointer%)=Def(pointer%)
NEXT
System(nnum%,11)=counters%(Def(0))
nnum%+=1
counters%(Def(0))+=1
ENDIF
ENDPROC

DEFPROCdelay(time$,NucNum%)
time=EVAL(time$)
PROCChemicalShift(time,NucNum%)
PROCJCoupling(time,NucNum%)
ENDPROC

DEFPROCHx(num,NucNum%)
cosr=COS(RAD(num))
sinr=SIN(RAD(num))
WhichOne%=System(NucNum%,11)
CASE System(NucNum%,0) OF
:
WHEN 1
REM : CH
:
REM Rotate Iy for each carbon component Sx Sy Sz So
FOR carbon=0 TO 3
TCH(carbon,2)=CH(WhichOne%,carbon,2)*cosr
TCH(carbon,3)=-CH(WhichOne%,carbon,2)*sinr
NEXT
:
REM Rotate Iz for each carbon component Sx Sy Sz So
FOR carbon=0 TO 3
TCH(carbon,3)+=CH(WhichOne%,carbon,3)*cosr
TCH(carbon,2)+=CH(WhichOne%,carbon,3)*sinr
NEXT
:
REM Put results back into main matrix
FOR carbon=0 TO 3
FOR comp%=2 TO 3
CH(WhichOne%,carbon,comp%)=TCH(carbon,comp%)
NEXT
NEXT
:
```

```
WHEN 2
REM : CH2
REM Rotate I1y for each component of S & I2
FOR  carbon=0 TO 3
FOR Proton2=0 TO 3
TCH2(carbon,2,Proton2)=CH2(WhichOne%,carbon,2,Proton2)*cosr
TCH2(carbon,3,Proton2)=-CH2(WhichOne%,carbon,2,Proton2)*sinr
NEXT
NEXT
:
REM Rotate I1z for each  component of S & I2
FOR  carbon=0 TO 3
FOR Proton2=0 TO 3
TCH2(carbon,3,Proton2)+=CH2(WhichOne%,carbon,3,Proton2)*cosr
TCH2(carbon,2,Proton2)+=CH2(WhichOne%,carbon,3,Proton2)*sinr
NEXT
NEXT
:
REM Re load I1 components.
FOR carbon=0 TO 3
FOR Proton2=0 TO 3
FOR Proton1=2 TO 3
CH2(WhichOne%,carbon,Proton1,Proton2)=TCH2(carbon,Proton1,Proton2)
NEXT
NEXT
NEXT
:
REM Rotate I2y for each component of S & I1
FOR  carbon=0 TO 3
FOR Proton1=0 TO 3
TCH2(carbon,Proton1,2)=CH2(WhichOne%,carbon,Proton1,2)*cosr
TCH2(carbon,Proton1,3)=-CH2(WhichOne%,carbon,Proton1,2)*sinr
NEXT
NEXT
:
REM Rotate I2z for each component of S & I1
FOR  carbon=0 TO 3
FOR Proton1=0 TO 3
TCH2(carbon,Proton1,3)+=CH2(WhichOne%,carbon,Proton1,3)*cosr
TCH2(carbon,Proton1,2)+=CH2(WhichOne%,carbon,Proton1,3)*sinr
NEXT
NEXT
:
REM Re load I2 components.
FOR carbon=0 TO 3
FOR Proton1=0 TO 3
FOR Proton2=2 TO 3
CH2(WhichOne%,carbon,Proton1,Proton2)=TCH2(carbon,Proton1,Proton2)
NEXT
NEXT
NEXT
:
WHEN 3
REM CH3
:
REM Rotate I1y for each component of S I2 & I3
FOR  carbon=0 TO 3
```

```
FOR Proton2=0 TO 3
FOR Proton3=0 TO 3
TCH3(carbon,2,Proton2,Proton3)=CH3(WhichOne%,carbon,2,Proton2,Proton3-
     )*cosr
TCH3(carbon,3,Proton2,Proton3)=-
     CH3(WhichOne%,carbon,2,Proton2,Proton3)*sinr
NEXT
NEXT
NEXT
:
REM Rotate I1z for each component of S I2 & I3
FOR  carbon=0 TO 3
FOR Proton2=0 TO 3
FOR Proton3=0 TO 3
TCH3(carbon,3,Proton2,Proton3)+=CH3(WhichOne%,carbon,3,Proton2,Proton-
     3)*cosr
TCH3(carbon,2,Proton2,Proton3)+=CH3(WhichOne%,carbon,3,Proton2,Proton-
     3)*sinr
NEXT
NEXT
NEXT
:
REM Re load I1 components.
FOR carbon=0 TO 3
FOR Proton3=0 TO 3
FOR Proton2=0 TO 3
FOR Proton1=2 TO 3
CH3(WhichOne%,carbon,Proton1,Proton2,Proton3)=TCH3(carbon,Proton1,Pro-
     ton2,Proton3)
NEXT
NEXT
NEXT
NEXT

:
REM Rotate I2y for each component of S I1 & I3
FOR  carbon=0 TO 3
FOR Proton1=0 TO 3
FOR Proton3=0 TO 3
TCH3(carbon,Proton1,2,Proton3)=CH3(WhichOne%,carbon,Proton1,2,Proton3-
     )*cosr
TCH3(carbon,Proton1,3,Proton3)=-
     CH3(WhichOne%,carbon,Proton1,2,Proton3)*sinr
NEXT
NEXT
NEXT
:
REM Rotate I2z for each component of S I1 & I3
FOR  carbon=0 TO 3
FOR Proton1=0 TO 3
FOR Proton3=0 TO 3
TCH3(carbon,Proton1,3,Proton3)+=CH3(WhichOne%,carbon,Proton1,3,Proton-
     3)*cosr
TCH3(carbon,Proton1,2,Proton3)+=CH3(WhichOne%,carbon,Proton1,3,Proton-
     3)*sinr
NEXT
NEXT
```

```
NEXT

REM Re load I2 components.
FOR carbon=0 TO 3
FOR Proton3=0 TO 3
FOR Proton1=0 TO 3
FOR Proton2=2 TO 3
CH3(WhichOne%,carbon,Proton1,Proton2,Proton3)=TCH3(carbon,Proton1,Pro-
    ton2,Proton3)
NEXT
NEXT
NEXT
NEXT
:
REM Rotate I3y for each component of S I1 & I2
FOR  carbon=0 TO 3
FOR Proton1=0 TO 3
FOR Proton2=0 TO 3
TCH3(carbon,Proton1,Proton2,2)=CH3(WhichOne%,carbon,Proton1,Proton2,2-
    )*cosr
TCH3(carbon,Proton1,Proton2,3)=-
    CH3(WhichOne%,carbon,Proton1,Proton2,2)*sinr
NEXT
NEXT
NEXT
:
REM Rotate I3z for each component of S I1 & I2
FOR  carbon=0 TO 3
FOR Proton1=0 TO 3
FOR Proton2=0 TO 3
TCH3(carbon,Proton1,Proton2,3)+=CH3(WhichOne%,carbon,Proton1,Proton2,-
    3)*cosr
TCH3(carbon,Proton1,Proton2,2)+=CH3(WhichOne%,carbon,Proton1,Proton2,-
    3)*sinr
NEXT
NEXT
NEXT
:
REM Re load I3 components.
FOR carbon=0 TO 3
FOR Proton1=0 TO 3
FOR Proton2=0 TO 3
FOR Proton3=2 TO 3
CH3(WhichOne%,carbon,Proton1,Proton2,Proton3)=TCH3(carbon,Proton1,Pro-
    ton2,Proton3)
NEXT
NEXT
NEXT
NEXT
:
ENDCASE
ENDPROC

DEFPROCHy(num,NucNum%)
cosr=COS(RAD(num))
sinr=SIN(RAD(num))
WhichOne%=System(NucNum%,11)
```

```
CASE System(NucNum%,0) OF
WHEN 1
REM : CH
:
REM Rotate Ix for each carbon component Sx Sy Sz So
FOR carbon=0 TO 3
TCH(carbon,1)=CH(WhichOne%,carbon,1)*cosr
TCH(carbon,3)=CH(WhichOne%,carbon,1)*sinr
NEXT
:
REM Rotate Iz for each carbon component Sx Sy Sz So
FOR carbon=0 TO 3
TCH(carbon,3)+=CH(WhichOne%,carbon,3)*cosr
TCH(carbon,1)-=CH(WhichOne%,carbon,3)*sinr
NEXT
:
REM Put results back into main matrix
FOR carbon=0 TO 3
FOR comp=1 TO 3 STEP 2
CH(WhichOne%,carbon,comp)=TCH(carbon,comp)
NEXT
NEXT

WHEN 2
REM : CH2
:
REM Rotate I1x for each component of S & I2
FOR  carbon=0 TO 3
FOR Proton2=0 TO 3
TCH2(carbon,1,Proton2)=CH2(WhichOne%,carbon,1,Proton2)*cosr
TCH2(carbon,3,Proton2)=CH2(WhichOne%,carbon,1,Proton2)*sinr
NEXT
NEXT
:
REM Rotate I1z for each  component of S & I2
FOR  carbon=0 TO 3
FOR Proton2=0 TO 3
TCH2(carbon,3,Proton2)+=CH2(WhichOne%,carbon,3,Proton2)*cosr
TCH2(carbon,1,Proton2)-=CH2(WhichOne%,carbon,3,Proton2)*sinr
NEXT
NEXT
:
REM Re load I1 components.
FOR carbon=0 TO 3
FOR Proton2=0 TO 3
FOR Proton1=1 TO 3 STEP 2
CH2(WhichOne%,carbon,Proton1,Proton2)=TCH2(carbon,Proton1,Proton2)
NEXT
NEXT
NEXT

:
REM Rotate I2x for each component of S & I1
FOR  carbon=0 TO 3
FOR Proton1=0 TO 3
TCH2(carbon,Proton1,1)=CH2(WhichOne%,carbon,Proton1,1)*cosr
TCH2(carbon,Proton1,3)=CH2(WhichOne%,carbon,Proton1,1)*sinr
```

```
NEXT
NEXT
:
REM Rotate I2z for each component of S & I1
FOR  carbon=0 TO 3
FOR Proton1=0 TO 3
TCH2(carbon,Proton1,3)+=CH2(WhichOne%,carbon,Proton1,3)*cosr
TCH2(carbon,Proton1,1)-=CH2(WhichOne%,carbon,Proton1,3)*sinr
NEXT
NEXT
:
REM Re load I1 components.
FOR carbon=0 TO 3
FOR Proton1=0 TO 3
FOR Proton2=1 TO 3 STEP 2
CH2(WhichOne%,carbon,Proton1,Proton2)=TCH2(carbon,Proton1,Proton2)
NEXT
NEXT
NEXT
:
WHEN 3
REM CH3
:
REM Rotate I1y for each component of S I2 & I3
FOR  carbon=0 TO 3
FOR Proton2=0 TO 3
FOR Proton3=0 TO 3
TCH3(carbon,1,Proton2,Proton3)=CH3(WhichOne%,carbon,1,Proton2,Proton3-
     )*cosr
TCH3(carbon,3,Proton2,Proton3)=CH3(WhichOne%,carbon,1,Proton2,Proton3-
     )*sinr
NEXT
NEXT
NEXT
:
REM Rotate I1z for each component of S I2 & I3
FOR  carbon=0 TO 3
FOR Proton2=0 TO 3
FOR Proton3=0 TO 3
TCH3(carbon,3,Proton2,Proton3)+=CH3(WhichOne%,carbon,3,Proton2,Proton-
     3)*cosr
TCH3(carbon,1,Proton2,Proton3)-
     =CH3(WhichOne%,carbon,3,Proton2,Proton3)*sinr
NEXT
NEXT
NEXT
:
REM Re load I1 components.
FOR  carbon=0 TO 3
FOR Proton1=1 TO 3 STEP 2
FOR Proton2=0 TO 3
FOR Proton3=0 TO 3
CH3(WhichOne%,carbon,Proton1,Proton2,Proton3)=TCH3(carbon,Proton1,Pro-
     ton2,Proton3)
NEXT
NEXT
NEXT
```

```
NEXT
:
REM Rotate I2y for each component of S I1 & I3
FOR  carbon=0 TO 3
FOR Proton1=0 TO 3
FOR Proton3=0 TO 3
TCH3(carbon,Proton1,1,Proton3)=CH3(WhichOne%,carbon,Proton1,1,Proton3-
     )*cosr
TCH3(carbon,Proton1,3,Proton3)=CH3(WhichOne%,carbon,Proton1,1,Proton3-
     )*sinr
NEXT
NEXT
NEXT
:
REM Rotate I2z for each component of S I1 & I3
FOR  carbon=0 TO 3
FOR Proton1=0 TO 3
FOR Proton3=0 TO 3
TCH3(carbon,Proton1,3,Proton3)+=CH3(WhichOne%,carbon,Proton1,3,Proton-
     3)*cosr
TCH3(carbon,Proton1,1,Proton3)-
     =CH3(WhichOne%,carbon,Proton1,3,Proton3)*sinr
NEXT
NEXT
NEXT
:
REM Re load I2 components.
FOR  carbon=0 TO 3
FOR Proton2=1 TO 3 STEP 2
FOR Proton1=0 TO 3
FOR Proton3=0 TO 3
CH3(WhichOne%,carbon,Proton1,Proton2,Proton3)=TCH3(carbon,Proton1,Pro-
     ton2,Proton3)
NEXT
NEXT
NEXT
NEXT
:
REM Rotate I3x for each component of S I1 & I2
FOR  carbon=0 TO 3
FOR Proton1=0 TO 3
FOR Proton2=0 TO 3
TCH3(carbon,Proton1,Proton2,1)=CH3(WhichOne%,carbon,Proton1,Proton2,1-
     )*cosr
TCH3(carbon,Proton1,Proton2,3)=CH3(WhichOne%,carbon,Proton1,Proton2,1-
     )*sinr
NEXT
NEXT
NEXT
:
REM Rotate I3z for each component of S I1 & I2
FOR  carbon=0 TO 3
FOR Proton1=0 TO 3
FOR Proton2=0 TO 3
TCH3(carbon,Proton1,Proton2,3)+=CH3(WhichOne%,carbon,Proton1,Proton2,-
     3)*cosr
TCH3(carbon,Proton1,Proton2,1)-
     =CH3(WhichOne%,carbon,Proton1,Proton2,3)*sinr
```

```
NEXT
NEXT
NEXT
:
REM Re load I3 components.
FOR  carbon=0 TO 3
FOR Proton3=1 TO 3 STEP 2
FOR Proton1=0 TO 3
FOR Proton2=0 TO 3
CH3(WhichOne%,carbon,Proton1,Proton2,Proton3)=TCH3(carbon,Proton1,Pro-
     ton2,Proton3)
NEXT
NEXT
NEXT
NEXT
:
ENDCASE
ENDPROC

DEFPROCClearTemp
TC()=0
TCH()=0
TCH2()=0
TCH3()=0
ENDPROC

DEFPROCCx(num,NucNum%)
REM rotate y and z components around x axis by "num" degrees
cosr=COS(RAD(num))
sinr=SIN(RAD(num))
WhichOne%=System(NucNum%,11)
CASE System(NucNum%,0) OF

WHEN 0
REM Q Carbon

REM Move y component
TC(2)=C(WhichOne%,2)*cosr
TC(3)=C(WhichOne%,2)*sinr

REM Move z component
TC(3)+=C(WhichOne%,3)*cosr
TC(2)+=C(WhichOne%,3)*sinr

REM Transfer back
C(WhichOne%,2)=TC(2)
C(WhichOne%,3)=TC(3)
WHEN 1
REM CH Carbon

REM Move y components
FOR Proton1=0 TO 3
TCH(2,Proton1)=CH(WhichOne%,2,Proton1)*cosr
TCH(3,Proton1)=-CH(WhichOne%,2,Proton1)*sinr
NEXT

REM Move z components
```

```
FOR Proton1=0 TO 3
TCH(3,Proton1)+=CH(WhichOne%,3,Proton1)*cosr
TCH(2,Proton1)+=CH(WhichOne%,3,Proton1)*sinr
NEXT

REM Transfer back changed results
FOR Carbon=2 TO 3
FOR Proton1=0 TO 3
CH(WhichOne%,Carbon,Proton1)=TCH(Carbon,Proton1)
NEXT
NEXT

WHEN 2
REM CH2 Carbon

REM Move y components
FOR Proton1=0 TO 3
FOR Proton2=0 TO 3
TCH2(2,Proton1,Proton2)=CH2(WhichOne%,2,Proton1,Proton2)*cosr
TCH2(3,Proton1,Proton2)=-CH2(WhichOne%,2,Proton1,Proton2)*sinr
NEXT
NEXT

REM Move z components
FOR Proton1=0 TO 3
FOR Proton2=0 TO 3
TCH2(3,Proton1,Proton2)+=CH2(WhichOne%,3,Proton1,Proton2)*cosr
TCH2(2,Proton1,Proton2)+=CH2(WhichOne%,3,Proton1,Proton2)*sinr
NEXT
NEXT

REM Transfer back changed results
FOR Carbon=2 TO 3
FOR Proton1=0 TO 3
FOR Proton2=0 TO 3
CH2(WhichOne%,Carbon,Proton1,Proton2)=TCH2(Carbon,Proton1,Proton2)
NEXT
NEXT
NEXT

WHEN 3
REM CH3 Carbon

REM Move y components
FOR Proton1=0 TO 3
FOR Proton2=0 TO 3
FOR Proton3=0 TO 3
TCH3(2,Proton1,Proton2,Proton3)=CH3(WhichOne%,2,Proton1,Proton2,Proto-
    n3)*cosr
TCH3(3,Proton1,Proton2,Proton3)=-
    CH3(WhichOne%,2,Proton1,Proton2,Proton3)*sinr
NEXT
NEXT
NEXT

REM Move z components
FOR Proton1=0 TO 3
```

```
FOR Proton2=0 TO 3
FOR Proton3=0 TO 3
TCH3(3,Proton1,Proton2,Proton3)+=CH3(WhichOne%,3,Proton1,Proton2,Prot-
     on3)*cosr
TCH3(2,Proton1,Proton2,Proton3)+=CH3(WhichOne%,3,Proton1,Proton2,Prot-
     on3)*sinr
NEXT
NEXT
NEXT

REM Transfer back changed results
FOR Carbon=2 TO 3
FOR Proton1=0 TO 3
FOR Proton2=0 TO 3
FOR Proton3=0 TO 3
CH3(WhichOne%,Carbon,Proton1,Proton2,Proton3)=TCH3(Carbon,Proton1,Pro-
     ton2,Proton3)
NEXT
NEXT
NEXT
NEXT
ENDCASE
ENDPROC

DEFPROCCy(num,NucNum%)
cosr=COS(RAD(num))
sinr=SIN(RAD(num))
WhichOne%=System(NucNum%,11)
CASE System(NucNum%,0) OF

WHEN 0
REM Q Carbon

REM Move x component
TC(1)=C(WhichOne%,1)*cosr
TC(3)=C(WhichOne%,1)*sinr

REM Move z component
TC(3)+=C(WhichOne%,3)*cosr
TC(1)-=C(WhichOne%,3)*sinr

REM Transfer back
C(WhichOne%,1)=TC(1)
C(WhichOne%,3)=TC(3)

WHEN 1
REM CH Carbon

REM Move y components
FOR Proton1=0 TO 3
TCH(1,Proton1)=CH(WhichOne%,1,Proton1)*cosr
TCH(3,Proton1)=CH(WhichOne%,1,Proton1)*sinr
NEXT

REM Move z components
FOR Proton1=0 TO 3
TCH(3,Proton1)+=CH(WhichOne%,3,Proton1)*cosr
```

```
TCH(1,Proton1)-=CH(WhichOne%,3,Proton1)*sinr
NEXT

REM Transfer back changed results
FOR Carbon=1 TO 3 STEP 2
FOR Proton1=0 TO 3
CH(WhichOne%,Carbon,Proton1)=TCH(Carbon,Proton1)
NEXT
NEXT

WHEN 2
REM CH2 Carbon

REM Move y components
FOR Proton1=0 TO 3
FOR Proton2=0 TO 3
TCH2(1,Proton1,Proton2)=CH2(WhichOne%,1,Proton1,Proton2)*cosr
TCH2(3,Proton1,Proton2)=CH2(WhichOne%,1,Proton1,Proton2)*sinr
NEXT
NEXT

REM Move z components
FOR Proton1=0 TO 3
FOR Proton2=0 TO 3
TCH2(3,Proton1,Proton2)+=CH2(WhichOne%,3,Proton1,Proton2)*cosr
TCH2(1,Proton1,Proton2)-=CH2(WhichOne%,3,Proton1,Proton2)*sinr
NEXT
NEXT

REM Transfer back changed results
FOR Carbon=1 TO 3 STEP 2
FOR Proton1=0 TO 3
FOR Proton2=0 TO 3
CH2(WhichOne%,Carbon,Proton1,Proton2)=TCH2(Carbon,Proton1,Proton2)
NEXT
NEXT
NEXT

WHEN 3
REM CH3 Carbon

REM Move y components
FOR Proton1=0 TO 3
FOR Proton2=0 TO 3
FOR Proton3=0 TO 3
TCH3(1,Proton1,Proton2,Proton3)=CH3(WhichOne%,1,Proton1,Proton2,Proto-
     n3)*cosr
TCH3(3,Proton1,Proton2,Proton3)=CH3(WhichOne%,1,Proton1,Proton2,Proto-
     n3)*sinr
NEXT
NEXT
NEXT

REM Move z components
FOR Proton1=0 TO 3
FOR Proton2=0 TO 3
FOR Proton3=0 TO 3
```

```
TCH3(3,Proton1,Proton2,Proton3)+=CH3(WhichOne%,3,Proton1,Proton2,Prot-
     on3)*cosr
TCH3(1,Proton1,Proton2,Proton3)-
     =CH3(WhichOne%,3,Proton1,Proton2,Proton3)*sinr
NEXT
NEXT
NEXT

REM Transfer back changed results
FOR Carbon=1 TO 3 STEP 2
FOR Proton1=0 TO 3
FOR Proton2=0 TO 3
FOR Proton3=0 TO 3
CH3(WhichOne%,Carbon,Proton1,Proton2,Proton3)=TCH3(Carbon,Proton1,Pro-
     ton2,Proton3)
NEXT
NEXT
NEXT
NEXT
ENDCASE
ENDPROC

DEFPROCChemicalShift(time,NucNum%)
LOCAL WhichOne%
WhichOne%=System(NucNum%,11)
REM Chemical Shift Evolution of Signals
:
REM Read correct data from definitions
CASE System(NucNum%,0) OF
WHEN 0:REM QC Carbon C.S only
PROCCarbonSC

WHEN 1:REM CH Carbon C.S. and Proton C.S.
PROCCarbonSC
PROCProton1SC

WHEN 2:REM CH2 Carbon C.S., Proton1 C.S. and Proton2 C.S
PROCCarbonSC
PROCProton1SC
PROCProton2SC

WHEN 3:REM CH3 Carbon C.S., Proton1 C.S., Proton2 C.S. and Proton3
     C.S.
PROCCarbonSC
PROCProton1SC
PROCProton2SC
PROCProton3SC
ENDCASE

REM Now let appropriate values in the matrices evolve
CASE System(NucNum%,0) OF
WHEN 0
REM QC

IF Cfreq<>0 THEN
REM Rotate X component
TC(1)=C(WhichOne%,1)*Ccosr
```

```
TC(2)=C(WhichOne%,1)*Csinr
REM Rotate Y component
TC(2)+=C(WhichOne%,2)*Ccosr
TC(1)-=C(WhichOne%,2)*Csinr
REM Reload main matrix
FOR Carbon%=1 TO 2
C(WhichOne%,Carbon%)=TC(Carbon%)
NEXT
ENDIF

WHEN 1
REM CH
REM First the Carbon C.S.
IF Cfreq<>0 THEN
FOR Proton1%=0 TO 3

REM Rotate X component
TCH(1,Proton1%)=CH(WhichOne%,1,Proton1%)*Ccosr
TCH(2,Proton1%)=CH(WhichOne%,1,Proton1%)*Csinr

REM Rotate Y component
TCH(2,Proton1%)+=CH(WhichOne%,2,Proton1%)*Ccosr
TCH(1,Proton1%)-=CH(WhichOne%,2,Proton1%)*Csinr
NEXT

REM Reload main matrix
FOR Carbon%=1 TO 2
FOR Proton1%=0 TO 3
CH(WhichOne%,Carbon%,Proton1%)=TCH(Carbon%,Proton1%)
NEXT
NEXT

ENDIF

REM Now the Proton1 C.S.
IF P1freq<>0 THEN

FOR Carbon%=0 TO 3
REM Rotate X component
TCH(Carbon%,1)=CH(WhichOne%,Carbon%,1)*P1cosr
TCH(Carbon%,2)=CH(WhichOne%,Carbon%,1)*P1sinr

REM Rotate Y component
TCH(Carbon%,2)+=CH(WhichOne%,Carbon%,2)*P1cosr
TCH(Carbon%,1)-=CH(WhichOne%,Carbon%,2)*P1sinr
NEXT

REM Reload main matrix
FOR Proton1%=1 TO 2
FOR Carbon%=0 TO 3
CH(WhichOne%,Carbon%,Proton1%)=TCH(Carbon%,Proton1%)
NEXT
NEXT
ENDIF

WHEN 2
REM CH2 System
```

```
REM First the Carbon C.S.
IF Cfreq<>0 THEN
FOR Proton1%=0 TO 3
FOR Proton2%=0 TO 3
REM Rotate X component
TCH2(1,Proton1%,Proton2%)=CH2(WhichOne%,1,Proton1%,Proton2%)*Ccosr
TCH2(2,Proton1%,Proton2%)=CH2(WhichOne%,1,Proton1%,Proton2%)*Csinr

REM Rotate Y component
TCH2(2,Proton1%,Proton2%)+=CH2(WhichOne%,2,Proton1%,Proton2%)*Ccosr
TCH2(1,Proton1%,Proton2%)-=CH2(WhichOne%,2,Proton1%,Proton2%)*Csinr
NEXT
NEXT

REM Reload main matrix
FOR Carbon%=1 TO 2
FOR Proton1%=0 TO 3
FOR Proton2%=0 TO 3
CH2(WhichOne%,Carbon%,Proton1%,Proton2%)=TCH2(Carbon%,Proton1%,Proton-
    2%)
NEXT
NEXT
NEXT
ENDIF

REM Now the Proton1 C.S.
IF P1freq<>0 THEN

FOR Carbon%=0 TO 3
FOR Proton2%=0 TO 3
REM Rotate X component
TCH2(Carbon%,1,Proton2%)=CH2(WhichOne%,Carbon%,1,Proton2%)*P1cosr
TCH2(Carbon%,2,Proton2%)=CH2(WhichOne%,Carbon%,1,Proton2%)*P1sinr

REM Rotate Y component
TCH2(Carbon%,2,Proton2%)+=CH2(WhichOne%,Carbon%,2,Proton2%)*P1cosr
TCH2(Carbon%,1,Proton2%)-=CH2(WhichOne%,Carbon%,2,Proton2%)*P1sinr
NEXT
NEXT

REM Reload main matrix
FOR Proton1%=1 TO 2
FOR Carbon%=0 TO 3
FOR Proton2%=0 TO 3
CH2(WhichOne%,Carbon%,Proton1%,Proton2%)=TCH2(Carbon%,Proton1%,Proton-
    2%)
NEXT
NEXT
NEXT
ENDIF

REM Now the Proton2 C.S.
IF P2freq<>0 THEN

FOR Carbon%=0 TO 3
FOR Proton1%=0 TO 3
REM Rotate X component
```

```
TCH2(Carbon%,Proton1%,1)=CH2(WhichOne%,Carbon%,Proton1%,1)*P2cosr
TCH2(Carbon%,Proton1%,2)=CH2(WhichOne%,Carbon%,Proton1%,1)*P2sinr

REM Rotate Y component
TCH2(Carbon%,Proton1%,2)+=CH2(WhichOne%,Carbon%,Proton1%,2)*P2cosr
TCH2(Carbon%,Proton1%,1)-=CH2(WhichOne%,Carbon%,Proton1%,2)*P2sinr
NEXT
NEXT

REM Reload main matrix
FOR Proton1%=0 TO 3
FOR Carbon%=0 TO 3
FOR Proton2%=1 TO 2
CH2(WhichOne%,Carbon%,Proton1%,Proton2%)=TCH2(Carbon%,Proton1%,Proton-
     2%)
NEXT
NEXT
NEXT
ENDIF

WHEN 3
REM CH3 System
REM First the Carbon C.S.
IF Cfreq<>0 THEN
FOR Proton1%=0 TO 3
FOR Proton2%=0 TO 3
FOR Proton3%=0 TO 3
REM Rotate X component
TCH3(1,Proton1%,Proton2%,Proton3%)=CH3(WhichOne%,1,Proton1%,Proton2%,-
     Proton3%)*Ccosr
TCH3(2,Proton1%,Proton2%,Proton3%)=CH3(WhichOne%,1,Proton1%,Proton2%,-
     Proton3%)*Csinr

REM Rotate Y component
TCH3(2,Proton1%,Proton2%,Proton3%)+=CH3(WhichOne%,2,Proton1%,Proton2%-
     ,Proton3%)*Ccosr
TCH3(1,Proton1%,Proton2%,Proton3%)-
     =CH3(WhichOne%,2,Proton1%,Proton2%,Proton3%)*Csinr
NEXT
NEXT
NEXT

REM Reload main matrix
FOR Carbon%=1 TO 2
FOR Proton1%=0 TO 3
FOR Proton2%=0 TO 3
FOR Proton3%=0 TO 3
CH3(WhichOne%,Carbon%,Proton1%,Proton2%,Proton3%)=TCH3(Carbon%,Proton-
     1%,Proton2%,Proton3%)
NEXT
NEXT
NEXT
NEXT
ENDIF

REM Now the Proton1 C.S.
IF P1freq<>0 THEN
```

```
FOR Carbon%=0 TO 3
FOR Proton2%=0 TO 3
FOR Proton3%=0 TO 3
REM Rotate X component
TCH3(Carbon%,1,Proton2%,Proton3%)=CH3(WhichOne%,Carbon%,1,Proton2%,Pr-
     oton3%)*P1cosr
TCH3(Carbon%,2,Proton2%,Proton3%)=CH3(WhichOne%,Carbon%,1,Proton2%,Pr-
     oton3%)*P1sinr

REM Rotate Y component
TCH3(Carbon%,2,Proton2%,Proton3%)+=CH3(WhichOne%,Carbon%,2,Proton2%,P-
     roton3%)*P1cosr
TCH3(Carbon%,1,Proton2%,Proton3%)-
     =CH3(WhichOne%,Carbon%,2,Proton2%,Proton3%)*P1sinr
NEXT
NEXT
NEXT

REM Reload main matrix
FOR Carbon%=0 TO 3
FOR Proton1%=1 TO 2
FOR Proton2%=0 TO 3
FOR Proton3%=0 TO 3
CH3(WhichOne%,Carbon%,Proton1%,Proton2%,Proton3%)=TCH3(Carbon%,Proton-
     1%,Proton2%,Proton3%)
NEXT
NEXT
NEXT
NEXT
ENDIF

REM Now the Proton2 C.S.
IF P2freq<>0 THEN

FOR Carbon%=0 TO 3
FOR Proton1%=0 TO 3
FOR Proton3%=0 TO 3
REM Rotate X component
TCH3(Carbon%,Proton1%,1,Proton3%)=CH3(WhichOne%,Carbon%,Proton1%,1,Pr-
     oton3%)*P2cosr
TCH3(Carbon%,Proton1%,2,Proton3%)=CH3(WhichOne%,Carbon%,Proton1%,1,Pr-
     oton3%)*P2sinr

REM Rotate Y component
TCH3(Carbon%,Proton1%,2,Proton3%)+=CH3(WhichOne%,Carbon%,Proton1%,2,P-
     roton3%)*P2cosr
TCH3(Carbon%,Proton1%,1,Proton3%)-
     =CH3(WhichOne%,Carbon%,Proton1%,2,Proton3%)*P2sinr
NEXT
NEXT
NEXT

REM Reload main matrix
FOR Carbon%=0 TO 3
FOR Proton1%=0 TO 3
FOR Proton2%=1 TO 2
```

```
FOR Proton3%=0 TO 3
CH3(WhichOne%,Carbon%,Proton1%,Proton2%,Proton3%)=TCH3(Carbon%,Proton-
     1%,Proton2%,Proton3%)
NEXT
NEXT
NEXT
NEXT
ENDIF
REM Now the Proton3 C.S.
IF P3freq<>0 THEN

FOR Carbon%=0 TO 3
FOR Proton1%=0 TO 3
FOR Proton2%=0 TO 3
REM Rotate X component
TCH3(Carbon%,Proton1%,Proton2%,1)=CH3(WhichOne%,Carbon%,Proton1%,Prot-
     on2%,1)*P3cosr
TCH3(Carbon%,Proton1%,Proton2%,2)=CH3(WhichOne%,Carbon%,Proton1%,Prot-
     on2%,1)*P3sinr

REM Rotate Y component
TCH3(Carbon%,Proton1%,Proton2%,2)+=CH3(WhichOne%,Carbon%,Proton1%,Pro-
     ton2%,2)*P3cosr
TCH3(Carbon%,Proton1%,Proton2%,1)-
     =CH3(WhichOne%,Carbon%,Proton1%,Proton2%,2)*P3sinr
NEXT
NEXT
NEXT

REM Reload main matrix
FOR Carbon%=0 TO 3
FOR Proton1%=0 TO 3
FOR Proton2%=0 TO 3
FOR Proton3%=1 TO 2
CH3(WhichOne%,Carbon%,Proton1%,Proton2%,Proton3%)=TCH3(Carbon%,Proton-
     1%,Proton2%,Proton3%)
NEXT
NEXT
NEXT
NEXT
ENDIF

ENDCASE
ENDPROC

DEFPROCJCoupling(time,NucNum%)
LOCAL WhichOne%
WhichOne%=System(NucNum%,11)

REM Load correct J values from matrix
Type%=System(NucNum%,0)
CASE Type% OF
REM No action on QC

WHEN 1
REM Load CH coupling constant
PROCch1J
```

```
WHEN 2
REM Load CH1, CH2 and H1H2 coupling constant
PROCch1J
PROCch2J

WHEN 3
REM Load CH1, CH2, CH3, H1H2, H1H3 and H2H3 coupling constant
PROCch1J
PROCch2J
PROCch3J
ENDCASE

REM Now let appropriate J couplings evolve
CASE Type% OF
REM No Action on Q.C.

WHEN 1
REM CH Coupling Evolution

REM Carbon
REM Sx > SyIz,
TCH(1,0)=CH(WhichOne%,1,0)*cosJCH1
TCH(2,3)=CH(WhichOne%,1,0)*sinJCH1

REM SyIz > -Sx
TCH(2,3)+=CH(WhichOne%,2,3)*cosJCH1
TCH(1,0)-=CH(WhichOne%,2,3)*sinJCH1

REM Sy > SxIz,
TCH(2,0)=CH(WhichOne%,2,0)*cosJCH1
TCH(1,3)=-CH(WhichOne%,2,0)*sinJCH1

REM SxIz > -Sy
TCH(1,3)+=CH(WhichOne%,1,3)*cosJCH1
TCH(2,0)+=CH(WhichOne%,1,3)*sinJCH1

REM Proton1
REM Ix > IySz,
TCH(0,1)=CH(WhichOne%,0,1)*cosJCH1
TCH(3,2)=CH(WhichOne%,0,1)*sinJCH1

REM IySz > -Ix
TCH(3,2)+=CH(WhichOne%,3,2)*cosJCH1
TCH(0,1)-=CH(WhichOne%,3,2)*sinJCH1

REM Iy > IxSz,
TCH(0,2)=CH(WhichOne%,0,2)*cosJCH1
TCH(3,1)=-CH(WhichOne%,0,2)*sinJCH1

REM IxSz > -Iy
TCH(3,1)+=CH(WhichOne%,3,1)*cosJCH1
TCH(0,2)+=CH(WhichOne%,3,1)*sinJCH1

REM Transfer back
FOR Carbon%=0 TO 3
CASE Carbon% OF
```

```
WHEN 0,3
FOR Proton1%=1 TO 2
CH(WhichOne%,Carbon%,Proton1%)=TCH(Carbon%,Proton1%)
NEXT
WHEN 1,2
FOR Proton1%=0 TO 3 STEP 3
CH(WhichOne%,Carbon%,Proton1%)=TCH(Carbon%,Proton1%)
NEXT
ENDCASE
NEXT
WHEN 2
REM CH2 Coupling Evolution
REM First C - H1 Evolution
FOR Proton2%=0 TO 3
REM Carbon to Proton1 Coulping
REM Sx > SyIz,
TCH2(1,0,Proton2%)=CH2(WhichOne%,1,0,Proton2%)*cosJCH1
TCH2(2,3,Proton2%)=CH2(WhichOne%,1,0,Proton2%)*sinJCH1

REM SyIz > -Sx
TCH2(2,3,Proton2%)+=CH2(WhichOne%,2,3,Proton2%)*cosJCH1
TCH2(1,0,Proton2%)-=CH2(WhichOne%,2,3,Proton2%)*sinJCH1

REM Sy> -SxIz,
TCH2(2,0,Proton2%)=CH2(WhichOne%,2,0,Proton2%)*cosJCH1
TCH2(1,3,Proton2%)=-CH2(WhichOne%,2,0,Proton2%)*sinJCH1

REM SxIz > Sy
TCH2(1,3,Proton2%)+=CH2(WhichOne%,1,3,Proton2%)*cosJCH1
TCH2(2,0,Proton2%)+=CH2(WhichOne%,1,3,Proton2%)*sinJCH1
NEXT

REM Transfer back
FOR  Proton2%=0 TO 3
FOR Carbon%=1 TO 2
FOR Proton1%=0 TO 3 STEP 3
CH2(WhichOne%,Carbon%,Proton1%,Proton2%)=TCH2(Carbon%,Proton1%,Proton-
    2%)
NEXT
NEXT
NEXT

REM Proton1 To Carbon Coupling
FOR Proton2%=0 TO 3
REM   Ix > IySz
TCH2(0,1,Proton2%)=CH2(WhichOne%,0,1,Proton2%)*cosJCH1
TCH2(3,2,Proton2%)=CH2(WhichOne%,0,1,Proton2%)*sinJCH1

REM IySz > -Ix
TCH2(3,2,Proton2%)+=CH2(WhichOne%,3,2,Proton2%)*cosJCH1
TCH2(0,1,Proton2%)-=CH2(WhichOne%,3,2,Proton2%)*sinJCH1

REM   Iy > -IxSz
TCH2(0,2,Proton2%)=CH2(WhichOne%,0,2,Proton2%)*cosJCH1
TCH2(3,1,Proton2%)=-CH2(WhichOne%,0,2,Proton2%)*sinJCH1

REM IxSz > Iy
```

```
TCH2(3,1,Proton2%)+=CH2(WhichOne%,3,1,Proton2%)*cosJCH1
TCH2(0,2,Proton2%)+=CH2(WhichOne%,3,1,Proton2%)*sinJCH1
NEXT

REM Transfer back
FOR Proton2%=0 TO 3
FOR Carbon%=0 TO 3 STEP 3
FOR Proton1%=1 TO 2
CH2(WhichOne%,Carbon%,Proton1%,Proton2%)=TCH2(Carbon%,Proton1%,Proton-
     2%)
NEXT
NEXT
NEXT

REM Now C - H2 Evolution
FOR Proton1%=0 TO 3
REM Carbon
REM Sx > SyIz,
TCH2(1,Proton1%,0)=CH2(WhichOne%,1,Proton1%,0)*cosJCH2
TCH2(2,Proton1%,3)=CH2(WhichOne%,1,Proton1%,0)*sinJCH2

REM SyIz > -Sx
TCH2(2,Proton1%,3)+=CH2(WhichOne%,2,Proton1%,3)*cosJCH2
TCH2(1,Proton1%,0)-=CH2(WhichOne%,2,Proton1%,3)*sinJCH2

REM Sy> -SxIz,
TCH2(2,Proton1%,0)=CH2(WhichOne%,2,Proton1%,0)*cosJCH2
TCH2(1,Proton1%,3)=-CH2(WhichOne%,2,Proton1%,0)*sinJCH2

REM SxIz > Sy
TCH2(1,Proton1%,3)+=CH2(WhichOne%,1,Proton1%,3)*cosJCH2
TCH2(2,Proton1%,0)+=CH2(WhichOne%,1,Proton1%,3)*sinJCH2
REM Transfer back
NEXT
FOR Carbon%=1 TO 2
FOR Proton1%=0 TO 3
FOR Proton2%=0 TO 3 STEP 3
CH2(WhichOne%,Carbon%,Proton1%,Proton2%)=TCH2(Carbon%,Proton1%,Proton-
     2%)
NEXT
NEXT
NEXT

FOR Proton1%=0 TO 3
REM Proton1
REM   Ix > IySz
TCH2(0,Proton1%,1)=CH2(WhichOne%,0,Proton1%,1)*cosJCH2
TCH2(3,Proton1%,2)=CH2(WhichOne%,0,Proton1%,1)*sinJCH2

REM IySz > -Ix
TCH2(3,Proton1%,2)+=CH2(WhichOne%,3,Proton1%,2)*cosJCH2
TCH2(0,Proton1%,1)-=CH2(WhichOne%,3,Proton1%,2)*sinJCH2

REM   Iy > -IxSz
TCH2(0,Proton1%,2)=CH2(WhichOne%,0,Proton1%,2)*cosJCH2
TCH2(3,Proton1%,1)=-CH2(WhichOne%,0,Proton1%,2)*sinJCH2
```

```
REM IxSz > Iy
TCH2(3,Proton1%,1)+=CH2(WhichOne%,3,Proton1%,1)*cosJCH2
TCH2(0,Proton1%,2)+=CH2(WhichOne%,3,Proton1%,1)*sinJCH2
NEXT

REM Transfer back
FOR Carbon%=0 TO 3 STEP 3
FOR Proton1%=0 TO 3
FOR Proton2%=1 TO 2
CH2(WhichOne%,Carbon%,Proton1%,Proton2%)=TCH2(Carbon%,Proton1%,Proton-
     2%)
NEXT
NEXT
NEXT

REM Now H1 - H2 Evolution
IF JH1H2<>0 THEN
FOR Carbon%=0 TO 3
REM Proton1
REM I1x > I1yI2z,
TCH2(Carbon%,1,0)=CH2(WhichOne%,Carbon%,1,0)*cosJH1H2
TCH2(Carbon%,2,3)=CH2(WhichOne%,Carbon%,1,0)*sinJH1H2

REM SyIz > -Sx
TCH2(Carbon%,2,3)+=CH2(WhichOne%,Carbon%,2,3)*cosJH1H2
TCH2(Carbon%,1,0)-=CH2(WhichOne%,Carbon%,2,3)*sinJH1H2

REM Sy> -SxIz,
TCH2(Carbon%,2,0)=CH2(WhichOne%,Carbon%,2,0)*cosJH1H2
TCH2(Carbon%,1,3)=-CH2(WhichOne%,Carbon%,2,0)*sinJH1H2

REM SxIz > Sy
TCH2(Carbon%,1,3)+=CH2(WhichOne%,Carbon%,1,3)*cosJH1H2
TCH2(Carbon%,2,0)+=CH2(WhichOne%,Carbon%,1,3)*sinJH1H2
REM Transfer back
NEXT
FOR Carbon%=0 TO 3
FOR Proton1%=1 TO 2
FOR Proton2%=0 TO 3 STEP 3
CH2(WhichOne%,Carbon%,Proton1%,Proton2%)=TCH2(Carbon%,Proton1%,Proton-
     2%)
NEXT
NEXT
NEXT

FOR Carbon%=0 TO 3
REM Proton2
REM   Ix > IySz
TCH2(Carbon%,0,1)=CH2(WhichOne%,Carbon%,0,1)*cosJH1H2
TCH2(Carbon%,3,2)=CH2(WhichOne%,Carbon%,0,1)*sinJH1H2

REM IySz > -Ix
TCH2(Carbon%,3,2)+=CH2(WhichOne%,Carbon%,3,2)*cosJH1H2
TCH2(Carbon%,0,1)-=CH2(WhichOne%,Carbon%,3,2)*sinJH1H2

REM   Iy > -IxSz
TCH2(Carbon%,0,2)=CH2(WhichOne%,Carbon%,0,2)*cosJH1H2
```

```
TCH2(Carbon%,3,1)=-CH2(WhichOne%,Carbon%,0,2)*sinJH1H2

REM IxSz > Iy
TCH2(Carbon%,3,1)+=CH2(WhichOne%,Carbon%,3,1)*cosJH1H2
TCH2(Carbon%,0,2)+=CH2(WhichOne%,Carbon%,3,1)*sinJH1H2
NEXT

REM Transfer back
FOR Carbon%=0 TO 3
FOR Proton1%=0 TO 3 STEP 3
FOR Proton2%=1 TO 2
CH2(WhichOne%,Carbon%,Proton1%,Proton2%)=TCH2(Carbon%,Proton1%,Proton-
    2%)
NEXT
NEXT
NEXT
ENDIF

WHEN 3

FOR Proton3%=0 TO 3
FOR Proton2%=0 TO 3
REM Carbon to Proton1 Coulping for all Proton2 & Proton3
REM Sx > SyIz,
TCH3(1,0,Proton2%,Proton3%)=CH3(WhichOne%,1,0,Proton2%,Proton3%)*cosJ-
    CH1
TCH3(2,3,Proton2%,Proton3%)=CH3(WhichOne%,1,0,Proton2%,Proton3%)*sinJ-
    CH1

REM SyIz > -Sx
TCH3(2,3,Proton2%,Proton3%)+=CH3(WhichOne%,2,3,Proton2%,Proton3%)*cos-
    JCH1
TCH3(1,0,Proton2%,Proton3%)-
    =CH3(WhichOne%,2,3,Proton2%,Proton3%)*sinJCH1

REM Sy> -SxIz,
TCH3(2,0,Proton2%,Proton3%)=CH3(WhichOne%,2,0,Proton2%,Proton3%)*cosJ-
    CH1
TCH3(1,3,Proton2%,Proton3%)=-
    CH3(WhichOne%,2,0,Proton2%,Proton3%)*sinJCH1

REM SxIz > Sy
TCH3(1,3,Proton2%,Proton3%)+=CH3(WhichOne%,1,3,Proton2%,Proton3%)*cos-
    JCH1
TCH3(2,0,Proton2%,Proton3%)+=CH3(WhichOne%,1,3,Proton2%,Proton3%)*sin-
    JCH1
NEXT
NEXT

REM Transfer back
FOR  Proton3%=0 TO 3
FOR  Proton2%=0 TO 3
FOR  Carbon%=1 TO 2
FOR  Proton1%=0 TO 3 STEP 3
CH3(WhichOne%,Carbon%,Proton1%,Proton2%,Proton3%)=TCH3(Carbon%,Proton-
    1%,Proton2%,Proton3%)
NEXT
```

```
NEXT
NEXT
NEXT

REM Proton1 To Carbon Coupling for all Proton2 and Proton3
FOR Proton3%=0 TO 3
FOR Proton2%=0 TO 3
REM   Ix > IySz
TCH3(0,1,Proton2%,Proton3%)=CH3(WhichOne%,0,1,Proton2%,Proton3%)*cosJ-
     CH1
TCH3(3,2,Proton2%,Proton3%)=CH3(WhichOne%,0,1,Proton2%,Proton3%)*sinJ-
     CH1

REM IySz > -Ix
TCH3(3,2,Proton2%,Proton3%)+=CH3(WhichOne%,3,2,Proton2%,Proton3%)*cos-
     JCH1
TCH3(0,1,Proton2%,Proton3%)-
     =CH3(WhichOne%,3,2,Proton2%,Proton3%)*sinJCH1

REM   Iy > -IxSz
TCH3(0,2,Proton2%,Proton3%)=CH3(WhichOne%,0,2,Proton2%,Proton3%)*cosJ-
     CH1
TCH3(3,1,Proton2%,Proton3%)=-
     CH3(WhichOne%,0,2,Proton2%,Proton3%)*sinJCH1

REM IxSz > Iy
TCH3(3,1,Proton2%,Proton3%)+=CH3(WhichOne%,3,1,Proton2%,Proton3%)*cos-
     JCH1
TCH3(0,2,Proton2%,Proton3%)+=CH3(WhichOne%,3,1,Proton2%,Proton3%)*sin-
     JCH1
NEXT
NEXT

REM Transfer back
FOR Proton3%=0 TO 3
FOR Proton2%=0 TO 3
FOR Carbon%=0 TO 3 STEP 3
FOR Proton1%=1 TO 2
CH3(WhichOne%,Carbon%,Proton1%,Proton2%,Proton3%)=TCH3(Carbon%,Proton-
     1%,Proton2%,Proton3%)
NEXT
NEXT
NEXT
NEXT
REM Now Carbon  To Proton2 Coupling for all Proton1 and Proton3
FOR Proton3%=0 TO 3
FOR Proton1%=0 TO 3
REM Carbon
REM Sx > SyIz,
TCH3(1,Proton1%,0,Proton3%)=CH3(WhichOne%,1,Proton1%,0,Proton3%)*cosJ-
     CH2
TCH3(2,Proton1%,3,Proton3%)=CH3(WhichOne%,1,Proton1%,0,Proton3%)*sinJ-
     CH2

REM SyIz > -Sx
TCH3(2,Proton1%,3,Proton3%)+=CH3(WhichOne%,2,Proton1%,3,Proton3%)*cos-
     JCH2
```

```
TCH3(1,Proton1%,0,Proton3%)-
     =CH3(WhichOne%,2,Proton1%,3,Proton3%)*sinJCH2

REM Sy> -SxIz,
TCH3(2,Proton1%,0,Proton3%)=CH3(WhichOne%,2,Proton1%,0,Proton3%)*cosJ-
     CH2
TCH3(1,Proton1%,3,Proton3%)=-
     CH3(WhichOne%,2,Proton1%,0,Proton3%)*sinJCH2

REM SxIz > Sy
TCH3(1,Proton1%,3,Proton3%)+=CH3(WhichOne%,1,Proton1%,3,Proton3%)*cos-
     JCH2
TCH3(2,Proton1%,0,Proton3%)+=CH3(WhichOne%,1,Proton1%,3,Proton3%)*sin-
     JCH2
REM Transfer back
NEXT
NEXT

FOR Carbon%=1 TO 2
FOR Proton1%=0 TO 3
FOR Proton2%=0 TO 3 STEP 3
FOR Proton3%=0 TO 3
CH3(WhichOne%,Carbon%,Proton1%,Proton2%,Proton3%)=TCH3(Carbon%,Proton-
     1%,Proton2%,Proton3%)
NEXT
NEXT
NEXT
NEXT

FOR Proton3%=0 TO 3
FOR Proton1%=0 TO 3
REM Proton1
REM   Ix > IySz
TCH3(0,Proton1%,1,Proton3%)=CH3(WhichOne%,0,Proton1%,1,Proton3%)*cosJ-
     CH2
TCH3(3,Proton1%,2,Proton3%)=CH3(WhichOne%,0,Proton1%,1,Proton3%)*sinJ-
     CH2

REM IySz > -Ix
TCH3(3,Proton1%,2,Proton3%)+=CH3(WhichOne%,3,Proton1%,2,Proton3%)*cos-
     JCH2
TCH3(0,Proton1%,1,Proton3%)-
     =CH3(WhichOne%,3,Proton1%,2,Proton3%)*sinJCH2

REM   Iy > -IxSz
TCH3(0,Proton1%,2,Proton3%)=CH3(WhichOne%,0,Proton1%,2,Proton3%)*cosJ-
     CH2
TCH3(3,Proton1%,1,Proton3%)=-
     CH3(WhichOne%,0,Proton1%,2,Proton3%)*sinJCH2

REM IxSz > Iy
TCH3(3,Proton1%,1,Proton3%)+=CH3(WhichOne%,3,Proton1%,1,Proton3%)*cos-
     JCH2
TCH3(0,Proton1%,2,Proton3%)+=CH3(WhichOne%,3,Proton1%,1,Proton3%)*sin-
     JCH2
NEXT
NEXT
```

```
REM Transfer back
FOR Carbon%=0 TO 3 STEP 3
FOR Proton1%=0 TO 3
FOR Proton2%=1 TO 2
FOR Proton3%=0 TO 3
CH3(WhichOne%,Carbon%,Proton1%,Proton2%,Proton3%)=TCH3(Carbon%,Proton-
     1%,Proton2%,Proton3%)
NEXT
NEXT
NEXT
NEXT
REM Now Carbon  To Proton3 Coupling for all Proton1 and Proton2
FOR Proton2%=0 TO 3
FOR Proton1%=0 TO 3
REM Carbon
REM Sx > SyIz,
TCH3(1,Proton1%,Proton2%,0)=CH3(WhichOne%,1,Proton1%,Proton2%,0)*cosJ-
     CH3
TCH3(2,Proton1%,Proton2%,3)=CH3(WhichOne%,1,Proton1%,Proton2%,0)*sinJ-
     CH3

REM SyIz > -Sx
TCH3(2,Proton1%,Proton2%,3)+=CH3(WhichOne%,2,Proton1%,Proton2%,3)*cos-
     JCH3
TCH3(1,Proton1%,Proton2%,0)-
     =CH3(WhichOne%,2,Proton1%,Proton2%,3)*sinJCH3

REM Sy> -SxIz,
TCH3(2,Proton1%,Proton2%,0)=CH3(WhichOne%,2,Proton1%,Proton2%,0)*cosJ-
     CH3
TCH3(1,Proton1%,Proton2%,3)=-
     CH3(WhichOne%,2,Proton1%,Proton2%,0)*sinJCH3

REM SxIz > Sy
TCH3(1,Proton1%,Proton2%,3)+=CH3(WhichOne%,1,Proton1%,Proton2%,3)*cos-
     JCH3
TCH3(2,Proton1%,Proton2%,0)+=CH3(WhichOne%,1,Proton1%,Proton2%,3)*sin-
     JCH3
REM Transfer back
NEXT
NEXT

FOR Carbon%=1 TO 2
FOR Proton1%=0 TO 3
FOR Proton2%=0 TO 3
FOR Proton3%=0 TO 3 STEP 3
CH3(WhichOne%,Carbon%,Proton1%,Proton2%,Proton3%)=TCH3(Carbon%,Proton-
     1%,Proton2%,Proton3%)
NEXT
NEXT
NEXT
NEXT

FOR Proton2%=0 TO 3
FOR Proton1%=0 TO 3
REM Proton1
```

```
REM    Ix > IySz
TCH3(0,Proton1%,Proton2%,1)=CH3(WhichOne%,0,Proton1%,Proton2%,1)*cosJ-
     CH3
TCH3(3,Proton1%,Proton2%,2)=CH3(WhichOne%,0,Proton1%,Proton2%,1)*sinJ-
     CH3

REM IySz > -Ix
TCH3(3,Proton1%,Proton2%,2)+=CH3(WhichOne%,3,Proton1%,Proton2%,2)*cos-
     JCH3
TCH3(0,Proton1%,Proton2%,1)-
     =CH3(WhichOne%,3,Proton1%,Proton2%,2)*sinJCH3

REM    Iy > -IxSz
TCH3(0,Proton1%,Proton2%,2)=CH3(WhichOne%,0,Proton1%,Proton2%,2)*cosJ-
     CH3
TCH3(3,Proton1%,Proton2%,1)=-
     CH3(WhichOne%,0,Proton1%,Proton2%,2)*sinJCH3

REM IxSz > Iy
TCH3(3,Proton1%,Proton2%,1)+=CH3(WhichOne%,3,Proton1%,Proton2%,1)*cos-
     JCH3
TCH3(0,Proton1%,Proton2%,2)+=CH3(WhichOne%,3,Proton1%,Proton2%,1)*sin-
     JCH3
NEXT
NEXT

REM Transfer back
FOR Carbon%=0 TO 3 STEP 3
FOR Proton1%=0 TO 3
FOR Proton2%=0 TO 3
FOR Proton3%=1 TO 2
CH3(WhichOne%,Carbon%,Proton1%,Proton2%,Proton3%)=TCH3(Carbon%,Proton-
     1%,Proton2%,Proton3%)
NEXT
NEXT
NEXT
NEXT

REM Now Coupling between H1 and H2 for all Carbon and Proton3
IF JH1H2<>0 THEN
FOR Proton3%=0 TO 3
FOR Carbon%=0 TO 3
REM Proton1
REM I1x > I1yI2z,
TCH3(Carbon%,1,0,Proton3%)=CH3(WhichOne%,Carbon%,1,0,Proton3%)*cosJH1-
     H2
TCH3(Carbon%,2,3,Proton3%)=CH3(WhichOne%,Carbon%,1,0,Proton3%)*sinJH1-
     H2

REM SyIz > -Sx
TCH3(Carbon%,2,3,Proton3%)+=CH3(WhichOne%,Carbon%,2,3,Proton3%)*cosJH-
     1H2
TCH3(Carbon%,1,0,Proton3%)-
     =CH3(WhichOne%,Carbon%,2,3,Proton3%)*sinJH1H2

REM Sy> -SxIz,
TCH3(Carbon%,2,0,Proton3%)=CH3(WhichOne%,Carbon%,2,0,Proton3%)*cosJH1-
     H2
```

```
TCH3(Carbon%,1,3,Proton3%)=-
     CH3(WhichOne%,Carbon%,2,0,Proton3%)*sinJH1H2

REM SxIz > Sy
TCH3(Carbon%,1,3,Proton3%)+=CH3(WhichOne%,Carbon%,1,3,Proton3%)*cosJH-
     1H2
TCH3(Carbon%,2,0,Proton3%)+=CH3(WhichOne%,Carbon%,1,3,Proton3%)*sinJH-
     1H2
NEXT
NEXT

REM Transfer back
FOR Carbon%=0 TO 3
FOR Proton1%=1 TO 2
FOR Proton2%=0 TO 3 STEP 3
FOR Proton3%=0 TO 3
CH3(WhichOne%,Carbon%,Proton1%,Proton2%,Proton3%)=TCH3(Carbon%,Proton-
     1%,Proton2%,Proton3%)
NEXT
NEXT
NEXT
NEXT

FOR Proton3%=0 TO 3
FOR Carbon%=0 TO 3
REM Proton2
REM   Ix > IySz
TCH3(Carbon%,0,1,Proton3%)=CH3(WhichOne%,Carbon%,0,1,Proton3%)*cosJH1-
     H2
TCH3(Carbon%,3,2,Proton3%)=CH3(WhichOne%,Carbon%,0,1,Proton3%)*sinJH1-
     H2

REM IySz > -Ix
TCH3(Carbon%,3,2,Proton3%)+=CH3(WhichOne%,Carbon%,3,2,Proton3%)*cosJH-
     1H2
TCH3(Carbon%,0,1,Proton3%)-
     =CH3(WhichOne%,Carbon%,3,2,Proton3%)*sinJH1H2

REM   Iy > -IxSz
TCH3(Carbon%,0,2,Proton3%)=CH3(WhichOne%,Carbon%,0,2,Proton3%)*cosJH1-
     H2
TCH3(Carbon%,3,1,Proton3%)=-
     CH3(WhichOne%,Carbon%,0,2,Proton3%)*sinJH1H2

REM IxSz > Iy
TCH3(Carbon%,3,1,Proton3%)+=CH3(WhichOne%,Carbon%,3,1,Proton3%)*cosJH-
     1H2
TCH3(Carbon%,0,2,Proton3%)+=CH3(WhichOne%,Carbon%,3,1,Proton3%)*sinJH-
     1H2
NEXT
NEXT

REM Transfer back
FOR Carbon%=0 TO 3
FOR Proton1%=0 TO 3 STEP 3
FOR Proton2%=1 TO 2
FOR Proton3%=0 TO 3
```

```
CH3(WhichOne%,Carbon%,Proton1%,Proton2%,Proton3%)=TCH3(Carbon%,Proton-
     1%,Proton2%,Proton3%)
NEXT
NEXT
NEXT
NEXT
ENDIF

REM Now Coupling between H1 and H3 for all Carbon and Proton2
IF JH1H3<>0 THEN
FOR Proton2%=0 TO 3
FOR Carbon%=0 TO 3
REM Proton1 To Proton 3
REM I1x > I1yI2z,
TCH3(Carbon%,1,Proton2%,0)=CH3(WhichOne%,Carbon%,1,Proton2%,0)*cosJH1-
     H3
TCH3(Carbon%,2,Proton2%,3)=CH3(WhichOne%,Carbon%,1,Proton2%,0)*sinJH1-
     H3

REM SyIz > -Sx
TCH3(Carbon%,2,Proton2%,3)+=CH3(WhichOne%,Carbon%,2,Proton2%,3)*cosJH-
     1H3
TCH3(Carbon%,1,Proton2%,0)-
     =CH3(WhichOne%,Carbon%,2,Proton2%,3)*sinJH1H3

REM Sy> -SxIz,
TCH3(Carbon%,2,Proton2%,0)=CH3(WhichOne%,Carbon%,2,Proton2%,0)*cosJH1-
     H3
TCH3(Carbon%,1,Proton2%,3)=-
     CH3(WhichOne%,Carbon%,2,Proton2%,0)*sinJH1H3

REM SxIz > Sy
TCH3(Carbon%,1,Proton2%,3)+=CH3(WhichOne%,Carbon%,1,Proton2%,3)*cosJH-
     1H3
TCH3(Carbon%,2,Proton2%,0)+=CH3(WhichOne%,Carbon%,1,Proton2%,3)*sinJH-
     1H3
NEXT
NEXT
REM Transfer back

FOR Carbon%=0 TO 3
FOR Proton1%=1 TO 2
FOR Proton2%=0 TO 3
FOR Proton3%=0 TO 3 STEP 3
CH3(WhichOne%,Carbon%,Proton1%,Proton2%,Proton3%)=TCH3(Carbon%,Proton-
     1%,Proton2%,Proton3%)
NEXT
NEXT
NEXT
NEXT

FOR Proton2%=0 TO 3
FOR Carbon%=0 TO 3
REM Proton3 To Proton 1
REM   Ix > IySz
TCH3(Carbon%,0,Proton2%,1)=CH3(WhichOne%,Carbon%,0,Proton2%,1)*cosJH1-
     H3
```

```
TCH3(Carbon%,3,Proton2%,2)=CH3(WhichOne%,Carbon%,0,Proton2%,1)*sinJH1-
     H3

REM IySz > -Ix
TCH3(Carbon%,3,Proton2%,2)+=CH3(WhichOne%,Carbon%,3,Proton2%,2)*cosJH-
     1H3
TCH3(Carbon%,0,Proton2%,1)-
     =CH3(WhichOne%,Carbon%,3,Proton2%,2)*sinJH1H3

REM   Iy > -IxSz
TCH3(Carbon%,0,Proton2%,2)=CH3(WhichOne%,Carbon%,0,Proton2%,2)*cosJH1-
     H3
TCH3(Carbon%,3,Proton2%,1)=-
     CH3(WhichOne%,Carbon%,0,Proton2%,2)*sinJH1H3

REM IxSz > Iy
TCH3(Carbon%,3,Proton2%,1)+=CH3(WhichOne%,Carbon%,3,Proton2%,1)*cosJH-
     1H3
TCH3(Carbon%,0,Proton2%,2)+=CH3(WhichOne%,Carbon%,3,Proton2%,1)*sinJH-
     1H3
NEXT
NEXT

REM Transfer back
FOR Carbon%=0 TO 3
FOR Proton1%=0 TO 3 STEP 3
FOR Proton2%=0 TO 3
FOR Proton3%=1 TO 2
CH3(WhichOne%,Carbon%,Proton1%,Proton2%,Proton3%)=TCH3(Carbon%,Proton-
     1%,Proton2%,Proton3%)
NEXT
NEXT
NEXT
NEXT
ENDIF

REM Now Coupling between H2 and H3 for all Carbon and Proton2
IF JH2H3<>0 THEN
FOR Proton1%=0 TO 3
FOR Carbon%=0 TO 3
REM Proton2 To Proton 3
REM I1x > I1yI2z,
TCH3(Carbon%,Proton1%,1,0)=CH3(WhichOne%,Carbon%,Proton1%,1,0)*cosJH2-
     H3
TCH3(Carbon%,Proton1%,2,3)=CH3(WhichOne%,Carbon%,Proton1%,1,0)*sinJH2-
     H3

REM SyIz > -Sx
TCH3(Carbon%,Proton1%,2,3)+=CH3(WhichOne%,Carbon%,Proton1%,2,3)*cosJH-
     2H3
TCH3(Carbon%,Proton1%,1,0)-
     =CH3(WhichOne%,Carbon%,Proton1%,2,3)*sinJH2H3

REM Sy> -SxIz,
TCH3(Carbon%,Proton1%,2,0)=CH3(WhichOne%,Carbon%,Proton1%,2,0)*cosJH2-
     H3
TCH3(Carbon%,Proton1%,1,3)=-
     CH3(WhichOne%,Carbon%,Proton1%,2,0)*sinJH2H3
```

```
REM SxIz > Sy
TCH3(Carbon%,Proton1%,1,3)+=CH3(WhichOne%,Carbon%,Proton1%,1,3)*cosJH-
     2H3
TCH3(Carbon%,Proton1%,2,0)+=CH3(WhichOne%,Carbon%,Proton1%,1,3)*sinJH-
     2H3
NEXT
NEXT
REM Transfer back

FOR Carbon%=0 TO 3
FOR Proton1%=0 TO 3
FOR Proton2%=1 TO 2
FOR Proton3%=0 TO 3 STEP 3
CH3(WhichOne%,Carbon%,Proton1%,Proton2%,Proton3%)=TCH3(Carbon%,Proton-
     1%,Proton2%,Proton3%)
NEXT
NEXT
NEXT
NEXT

FOR Proton1%=0 TO 3
FOR Carbon%=0 TO 3
REM Proton3 To Proton 1
REM   Ix > IySz
TCH3(Carbon%,Proton1%,0,1)=CH3(WhichOne%,Carbon%,Proton1%,0,1)*cosJH2-
     H3
TCH3(Carbon%,Proton1%,3,2)=CH3(WhichOne%,Carbon%,Proton1%,0,1)*sinJH2-
     H3

REM IySz > -Ix
TCH3(Carbon%,Proton1%,3,2)+=CH3(WhichOne%,Carbon%,Proton1%,3,2)*cosJH-
     2H3
TCH3(Carbon%,Proton1%,0,1)-
     =CH3(WhichOne%,Carbon%,Proton1%,3,2)*sinJH2H3

REM   Iy > -IxSz
TCH3(Carbon%,Proton1%,0,2)=CH3(WhichOne%,Carbon%,Proton1%,0,2)*cosJH2-
     H3
TCH3(Carbon%,Proton1%,3,1)=-
     CH3(WhichOne%,Carbon%,Proton1%,0,2)*sinJH2H3

REM IxSz > Iy
TCH3(Carbon%,Proton1%,3,1)+=CH3(WhichOne%,Carbon%,Proton1%,3,1)*cosJH-
     2H3
TCH3(Carbon%,Proton1%,0,2)+=CH3(WhichOne%,Carbon%,Proton1%,3,1)*sinJH-
     2H3
NEXT
NEXT

REM Transfer back
FOR Carbon%=0 TO 3
FOR Proton1%=0 TO 3
FOR Proton2%=0 TO 3 STEP 3
FOR Proton3%=1 TO 2
CH3(WhichOne%,Carbon%,Proton1%,Proton2%,Proton3%)=TCH3(Carbon%,Proton-
     1%,Proton2%,Proton3%)
```

```
NEXT
NEXT
NEXT
NEXT
ENDIF

ENDCASE

ENDPROC

DEFPROCch1J
REM Load CH1 coupling constant
JCH1=System(NucNum%,2+Type%)
radian=PI*time*JCH1
cosJCH1=COS(radian)
sinJCH1=SIN(radian)
ENDPROC
:
DEFPROCch2J
REM Load CH2 & H1H2 coupling constants
JCH2 =System(NucNum%,3+Type%)
radian=PI*time*JCH2
cosJCH2=COS(radian)
sinJCH2=SIN(radian)

JH1H2=System(NucNum%,4+Type%)
radian=PI*time*JH1H2
cosJH1H2=COS(radian)
sinJH1H2=SIN(radian)
ENDPROC
:
DEFPROCch3J
REM load CH3, H1H3 & H2H3 coupling constants
JCH3 =System(NucNum%,8)
radian=PI*time*JCH3
cosJCH3=COS(radian)
sinJCH3=SIN(radian)

JH1H3=System(NucNum%,9)
radian=PI*time*JH1H3
cosJH1H3=COS(radian)
sinJH1H3=SIN(radian)

JH2H3=System(NucNum%,10)
radian=PI*time*JH2H3
cosJH2H3=COS(radian)
sinJH2H3=SIN(radian)
ENDPROC


DEFPROCCarbonSC
REM Set Ccosr and Csinr for Carbon C.S.
Cfreq=System(NucNum%,1)
radian=2*PI*time*Cfreq
Ccosr=COS(radian)
Csinr=SIN(radian)
ENDPROC
```

```
DEFPROCProton1SC
REM Set P1cosr and P1sinr for Proton1
P1freq=System(NucNum%,2)
radian=2*PI*time*P1freq
P1cosr=COS(radian)
P1sinr=SIN(radian)
ENDPROC

DEFPROCProton2SC
REM Set P2cosr and P2sinr for Proton2
P2freq=System(NucNum%,3)
radian=2*PI*time*P2freq
P2cosr=COS(radian)
P2sinr=SIN(radian)
ENDPROC

DEFPROCProton3SC
REM Set P3cosr and P3sinr for Proton3
P3freq=System(NucNum%,4)
radian=2*PI*time*P3freq
P3cosr=COS(radian)
P3sinr=SIN(radian)
ENDPROC


DEFPROCmatrix(NucNum%)
WhichOne%=System(NucNum%,11)
CASE System(NucNum%,0) OF
WHEN 0
PRINT'"C:"
FOR x=0 TO 3
PRINT C(WhichOne%,x);" ";
NEXT
WHEN 1
PRINT'"CH:"
FOR y=0 TO 3
FOR x=0 TO 3
PRINT CH(WhichOne%,x,y);" ";
NEXT
PRINT
NEXT
WHEN 2
PRINTTAB(0,0);" "
PRINT'"CH2:"
FOR z=0 TO 3
FOR x=0 TO 3
FOR y=0 TO 3
IF ABS(CH2(WhichOne%,x,y,z))>1E-6 THEN
PRINTTAB(y*17+2);CH2(WhichOne%,x,y,z);" |";
ELSE
PRINTTAB(y*17+2);"0 |";
ENDIF
NEXT
PRINT"                          "
NEXT
PRINT'
```

```
NEXT

WHEN 3
FOR w=0 TO 3
PRINTTAB(0,0);" "
PRINT'"CH2:"
FOR z=0 TO 3
FOR x=0 TO 3
FOR y=0 TO 3
IF ABS(CH3(WhichOne%,x,y,z,w))>1E-6 THEN
PRINTTAB(y*17+2);CH3(WhichOne%,x,y,z,w);" |";
ELSE
PRINTTAB(y*17+2);"0 |";
ENDIF
NEXT
PRINT"                              "
NEXT
PRINT'
NEXT
fgh=GET
NEXT
ENDCASE
ENDPROC

DEFPROCerr
ON ERROR OFF
REPORT:PRINT;" at line ";ERL
PROCmatrix(WhichOne%)
END
```

Appendix 5

Computer Program used in the Optimisation of SNARE.

```
*close
MODE "X1024 Y768 C256 EX1 EY1 F60"
CLG
OFF
ON ERROR PROCerr
*KEY 1 "QUIT|M "
REM@="F4.2"
LIBRARY SymLib

REM Start
*CLOSE
OA%=OPENOUT("ADFS::210MB.$.Works.PhD.Snare.SNARETrans.OUTPUT.A")
OB%=OPENOUT("ADFS::210MB.$.Works.PhD.Snare.SNARETrans.OUTPUT.B")
OC%=OPENOUT("ADFS::210MB.$.Works.PhD.Snare.SNARETrans.OUTPUT.C")
AJ=145 : REM Must define Average J value
PROCInit(9) : REM Inititialize for (x) nuclei of each type

REM Define system:
PROCDefine(1,0,0,140,0,0,0,0,0,0,0)
PROCDefine(1,0,0,160,0,0,0,0,0,0,0)
PROCDefine(1,0,0,180,0,0,0,0,0,0,0)
PROCDefine(2,0,0,0,120,120,0,0,0,0,0)
PROCDefine(2,0,0,0,130,130,0,0,0,0,0)
PROCDefine(2,0,0,0,130,130,0,0,0,0,0)
PROCDefine(3,0,0,0,0,120,120,0,120,0,0)
PROCDefine(3,0,0,0,0,130,130,0,130,0,0)
PROCDefine(3,0,0,0,0,140,140,0,140,0,0)

REM Pulse Sequence:

REM PULSE CODE,   ACTION, PARAM
REM H+X, Proton  X Pulse, Angle in degrees
REM H+Y, Proton  Y Pulse, Angle in degrees
REM H-X, Proton -X Pulse, Angle in degrees
REM H-Y, Proton -Y Pulse, Angle in degrees
REM C+X, Carbon  X Pulse, Angle in degrees
REM C+Y, Carbon  Y Pulse, Angle in degrees
REM C-X, Carbon -X Pulse, Angle in degrees
REM C-Y, Carbon -Y Pulse, Angle in degrees
REM ————————————————————————
CLS

REM Definre starting magnetizations.
PROCBoltzmann
FOR Nucleus%=0 TO nnum%-1
PROCpulse("C+X",90,Nucleus%)
NEXT
SC()=C()
SCH()=CH()
SCH2()=CH2()
SCH3()=CH3()

REM Main loop
FOR Xtime=0 TO 1/(AJ) STEP 1/(AJ)/100
FOR Ytime=0 TO 1/(AJ) STEP 1/(AJ)/100
PROCMStart
FOR Nucleus%=0 TO nnum%-1
```

```
PROCdelay("Xtime",Nucleus%)
PROCpulse("H-Y",90,Nucleus%)
PROCpulse("C-Y",90,Nucleus%)
PROCdelay("Ytime",Nucleus%)
NEXT
PRINT "XTIME : ";Xtime*AJ;",    YTIME : ";Ytime*AJ
a=0
b=0
c=0
FOR Nucleus%=0 TO nnum%-1
XType%=System(Nucleus%,0)
XNumber%=System(Nucleus%,11)
CASE XType% OF
WHEN 0
WHEN 1
a+=CH(XNumber%,0,2)
WHEN 2
b+=CH2(XNumber%,0,2,0)+CH2(XNumber%,0,0,2)
WHEN 3
c+=CH3(XNumber%,0,2,0,0)+CH3(XNumber%,0,0,2,0)+CH3(XNumber%,0,0,0,2)
ENDCASE
NEXT
PRINT#OA%,a
PRINT#OB%,b
PRINT#OC%,c
NEXT
NEXT
END

DEFPROCMStart
C()=SC()     :  TC()=0
CH()=SCH()   : TCH()=0
CH2()=SCH2():TCH2()=0
CH3()=SCH3():TCH3()=0
ENDPROC

DEFPROCBoltzmann
      C()=0:  TC()=0
     CH()=0: TCH()=0
    CH2()=0:TCH2()=0
    CH3()=0:TCH3()=0

    FOR Nucleus%=0 TO nuclei%-1
    C(Nucleus%,3)=1
    CH(Nucleus%,3,0)=1
    CH2(Nucleus%,3,0,0)=1
    CH3(Nucleus%,3,0,0,0)=1
    NEXT
ENDPROC

DEFPROCerr
ON ERROR OFF
*close
REPORT:PRINT;" at line ";ERL
PROCmatrix(WhichOne%)
END
```

Appendix 6

NMR Acquisition Parameters.

A6.1 Parameters for the 23Na NMR spectra of Fluidized and Static TSP (Figures 4.9, 4.10, 4.12, 4.15-4.17).

Parameter	Value
NMR Nucleus Under Observation	^{23}Na
Observation Frequency	23.64 MHz
Observation Offset	60.15 kHz
Data Points	8192
Spectral Width	30030 Hz
Delay	100 µs
Deadtime	5 µs
Number of Scans	14000
Pulse Width	25µs / 45°
Pulse Delay	200 ms
Line Broadening	9.9 Hz

A6.2 Parameters for the 31P NMR spectra of Fluidized and Static TSP (Figures 4.11, 4.13).

Parameter	Value
NMR Nucleus Under Observation	^{31}P
Observation Frequency	36.20 MHz
Observation Offset	77.70 kHz
Data Points	8192
Spectral Width	30030 Hz
Delay	100 µs
Deadtime	5 µs
Number of Scans	64
Pulse Width	15µs / 45°
Pulse Delay	1 min
Line Broadening	0 Hz

A6.3 Parameters for the 23Na NMR spectra of Partially Dehydrated TSP (Figure 4.18).

Parameter	Value
NMR Nucleus Under Observation	^{23}Na
Observation Frequency	23.64 MHz
Observation Offset	60.15 kHz
Data Points	8192
Spectral Width	30030 Hz
Delay	80 µs
Deadtime	5 µs
Number of Scans	329
Pulse Width	20µs / 36°
Pulse Delay	100 ms
Line Broadening	0 Hz

A6.4 Parameters for the 31P NMR spectra of Partially Dehydrated TSP (Figure 4.19).

Parameter	Value
NMR Nucleus Under Observation	^{31}P
Observation Frequency	36.20 MHz
Observation Offset	77.58 kHz
Data Points	8192
Spectral Width	30030 Hz
Delay	80 µs
Deadtime	5 µs
Number of Scans	1024
Pulse Width	8µs / 24°
Pulse Delay	4 s
Line Broadening	0 Hz

A6.5 Parameters for the 27Al NMR spectra of Fluidized and Static Aluminium Granules (Figures 4.20- 4.28)

Parameter	Value
NMR Nucleus Under Observation	^{27}Al
Observation Frequency	23.30 MHz
Observation Offset	77.70 kHz
Data Points	8192
Spectral Width	30030 Hz
Delay	100 µs
Deadtime	5 µs
Number of Scans	14000
Pulse Width	30µs / 45°
Pulse Delay	200 ms
Line Broadening	9.9 Hz